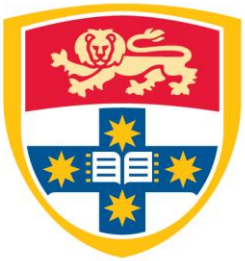

THE UNIVERSITY OF SYDNEY

An experimental investigation into the role of autoignition in turbulent flame stabilisation

by

Andrew Ralph William Macfarlane

A thesis submitted in fulfilment for the degree of Doctor of Philosophy

PhD

in the

Faculty of Engineering and I.T.

School of Aerospace, Mechanical and Mechatronic Engineering

Declaration of authorship

I, Andrew Macfarlane, hereby declare that the work presented in this thesis is entirely my own work and to the best of my knowledge it is all original work. The work presented in this thesis includes work published previously in the: *Combustion and Flame Journal* and the *Proceedings of the Institute of Combustion* Journal, these published papers are recognised in the publication section on page *vi*. This thesis also presents work from three conferences: Two papers from the *11th and 12th Asia-Pacific Conference on Combustion* and a one paper from the *Australian Conference on Laser Diagnostics in Fluid Mechanics and Combustion*. References are included where relevant to indicate the acknowledgement of others work.

(Andrew Macfarlane)

Dedication

This thesis is dedicated to my late mother, Julia, without whom I would never have started my PhD. Her motivation to complete any challenge inspired me to finish this thesis and will always inspire me to succeed in any situation. Who knows you may now have the answers to all we seek.

Acknowledgements

Throughout my PhD I was lucky enough to have Dr. Matthew Dunn as my main supervisor and Prof. Assaad Masri as my auxiliary supervisor. They provided constant guidance and support throughout my research, their passion and discussions in the field of combustion provided inspiration and dedication throughout my studies. Their extensive knowledge in both theoretical and experimental combustion enabled me to complete this thesis with understanding and confidence. I would therefore like to thank them for all their time and effort they gave me throughout my studies.

I would also like to thank all my co-workers at Sydney University, and further, the help from Mrinal Juddoo who has great experience and knowledge in the field of experimental combustion. Without his help I wouldn't have been able to navigate the combustion lab, setting up: cameras, lasers, optics and the experiments.

I want to thank Georgia Regan for providing unwavering support while working on papers and in the days leading up to final submission. Also thankyou to the help from Gajendra Singh with operating the cameras and enabling a large campaign of experimental work, your attention to detail and diligence was appreciated. Thank you to Sebastian Galindo Lopez with whom I have shared my office with at Sydney University, providing support through long hours of work. Also, for providing someone with whom I could 'bounce' ideas off and get feedback from.

Finally, thank you to my family, my mother, father and sister who always provide unwavering encouragement and support for whatever I engage in.

Publications

Research towards this thesis has resulted in the publication of three journal papers, in two different journals: *Combustion and Flame* and the *Proceedings of the Institute of combustion*. It further includes papers from conferences at the *Asia-Pacific Conference on Combustion* and from the *Australian Conference on Laser Diagnostics in Fluid Mechanics and Combustion*. For these three journal papers, I was lead author with Dr. Matthew J. Dunn, Prof. Assaad R. Masri and Dr. Mrinal Juddoo as co-authors. As lead author I setup and ran the parametric fuel campaign and setup and ran the PLIF high-speed experiment with Dr. Dunn and Dr Juddoo. In addition, I wrote all the processing code and created the papers and their: figures, tables and the initial paper drafts.

The published journal papers full references are listed below:

- A.R.W. Macfarlane, M.J. Dunn, A.R. Masri, The influence of fuel type and partial premixing on the structure and behaviour of turbulent autoigniting flames, Proc. Combust. Inst. 37 (2019) 2277-2285[1].
- A.R.W. Macfarlane, M.J. Dunn, M. Juddoo, A.R. Masri, Stabilisation of turbulent auto-igniting dimethyl ether jet flames issuing into a hot vitiated coflow, Proc. Combust. Inst. 36 (2017) 1661-1668 [2].
- A.R.W. Macfarlane, M. Dunn, M. Juddoo, A. Masri, The evolution of autoignition kernels in turbulent flames of dimethyl ether, Combust. Flame 197 (2018) 182-196 [3].

The conference papers include:

- A.R.W. Macfarlane, M.J. Dunn, M. Juddoo, A.R. Masri Stabilization of Turbulent Auto-Igniting DME Jets Issuing in Hot Vitiated Coflows, Australian Combustion Symposium (2015) [4].

- A.R.W. Macfarlane, M.J. Dunn, M. Juddoo, A.R. Masri High-Speed PLIF Measurements of OH and CH_2O in Turbulent Auto Igniting Flames of DME, 7th Australian Conference on Laser Diagnostics in Fluid Mechanics and Combustion (2015) [5].
- A.R.W. Macfarlane, M.J. Dunn, M. Juddoo, A.R. Masri Stabilization of Turbulent Auto-Igniting Hydrogen Jets Issuing in a Hot Vitiated Coflow,11th Asia-Pacific Conference on Combustion (2017) [6].

The chapters in this thesis that predominantly contain published work are: The Parametric fuel study (Chapter 4) which includes the paper: *The influence of fuel type and partial premixing on the structure and behaviour of turbulent autoigniting flames.* The High-speed (10 kHz) results: CH2O/OH PLIF chapter (Chapter 7) predominantly consists of two papers: *Stabilisation of turbulent auto-igniting dimethyl ether jet flames issuing into a hot vitiated coflow [2]* and *The evolution of autoignition kernels in turbulent flames of dimethyl ether [3]*.

Abstract

This thesis presents experimental and complimentary numerical results based on a turbulent jet in a hot coflow burner (JHC). The thesis focuses on understanding and exploring the relative importance of autoignition in the flame stabilisation process for the conditions, temperatures and fuels considered. The influence of fuel type is explored using a range of gaseous fuels including: alkanes, alkenes, H_2 and dimethyl ether (DME). High-speed (10 kHz) measurements of chemiluminescence and sound are applied to all flame cases, for all fuels, the measurements are used to temporally resolve the interaction of the flame base with ignition kernels. Similar flame-base and ignition kernel interaction characteristics are found for all fuels where the formation and merging of rapidly growing ignition kernels stabilise these flames. A measurement campaign employing 10 kHz OH and CH_2O Planar Laser Induced Fluorescence combined with volumetric chemiluminescence imaging is applied to the ignition kernel formation region in DME flames. The measurements identify regions of low and high-temperatures respectively, with their spatial overlap representing heat release. The kernel heat release measurements indicate that differing degrees of autoignition stabilisation occurs for DME flames, specific to high and low coflow temperature flames. High coflow temperature flames produce lower heat release ignition-kernels; hence these flames are believed to have reduced dependence on autoignition for stability.

Zero-dimensional and one-dimensional numerical simulation results, obtained in this thesis, agree with the findings from the hot coflow experiments. The 0-D ignition delay times are shown to successfully capture the different fuels lift-off height sensitivities with coflow temperature. The sensitivity of relatively low coflow temperatures are particularly well represented by delay times, with a linear correlation between delay times and experimental lift-off heights. To replicate the strained and diffusive conditions induced by the JHC burner, unsteady 1-D counter-flow simulations were applied. These simulations, using DME, identify that for high coflow temperature flames, the

ignition kernels produce lower heat release, since they are igniting leaner. Using CH_4 with the same counter-flow setup, the effect of strain-rate was explored. It was found that increased strain rate delays ignition, since the unity balance between diffusion and production fluxes of CH_2O is also delayed. Furthermore, under autoignition conditions, the counter-flow solver, in addition to a premixed solver, show CH_2O convection and production fluxes increase, with a corresponding diffusive decrease.

Contents

Table of Figures

List of Tables

Abbreviations

0-D	Zero Dimensional
1-D	One Dimensional
2-D	Two Dimensional
3-D	Three Dimensional
L_H	Lift-off Height
HR	Heat Release
PLIF	Planar Laser Induced Fluorescence
LIF	Laser Induced Fluorescence
Nd:YAG	Neodymium-doped Yttrium Aluminium Garnet
CMOS	Complimentary Metal-Oxide-Semiconductor
DNS	Direct Numerical Simulation
RANS	Reynolds Average Navier Stokes
SNR	Signal-to-Noise Ratio
FOV	Field Of View
RMS	Root Mean Squared
STD	Standard Deviation
PDF	Probability Density Function
PAH	Polycyclic Aromatic Hydrocarbon
SI	Spark Ignition

CI	Compression Ignition
AIT	Autoignition Temperature
JHC	Jet in Hot Coflow
EGR	Exhaust Gas Recirculation
FWHM	Full Width Half Maximum
MW	Molecular Weight
PPM	Parts Per Million

Symbols

a	Strain Rate
x	Axial length
r	Radial length
x/D	non-dimensional axial length
r/D	non-dimensional radial length
D	Diameter
U	Velocity
P	Pressure
T	Temperature
S_L	Flame Speed
V_L	Propagation velocity

Re	Reynolds Number
Da	Damköhler Number
Sc	Schmidt number
f	Boltzmann fraction
Q	PLIF quenching
$Ø$	Diameter
S_{LIF}	PLIF signal

Subscripts

J	Jet
C	Coflow
St	Stoichiometric
LIF	Laser induced Fluorescence
MR	Most Reactive
Le	Leading edge
Tr	Trailing edge
K	Kernel

Greek symbols

$Φ$	Equivalence ratio
$τ$	Delay time

ζ	Mixture fraction
ρ	Density
μ	Dynamic viscosity or mean
χ	Scalar Dissipation
$\dot{\omega}$	Species production rate

Chemical Symbols

CH_3OCH_3	Dimethyl Ether
CH_4	Methane
H_2	Molecular Hydrogen
C_2H_6	Ethane
C_2H_4	Ethylene
C_3H_8	Propane
C_3H_6	Propene
C_4H_8-1	1-Butene
NO_2	Nitrous Oxide
NO	Nitric Oxide
CH_3	Methyl radical
OH	Hydroxyl radical

HO_2	Hydroperoxyl radical
H_2O_2	Hydrogen peroxide radical
CH_2O	Formaldehyde radical
HCO	Formyl radical

Chapter 1. **Introduction**

With a constantly increasing worldwide population, industry and urbanisation, the demand for energy is predicted to rise by 30% in 2040 [7], with the most substantial energy demand increase from China and India. Furthermore, the United Nations, in 2015, agreed upon a specific target on ensuring access to affordable, reliable and 'modern energy' for all by 2030, to provide universal access to electricity and clean cooking. Current energy demands are predominantly 'met' by carbon-based, 'fossil fuels', with coal accounting for 29.2 % of the global energy production, and oil and gas accounting for 32.9% and 24% respectively [8]. The use of 'fossil fuels' contributes to a net increase in CO_2 emissions, with most of the energy extracted through combustion-based means, typically through converting heat energy into mechanical energy.

The global renewable energy consumptions is broken up predominantly by hydro and wind energy, at 6.8 % and 1.4 % respectively, with other fuels including nuclear (4.4 %), solar, geothermal and bioenergy making up the rest [8]. Despite the large increase in renewable fuels, global oil and natural gas demand is still increasing, where natural gas demand is expected to increase by 70% in 2050 [9]. Furthermore, the energy density requirements of fuel, in particular, for the transportation industry are such that combustion will remain prevalent in the near future [10, 11]. The current and projected significant future usage of combustion, using renewable and fossil fuels, sets the motivation of this thesis, and combustion research in general. Therefore, the combustion community's research primarily focuses on maximising energy efficiency, minimising pollutants, including: CO_2, CO, SO_X, NO_X, particulate matter and developing predictive design tools [12, 13].

Combustion processes can be broadly broken into two categories: premixed and non-premixed combustion, with partial premixing of the fuel and oxidant at various degrees occurring in between.

An effective method of controlling a fuels power output and achieving desired flame velocities, is to premix the fuel with an oxidiser in the required ratio (Air/Fuel). Furthermore, being pre-mixed these flames are not limited by mixing time scales. The premixing of fuel and oxidiser, however, at stoichiometric conditions produces high NOx levels; additionally, it can lead to an explosive environment and potential flashback conditions. As such, Non-premixed flames are often used; these flames are more stable and less prone to blow-off than premixed fuels, in addition to being less susceptible to thermo-acoustic oscillation. Furthermore, since it is not necessarily safe to store fuels mixed with an oxidant, and non-premixed flames are more stable, non-premixed fuels are often used, such as the household gas stove and older gas turbine designs. The non-premixed flame has the fuel and oxidant separate, therefore, the combustion characteristics become mixing and diffusive rate dependant [14-17].

Fuel ignition of premixed or non-premixed fuels can occur via spark ignition or autoignition, where the latter is explored in this thesis. Spark ignition or 'forced' ignition occurs when excessive and finite heat/energy is supplied to form an ignition kernel that grows and can be self-sustained [18]. The minimum ignition energy (MIE) is the minimum amount of energy that is required to be deposited, by a spark into a homogenous fuel and oxidant mixture, to achieve ignition; it is primarily considered to be a function of the mixture composition, temperature, pressure and the sparks geometry relative to the flame thickness [19-21]. Compared to spark ignition, autoignition occurs when a mixture is heated such that the exothermic chain generation exceeds chain termination [22]. The conditions for autoignition to occur are dependent on the mixture's initial temperature, composition and pressure as well as for turbulent flows, the local turbulence levels and composition gradients. The initial temperature above the given fuels autoignition temperature (AIT), dictates the ignition time (delay time) and chain branching pathways.

The autoignition of fuels has an important role in certain applications including: compression ignition (CI) engines, second stage/ reheat turbines and exhaust gas recirculation (EGR). Compression ignition (CI) engines produce autoignition conditions due to high pressures [23], inducing high-temperatures. Second stage gas turbines/ sequential combustors [24-26] use the hot products, from the first stage combustor to ignite and stabilise the flame in the second stage process. Exhaust gas recirculation (EGR) [27] is used to reduce engine temperatures, to minimise thermal NO, and to alter fuel ignition delay times [28]. Autoignition has also been identified to be an important mechanism in flame stabilisation, in modelling swirled flow burners, relevant to gas turbine combustors [29]. Furthermore, autoignition based combustion needs to be controlled in a range of systems such as spark ignition engines [30] in the form of 'knocking', which is caused by autoignition of a portion of the end-gas [31]. It is important to understand the conditions for which autoignition will occur, in order to prevent damages [32-34] and increase operating efficiency.

Understanding the dynamics leading to autoignition in industry-based applications, such as within engines is significantly complicated by the environment for which the fuel is combusted within. These complications include: stratified fuel composition, pressure fluctuations, acoustic feedback/ instabilities [35, 36], wall interactions and unquantified turbulent fields. The additional complexity of turbulence occurs when the fuel or oxidant is injected at high velocities, required to increase fuel consumption and power output. Turbulence, however, is still under significant investigation to further understand how it affects any flow parameter such as: velocity, temperature and pressure. The effect of turbulence on autoignition, whether it delays or improves ignition due to additional mixing and temperature/species diffusion, is investigated in this thesis. Due to the multiple complexities in industrial setups, simplified laboratory flames are studied, the experiments are designed to decouple the effect of premixing, pressure and turbulence interaction, and for the focus of this thesis, their effect on autoignition.

To study autoignition from a fundamental kinetics perspective, autoignition is predominantly studied using a shock-tube setup, where the rapid pressure and temperature rise from a shock wave is used to auto-ignite the gas mixture [37]. Shock tubes, study the effect of premixing, temperature, composition and pressure on autoignition delay times, for a given fuel in a quiescent homogenous environment. To study the impact of flow field strain variations and composition gradients on autoignition, hence species diffusion, the Jet in Hot Coflow (JHC) burner, as explored in this thesis, has been utilised by many other studies in literature. The JHC setup injects a central fuel jet into a hot shrouding coflow that ignites the fuel. Autoigniting JHC flames have been studied under laminar [38] and turbulent conditions, with some of the first turbulent autoigniting measurements reported by Cabra et al. [39]. This thesis focuses on studying the characteristics of the flame stabilisation process for turbulent JHC flames, with a focus on understanding the relative importance of autoignition and premixed flame propagation in the flame stabilisation process.

The experimental measurements in flames can be broken into two main categories: intrusive and non-intrusive measurements. Intrusive measurements are typically simple and inexpensive; however, the flow is disturbed, i.e., thermocouple or physical probing of products results in spatial and temporal averaging, and overall a biasing of the results that is often unable to be quantified. Non-intrusive measurements occur when a laser or other optical technique is used to ‘probe’ or record the flame, such non-intrusive measurements form the core of the experimental measurements reported in this thesis. These measurements range from a multi camera planar laser-induced fluorescence (PLIF) through to high-speed chemiluminescence imaging with sound.

Since experimental measurements cannot currently measure the temporal and full 3-D spatial evolution of all species and velocity simultaneously in a turbulent flow, numerical simulations are a valuable tool to investigate turbulent combustion either in their own right, or as a complementary tool to experimental measurements. Numerical simulations span a broad range of complexities ranging from 0-D to 3-D cases and from laminar to turbulent simulations. The more complex

turbulent models either fully resolve the full 3-D flow field using direct numerical simulations (DNS) [40] or model the stochastic turbulent fields using various turbulent models such as PDF methods [41]. Laminar calculations ranging from 0-D to transient 1-D calculations, as is used in this thesis, provide indicative species measurements in the turbulent JHC flames, and are used to indicate if delay times represent the global characteristics of these flames [42]. Modelling results using a simplified turbulent DNS model have been able to successfully determined that JHC flames are stabilised by autoignition, and that autoignition in partially premixed flames occurs for lean mixture fractions [40, 43] (most reactive mixture fractions), since the oxidiser is much hotter than the fuel in JHC flames. The concept of the most reactive mixture fraction occurring in the lean region is further investigated in this thesis using laminar based calculations for a variety of fuels.

Significant experimental work has been done on the turbulent JHC burner for jets using H_2 and CH_4, as the fuel, by various groups, including: Cabra et al. [39], Ardnt et al [44], Oldenhof et al [45] and Gordon et al. [46]. Numerous studies have explored the numerical modelling of the JHC burner, with notable example papers in the field being by Yoo et al. [40, 43], Hilbert et al. [47] and Gordon et al. [48], with the primary finding of these papers being that the flames studies are stabilised by autoignition. However, there have not been many studies that have looked at simulating the JHC burner for a range of fuels; cases which are explored in this thesis, experimentally, including fuels such as: complex oxygenated fuels (dimethyl ether) and heavier gaseous fuels, including ethane, ethylene, propane, propylene and butane. It is noted recent work reported by Sakensa et al. on investigating DME and C_3H_8 under JHC conditions [49] is one of the few experimental studies looking at the influence of fuel type for JHC burners. The newly explored fuels in this thesis that feature a wide variety of fuel reactivity and chemical structure are examined using the JHC burner to determine: 1) If common features exist between fuels with respect to the stabilisation dynamics. 2) If all fuels are stabilised by autoignition and exhibit the characteristic trait of ignition kernels forming and growing to meet the down-stream advecting flame base, as observed for CH_4 [50]. And 3) If the

global flame features such as lift-off height for each fuel can be well represented using laminar calculations.

Dimethyl ether (DME) is of particular interest in this thesis as it is a promising second-generation biofuel that can be made at large scale [51] and it is a viable alternative fuel to diesel under compression ignition conditions [52]. DME features a more complex chemical kinetic mechanism and pathway, compared to similar sized hydrocarbons, the fuel bound oxygen in DME enhances the richness of the low temperature chemistry and the autoignition process. This therefore makes DME an important fuel to investigate and compare to other similar molecular weight hydrocarbon fuels under turbulent JHC conditions, where low-temperature chemistry could potentially be important.

Thesis content

The aim of this thesis is to investigate and understand the role of autoignition in turbulent flame stabilisation, for a range of fuels, in well-controlled laboratory scale experiments, using advanced optical diagnostics. These measurements are studied at the Sydney University, using the jet in hot coflow burner (JHC), using non-intrusive optical diagnostics. For all fuels, chemiluminescence at high-speed (10 kHz) simultaneously with measurements of sound identifies the interaction of ignition events into the main flame. Using ignition statistics and the relevant measured flame velocities, the importance of ignition kernels for stability in these flames is studied for all fuels. To further diagnose the autoignition events, a separate experiment to the parametric study of fuel type is performed for DME flames. This experiment uses high-speed (10 kHz) OH and CH_2O PLIF measurements for a range of premixed and diluted DME flames. The high abundance of CH_2O in DME flames enabled high-speed kernel heat release (spatial product of OH and CH_2O) measurements to be obtained. The heat release measurements are used to diagnose the relative importance of ignition kernels ‘feeding’ into and stabilising the flame. Using these high-speed

diagnostics, it is shown that higher coflow temperatures have reduced kernel heat release, and therefore autoignition is less fundamental to stabilisation.

The experimental results from the JHC are interpreted using laminar calculations which identify the dependence, or lack thereof, for fuel ignition delay times on flame stability/lift-off heights. Separate calculations employ an unsteady solver for counterflow and premixed propagating flames. These simulations explore the ignition mixture fraction (most reactive mixture fraction) and the effect of strain rate on transport budgets leading to and delaying ignition. Finally, counter-flow simulations are employed to identify the effect of the ignition mixture fraction due to varying coflow temperatures and jet premixing. The laminar simulations indicate that higher coflow temperatures ignite at leaner mixtures with a smaller delay time in addition to being more resistant to higher strain rate.

The aims of this thesis are summarised as follows:

1. To understand the degree to which autoignition stabilises flames issuing into a JHC burner, using high-speed (10 kHz) sound and chemiluminescence measurements.
2. Whether fuels ranging from hydrogen through to C_4 hydrocarbons, exhibit similar stabilising characteristics despite the range of coflow temperatures required for each fuel.
3. Measure the relative formation of PLIF CH_2O and OH in DME flames at high-speed (10 kHz), focusing on the formation of CH_2O relative to the OH flame base.
4. Measure ignition kernel heat release in DME flames at various coflow temperatures, at high-speed (10 kHz), to determine the relative importance of kernels.
5. Verify the high-speed chemiluminescence experimental results using laminar numerical simulations.

6. Investigate the use of an unsteady numerical counter-flow solver to identify the effect of strain rate on autoignition and the most reactive mixture fraction. Then use the solver to understand the heat release PLIF results from the DME experiment.

The JHC burner used for most of this work has the fuel jet protruding 70 mm into the heated environment, as such, a degree of preheat is observed for various fuels and fuel injection velocities. Therefore, this thesis introduces a new actively cooled jet; the new jet keeps the fuel approximately at room temperature as it exits the nozzle into the heated environment. Measurements based on this burner are presented for three fuels with various coflow temperature ranges, identifying the effect of active cooling relative to the 'old' burner.

The thesis chapter breakdown is as follows:

Chapter 2 examines previous work in literature for experimental and numerical studies on the autoignition burners, including the low-temperature chemistry and conditions promoting ignition. These fundamental concepts will be further referenced within this thesis. This chapter will also explore the diagnostic techniques used for combustion and those further utilised in this thesis.

Chapter 3 introduces the burner used for most of this thesis work, the fuels and coflow flow conditions used to obtain repeatable experimental conditions. It further describes the variations in the fuel Reynolds number and stoichiometric quantities for the various fuels and velocities implemented.

Chapter 4 presents the fuel parametric study for a range of gaseous hydrocarbons and presents the high-speed chemiluminescence results for the flame base and kernel interaction. Comparative observations are made across all fuels, despite the relative difference in coflow temperatures.

Chapter 5 introduces the high-speed (10 kHz) OH/CH_2O PLIF setup; it further describes the correction methods used for post processing of these signals.

Chapter 6 presents the high-speed OH PLIF kernel formation results for fuels, H_2 and CH_4.

Chapter 7 explores the high-speed (10 kHz) OH and CH_2O PLIF for DME, focusing upon autoignition kernels. The chapter determines the physical kernel formation properties: size, growth-rate and aspect ratio, and more importantly the heat release for various premixing ratios of DME and air for two jet velocities.

Chapter 8 presents results with a focus on CH_4, for two unsteady laminar simulations: counter-flow and premixed flames. The counter-flow simulation identifies the ignition mixture fraction for various strain rates and premixing air ratios, CH_2O transport budgets identify the conditions required for ignition.

Chapter 9 provides a discussion of all the chapters, interlinking the parametric study of fuel types with the DME heat release measurements, how the laminar calculations verify the results discovered in each section.

Chapter 10 introduces the new actively cooled jet and new lift-off-height results compared to those obtained from the old burner.

Chapter 11 presents the thesis conclusion, outlining the major findings and results within this thesis.

Chapter 12 presents future experimental work to be done on the JHC burner, to improve and confirm the results found in this thesis.

.

Chapter 2. **Background**

This chapter reviews and analyses the background and literature relevant to this thesis, namely the stabilisation of turbulent auto-igniting flames. A large variety of gaseous fuels, from hydrocarbons to H_2, are explored in the hot coflow burner, with a focus on the second-generation biofuel dimethyl ether (DME). Therefore, a summary of these fuels under autoignition conditions is explored in this chapter with emphasis given to DME. Autoignition has been previously studied both numerically and experimentally in zero-dimensional reactors, and for 1-D, 2-D and 3-D laminar and turbulent flames, which will be reviewed in this chapter. An emphasis will be placed on reviewing studies that investigate lifted flame stabilisation from the aspect of kinetics, combustion modes and flow geometries, such as a jet in a hot coflow (JHC) or hot crossflow.

Experimental techniques that are employed in this thesis are high-speed Planar Laser Induced Fluorescence (PLIF) and line of sight chemiluminescence imaging, with the relevant literature for these techniques reviewed in this chapter. Although the main investigation method utilised in this thesis is experimental, laminar flame simulati2ons are utilised extensively to interpret experimental results, with unsteady 1-D simulations further used as an investigation tool within its own right. As such, a brief review of the laminar flame simulation methods and relevant literature is also investigated.

2.1 **Autoignition kinetics**

The autoignition of a fuel depends on the exothermic reactions of species which involve: chain initiation, chain propagation and finally chain termination [53]. Chain branching produces exothermic reactions, and through radical recombination, lead to ignition and thermal runaway. The reaction process is given by Glassman [22], where ignition is determined by the competition between

the forward chain branching and chain termination reactions. Chain branching must be larger than chain termination for ignition to occur, where these reactions depend on the initial fuel temperature and pressure. The minimum autoignition temperature (AIT) for ignition to occur, for hydrocarbons has been significantly investigated by Robinson et al. and Suzuki et al. [54, 55]. Furthermore, relatively high or low temperature chain branching will further occur through various pathways leading to radical pooling or termination, determined predominantly by the initial temperature [22].

For paraffinic/alkane hydrocarbons, low temperature ignition and chain branching occurs through the oxidation of the alkyl ($R^{\cdot}$) radical ($R^{\cdot} + O_2 \overset{K_c}{\rightarrow} R^{\cdot}O_2$), where a sequence of alkyl-peroxy and alyl-hydroperoxy reactions leads to the branching mechanism for ignition. An indication of ignition is based on the balance of forward and reverse reactions, given by the reaction rate (K_c) in Eq. (2.1) which is dependent on temperature (T), pressure (P) and the O_2 mole fraction (X_{O_2}) given by Eq. (2.2).

$$\frac{[R^{\cdot}O_2]}{[R^{\cdot}][O_2]} = k_c \tag{2.1}$$

$$P = \frac{RT}{X_{O_2} K_c} \tag{2.2}$$

Westbrook et al.[56] determined that at higher temperatures the $R^{\cdot}O_2$ reaction decreases and the alkyl radical leads to the hydroperoxyl radical ($R^{\cdot} + O_2 \rightarrow R' + HO_2$) and ignition is due to the production of OH ($H_2O_2 + M \rightarrow 2OH + M$). The time leading up to the formation of H_2O_2 is the induction time, $\tau_{C,}$ ultimately leading to ignition (τ). For intermediate temperatures, the H_2O_2 ($H + O_2 \overset{k_2}{\rightarrow} HO_2 + M$) radical may form and this is in competition to chain branching: $H + O_2 \overset{k_3}{\rightarrow} OH + O$. Westbrook [57] further identifies that when H_2O_2 decomposes rapidly, a flood of reactive OH radical species is generated which completes the consumption of fuel, leading to further

chain branching, producing autoignition. It is argued by Peters et al. [58] that rapid reaction with fuel molecules keeps radical levels suppressed, and not until the fuel is completely consumed does ignition occur.

The dependence of these low and higher temperature reactions on pressure and temperature is seen in Fig. 2-1. The region to the right or left of each reaction indicates higher or lower temperature ignition. For a specific temperature and pressure, chain branching and ignition doesn't occur, indicated by the grey region in Fig. 2-1. If oxygen levels are decreased, the region of no chain branching increases, leading to MILD or flameless combustion [59].

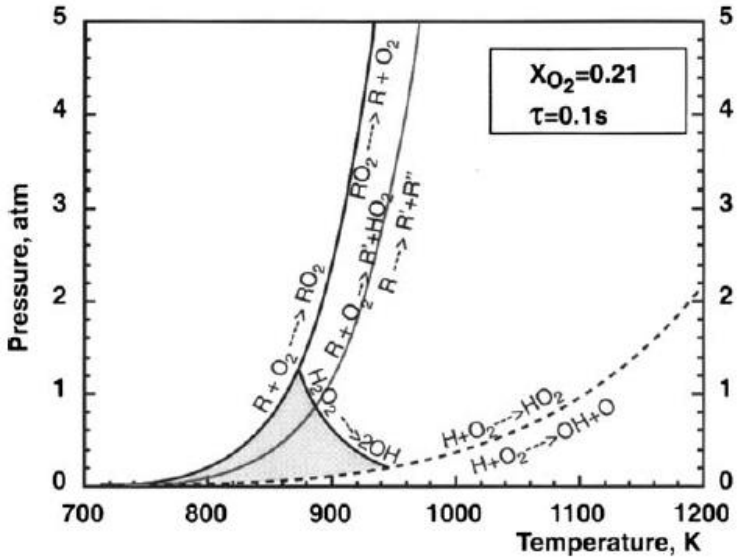

Fig. 2-1 The dependency of pressure and temperature on chain branching leading to ignition. Reproduced from Cavaliere et al. [59].

Miller et al. [60] further identifies that for hydrogen, ignition similarly involves chain initiation through the H radical, through the decomposition of O_2 with chain branching and termination leading to ignition from the HO_2 and finally the OH radical. The rate constants for dominant reactions leading to ignition such as H-abstraction of oxygen have been a topic of

discussion for kinetic modellers such as Baulch et al. [61], with further debate over rate constants for low and high temperature pathways [62].

The modelled ignition delay time results are typically compared to: shock tube results such as those from Burcat et al. [63] and rapid compression engine results from Aleiferis et al. and Goyal et al. [64, 65], these reactors access a range of ignition temperatures and pressures [66]. The results for gaseous alkanes are presented for shock tube measurements in Fig. 2-2 [67], they present similar results to Burcat et al. [63]. The short delay time for ethane (C_2H_6) relative to CH_4 is explained by the chain termination equation with the methyl radical: $CH_3 + CH_3 \rightarrow C_2H_6(+M)$ and chain branching equation with the ethyl radical $C_2H_5(+M) \rightarrow C_2H_4 + H(+M)$, these intermediate reactions agree with both free flame propagation [68] and autoignition [57]. All alkanes up to C_5 exhibit a mix of methyl and ethyl radicals and as such have delay times between the two extremes, ethane and CH_4.

For most alkanes and hydrocarbons, the major rate constants for reactions involving low temperature pathway species include: CH_3, HO_2, CH_3O_2, C_2H_5 and C_2H_4, which are typically altered to match experimental results, such as those done by Simmie et al. [69]. The delay times for alkanes are shown in Fig. 2-2 a) with the corresponding modelled NUI C4 mechanism [70] results, the mechanism includes: the species chemical, transport and thermodynamic properties. A 'sensitivity' of the ethyl rate constant is given in Fig. 2-2 b where improved rate constants for C_2H_4, improves the correlation of the simulation.

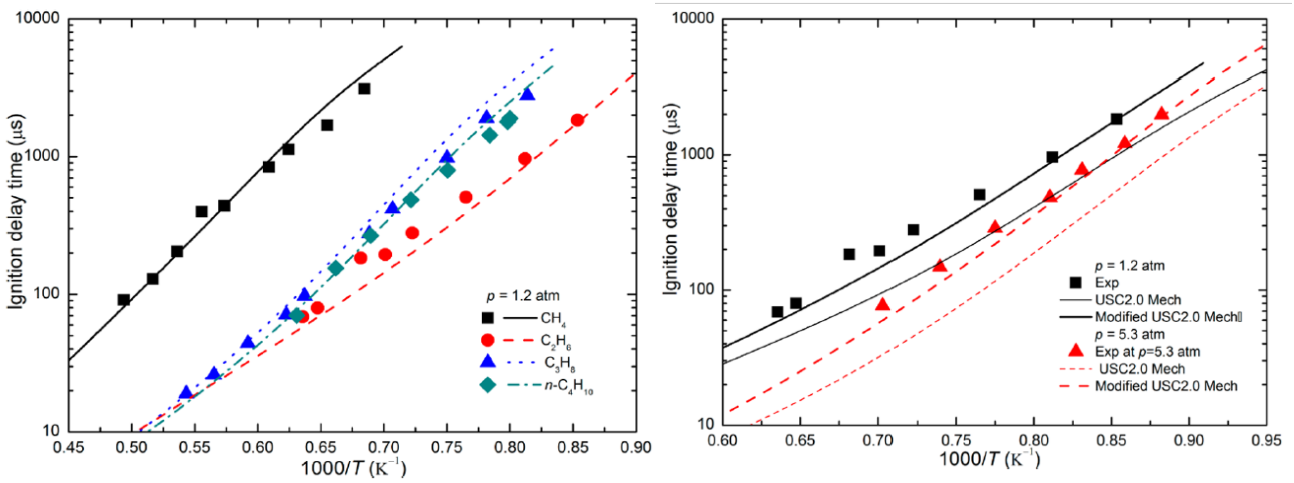

Fig. 2-2 Ignition delay times for alkanes up to C_4 from a shock tube (a), improved rate constants of the ethyl reaction for ethane (b). Reproduced from Metcalfe et al. [70].

Ignition delay times of alkenes (ethylene and propene) are shorter relative to their corresponding alkane's ethane and propane respectively [37]. The addition of ethylene to methane further reduces delay times, as the pooling of radicals leading to ignition increases. The analysis of the ARAMCO [70] mechanism and the USC Mech2 [71] mechanism indicate that to improve experimental and modelling correlations the increased reaction rates for: $C_2H_4 + OCH_2 \rightarrow CHO + H$ and $C_2H_4 + O \rightarrow CH_3 + HCO$ would enhance and decrease the equivalence ratio and pressure dependence respectively.

The investigation of more complex fuels such as DME (CH_3OCH_3) exhibit different phenomena, including negative temperature coefficient (NTC) behaviour. That is, at specific temperatures, non-chain branching reactions dominate the slower chain branching pathways, slowing ignition [22], seen in Fig. 2-3. Dimethyl ether exhibits NTC behaviour at lower pressures, shown by Fast et al. [72], and lower temperatures than other gaseous hydrocarbon fuels. For DME, increased temperature and equivalence ratio increases the temperature for which NTC behaviour occurs, seen by the work from Burke et al. [73]. The most inhibiting chain terminating reaction is $CH_2OCH_2H \rightarrow 2CH_2O + OH$, this reaction competes with the chain branching reaction involving molecular oxygen

[73]. Fast et al. [72] further identifies the peroxy radicals are deterred in the low temperature NTC region.

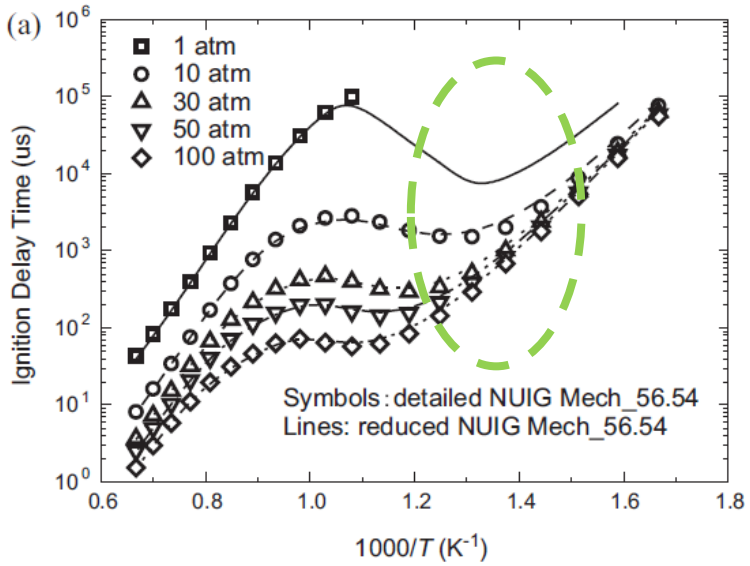

Fig. 2-3 Ignition delay times of DME with temperature for a range of pressures, comparing the Pan (reduced NUIG) [74] to the Burke (detailed NUIG) [73] mechanism. The NTC behaviour is indicated by the dashed ellipse. Reproduced from Pan et al. [75].

At high temperatures the most inhibiting reaction for DME, like methane, involves the methyl radical CH_3. The chemical pathway compilation of low and high temperatures reactions led to the formulation of the Burke mechanism [73]. This mechanism has been reduced by Pan et al.[74, 76, 77], identifying at high (T = 1400 K) and low temperatures (T = 600 K) DME is primarily consumed by H-abstraction (87%), OH and CH_3, and only by a small amount from pyrolysis. At higher temperatures, reactions produce CH_3OCH_2 and undergo β-scission to form: CH_3, CH_2O and CH_3O. At lower temperatures the radicals created from CH_3OCH_2O lead to a further 5 isomerization reactions, creating the same CH_3, CH_2O and CH_3O reactions leading to final oxidation pathways.

The comparison between the parent Burke and reduced Pan mechanism is seen Fig. 2-3, with both mechanisms implemented in this thesis.

2.2 Effect of flow conditions and diffusion on ignition

The previous section explored the temperature dependency of ignition of premixed fuels, neglecting compositional space and the effect of species diffusion and transport. The effect of transport is commonly examined using counter-flow experiments as done by Tsuji et al. [78], where a fuel jet is opposed against heated oxidants. It was found that ignition forms on the lean oxidant side since temperature controls the fuel reactivity, recognised as the most reactive mixture fraction (ξ_{MR}).

For counter-flow measurements, ignition is governed like the premixed ignition for CH_4, where the reaction: $H + O_2 \rightarrow OH + O$ and reactions involving CH_3 is critical for ignition. An S shape response of CH_3 pooling with oxidant temperature (a peak in CH_3 at a moderate oxidant temperatures) occurs, this shape identifies that under diffusive conditions, like premixed ignition, competing low and high temperature branching pathways exist. Fotache et al. [79] found that increasing strain rate increases the convection and diffusion of species: CH_3, CH_2O and C_2H_6 out of the ignition reactions, increasing the ignition temperatures. Results from Deng et al. [80] for DME show that as strain rate is increased the ignition temperature with low temperature/NTC reactions increase. The low temperature reactions proceed the reaction flame front, producing a more 'pronounced' S-shape curve than CH_4 given by Zeng et al. [81].

Excluding enclosed flow [82] and counter-flow reactors, the interaction of fuel and the oxidant, and its impact on autoignition is typically studied within hot coflow (JHC) burner configurations, as done by Cabra et al. [39] using a turbulent jet or in laminar jets by Choi et al. [83]. The JHC burner comprises a heated oxidant (air or other) that shrouds a central fuel jet, it enables the study of

autoignition due to mixing and kinetic time scales. The stabilisation of these flames is believed to be partially or strongly dependant on autoignition, opposed to free flame propagation. The stabilisation mechanism in JHC flames (turbulent) is the main focus of this thesis and this background section.

2.2.1 **Laminar-flow autoignition**

The main theory for the free flame stabilisation of lifted non-premixed, non-auto-igniting laminar lifted flames, given by Buckmaster [84] and Dold [85], is that the fuels propagation velocity matches the local flow field velocity. The mixing of non-premixed flames leads to a tribrachial/triple point structure, with a: lean premixed branch, rich premixed branch and a trailing diffusive flame, identified initially by Phillips in 1965 [86]. Laminar non-auto-igniting flames will only lift-off for flames with Schmidt numbers less than unity, excluding coflowing jets shown by Lee et al. and Lawn et al. [87, 88]. The Schmidt (*Sc*) number given in Eq. (2.3) is defined as the ratio of viscosity (υ) to mass diffusion (*D*).

$$Sc = \frac{\upsilon}{D} \tag{2.3}$$

In comparison to laminar free flame propagation, the influence of autoignition in JHC burners for flame stabilisation is evident for fuels that cannot lift-off (due to their low Schmidt number), shown by choi et al. [89] with Schmidt numbers less than unity, such as CH_4 [90, 91]. For these laminar lifted flames, the downstream location of the flame base becomes a competition between premixed, non-premixed [53, 92] and autoignition. In laminar lifted JHC flames with increased coflow temperature, the flames of methane with a relatively low temperature [89] have a tribrachial structure, scaling well with the flow (U_0) and stoichiometric burning velocity (U_0/S_L). Flames with a coflow temperature exceeding T = 1120 K auto-ignited, still displaying a tribrachial

structure, with the lift-off height scaling with the square of ignition delay times. Numerical studies by Al-Noman et al. [93] with methane, confirm a tribrachial flame structure for non-auto-igniting and auto-igniting flames, with autoignition stabilisation indicated by the build-up of: CH_3, CH_2O, HO_2 and H_2O_2. The flame base is established by autoignition chemistry, whilst downstream, species balancing is closer to a 1-D propagating flame structure.

Choi et al. [94] added hydrogen to a methane jet, showing that it decreases the lift-off height, identifying differential diffusion increases the H-abstraction and chain branching reactions, increasing stabilisation. Choi et al. [95] further showed other fuels: ethane, ethylene and propane exhibiting the same autoignition behaviour as CH_4, at temperatures: T = 890 K, 910 K and 890 K respectively. Al-Noman et al. further showed DME [96] to have the same autoignition tribrachial behaviour as hydrocarbons, for a temperature of 900 K. These temperatures correspond to the relative temperature differences in premixed delay times from Fig. 2-2. The preheating of the CH_4 jet, for non-auto-igniting flames, serves to reduce the flame lift-off height, whilst still exhibiting a tribrachial structure [97].

For DME under laminar JHC conditions, NTC behaviour was observed [38] and autoignition stability was identified using the $H_2O_2 + M \rightarrow OH + OH + M$ reaction/explosive modes [98]. Kinetically-stabilised flames are determined for low temperatures: T = 700, 800 and 900 K, with the characteristic low temperature chemistry of DME identified upstream of the flame base. The β-scission $CH_2OCH_2H \rightarrow 2CH_2O + OH$ prevented explosive chain branching/ ignition, whilst downstream, the H-abstraction is prevalent with hydrogen chain branching being important ($H + O2 \rightarrow O + OH$). Increased temperature, T = 1100 K, stops low temperature reactions indicating stabilisation from local premixed flame propagation balancing the local flow velocity.

Krisman et al. [99] concluded for DME flames that premixed conditions influenced stabilisation under autoignition conditions. For lower temperatures (700 K), flames appeared to be

stabilised under premixed flame propagation, with a tribrachial branch structure observed in Fig. 2-4, where the stabilisation point meets the stoichiometric contour (*). Increased temperature led to multiple branches of heat release, producing low temperature chemistry i.e., producing the $CH_3OCH_2O_2$ radical. The $CH_3OCH_2O_2$ radicals were found in richer regions (right side of the solid line, squares) for relatively lower temperatures (900 and 1100 K), whilst in leaner regions for higher temperatures (1300 and 1500 K).

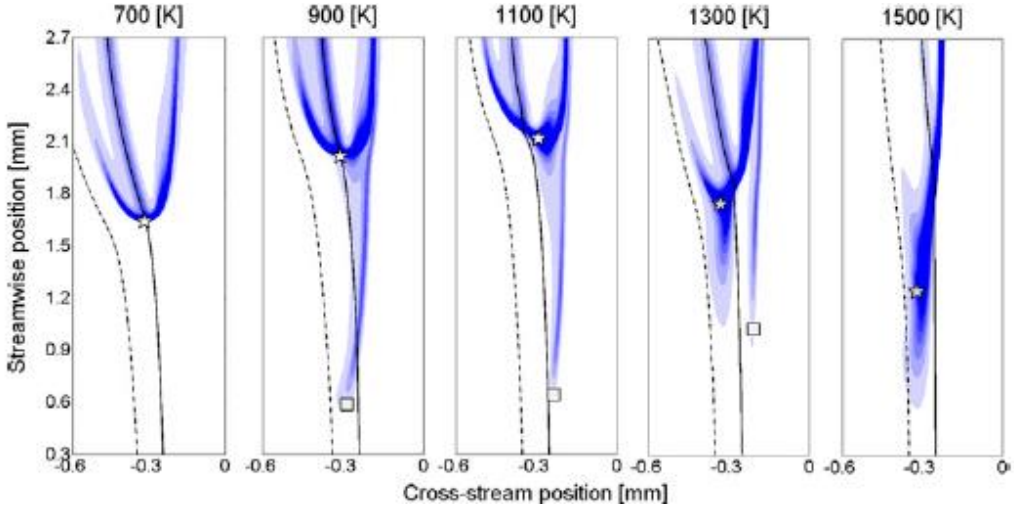

Fig. 2-4 Heat release results reproduced from the work by Krisman et al. [99]. Different shading marks heat release, the solid line marks the stoichiometric contour and the dashed lean marks lean regions ($\varphi = 0.1$). The star (*) indicates the stabilisation point, whilst the square marks the furthest point upstream of ignition.

2.2.2 **Turbulent autoignition**

The effect of turbulence on ignition dynamics for partially premixed fuels is identified to create premixed or partially premixed conditions, where the ignition of lean premixed pockets influences the ignition of non-premixed mixtures, identified by Domingo et al. [100]. Counter-flow simulations with imposed turbulence identifies, for mild turbulence, the ignition temperature is decreased, where

the HO_2 branching is suppressed. However, as turbulent mixing increases the ignition temperature increases [101], explained due to relevant auto ignition species diffusing out of the reaction front [102]. Furthermore, stratified mixtures under turbulent conditions increases auto ignition prevalence [103].

Competing theories to the stabilisation of turbulent lifted non-premixed flames (non-auto-igniting flames) indicate that stabilisation is mixing controlled. The flames stabilise at locations where the premixed stoichiometric flame propagation speed matches the local flow velocity [15, 104, 105]. To maintain ignition, the chemical reaction rate should be larger than a critical strain so flame extinction doesn't occur [14]. In the turbulent regime, the lift-off height varies linearly with velocity [16] proportional to the: laminar flame speed, thermal diffusivity, fuel concentration and the flow velocity; where flames transitioning from laminar to turbulence decreases the lift-off height. Lift-off heights for a fixed turbulent jet is observed to be a power law fit with temperature, extracted from the work by Choi et al. [83], indicated in Fig. 2-5. As with laminar lifted flames the lift-off height for preheated turbulent flames scale well with increased laminar stoichiometric flame speed [106, 107].

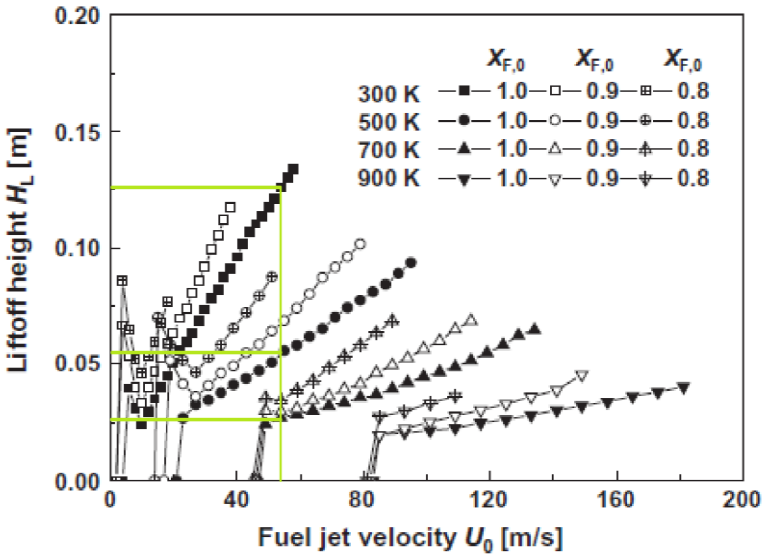

Fig. 2-5 Turbulent lift-off heights vs. velocity for heated CH_4 jets, the vertical lines indicate the extracted data for various preheated jets at the same fuel jet velocity to highlight the effect of preheating. Reproduced from the work by Choi et al. [83].

2.2.2.1 Turbulent vitiated coflow burner

The turbulent autoignition burners are like the laminar JHC, where they provide heated autoignition conditions with the added complexity of turbulent fields, due to increased inlet jet velocities. Typically the turbulent JHC has a 'cold' central fuel jet (298 K), shrouded by high temperature products from premixed H_2/air flames, explored initially by Cabra et al. [39, 108] seen in Fig. 2-6 a. The JHC has been studied extensively using hydrogen [39, 109-111], methane [50, 112], ethylene [113, 114] and more recently heptane [115], showing qualitatively similar stability of lift-off height being dependent on the temperature of the coflow.

The lift-off height results for methane with air is seen in Fig. 2-6 (b) for a coflow velocity of U_C = 4.2 m/s, where the increase in coflow velocity from U_C = 3.5 – 6 m/s further increases the lift-off height [109]. For methane, the coflow temperature is higher, T_C = 1375 – 1450 K, compared to the turbulent non-auto-ignited lifted flames ~ 900 K. This implies that a colder central fuel jet

significantly affects the coflow temperature range, noting they are operating at different Reynolds numbers. The addition of 5% hydrogen to a methane jet has been found to vastly improve its stabilisation characteristics [116], similar to the laminar lifted autoignition flames. Furthermore, it has been shown that the addition of H_2O, OH and CO_2 in the coflow, reduces the ignition temperature, reducing lift-off heights [117].

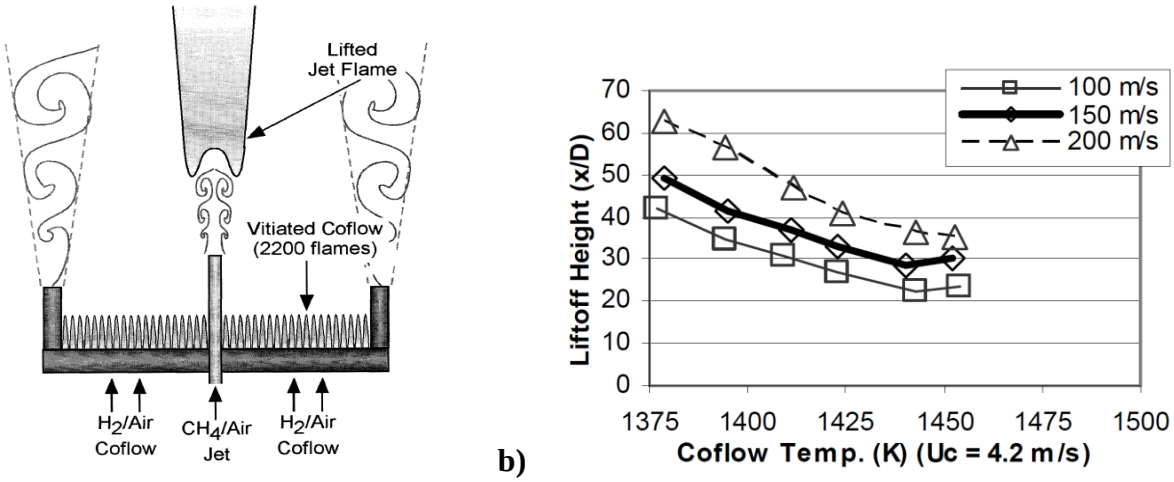

Fig. 2-6 Hot coflow autoignition burner schematic by Cabra et al. [118] b) Methane lift off heights for a range of coflow temperatures and fuel jet velocities for two parts air to one part methane, reproduced from Gordon et al. [109].

Contrary to laminar flames, the leading flame edge of the main flame body in lifted turbulent flames, with relatively low coflow temperatures, oscillates axially significantly. As such, Oldenhof et al. [42, 50] [46] identified for CH_4 flames that ignition kernels dictate the flame leading edge location, using ignition statistics to identify autoignition as the main stabiliser. The kernels grow and convection downstream to meet the main flame body. Arndt et al. [119] used kernel formation PDF's and mean lift-off height PDF's to identify low coflow temperature flames of CH_4 to be stabilised by autoignition, whilst for high coflow temperatures premixed flame propagation is potentially

dominant. Saksena et al. [49] also used pulsed jets to show 'steady-state' jet flames have lower mean lift-off heights, identifying that flame propagation potentially plays a role in flame stabilisation. Arndt et al. [119] further used pulsed jets, opposed to continuous fuel injection to investigate the transient behaviour of autoignition. Pulsed methane jets issuing into a hot vitiated coflow identify that ignition occurs in very lean mixture pockets, with low scalar dissipation rates (Arndt et al. and Papageorge et al. [120-122]), similar to the finding from opposed flow simulations, where strain increased the ignition temperature. Scalar dissipation χ is given in Eq. (2.4) defined by the spatial mixture fraction gradient $d\xi/dx$ and thermal diffusion (D).

$$\chi = 2D\left(\frac{d\xi}{dx}\right)^2 \tag{2.4}$$

Using heated air to initiate autoignition in a JHC configuration, Markides and Mastorakos [123] studied the effect of turbulence on ignition delay times, showing that increasing the turbulent length scale, by altering the fuel nozzle diameter, increases the ignition time [32]. However, increased Reynolds number increases the entrainment of the hot coflow, lowering the location for initial reactions to occur [33]. For low coflow temperature DME flames, first stage ignition occurs in lean mixtures, indicated by the pooling of CH_3OCH_2O, which is delayed by turbulence. However richer second stage ignition times are decreased due to turbulence [124] this is supported by more complex NTC heptane flames [125]. For higher temperatures, turbulence delays DME flame ignition throughout mixture fraction space.

2.2.2.2 Turbulent JHC: Numerical studies

A significant number of numerical studies on the autoignition of turbulent JHC flames have been done, classified into two broad categories: direct numerical simulation (DNS) and modelled approaches. A DNS study by Yoo et al. [40, 43] has shown that flames are stabilised by auto

ignition, identifying chemical explosive modes upstream of the flame base, the explosive mode is further described by Shan et al. in their study [98]. Auto ignition events are responsible for the 'jumps' in the flame base upstream, and the flame cannot propagate upstream on its own, described by Yoo et al. [40] and Luo et al. [126] in their respective studies. Since the flames are governed by autoignition, studies focus on how and where ignition occurs in the jet stream, determining that it occurs in lean mixture fractions (most reactive mixture fractions, ξ_{MR}) at low scalar dissipation rates [47, 127]. These results are verified experimentally by Arndt et al. [120]. An OH ignition event (detached OH-island) is given in Fig. 2-7 forming in lean mixtures at relatively low velocity fields.

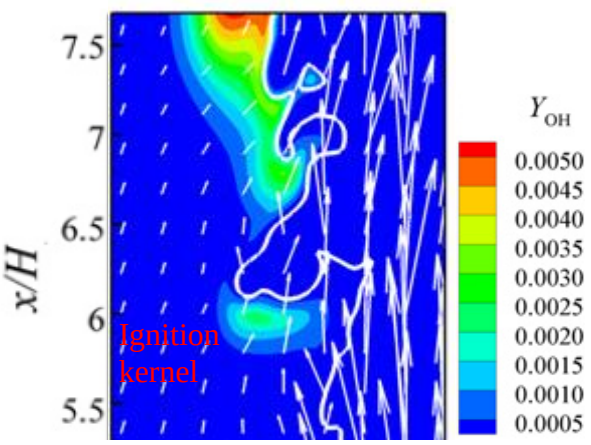

Fig. 2-7 Formation of an ignition kernel, the solid white line identifies the stoichiometric contour and the arrows indicate the velocity field, reproduced from the work of Yoo et al. [43].

Ignition is found to occur for a unity Damköhler number [128] defined in Eq. (2.5) as a balance between chemical production ($\dot{\omega}$) and species diffusion ($V_{j,k}$).

$$Da = \frac{\dot{\omega}}{(-\partial/\partial x_j(\rho Y_K V_{j,k})} \tag{2.5}$$

This unity Damköhler number identifies that the fuel diffuses into leaner mixtures prior to ignition, noting extinction will occur if the kernel core temperature drops below the 'cross over'

ignition temperature. Thermal run away is characterised by a large increase in Damköhler number with kernel extinction, occurring as diffusion exceeds production, with an increased delay time due to equal species diffusion and chemical production [128]. Yoo et al. [40] indicated that ignition events occur at lean mixtures with scalar dissipation rates lower than those of laminar extinction simulations, in regions where the oxidant and fuel gradients are opposed. Lower coflow temperatures form kernels further downstream, where the local temperature exceeds the cross over temperature, with increased premixing and mixing dependence. The mass diffusion reduces the peak temperature, occurring after the kernel propagates from lean to stoichiometric conditions. Cao et al. [129] further identified the influence of turbulence, where increased turbulence promoted leaner combustion [129], while low turbulences promotes lean, rich premixed and non-premixed flames.

The effect of turbulence delays ignition with the corresponding most reactive mixture fraction and low scalar dissipation rates at the centre of vortices, described by Sreedhara et al. [130]. However it was determined by Echekki et al. [131] that vorticity shedding in 3-D DNS produces faster ignition, also confirmed by Sreedhara et al. [130, 132]; compared to 2-D DNS. Cao et al. [129] performed 3-D DNS, indicating lean autoignition kernels initially propagate in a similar ζ_{MR} field extending into richer regions. After kernel initiation, the kernels are identified to propagate into richer mixtures crossing stoichiometric contours into richer regions. A delay in kernel species pooling, low temperature species such as CH_2O, and hence ignition propagation is due to species and thermal diffusion out of the kernel. Further details on autoignition propagation and the coflow burner topic are found in the review by Mastorakos [34].

Numerical simulations by Gkagkas et al. [133] have identified that a radical build-up (HO_2, H_2O_2 and CH_2O) occurs in the lead-up to CH_4 autoignition. Similar to premixed combustion, HO_2 and OH is important for thermal run away as investigated by Yoo et al. and Najafizdeh et al. [40, 134] with heat release occurring upstream of the flame base [40]. Analysing the concentration of

radicals and transport budgets in JHC flames, at different coflow temperatures, Gordon et al. [48, 135] identified that a convective-reactive balance leads to autoignition. An autoignition index (AI), given by eqn (2.6), based on the reaction $HO_2 + OH \overset{R8}{\rightarrow} H_2O + O_2$ exceeding the reaction of $HO_2 + H \overset{R6}{\rightarrow} OH + OH$ is used in CH_4 flames to identify autoignition stabilisation to be dominant [136].

$$AI = \left| \frac{\dot{\omega}_{HO_2}^{(R8)}}{\dot{\omega}_{HO_2}^{(R8)} + \dot{\omega}_{HO_2}^{(R6)}} \right| \tag{2.6}$$

Downstream of the autoignition base, a diffusive-reactive balance occurs as premixed flame propagation is more relevant [134, 136-138]. Large-eddy simulations show the turbulent flame base is stabilised by premixed autoignition [139] while the chemistry down-stream is driven by premixed propagation [140]. Finally, the ignition process and hence stabilisation is seen to be largely controlled by chemistry not mixing rates. [41].

Similar stabilising modes are observed in the more complex cross-flow burner, where a fuel is issued into a chamber with a downstream cross flow of heated air. The combustion zone produces a turbulent wake where autoignition is identified to stabilise flames, with down-stream tribrachial and stratified premixed behaviour [141] observed. Increased cross flow oxidant temperatures above the autoignition temperature led to autoignition with a premixed flame base and downstream thickened flamelets. The thickened flamelet is caused by the fuel being premixed due to vorticity interactions, whilst lower strain rates downstream produce premixed stabilisation. Premixed flame propagation is suggested in the bulk flow of the jet, whilst in the shear a combination of autoignition, flame propagation and flame extinction are responsible [142].

2.3 **Laminar autoignition calculations**

If the flames are dominated by autoignition stabilisation, calculated delay times should trend with lift-off heights of the fuels being studied. Therefore, simple isobaric reactors are typically used [143], these simulations are comparable to the shock tube experiments that ignite homogenous mixtures for fixed initial temperatures. Oldenhof et al. [42] has shown that leaner mixtures produce the fastest ignition, however, the reaction temperature only exceeds 10 K above the initial mixture temperature after ignition. Therefore, the mixture fraction that exceeds an equilibrium temperature of 50 K has been identified as the most reactive mixture, found to be 1% of the stoichiometric mixture [42]. The constant pressure reactor has further been used to demonstrate DME's NTC behaviour [144] and dual stage ignition [124].

For simulations, the ignition parameter has been defined by Mastorakes et al [127] based on specific peak species reaction rates such as a build-up of: HO_2, CH_3, CH_2O, C_2H_2, C_2H_4, C_2H_6 and HO_2 and H_2O_2 precursors [135], where ignition times decrease with the addition of CH_2O in CH_4 flames [145]. However, the parameter used to define ignition isn't too sensitive, where Im et al. [102] defined it by the peak reaction rate of the H radical, whilst Hilbert et al. [47] defined it by the second derivative of temperature with time.

Scalar dissipation rate and species diffusion is not present in homogenous reactors, however, in the previous section it is identified to influence ignition, as such laminar 1-D counter-flow simulations, with compositional gradients, are implemented [146]. The dissipation/strain rate has been shown to affect the dominant chemistry and radicals for ignition, increasing ignition temperatures in steady state opposed flow solvers [147]. Differential diffusion is found to have a small effect on delay times for hydrocarbons [148] whilst being non-negligible for hydrogen [47, 149]. Opposed-flow simulations between cold fuel and heated oxidants have shown S-shaped

responses to Damköhler number and temperature with the lower turning point corresponding to autoignition [150].

Most counter-flow solvers, including those from Chemkin [151] and Cantera [152], solve steady state problems, where the transient solution is inaccurate. Therefore transient/ unsteady reactors such as the unsteady counter-flow setup have previously been explored [153, 154]. The effect of scalar dissipation rate on ignition delay times can be determined, where close to extinction delay times becomes sensitive to strain rates [122]. Strain rates delayed ignition, with ignition delay times becoming more sensitive as it approaches the steady ignition limit for both methane [155] and hydrogen [156], attributing the delay to the diffusion out of species from the reaction zone.

Unsteady counter flow simulations using a unity Lewis number have been used to identify species pooling in the lead up to ignition [46], approximating the local strain rate in a CH_4 jet as a = 50 s^{-1} for 15 D's down-stream of the nozzle in their JHC experiment. As per Gordon et al. [135] autoignition is identified to be a balance between the species reaction budgets and convection budgets, with minimal diffusive in counter-flow simulations. The effect of strain rate has further been identified for DME [72], heptane [153] and CH_4-air flames [155] all experiencing delayed ignition for increased strain rate. Ignition has further been identified using a heat release dependent Damköhler number, given in Eq. (2.7), which is a balance between: heat release (q), scalar dissipation (χ_K), fuel mole fraction (Y_F) and heptane heat of combustion (H_0).

$$Da_T = \frac{q}{\chi_k Y_F H_0} \tag{2.7}$$

Laminar premixed flames are further used to identify the propensity of premixed flame propagation vs. autoignition for potential ignitable kernels under preheated conditions, used to model flame speeds [24]. However, laminar flame speeds from a typical 1-D laminar solver is based on the Eigenvalue problem, as such, temperatures exceeding the autoignition temperature have no flame speed. Schulz et al. [24] varied the domain length to identify how the flame position (x) and inlet

velocity (u_{in}) altered the flame residence time ($t_{res}=x/u_{in}$) or velocity. Temperatures were varied within the domain and autoignition stabilisation was identified for temperatures exceeding 1350 K for CH_4 flames. Transient premixed flames have further been used under auto-igniting conditions to estimate the flame speed [157]. Krisman et al. [158] used a 1-D transient numerical solver to estimate a reference flame speed under autoignition conditions to identify distinct stabilisation regions.

2.4 **Experimental diagnostics**

Experimental diagnostics on combustion have been reviewed by Eckbeth and Egon [159, 160], describing how lasers can measure temporal and spatial results for: temperature, composition and velocity measurements within a flame [160] with non-intrusive benefits. These results are measured using an array of laser setups, such as: solid state (neodymium-YAG), gaseous (Argon), Excimer (using reactive gas medium) or dye (such as Rhodamine.). The lasers are further defined by a continuous wave or pulsed emission. Lasers are typically 'tuned' to specific wavelengths, to interact with fuel molecules based on elastic or inelastic molecular electronic excitation [161].

Laser diagnostics include: elastic, Rayleigh scattering, where the same light frequency is emitted as was absorbed. Inelastic scattering of light includes Laser Induced Fluorescence (LIF) and Raman scattering [162], where the frequency of light emitted is altered relative to the excited wavelength. The imaging of LIF (used in this study) is typically applied to measure species and temperature, where quenching effects the emitted signal. Laser Induced Fluorescence (LIF) is performed at a variety of excitation wavelengths, where the chosen wavelength is determined based on the molecule/species of interest.

Using LIF has increased benefits over other techniques, such as Raman scattering, as it could detect minor species such as: CO, OH and CH_2O radicals, owing to the increased signal from stronger species cross sections. However, LIF is limited to certain species and subjected to high levels of quenching, making it difficult to quantify the species being diagnosed. The LIF signal (S_{LIF}) seen in Eq. (2.8) is proportional to the molecular number density (N_{LIF}) and the molecular ground state population density (f_1) which is being 'probed'. The signal species level is reduced by quenching (Q), which can be difficult to determine, particularly for larger molecules. The quenching effects are due to multiple energy loss pathways rather than fluorescence emission, including: dissociation, chemical reactions, energy transferred to other molecules or between internal energy states within the same molecule. In order to quantify a LIF signal into molecular quantities these values need to be determined, where Kohse-Höinghaus [162] describes the steps to quantifying a LIF signal.

$$S_{LIF} \propto N_{LIF} f_1 \frac{A}{A+Q} \tag{2.8}$$

2.4.1 **OH/CH_2O LIF measurements**

The PLIF measurements in this thesis are focused on the imaging of OH and CH_2O with their product used for a marker of heat release. Imaging of OH is used as a flame front marker to identify higher temperature, and more complete reactions. Optimal wavelengths have been achieved for OH by 'tuning' a dye laser, 'pumping' it with an Nd-Yag laser, producing OH excitation wavelengths at: 308 nm, 248nm and 283 nm [163]. The OH radical is predominantly excited at 283 nm [164], as it has reduced dependence on temperature. Population and quenching species cross sections for OH, at this wavelength, are well understood, where quantification has been performed by Tamura et al [165] and Kelman et al. [166]. A detailed correction method has identified the importance of collisional

quenching, absorption and fluorescence trapping [167, 168]. Theoretical transition states and temperature dependence is given by the LIFBASE software for OH [169].

Autoignition has been identified to require a build-up of low temperature radicals such as the formaldehyde radical (CH_2O), prior to ignition [46, 142] [170, 171], therefore, CH_2O PLIF is used in this thesis. The fluorescence of CH_2O has been used as a low temperature and ignition marker in high-pressure experiments [172], identifying first and second stages of ignition for DME [72]. The excitation of CH_2O has been done at multiple wavelengths, where a typical trade-off is between laser energy and strength of the excitation band. The strongest excitation band is at 339 nm [173-176], however, excitation at 340 nm [113] has shown to minimised the impact of PAH's, where narrow band fluorescence [177] also removes interferences. A frequency tripled Nd: YAG laser near 355 nm is most commonly used to excite the weak sidebands [178] due to the readily available wavelength, this is the wavelength utilised in this work.

The polyatomic nature of CH_2O makes the PLIF signal difficult to quantify and therefore comparisons between theoretical LIF signals are typically done [179-182] using a temperature dependant cross section. This correlation is misinterpreted for larger polyatomic molecules, as the quenching decay rates increase with temperature, rather than decrease [183], the contrary is found for smaller molecules, such as CO [184]. This has been proven by temperature dependant measurements [185], in particular from the measurements by Yamasaki et al.[186, 187]. These measurements show that the quenching capacity of molecules such as: O_2 and N_2, on the CH_2O signal increase with temperature in an Arrenhius manner. The additional complication of quantifying CH_2O is identifying the temperature-dependant ground-state for a 355 nm laser fluorescence, the Boltzmann fraction. Kyritsis et al. [188] has shown the Boltzmann fraction relationship for a 355 nm fluorescence band, based on the particular transitions given by Clouthier et al. [189]. The correction used by Kyritsis et al. [188] will be applied in this thesis.

The imaging of OH and CH_2O LIF simultaneously has been done [105, 190-193] to identify low and high-temperature regions. The spatial overlap is identified as a marker for the HCO radical, indicating regions of high reactivity and hence heat release [179, 191]. Their overlap, or lack thereof, has been defined as regions of re-ignition and quenching respectively [194]. The product of CH_2O onto OH has been used previously in the JHC to analyse auto ignition, identifying growing kernels produce more heat release [190]. Heat release measurements in the heated air experiment, using a plasma induced chamber identified increased heat release levels for increasing kernel size [191]. This thesis will use OH and CH_2O PLIF measurements to analyse kernel heat release from DME flames.

2.5 **Background summary**

This chapter explored the literature required to understand autoignition and the conditions for it to be realised, i.e. the chemical pathways and kinetics of specific fuels. Through the study of the literature available, the effect of preheat and premixing has been determined to increase autoignition, whilst excessive strain rate delays ignition due to thermal and species diffusion out of the reaction zone. Ignition occurs at conditions where low scalar dissipation occurs and for conditions where temperatures are high, i.e., in the hot coflow burner with heated oxidants this is in lean mixtures.

The literature, however, is restricted to the study of a few fuels in the JHC setup, including hydrogen and methane, studied both numerically and experimentally. The literature neglects to investigate whether other fuels exhibit the same response under autoignition conditions. Furthermore, the literature identifies that these JHC flames are stabilised by autoignition, however, do not determine the degrees of stabilisation, from premixed to autoignition, between highly lifted flames and more stable flames at a range of coflow temperatures. Finally, numerical studies have been done in literature identifying the effect of strain rate on ignition delay times, however, they do

not provide a conclusive identification as to the cause, nor are the studies focused upon the effect of coflow temperature on the most reactive mixture fraction.

This thesis as such expands upon the literature, studying additional fuels within the JHC setup, exploring heat release using PLIF of OH and CH_2O in DME flames. It further uses unsteady numerical simulations to better understand the effect of strain rate upon ignition and how coflow temperature effects the most reactive mixture fraction.

Chapter 3. **Burner setup and flow conditions**

This chapter describes a version of the hot vitiated coflow burner used throughout most of this thesis. Autoignition conditions are provided by a shroud of coaxial hot H_2/air coflow products, at atmospheric pressure, that surrounds the central fuel jet. This chapter further identifies the fundamentals of the hot coflow burner and how coflow temperatures are dictated by the H_2/air equivalence ratio. It lists the types of fuels explored in this thesis for experiments done on the hot coflow burner. Furthermore, it describes the differences in the stoichiometric mixture fractions and Reynolds numbers associated with the various fuels and changes in coflow temperature. An actively cooled jet has been designed and implemented in this thesis and preliminary results are presented in the final chapter, Chapter 10.

3.1 **Vitiated coflow burner**

The burner used for the majority of this work is a slightly modified burner that was used originally by Cabra [118], the Cabra burner had a 210 mm brass plate with 87% blockage, containing 2184 holes. It has a 4.57 mm inner diameter central jet that sits 70 mm above the base plate. The current burner (Fig. 3-1), however, has an inner jet diameter, D_J = 4.45 mm (1/4" tube, 1 mm wall thickness) with a coflow diameter of D_C = 197 mm, the brass plate contains ~ 1800 holes. The 70 mm extrusion of the fuel jet into the coflow ensures the H_2/air coflow premixed flames have reached chemical equilibrium prior to mixing with the fuel, including both: species and temperature equilibrium. The current setup at Sydney University is the same implemented by Gordon et al. [109] and Duwig and Dunn [112]; a section view of the burner setup is seen below in Fig. 3-1.

The separate segments within the burner consist of mesh and glass beads to create a uniform flow of H_2/air that entered the burner in four individual ports, the beads additionally prevent flash

back into the fuel lines. Above these glass beads is a pressure sensor connected to a solenoid valve on the H_2 line. The pressure sensor identifies the burners back pressure, below the brass coflow plate, if the pressure is to low, not enough air is flowing so the H_2/air mixture would be too rich (with an excessively fast propagation speed). However, if the pressure is too high a flash back scenario may be occurring, and as such, under both high and low-pressure conditions no H_2 can flow, this ensures safety requirements are met. The burner additionally sits within a wind tunnel that further provides an axial stream of filtered air that further separates the jet and coflow from the laboratory air.

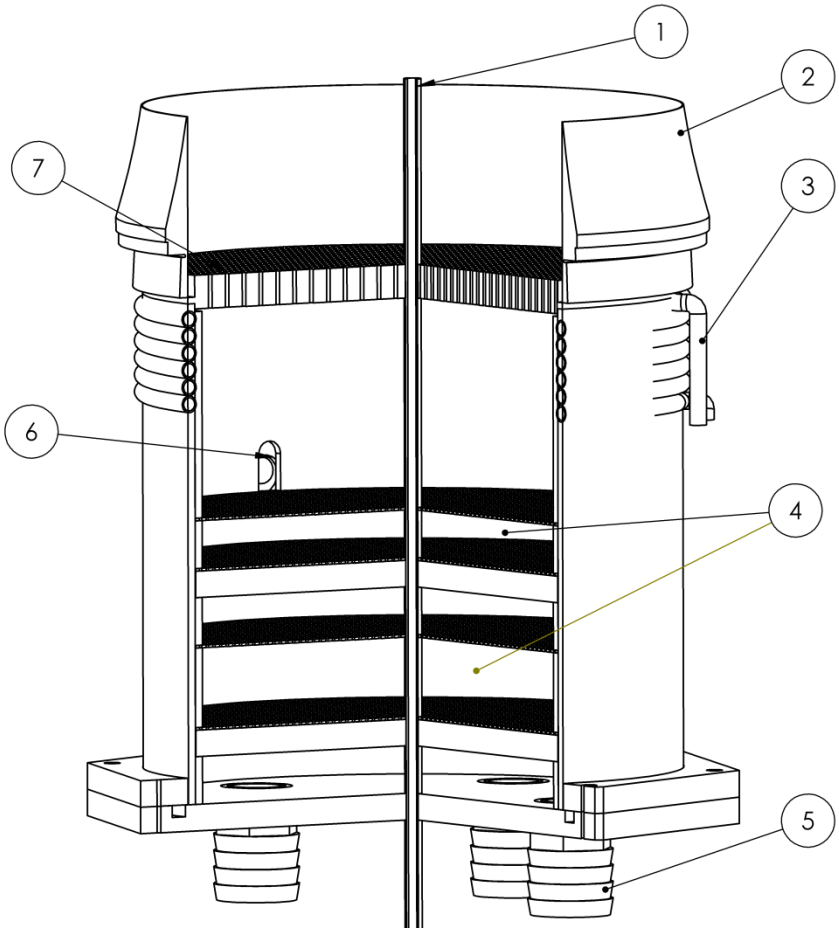

Fig. 3-1 Coflow burner: (1) Fuel jet, D_J (2) Coflow shroud, D_C (3) Base plate and burner cooling coil (4) Glass beads and gauze beds (5) Coflow (H_2/air) inlet (6) Over or under pressure sensor port (7) Coflow bass plate (~1800 holes).

The D_C = 197mm wide coflow of H_2/air provides a shrouded and heated environment that extends 60 jet diameters (60 D_J), downstream of the exit nozzle, after which the flow is corrupted by the entrainment of laboratory air, it is termed the 'valid cone', shown in Fig. 3-2. The fuel jet is operated under constant flow conditions such that a flame base (furthest upstream point of the main flame body) is always present within the coflow, 'valid cone'. The temporally present (steady state) flame base is opposed to a pulsed fuel jet (pulsed over millisecond intervals), such as the conditions from Ardnt et al. [44]. A flame base is pictured in Fig. 3-2 with ignition kernels forming below it and feeding into the flame base.

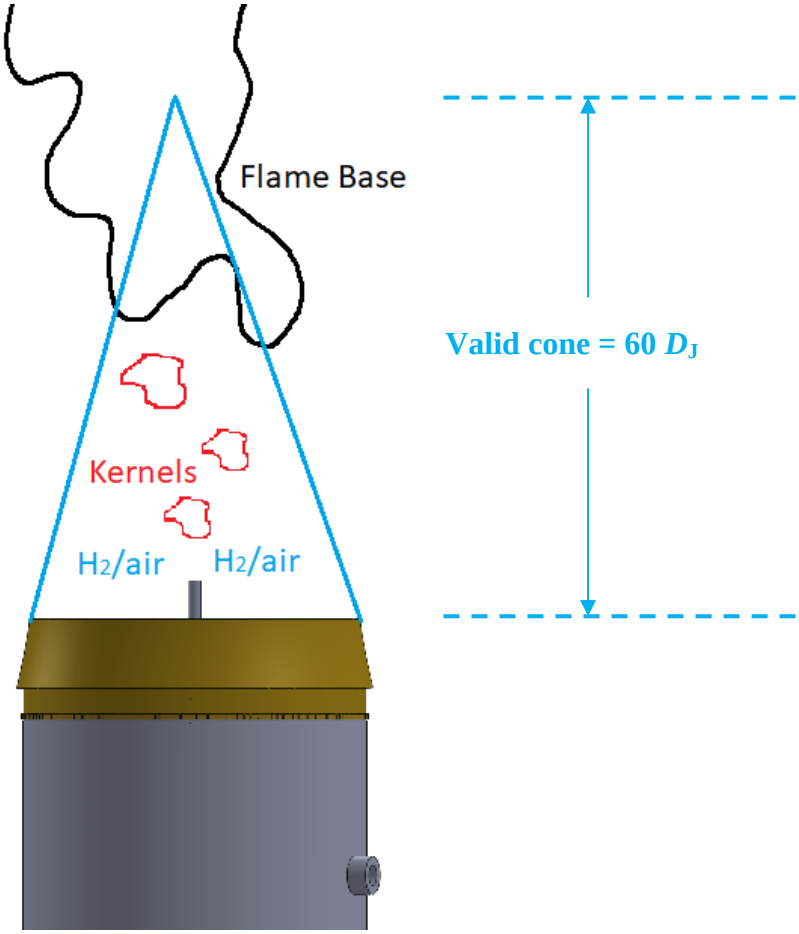

Fig. 3-2 Burner schematic indicating the: Flame base, Ignition kernels, H_2/air coflow and the triangular valid cone.

The controlling parameters for the coflow burner are the: jet velocity and coflow temperature. That is, for the coflow burner, autoignition temperatures are being explored, and as such, the location of the flame base (lift-off height) with coflow temperature best describes the fundamental characteristics of a given fuel issuing into the burner. Presented in Fig. 3-3 is an example of a DME flame (further explored later) where a seated (low flame base height) to highly lifted flame sits between the coflow temperature bounds of T_C = 1500 K – 1250 K. A 'seated' flame, and corresponding low-lift off height, corresponds to minimal flame base axial oscillation of 5 x/D. The lifted flame is measured at T_C = 1250 K, rather than T_C = 1200 K such that the extreme fluctuation locations of the flame base sits lower than the 'valid cone' of 60 D_J's. Other fuels will have a different coflow temperature range for which a seated to lifted flame occurs due to the variation in fuel reactivity (explored in the following section).

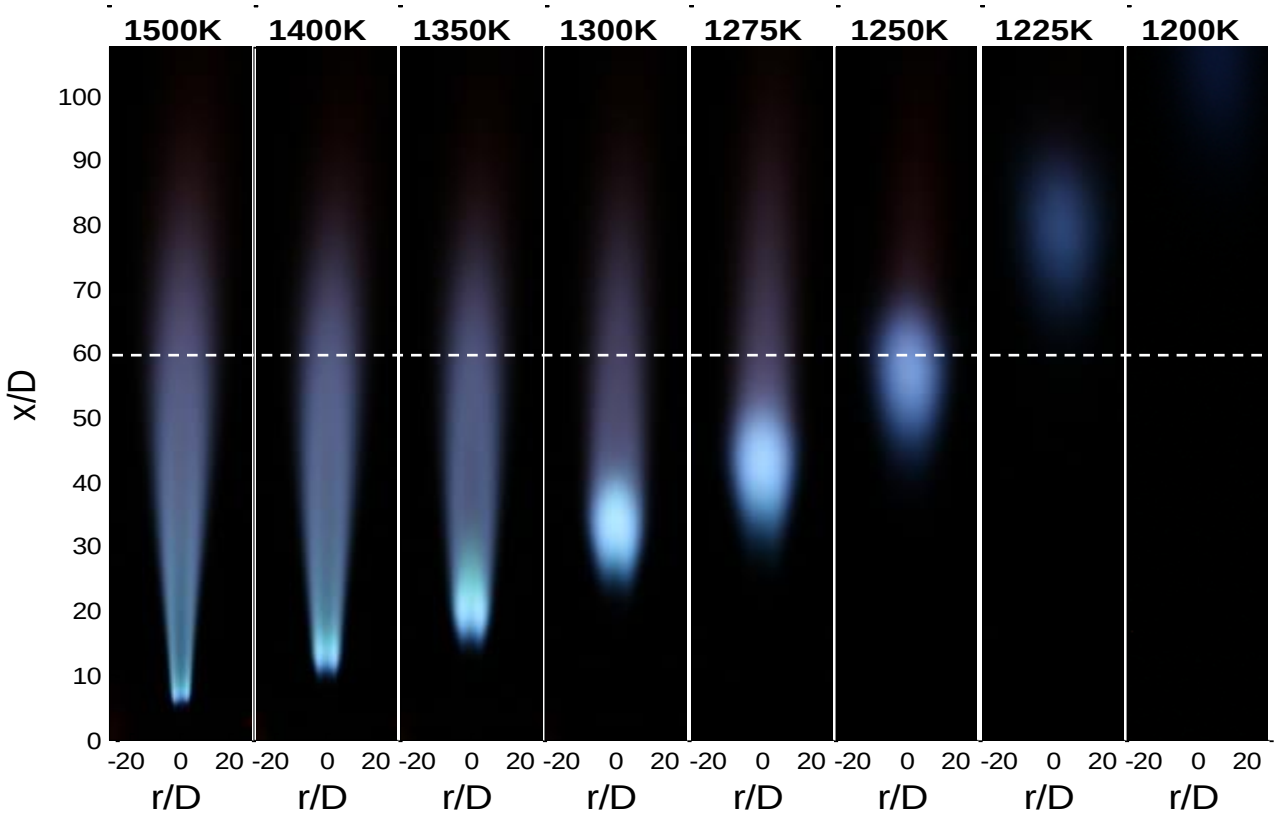

Fig. 3-3 Digital images of DME flames with varying coflow temperatures (T_C = 1500 K -1200 K). The valid cone, axial location, is indicated by the dotted line at 60 *x*/*D*.

3.2 Flow meters and repeatability

The hot coflow setup at Sydney University uses a range of digital ALICAT mass flow controllers that control the flow rate of gases to the burner. A large 3000 SLM meter is used for the coflow air supply, a 500 SLM meter controls the H_2 supply, a 50 SLM meter controls the fuel jet and a 200 SLM meter controls the N_2 dilution/ air premixing flow rates. The controllers operate on a PID feedback system, where the proportional gain (P) was proven to be the dominant controlling property, with the differential (D) component controlling the more rapid valve oscillations. The various fuels are programmed into the meters to adjust for the fuel's relative viscosities, densities and ideal gas compressibility factors. Other smaller ALICAT meters were used to operate the Bunsen and Flat flames: 5 SLM and 20 SLM respectively, with the 20 SLM meter further used to add N_2O to the jet (explored within this thesis).

Despite the accuracy of the ALICAT meters, additional precision precautions were taken, including: a S-type thermocouple placed within the hot coflow, a second monitoring meter on the H_2 supply, and a sound level meter. This setup enabled a coflow temperature precision of ± 1 K daily, and a day to day repeatability of ± 6 K (verified by the H_2 flames sensitivity to coflow temperature). The sound level meter was proven to be very sensitive to a given flames lift-off height and coflow temperature, this in addition to converging kernel formation PDF's (explored later in this thesis) identifies the coflow temperature repeatability.

3.3 Coflow temperature

The variation in coflow temperature is based on the adiabatic temperature from the H_2/air stoichiometric ratio. That is an equivalence ratio of φ = 0.39, gives a coflow temperature of T_C = 1400 K, where the mole fraction ratio of H_2 to air corresponds to the volumetric flow rate ratios for

the experiment to achieve a given coflow velocity. A polynomial correlation between coflow temperature (T_C) and equivalence ratio (φ_C) is given in Eq. (3.1), it is based on a 3rd order polynomial fit for the equilibrated temperature of H_2/air from Cantera [152]. A third order polynomial was found in Matlab to have the most accurate fit, where the curve fit is accurate to within ±1 K for the relevant coflow temperature range and equivalence ratio: $469 < T_C < 1641$ or $0.05 < \phi_C < 0.5$.

$$T_C = 922.3\varphi^3 - 2126\varphi^2 + 3522\varphi + 297.8 \qquad (3.1)$$

3.4 **Stoichiometric fuel mixture fractions**

For the varying coflow temperatures issuing into the burner, a resulting variation in equilibrated products occurs, this alters the oxidant that is mixed/entrained with the fuel jet. Previous tests on the hot coflow burner have shown that the hot coflow H_2/air flames have reached equilibrium by the time they mix with the fuel jet, 70 mm downstream, tests were done for the highest coflow burnt velocity of 5 ms^{-1}. The oxygen level for T_C = 1000 K is 14% O_2 while a T_C = 1400 K coflow has 11% O_2 content from the products of a Cantera [152] equilibrium solver with H_2/air seen in Fig. 3-4. The effect of the O_2 content on DME flames has been measured by Saksena et al. [49], who determined that for C_3H_8 flames the effect was small (< 25%), whilst much larger for DME flames.

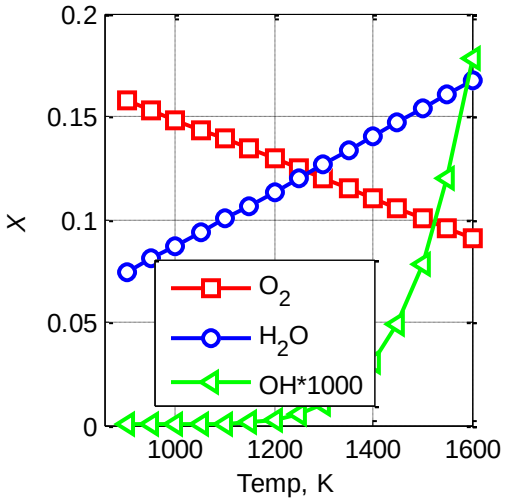

Fig. 3-4 Mole fractions (X) of O_2 and H_2O and OH from equilibrated H_2/air mixtures, for a range of temperatures.

The variation in O_2 and H_2O (Fig. 3-4) for varying coflow temperatures and in turn equivalence ratios has a small effect on the stoichiometric mixture fraction of fuels. The stoichiometric mixture fraction is defined by the mass originating in the jet (M_{Jet}) divided by the total mass of fuel and coflow products (M_{Jet}+ M_{Co}) at stoichiometric conditions, given in Eq. (3.2). The mass (M) is equal to the species molecular weight (MW) multiplied by the number of moles (n). Noting there is additional N_2, O_2 and H_2O molecules from the coflow stream, however only the major H_2O molecule is included from the products.

The fuels studied are either premixed with air ($*n_{N_2}MW_{N_2} + *n_{O_2}MW_{O_2}$, the (*) indicates that it originates in the jet) or partially diluted with N_2, this in turn alters the stoichiometric mixture fraction, moving the stoichiometric contour outward from the jet if less premixing occurs. If N_2 dilution is used in the fuel jet instead of air, the volumetric flow rate of N_2 is adjusted to match the equivalent air premixing rate, where the stoichiometric values are slightly adjusted with the absence of O_2.

$$f_{st} = \left(\frac{M_{jet}}{M_{Jet}+M_{Co}}\right)_{st} \tag{3.2}$$

$$M_{Jet_{st}} = n^*_{Fuel} MW_{Fuel} + n^*_{N_2} MW_{N_2} + n^*_{O_2} MW_{O_2}$$

$$M_{Co_{st}} = n_{N_2} MW_{N_2} + n_{O_2} MW_{O_2} + n_{H_2O} MW_{H_2O}$$

The variation of the stoichiometric mixture fraction for an array of fuels (studied within this thesis) using a nitrogen dilution is given in Fig. 3-5, the stoichiometric mixture fraction of H_2 is very sensitive to N_2 addition owing to hydrogens low molecular weight. Mixing with air gives very similar stoichiometric mixture fractions, since the molecular weight of air to nitrogen is similar. The stoichiometric quantities for the relevant premixing or dilution ratio will be given in the appropriate experimental setups in each chapter.

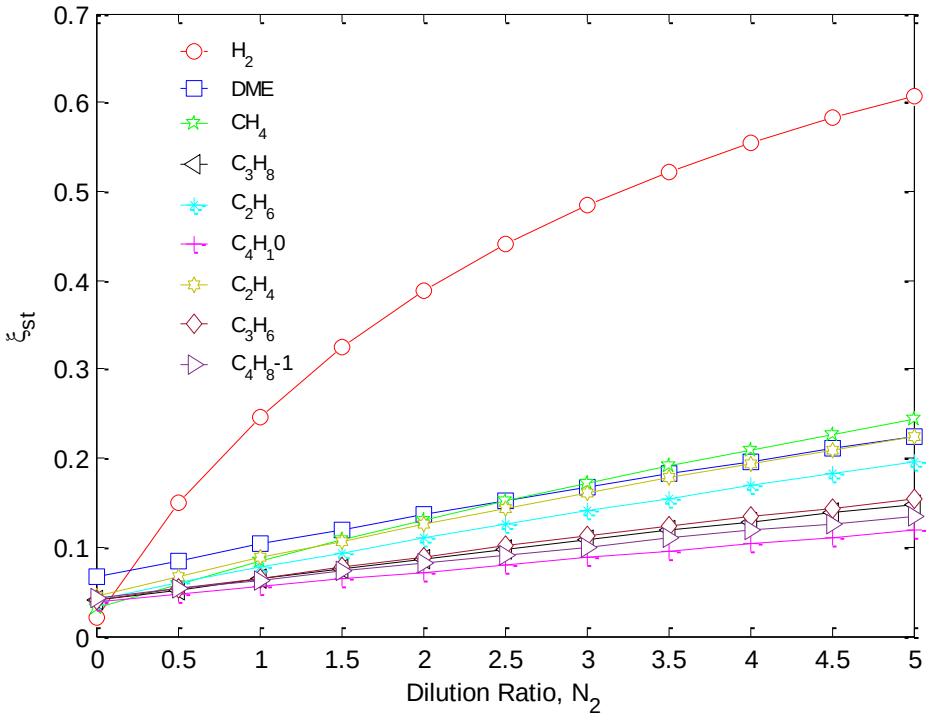

Fig. 3-5 Stoichiometric mixture fraction variation of fuels for a premixing with N_2.

The mixture fraction space is given below in Fig. 3-6 for a ‘cold’ (298 K) unreacted jet issuing into the JHC from the thesis of Dunn [195]. Rayleigh scattering was used to obtain radial line mixture fractions at certain axial locations, linear interpolation was used to create the mixture fraction space as given. Overlain are the stoichiometric scalars from DME jets of different partial premixing quantities. Premixing can be seen to move the stoichiometric mixture fraction inward, closer to the jet, while changing the coflow temperature has minimal effect upon the stoichiometric mixture fraction, moving stoichiometry slightly outward. The stoichiometric values are useful to indicate the composition ‘fed’ into the isobaric homogenous laminar reactor (following sections) and further identify the effects of stoichiometry between pre-mixing/ dilution.

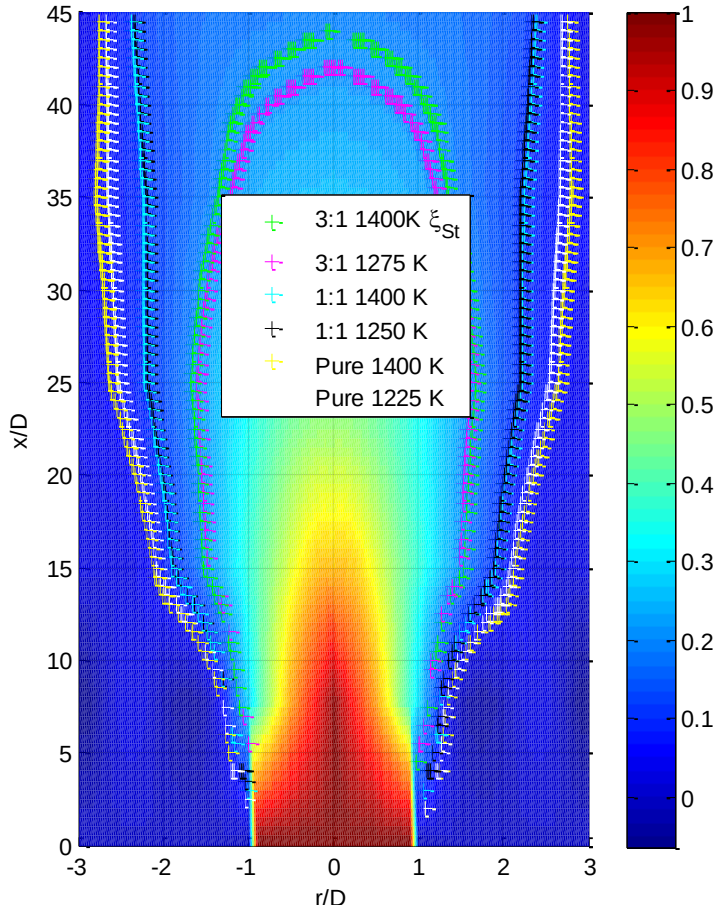

Fig. 3-6 The 2-D JHC mixture fraction (ξ) space overlain by the stoichiometric mixture fractions (ξ_{St}) for three premixed DME cases with two corresponding temperatures. The symbols indicate the stoichiometric mixture fractions for the different DME cases.

3.5 **Coflow burnt velocity**

For various fuels issuing into the burner, the coflow temperature range is large, leading to a range of burnt coflow velocities, varied, as to maintain reasonable heat conduction to the burner, such that the coflow doesn't lift-off from the shroud. The lowest H_2 fuel jet has a coflow ignition temperature of $T_C \approx 1040$ K, while a methane (CH_4) jet requires a maximum temperature of $T_C \approx 1540$ K. This large range of 500 K necessitates a variation in coflow burnt velocity of $U_c = 0.7$ m/s between fuels being used. This difference is required due to the thermal convection properties, to remove more or less heat from the brass JHC burner shroud, where a velocity $U_C = 4.2$ m/s is used for CH_4 and $U_C = 3.5$ m/s is used for H_2 (this is consistent with Cabra et al. [39]). Furthermore, a relatively low coflow velocity is used for H_2 since the heat produced from a $T_C \approx 1040$ K coflow is small, the coflow flame begins to lift-off around the shroud at higher velocities. A fixed coflow velocity, $U_C = 4$ m/s, was used for all other hydrocarbons. Measurements were obtained in this work to verify that a minimal difference in coflow velocity of $U_C = 4$ m/s and $U_C = 4.2$ m/s for CH_4 occurs. Previous work from Gordon et al. [109] and Cabra et al. [118] have studied a larger range of coflow velocities: $U_C = 4.2$ m/s, 5.4 m/s and 6.5 m/s, indicating a difference between velocities and the stability of a CH_4 jet for a given coflow temperature.

The burnt velocity is obtained from mass conservation, where a decrease in density, i.e., burnt products, increases the velocity; the coflow burnt velocity (U_{Burnt}) is given in Eq. (3.3).

$$U_{Burnt} = U_{Cold} \frac{T_{Cold} MW_{COLD}}{T_{Burnt} MW_{Burnt}} \tag{3.3}$$

The burnt mixture molecular weight is obtained from the Cantera equilibrium solver. The non-linear correlation of the coflow equivalence ratio to coflow temperature in Eq. (3.3) implies that a

non-linear relationship between the experimental flow rates and the required coflow temperature is required for a fixed burnt coflow velocity (U_C).

3.6 **Jet velocity**

The jet velocity was chosen for the fuels to obtain consistency between previous work from Cabra et al. [39, 108] and Gordon et al. [46]. This led to a H_2 jet velocity of U_J = 107 m/s and U_J = 100 m/s for CH_4, two velocities were used for the DME case of U_J = 100 m/s and U_J = 50 m/s to provide high temporal camera resolution at 10 kHz, and to measure the effect of turbulence. Other hydrocarbon fuels selected for study in this thesis were fixed at U_J = 100 m/s. A summary of the fuel jets used and their burnt coflow and jet velocities are given in Table 3-1.

Table 3-1 Coflow and fuel Jet properties.

Fuel	H_2	CH_4	C_2H_4	C_2H_6	C_3H_6	C_3H_8	C_4H_8	DME
U_C (m/s)	3.5	4.2	4	4	4	4	4	4
U_J (m/s)	107	100	100	100	100	100	100	50/100

The variation in fuel properties and flow velocity leads to varying jet Reynolds numbers, where the Wilke [196] viscosity mixing model was used for fuel mixtures given in Fig. 3-7, given in equation (3.4). The combined Wilke viscosity is the sum of the individual gas viscosities (μ_i) and their corresponding mole fraction x_i all normalised by the inter collisional parameter (ϕ_{ij}); with the collisional parameter made up from the: gas viscosities and the individual molecular weights (M_i).

$$\mu = \sum_{i=1}^{ns} \frac{x_i \mu_i}{\sum_{j=1}^{ns} x_j \phi_{ij}} \tag{3.4}$$

$$\phi_{ij} = \frac{1}{\sqrt{8}}\left(1 + \frac{M_i}{M_j}\right)^{\frac{1}{2}}\left(1 + \left(\frac{\mu_i}{\mu_j}\right)^{\frac{1}{2}}\left(\frac{M_j}{M_i}\right)^{\frac{1}{4}}\right)^2 \quad (3.5)$$

The jet Reynolds (Re_J) numbers presented are presented below for a varying nitrogen dilution and a constant jet velocity, U_J = 100 m/s.

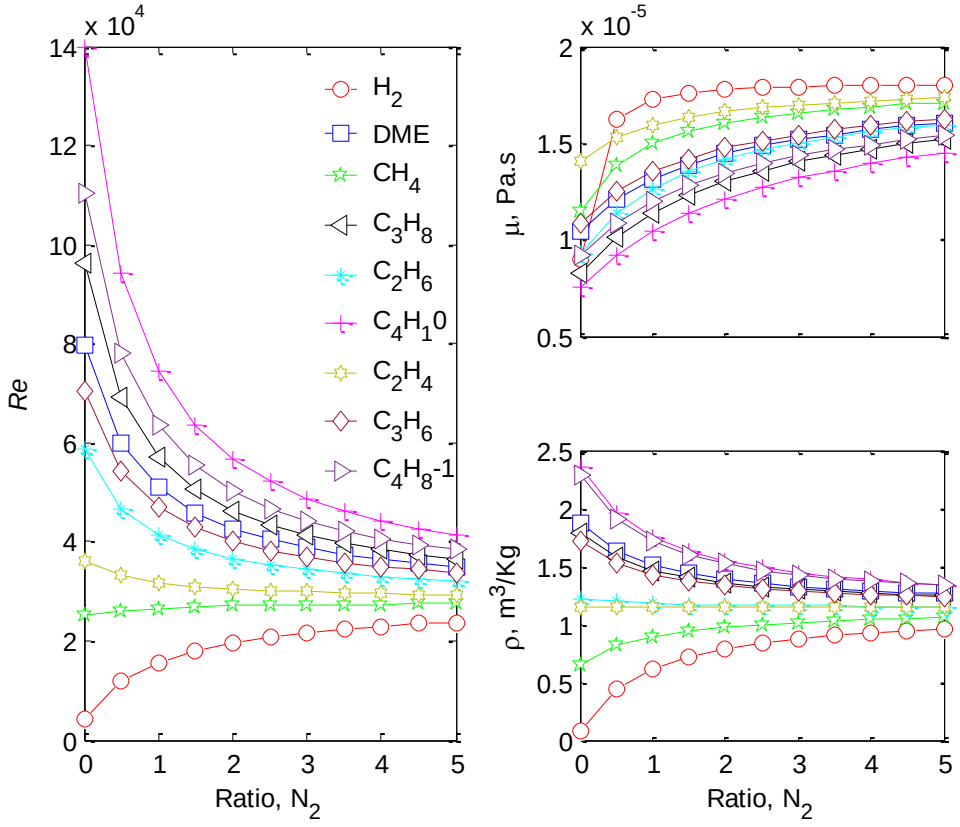

Fig. 3-7 Variation of Reynolds number (*Re*, left), viscosity (μ, top right) and density (ρ, bottom right) are presented for a range of N_2 dilution, for different fuels. Reynolds numbers are calculated for a diameter $Ø_J$ = 4.45 mm at room temperature of 298 K.

Fig. 3-7 identifies that CH_4 has a small change in Reynolds number for the addition of nitrogen or air (not displayed), this is due to the small decrease in viscosity and density at increased dilution levels. This attribute of CH_4 was not explored in this thesis, however, it is of interest for future work.

On the contrary, C_4H_{10} has a large variation in Reynolds number, since the density and viscosity vary significantly with the addition of nitrogen, in an inverse manner.

3.7 **Experimental controls**

It has been shown that for a fixed jet velocity there is a large variation in both stoichiometric mixture fraction and Reynolds number for the given fuel premixing or dilution ratios. The stoichiometric and Reynolds number is difficult to fix for each fuel without altering the premixing levels and jet velocity. These variations would alter the reactivity of the fuel, that is the autoignition temperature and delay times, in addition to the turbulence/ mixing fields respectively. Therefore, throughout this thesis the flow velocities, both the coflow and jet velocities, are maintained as to fix the flow field between fuels, as such different coflow temperatures are used as the variable.

The following section maintains the coflow and fuel jet velocities such that coflow temperatures are the only variable between cases to achieve seated and lifted flames. Since the coflow temperature and Reynolds number change for the different fuels implemented, a point of comparison between fuel cases is based on similar lift-off heights at their corresponding coflow temperature.

Chapter 4. **Parametric fuel study**

This chapter explores the interaction and dynamics of ignition kernels and the flame base, using statistics from high-speed chemiluminescence imaging and sound measurements of the jet in a hot-vitiated coflow burner (JHC), at the University of Sydney. The novelty of the work presented in this chapter is the wide range of gaseous fuels explored, which include alkanes and alkenes up to C_5, H_2 and dimethyl ether (DME). In addition to exploring the influence of fuel type, the impact of: jet velocity, fuel partial premixing, fuel dilution and coflow temperature is also examined.

This chapter further includes the fuels and their flow conditions previously explored extensively by groups such as Cabra et al. [39, 108] and Gordon et al [109] for CH_4 and H_2 issuing into the hot vitiated coflow burner. The focus of this chapter is to determine if all fuels exhibit similar characteristics of flame stabilisation as determined by Oldenhof et al. [50], whereby ignition kernels form and feed into the constantly advecting flame base. The experiment is therefore designed to observe the interaction of the base of the flame body (flame base) with autoignition kernels.

The flame's average lift-off height and flame base oscillation is measured using a digital camera, measured simultaneously to the high-speed chemiluminescence camera and sound measurements. The digital camera provides a long recording period to observe slow modes of the flame base oscillations. High-speed (10 kHz) chemiluminescence imaging is additionally used consecutively to determine the kernel/flame base interactions, using kernel formation and lift-off height location PDF's. Relative comparison between fuels is determined based on the locations of the relevant flames lift-off height, opposed to coflow temperatures, since the operating coflow temperatures vary significantly between fuels. The comparisons are drawn for fuel dynamics such as the kernel formation rate, lift-off height PDF's and kernel merging velocities.

4.1 Experimental setup: fuels and 10 kHz chemiluminescence

The lift-off heights of different fuels have different sensitivity and range of coflow temperature over which such fuels undergo a transition from autoignition to stable combustion. However, the trends of lift-off height as a function of coflow temperature between fuels is similar, whereby a relatively low coflow temperature, for a given fuel, corresponds to a highly lifted flame, and a relatively high coflow temperature corresponds to a low lifted-flame.

To devise a common reference point for all fuels studied here, the co-flow temperature that corresponds to a lift-off height of 20 D_J is employed, noting that lift-off heights are dependent on coflow temperature. This temperature is shown in Table 4-1 (row 5) along with other relevant parameters for the eight fuel mixtures studied here. The coflow temperatures are based on the adiabatic flame temperature for the flow rates of H_2 and air, noting the actual temperature will be lower than the adiabatic temperature due to radiation and heat transfer losses. The precision can be verified by the flames lift-off height distribution and sound emission, which are both very sensitive to coflow temperature. Although the jet velocity is held constant, due to the different densities and kinematic viscosities of the jet mixtures there is a large variation in Reynolds number (explored in Fig. 3-7), approximately a factor of 2, between cases as shown in Table 4-1. The stoichiometric mixture fraction (ξ_{st}) shown in Table 4-1 varies considerably between fuels and mixing cases, where ξ_{st} is reported for the coflow temperature leading to a lift-off height of x/D = 20. The stoichiometric mixture fraction, ξ_{st}, changes by a small amount for a change in coflow temperature due to the change in H_2O and O_2 products (described in section 3.4). The stoichiometric delay times τ_{st} (calculated later in this thesis) provide additional comparison between fuels.

Table 4-1. A summary of the conditions for the flames examined in this study.

Jet Mixing	H_2 :N_2	CH_4 :air		C_2H_4 :air			C_2H_6 :air		C_3H_8 :air		C_3H_6:air		C_4H_8:air	DME:air
Ratio	3:1	2:1	3:1	2:1	3:1	4:1	2:1	3:1	2:1	3:1	2:1	3:1	5:1	3:1
V_J **(m/s)**	107	100		100			100		100		100		100	100
V_C **(m/s)**	3.5	4.2		4			4		4		4		4	4
Tc **(K) @**L_H**=20 D**	1048	1480	1490	1150	1158	1166	1190	1200	1310	1290	1370	1375	1280	1325
Re	27186	28642	28347	34538	32586	31416	37075	34424	46004	40704	43862	39206	38226	42064
ζ**st**	0.37	0.09	0.20	0.10	0.14	0.18	0.09	0.12	0.07	0.09	0.08	0.10	0.10	0.16
τ_{st} **(ms)**	-	103	356	13	37	96	30	60	11	15	26	38	20	20

High-speed chemiluminescence image sequences are collected at 10 kHz perpendicular to the flame axis using an intensified CMOS camera (Lavision HSS5 and IRO). Sequences of $1x10^4$-2.2 $x10^4$ images (1.0-2.2 seconds) were typically recorded for each flame. Complementary lower repetition rate movie sequences of 30 seconds, in duration, indicate that all flames are statistically steady, featuring no slow modes of oscillation that would not be captured by the 10 kHz sequence. For each coflow temperature and flame case, the field of view and lens selected is optimised to capture the entire flame base and ignition kernel region, also maximising the spatial resolution and signal to noise ratio (SNR). A range of visible, $f_{\#}1.2$ and $f_{\#}1.4$, camera lenses are used to record the chemiluminescence signal, therefore, the collected chemiluminescence signal is broadband and limited to visible wavelengths.

In non-sooting flames of hydrocarbon fuels, emissions from CH^* is dominant with smaller C_2^* emissions observed, in DME flames and methane based flames [197], where the emission of CH^* is occurring in both the reaction and at a significantly lower intensity in burnt gas region [198]. Since the collected signal is in the visible wavelength, no OH^* is observed, where OH^* emits light at a wavelength of 306 nm [199], noting the visible spectrum is 390 – 700 nm. Hydrogen fuels additionally produce OH^* [200], however in the visible spectrum, the chemiluminescence is due to

H_2O^* and $H_2O_2^*$ [201] with $H_2O_2^*$ being dominant, where the visible emission occurring is greater than 600 nm [202]. This setup therefore images CH^* and some C_2^* from the hydrocarbon flames, and predominantly $H_2O_2^*$ from the H_2 flames; the setup does not capture UV emissions from species such as OH^*. Simultaneous to the high-speed image sequences, acoustic emission from the flame is recorded at 48 kHz using a sound level meter (Brüel & Kjær Type 2250) connected to a digital storage oscilloscope (Tektronix DSA70404C). The sound level meter is positioned 300 mm from the burner, which enabled the correction for speed of sound versus high speed imaging. Background sound of the laboratory, and the sound of the coflow without the flame at varying temperatures, was used to verify that the flame acoustics were substantially above the background level even for relatively quiet flames. Furthermore, the background sound levels were used to identify any frequencies that are attributed to the lab during sound processing.

4.2 High-speed image processing and kernel tracking

An unprocessed chemiluminescence (CH^*) image from an air:CH_4 = 2:1 flame is presented in Fig. 4-1 for kernel initiation (300 µs) and kernel merging (1100 µs). These images are sampled at intervals of two (200 µs) from the image sequence taken at 10 kHz. The kernel (CH^*-kernel) is defined by an 'island' of CH^* upstream of the main CH^* flame body (most downstream flame structure), noting there is a steady state flame base present. The kernel island is identified in Fig. 4-1 by the dashed line. The time between kernel ignition (first appearance of the kernel) and consumption, identifies the time for the kernel to grow and advect downstream. The formation of the kernel, its relative growth and then consumption by the main flame body is the focus of the tracking algorithm.

Following kernel detection, the image has a background subtraction from the camera noise, with the CH^* image being further processed using a simple [3 x 3] median filter to remove any image

noise. Owing to the 'sharp' CH^* boundaries of both the kernels and flame base from the 'background', minimal processing was required before a pixel threshold was used to isolate the CH^* - kernel from the CH^* flame bodies. For the H_2 flame the chemiluminescence is from H_2O^*, not CH^*, where the same processing method is used. Kernel initiation or autoignition is defined at 300 µs (Fig. 4-1) where it grows until 900 µs before being consumed/ merged into the flame base, the uniform down-stream advection of the kernel centroid enables it to be tracked with minimal computational effort (identified by the dashed green line). A bounding box for the somewhat predictable kernel advection is given in the CH^* image at 900 µs, if this kernel remains in this bounding box, for the following image, whilst having an increasing number of pixels, the kernel is deemed to have grown. If the kernel centroid sits outside this bounding box with fewer pixels, it is deemed a new kernel and is added to the formation rate of new kernels.

In addition to the flame base location being tracked shot-to-shot to identify the flame's fluctuation, the flame base further provides the ability to condition and filter the image. From experimental observation, no kernel forms significantly downstream of the leading flame body edge, or outside of the flame width boundary, indicated by the red dashed bounding box at 100 µs. This flame base conditioning and filtering technique was required for flames with a reduced SNR, such as H_2, where the chemiluminescence emission (HO_2^* and HO_2^*) is smaller.

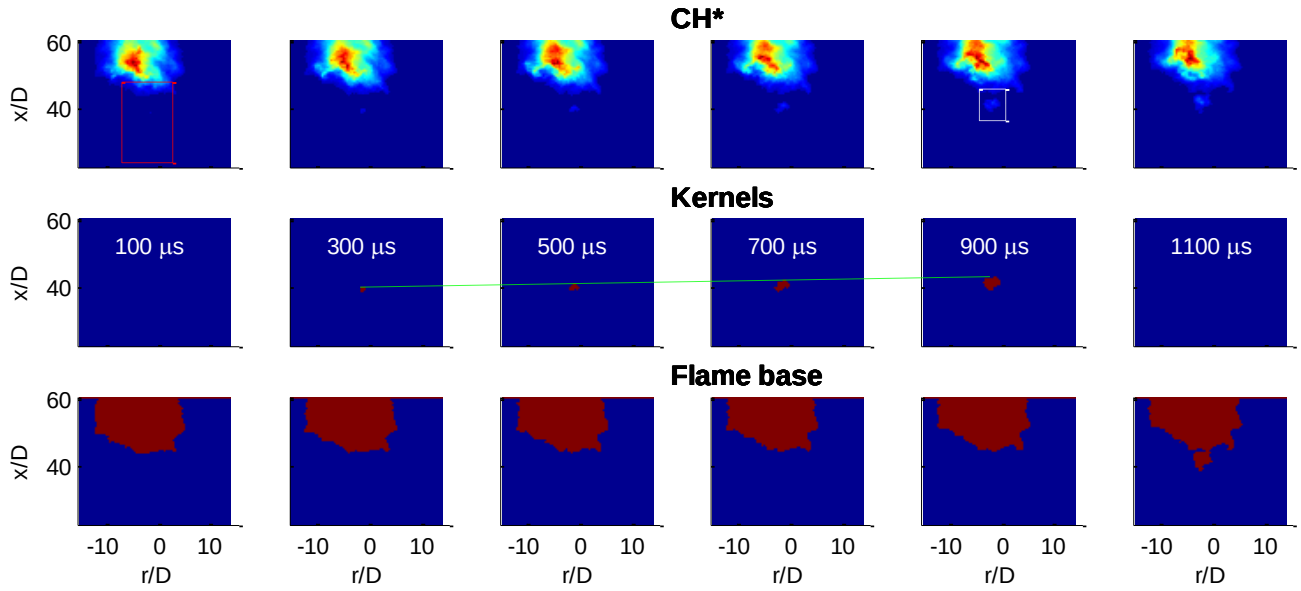

Fig. 4-1Consecuative CH^* kernel images indicating the tracking and processing methods. The dashed red box (100 μs) defines the bounding location where kernels can form, the solid white box (900 μs) highlights the tracking bounding box for a growing kernel and the dashed greed line (300 μs – 900 μs) identifies the kernel centroids linear downstream advection.

Slightly different median filters and pixel thresholding was used between different fuels owing to the varying levels of chemiluminescence emitted, and therefore varying SNR's. The level of flame emission intensities is given as: H_2, CH_4, ethane, DME, propene, ethylene and propane in order of least signal emission to the greatest respectively. The emission levels from each flame were not directly measured, however, the intensifier gain levels were adjusted to suit each case, as such the kernel dynamics: formation rates and growth size is only measured.

4.3 **Results**

This section presents the results for the average and RMS of lift-off heights from the digital movie sequence, and the results from the high speed chemiluminescence. The results include: kernel formation rates and their distribution, the PDF for lift-off heights, the relative growth rates of

kernels, the differences between flame base and kernel velocities, and finally the sound measurements.

4.3.1 **Average Lift-off height and RMS for fuels**

A digital movie sequence (25 Hz) was used in this setup for all fuel cases to capture the mean flame base location and the respective flame base oscillation (RMS). Movie frames are superior to still frames as they reduce temporal blurring in addition to providing temporal information on the oscillation of the flame base of these flames. Furthermore, the ease and download speed with which digital movies can be taken, compared to the high-speed camera, means the lift-off height curves are constructed based on the digital movies.

The mean lift-off heights versus coflow temperatures for the flames studied are presented in Fig. 4-2. Each fuel composition has a range of coflow temperatures to yield a series of lifted flames. The flames range from: a slightly lifted flame (~ 8 x/D) with little temporal fluctuation in lift-off height, through to flames with large fluctuation and mean lift-off heights greater than 50 D_J. The hydrogen flame series has the lowest coflow temperature range for the flames lift-off heights (~T_C = 1036-1070 K) with the highest coflow temperature sensitivity (dL_H/dT_C).

Methane flames, however, compared to H_2 flames operate with the highest coflow temperature range ~ T_C = 1400 K -1550 K with the least sensitivity. The operating coflow temperatures for the new alkane and alkene cases in Fig. 4-2 are found between the extremes of the established hydrogen and methane coflow temperatures. The measured trend of the mean lift-off height with coflow temperature reported in Fig. 4-2 agrees well with previous measurements for the methane and hydrogen flames [39, 108].

From Table 4-1 and Fig. 4-2 for a given coflow temperature increased premixing is shown to increase the mean lift-off height, or equivalently require a lower coflow temperature for a given lift-off height for: CH_4, C_2H_4 and C_2H_6. The lift-off height variation is consistent with the autoignition delay times for these flames reported in Table 1. However, for C_3H_8 increased premixing is shown to decrease the lift-off height, which does not agree with the trends of the autoignition delay times reported in Table 4-1. This same phenomenon occurs for the alkene of C_3H_8, C_3H_6, where increased premixing from two parts with air to three parts, decreases the lift-off height. It is possible that the difference occurs due to the fuel's diffusive properties, such as, the Lewis or Schmidt number, however, this needs further investigation, in addition to the investigation of Reynolds number effects. The effect of two parts N_2 dilution on CH_4 and C_2H_6 flames is given in the appendix A.1. The dilution addition gave a small increase in lift-off height in comparison to air premixing. Furthermore, the N_2 dilution also gave a small reduction in the flame base fluctuation range.

The mean $\mu(L_H/D)$ and standard deviation $\sigma(L_H/D)$ of the lift-off height can be computed from their instantaneous values, as shown in Fig.. 1b for all flames examined. A broadly linear trend of $\sigma(L_H/D)$ with $\mu(L_H/D)$ is shown in Fig.. 1b. The standard deviation $\sigma(L_H/D)$ is found to decrease with increased degrees of premixing for the C_2H_4 and C_3H_8 cases. The hydrogen flame has the largest deviation from an approximate linear trend of $\sigma(L_H/D)$ with $\mu(L_H/D)$, displaying the smallest $\sigma(L_H/D)$ at low $\mu(L_H/D)$, and the largest $\sigma(L_H/D)$ at highest $\mu(L_H/D)$.

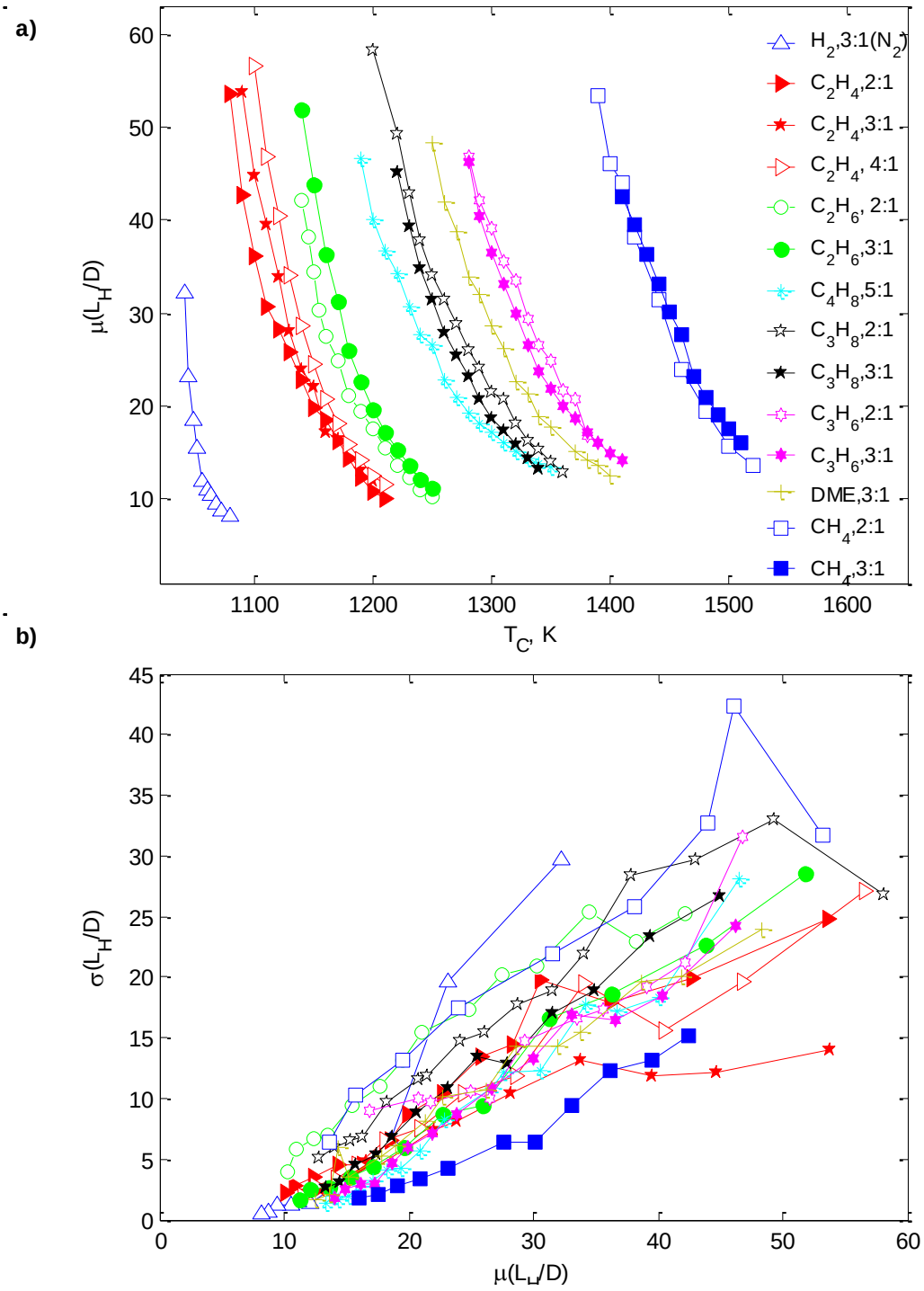

Fig. 4-2 Mean lift-off heights $\mu(L_H/D)$ vs. coflow temperature (T_C) a), and lift-off height standard deviation $\sigma(L_H/D)$ vs. mean lift-off height $\mu(L_H/D)$ b). Fuels and the degrees of the fuel jet premixed with air or dilution with nitrogen is shown in the legend for each case.

4.3.2 Fuel dependent kernel formation rates, lift-off height PDF and growth rates

This section describes the results from the high speed 10 kHz chemiluminescence data for all the fuels studied, based on the tracking of ignition kernels and the flame base. The high-speed data has proven to be insightful for understanding the dynamics of the flame base, the axial movement of the most upstream point of the main flame body, and kernel interaction, as described in Fig. 4-1. This section therefore includes: lift-off height PDF's, kernel formation rates, kernel growth rates and the relevant stabilising flame velocities: flame base advection, kernel leading and trailing edge velocities and a calculated approximate propagation velocity.

4.3.2.1 Formation rates

For each fuel and coflow temperature, new ignition kernels formed within a certain axial range above the fuel nozzle exit, below the axially oscillating flame base, exhibiting a peak kernel formation location (*x/D*). For example, new ignition events may be distributed as: 40 kernels at 5 *x/D*, 100 kernels at 10 *x/D* and 60 kernels at 15 *x/D*, indicating a peak formation at 10 *x/D*. For this example, 200 new kernels occurred over one second, producing a new kernel formation rate of 200 kern/s.

Formation rates for all fuels studied and their respective range of coflow temperatures from high to low are given in Fig. 4-4. The formation of new kernels has been binned at intervals of 3 *x/D* axial locations to produce the formation rates of all fuels. For all fuels, a relatively high coflow temperature forms kernels downstream, close to the nozzle exit, over a narrow axial formation range, i.e., for C_2H_4 2:1, T_C = 1130 K, the peak formation location is 20 *x/D* while the formation range is small at: 15 – 35 *x/D*.

An example of new kernels forming and growing is seen in Fig. 4-3 a) for C_2H_4 2:1, T_C = 1130 K. A new kernel is forming at 0 ms (indicated by the arrow), at approximately 28 *x/D*. The kernel grows for 0.2 ms before merging with the flame base at 0.3 ms. A second kernel event (indicated by the arrow) forms at 0.5 – 0.6 ms (26 *x/D*) slightly further upstream of the leading edge of the flame base (~ 29 *x/D*), so it has more time to grow before merging at ~0.9 ms. The new kernel forming at 28 *x/D* is within the formation bin 27 - 30 *x/D*, where the formation rate at this location is 90 kern/s (Fig. 4-4). Whilst the kernel forming at 26 *x/D* sits in the bin between 24-27 *x/D* and the formation rate at this axial location is smaller (60 kern/s).

Decreasing the coflow temperature to T_C = 1090 K for C_2H_4, 2:1, increases the axial location for the peak formation, now occurring at~ 42 *x/D* (60 kern/s). The formation range has also increased to 25 – 55 *x/D* (Fig. 4-4). Similarly, an example of new kernel formation is seen in Fig. 4-3 b for this coflow temperature. A new kernel forms at 0.0 ms (40 *x/D*, indicated by the arrow), approximately 5 *x/D* upstream of the flame base (45 *x/D*). The kernel is growing for 0.6 ms (note the data is sampled at 0.2 ms intervals opposed to 0.1 ms) before merging into the flame base at 0.6 ms. A second kernel event forms at 1.2 ms (30 *x/D*, indicated by the arrow), further upstream of the flame base (38 *x/D*), and as such grows over 0.8 ms merging at 2 ms (not displayed)

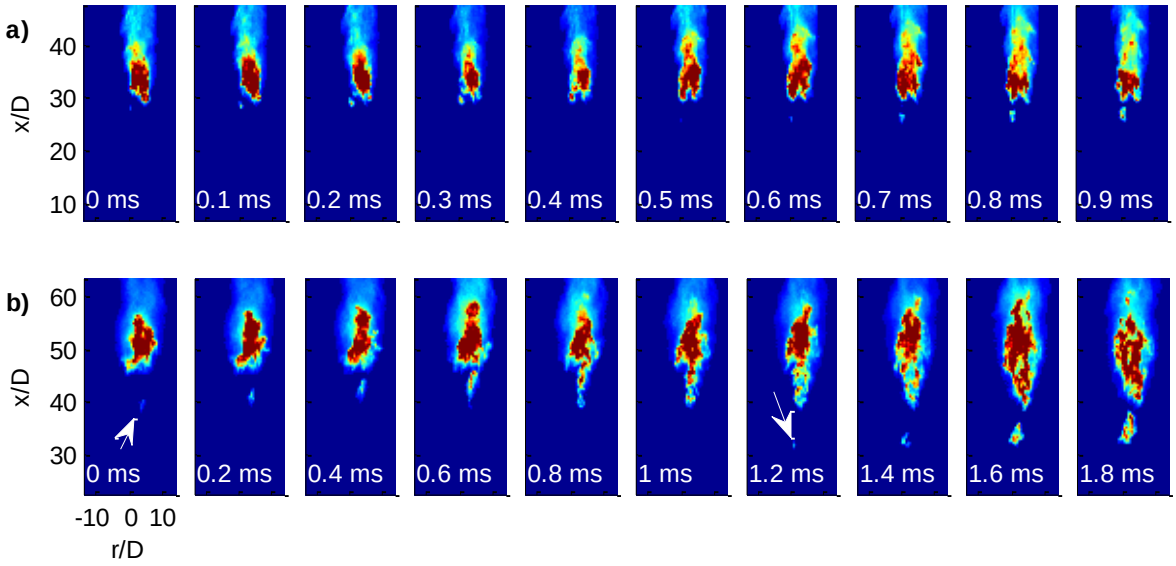

Fig. 4-3 An example of consecutive images indicating kernel initiate, growth and merging with the flame base for C_2H_4 2:1 flames. A high coflow temperature, T_C = 1130 K (a) and low coflow temperature, T_C = 1090 K (b) is presented for a sample rate of 0.1 and 0.2 ms respectively. The arrow indicates new kernel formation events.

The total formation rate for all flame axial locations is also given in Fig. 4-4 within the legend for each fuel at their corresponding coflow temperatures and mixing ratios. Whilst the higher coflow temperature, for a given fuel, has a greater peak formation rate, the total integrated rates (sum of all axial formation rates) are similar compared to lower temperatures. That is, for C_2H_4 2:1 at a high coflow temperature (T_C = 1130 K) the integrated formation rate is 207 kern/s, while the peak formation rate is 90 kern/s. The lower coflow temperature (T_C = 1090 K) has a lower peak formation rate of 70 kern/s. However, the integrated formation rate is like the higher coflow temperature of 231 kern/s.

The formation rate of new kernels increases slightly as the coflow temperature is further increased, i.e., for C_2H_4: T_C= 1150 K, 1170 K and 1190 K, the integrated formation rates are 234, 254 and 266 kern/s respectively. Other fuels have a decrease in kernel formation rate for increasing coflow temperature, where the impact of kernels on the flame base for higher coflow temperatures is

explored in the next chapter for DME flames, analysing kernel heat release. The kernels for higher coflow temperatures form very close to the flame base and as such can be difficult to identify if they are distinct from the flame base in this chemiluminescence experiment.

There is notable behaviour occurring at intermediate temperatures for hydrogen, near T_C =1044 K, where two peaks in formation rates occur; these observations have been confirmed by multiple, repeated measurements. The somewhat bimodal formation position, of new kernels, at this temperature is believed to be predominately due to: a combination of turbulence/mixing and the location of the flame base. Since a new kernel can only form below the flame base, as the definition for new kernels describes, if the flame base is upstream, near the nozzle, no new kernel can form at axial positions further downstream. Therefore, conversely, if the flame base is farther downstream, a new kernel can form at multiple positions downstream of the exit nozzle. This therefore, means that for a new kernel to form at a given axial position, the position depends on mixing and flame propagation speeds; that is, the mixing required to achieve the correct ignition temperature (equivalence ratio), and also the relative distance of this premixed pocket relative to the flame base. Noting, the position of the flame base is dependent on the kernel formation rate and flame base advection speed, or the speed with which the flame base is propagating into the unburnt gases.

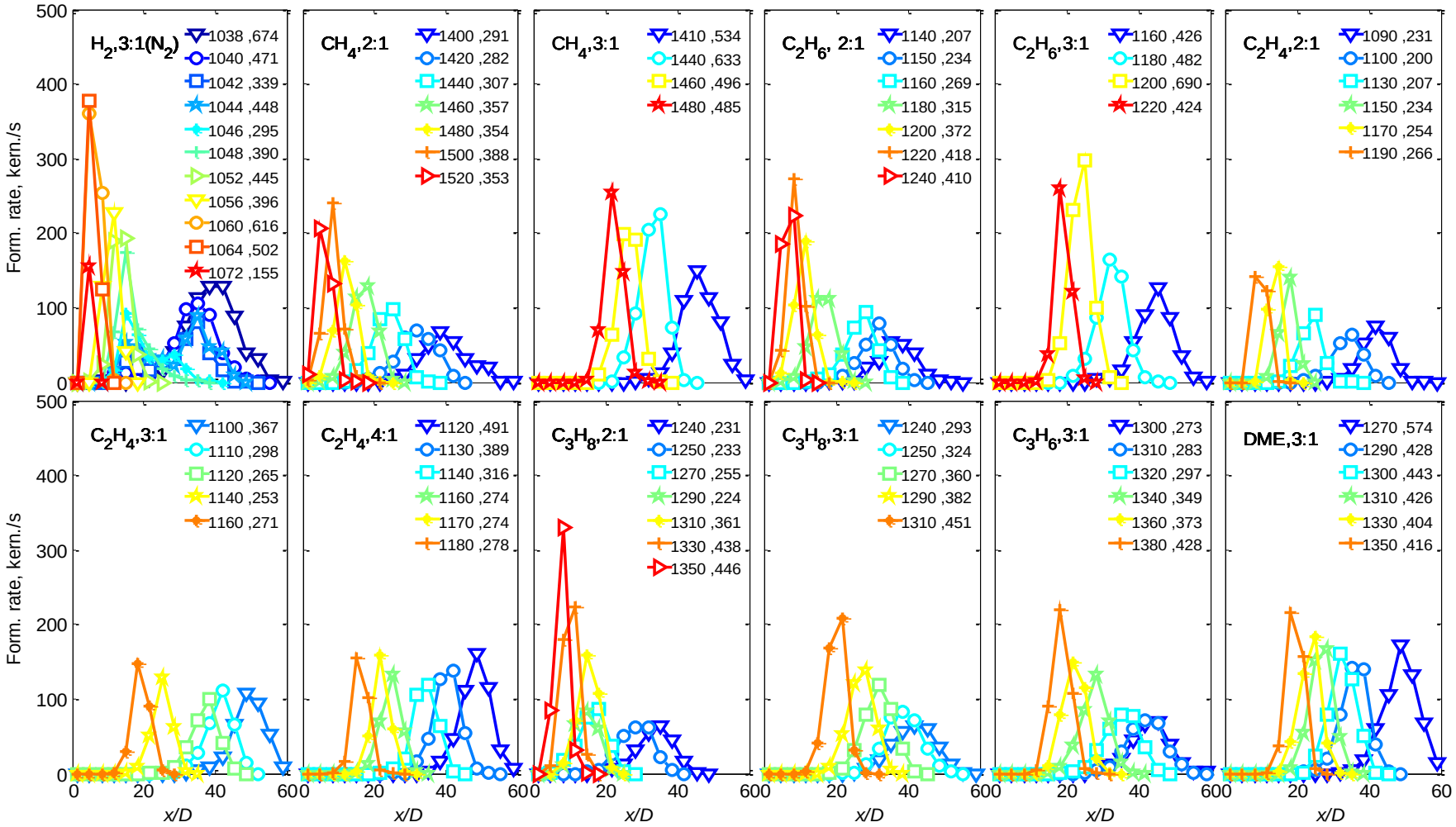

Fig. 4-4 Formation rates for all fuels studied for a range of coflow temperatures, from high to low (indicated in each legend, left. Total formation rates are also presented within each legend (right value) for various air premixing levels, for all hydrocarbons, an additional H_2 case diluted with N_2 is also given. The second number in the legend indicates the integrated formation rate for each fuel at a given coflow temperature, given in kernels per second.

4.3.2.2 Lift-off height PDF

Similarly, to the formation of new kernels there is a location where the flame base (lift-off height) is more frequented during the flame's fluctuation, locations are converted to a PDF and a peak location (*x/D*) additionally occurs. Like the formation rates presented in Fig. 4-4 the leading edge, axial location of CH^*, of the flame base (lift-off height) has a larger axial range for lower coflow temperatures. For C_2H_4, 2:1 at T_C = 1090 K, the location of the flame base is typically at 40 *x/D* (PDF = 0.1), with a range of 25- 55 *x/D*. The flame base range for the lower temperature is seen by the consecutive images from Fig. 4-3 b, where the axial range is 30 - 60 *x/D*, with the flame oscillating between those bounds.

For C_2H_4, 2:1 at T_C = 1130 K the location of the flame base is typically at 20 *x/D* (*PDF* = 0.15), with a range of 18 - 26 *x/D*, a smaller range than the lower coflow temperature (Fig. 4-3b). An example of the flame oscillation is seen above in Fig. 4-3a where the image boundary is small, and the flame oscillates further upstream than the lower coflow temperature.

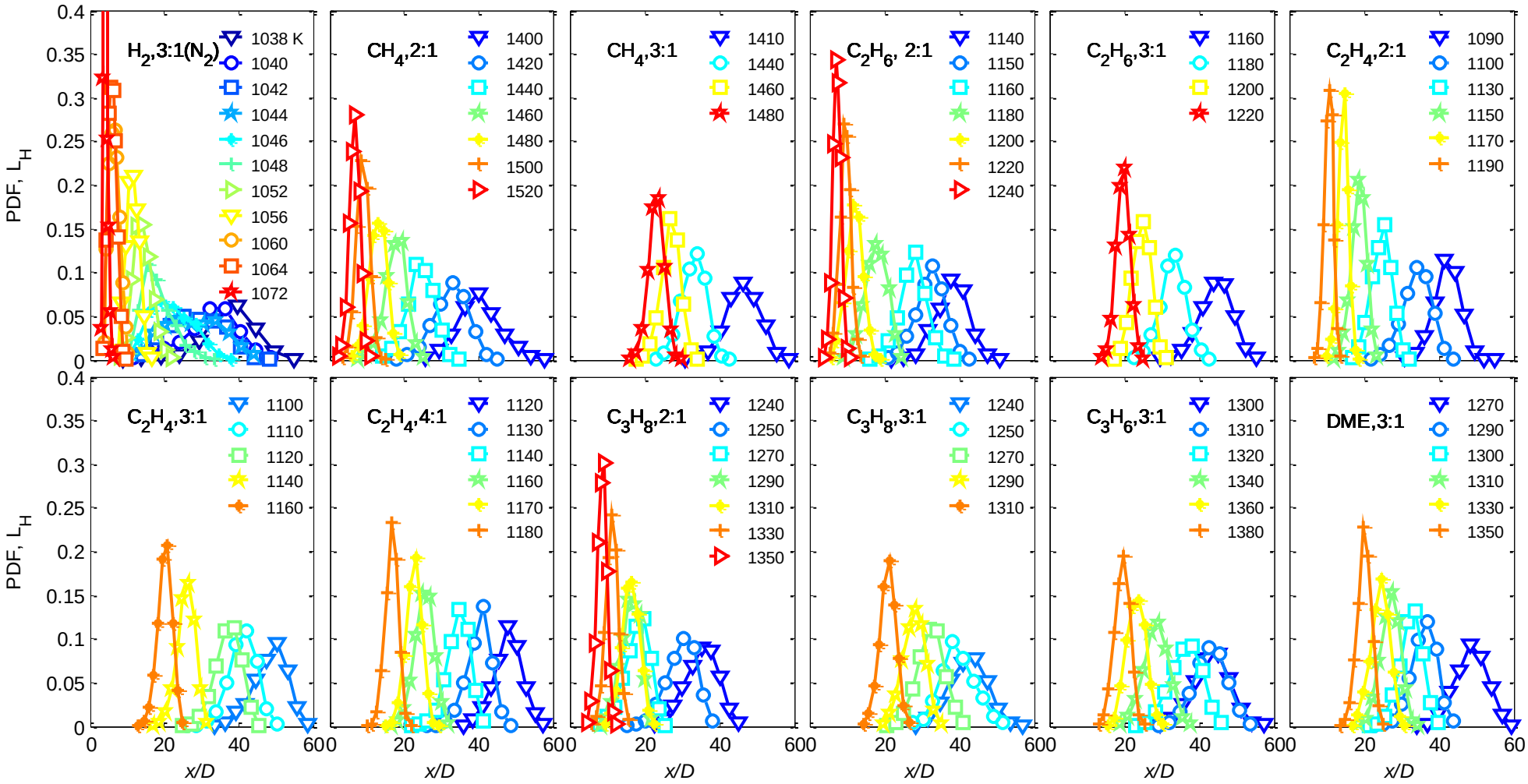

Fig. 4-5 PDF's for lift-off heights at a range of axial locations of various fuels and coflow temperatures (given in the legends). PDF's for certain fuels are given for various premixing levels. The H_2 L_H PDF height for1072 K is 0.5 (not displayed).

4.3.3 **New kernel formation and flame base location PDF's**

By analysing the formation rate and the peak rate location (Fig. 4-4) for a given temperature, it can be seen that the formation locations overlap onto the *PDF* location of the flame base (Fig. 4-5). It is indeed found that once converting the formation rates of new kernels to a PDF, based on their axial formation, kernels on average only form slightly upstream of the flame base, with a similar probability, seen in Fig. 4-6. Four *PDF's* are presented for each fuel case (C_2H_6 and CH_4) in Fig. 4-6, for a relatively high and low coflow temperature, two *PDF's* each, for the location of formation rates and lift-off heights respectively.

The peak in the *PDF's* in Fig. 4-6 for both fuels indicates the most probable location for ignition relative to the flame base. The peak in new kernel formation rates (closed squares) for the high-temperature coflow case of CH_4 and C_2H_6 are seen to occur slightly upstream of the lift-off height *PDF* (open squares). The broadening and reduced peak in the *PDF* with reduced coflow temperature is due kernels forming at a larger axial range which is observed for all fuel types.

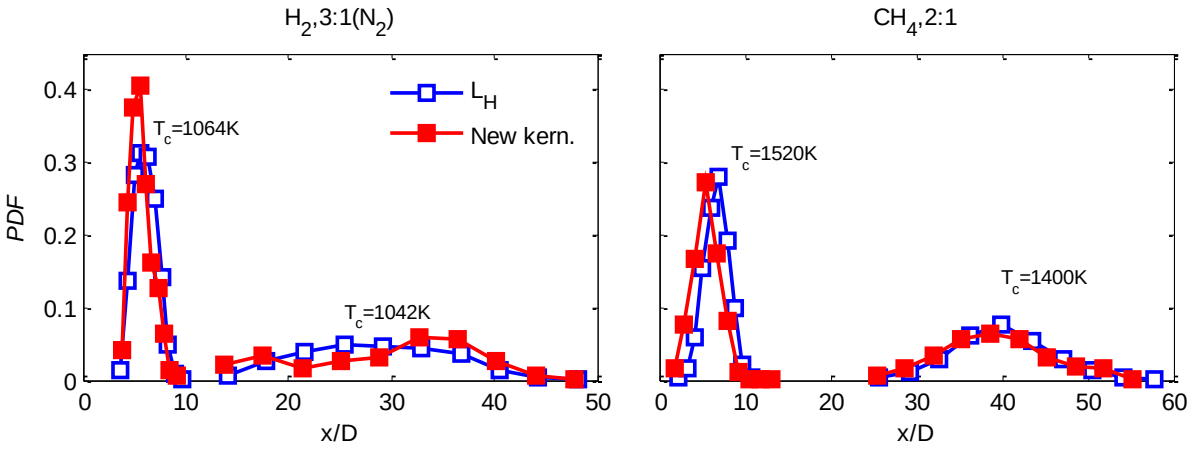

Fig. 4-6 The axial location PDF's for new kernel formation (closed squares) and lift-off heights (open squares) for two fuels, C_2H_6 (left) and CH_4 (right), for a high and low coflow temperature. Coflow temperatures are shown in the Figure.

The overlap in the *PDF*'s is due to the flame base and downstream edge of the kernel advecting at approximately the same low velocity, with the upstream edge of the kernel growing faster seen in Fig. 4-7. The faster leading-edge of the kernel means the kernel merges and forms a new flame base location close to where the kernel initiated. The new kernel initiates at 0 ms and the merging event and new flame base location at occurs at 1.2 ms. An increase in coflow temperature for all fuels shifts the kernel formation *PDF* further upstream of the lift-off height *PDF* seen in Fig. 4-6. The upstream shift is believed to be due to the flame base advecting at a similar rate to the lower coflow temperature case, however, the kernels are growing at a slower rate, given in Fig. 4-8.

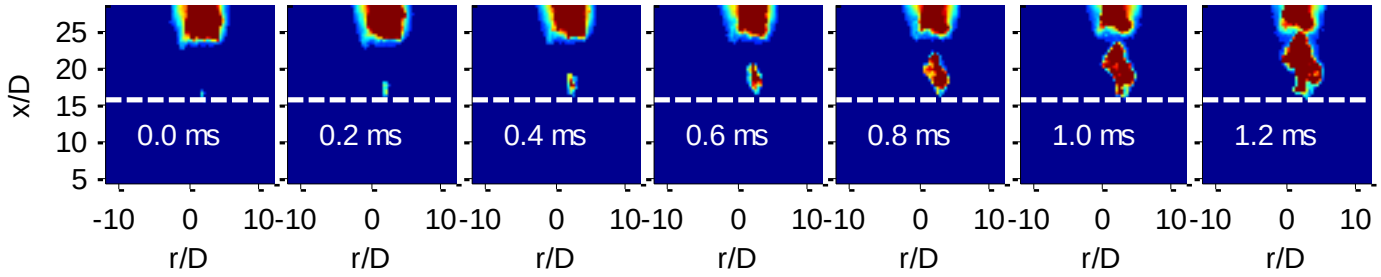

Fig. 4-7 High-speed image sequence for a C_2H_6:air = 1:2 flame at T_C = 1190 K. The horizontal dashed line indicates the upstream kernel formation tip location.

4.3.3.1 Kernel growth rates

A new kernel is defined by the occurrence of a new centroid, kernel growth, hence, is defined as the increase in the number of kernel pixels following initiation prior to the kernel merging into the flame base. The kernels are a 2-D projection of the volumetric chemiluminescence, where the kernels are believed to be axi-symmetric or somewhat spherical in nature (this assertion needs investigating using volumetric or tomographic measurements). The 2-D kernel projection is converted to a mm^2 area seen in Fig. 4-8 using the camera resolution ~ 4 pixels/mm. The pixel resolution of ~4 pixels/mm was constant for all hydrocarbon flames and for low coflow temperatures (highly lifted flames) with hydrogen. However, to improve the resolution of hydrogen flames, a higher resolution (different lens setup) was used for high coflow temperatures (low flame lift-off

heights). Since the images are taken at high speed (10 kHz) the flames are temporally resolved, and kernel sizes are given per millisecond. The kernels sizes are seen to be increasing somewhat linearly with time, as such an approximate linear fit (growth rate) is given in each plot in mm^2/s.

For all fuels and coflow temperatures, ignition kernels are seen to form at the same relatively small size of 1 mm^2. Since kernels initiating in relatively low coflow temperatures for a given fuel are further upstream of the flame base, they have more time to grow and hence grow to larger sizes (observed for all fuels). The larger kernel growth of lower coflow temperatures can be seen visually in Fig. 4-3 b for T_C = 1090 K compared to Fig. 4-3a T_C = 1130 K, where the maximum kernel size is 2000 and 1200 mm^2 respectively. Noting, all kernel sizes are for kernels prior to merging into the main flame body.

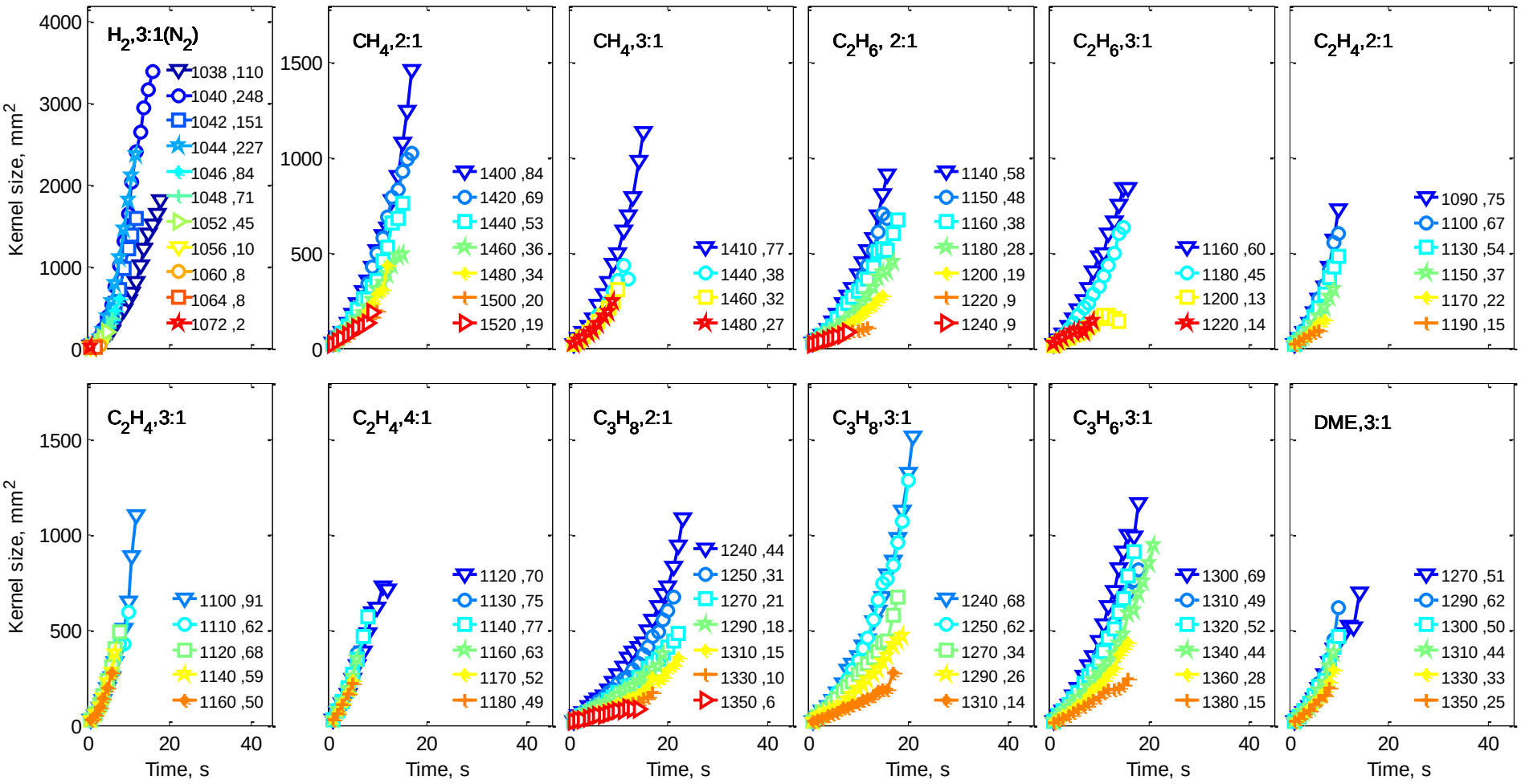

Fig. 4-8 2-D projected CH* kernel size versus time for the range of fuels studied, including a range of coflow temperatures (listed as the first value in the legend) and premixing ratios. The second value in the legend describes the kernel growth rate in mm^2/s.

For most fuels, a lower coflow temperature produces faster growing kernels, this increase in growth rate with lower coflow temperature is counter-intuitive, as increased temperature increases the flame speed. The growth rates therefore potentially identify that lower coflow cases are propagating into more ignitable mixtures. That is, for CH_4, 2:1 the low coflow temperature, T_C = 1400 K, kernels grow at a rate of 84 mm^2/s, while for a higher temperature, T_C = 1520 K, kernels are growing at 19 mm^2/s. This growth rate of kernels, growing faster for most fuels, however, is not the case for ethylene, where it has an optimal temperature of T_C = 1140 K corresponding to a peak growth rate of 77 mm^2/s, discussed further in relation to the sound measurements.

For all hydrocarbons, the maximum size of kernels is ~800 – 1500 mm^2 for low temperature coflow kernels, prior to merging with the main flame base seen in Fig. 4-8. However, for H_2, kernels are growing to a significantly larger size, of ~ 3500 mm^2, compared to hydrocarbons (note the different y-axis scale, Fig. 4-8). This larger kernel size is attributed to the distance of kernel formation being well upstream of the flame base in addition to the kernels growth rate. The difference in low coflow temperature size for the H_2 case is seen in Fig. 4-9b (T_C = 1038 K). The kernel initiates at 0 ms, growing until 2.4 ms at a rate of 100 mm^2/s (Fig. 4-8) until it merges into the flame base at 2.7 ms. At this time the kernel is larger than the flame base, additionally growing to a size larger than other hydrocarbons, such as C_2H_4, seen previously in Fig. 4-3 b. For reference, the high-temperature H_2 case of T_C = 1064 K is given in Fig. 4-9a, the resolution is much larger (as a different lens was implemented) to identify the smaller kernels near the flame base.

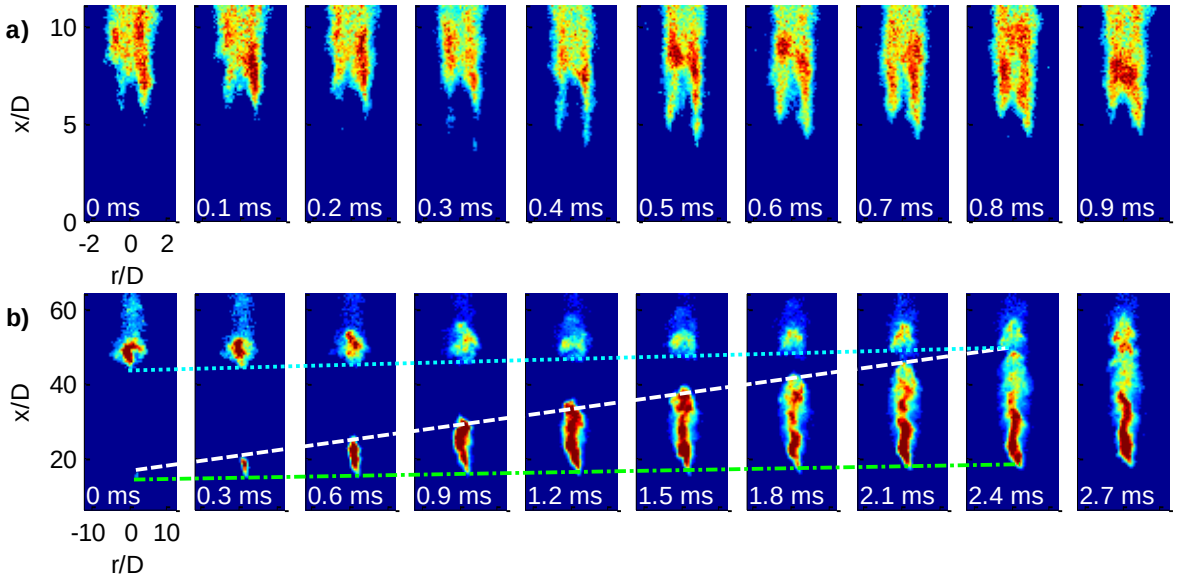

Fig. 4-9 An example of consecutive images indicating kernel initiation, growth and merging with the flame base for two H_2 flames. A high coflow temperature, T_C = 1064 K (a), operating between 0-10 x/D, and low coflow temperature, T_C = 1040 K (b), operating between 0-10 x/D, is presented for a sample rate of 0.1 and 0.3 ms respectively. The lines indicate: the flame base advection velocity (blue, dotted), kernel leading edge velocity (white-dashed) and the kernel trailing edge (green, dot-dashed).

Furthermore, the size of the kernel grows to a given size before merging with the flame base, this is due to the distance the kernel forms upstream relative to the flame base, in addition to the relative leading-edge velocity with respect to the flame base velocity. A representation of the velocity for the flame base advection velocity (dotted blue line) and the velocity of the kernel leading edge (dashed white line) is given in Fig. 4-9b. The kernel trailing edge is also given (dashed, dotted green line), it has a similar velocity to the flame advection velocity. The kernel leading-edge velocity is seen to form far upstream of the flame base, it grows and finally merges with the flame base due to the much greater velocity. These relative flame base advection and kernel velocities are determined in the following section.

4.3.4 **Flame base dynamics**

Representative, consecutive, CH^* 10 kHz images are seen in Fig.. 4-10 for a DME fuel jet of air:DME = 3:1; where all hydrocarbon fuels exhibit similar sized ignition kernels forming upstream of the flame base for relatively high to low coflow temperatures (presented later in this chapter). The figure highlights the flame base fluctuation (flame base advection and kernel merging), kernel initiation and consumption events (kernels merging with the flame base).

The T_C = 1400 K coflow case (high coflow temperature) shows very little oscillation of the flame base location, ~ 8 *x/D*. A small autoignition kernel forms below the base at 5.2 ms (Fig.. 4-10a), it joins the flame base in the next frame at 5.3 ms. By referencing the average lift-off height, the flame base is also 'pulled' upstream without kernel consumption shown at 5.5 - 5.6 ms, attributed potentially to flame propagation.

For the relatively high coflow temperature, T_C = 1275 K in Fig.. 4-10, the flame has differing characteristics to the T_C = 1400 K case. A comparably sized kernel relative to the T_C = 1400 K coflow forms below the flame base at 29.1 ms, however, it forms farther upstream of the flame base and therefore has time to grow over 8 frames and be consumed at 29.9 ms. At this time the location of flame base incurs a significant upstream 'jump' of ~ 5 *x/D*'s, where the new flame base is defined by the bottom of previously consumed kernel.

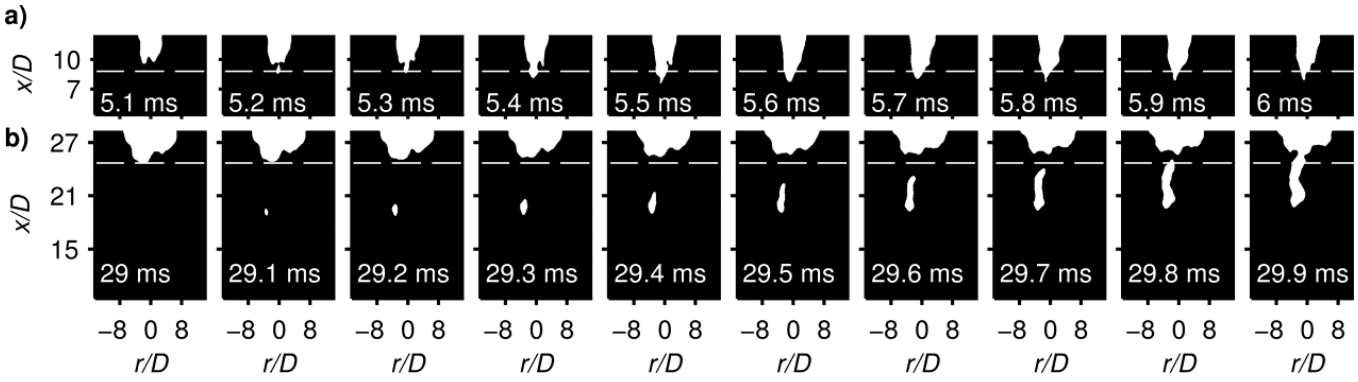

Fig.. 4-10 Consecutive 10 kHz images for 3:1 cases at T_C = 1400 K (a) and T_C = 1275 K (b). The horizontal line is the average lift-off height for the set of images.

The axial fluctuation in the temporal flame base is seen in Fig.. 4-11 which shows the dependency of flame base stabilisation due to kernel consumption where listed times correlate to Fig.. 4-10. The T_C = 1400 K coflow indicates that kernel consumption only induces small 'jumps' in the lift-off height, and comparably sized upstream premixed flame propagations occur more readily, they exhibit a 'sinusoidal' profile structure in lift-off height. Examples of such kernel and premixed stabilisations are seen in Fig.. 4-10 at 5.3 ms and 5.5 ms respectively. The increased stabilisation of higher coflow temperature flames via premixed propagation is further observed by Ardnt et al. [119] using similar OH^* measurements on CH_4 JHC flames

The coflow temperature of T_C = 1275 K results in differing flame stabilisation characteristics to the T_C = 1400 K case. Temporally, the lift-off height relationship is not sinusoidal but exhibits more extreme 'ramp/ cliff' structures; larger kernels induce large jumps in flame base location. Any significant upstream propagation correlates directly with a kernel being consumed by the flame base. This indicates that a low coflow temperature, T_C = 1275 K, is highly dominated by autoignition flame stabilisation. The two coflow temperatures fluctuate around a mean value, where for T_C = 1400 K it is ~ 9 *x/D* and 25 *x/D* for T_C = 1275 K, and mean lift-off heights are typically captured using a digital camera due the longer recording period, seen in the following section.

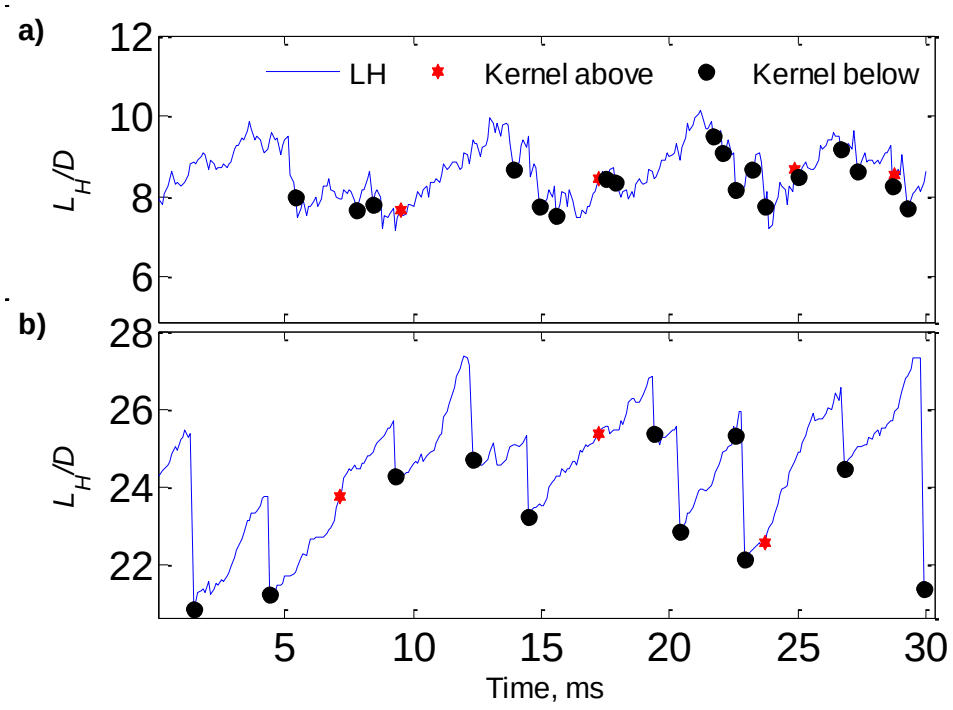

Fig.. 4-11 Continuous lift-off height fluctuations for air:DME=3:1 flames: T_C = 1400 K (a) T_C = 1275 K (b). Red stars indicate kernels that are consumed above the instantaneous flame base (due to the flame base's asymmetric nature). The black circles indicate where a kernel is consumed below the flame base.

4.4 **Kernel velocity and flame base advection**

As discussed previously, the flame base advects consistently downstream (Fig. 4-9, excluding kernel merging events), where this flame base advection velocity is somewhat constant for an entire flame series Fig. 4-12. Fig. 4-12 displays the temporal flame base displacement downstream of the nozzle with the formation of new kernels and the 'discontinuity' that occurs as the kernel merges into the flame base. The displacement of the flame base is given in *x/D* with respect to time, the advection of the flame base (*d(x/D)/dt)*) is particularly evident between 62 - 78 ms, where other instances of flame base advection are somewhat parallel and hence the advection velocity is constant for a given fuel and coflow case.

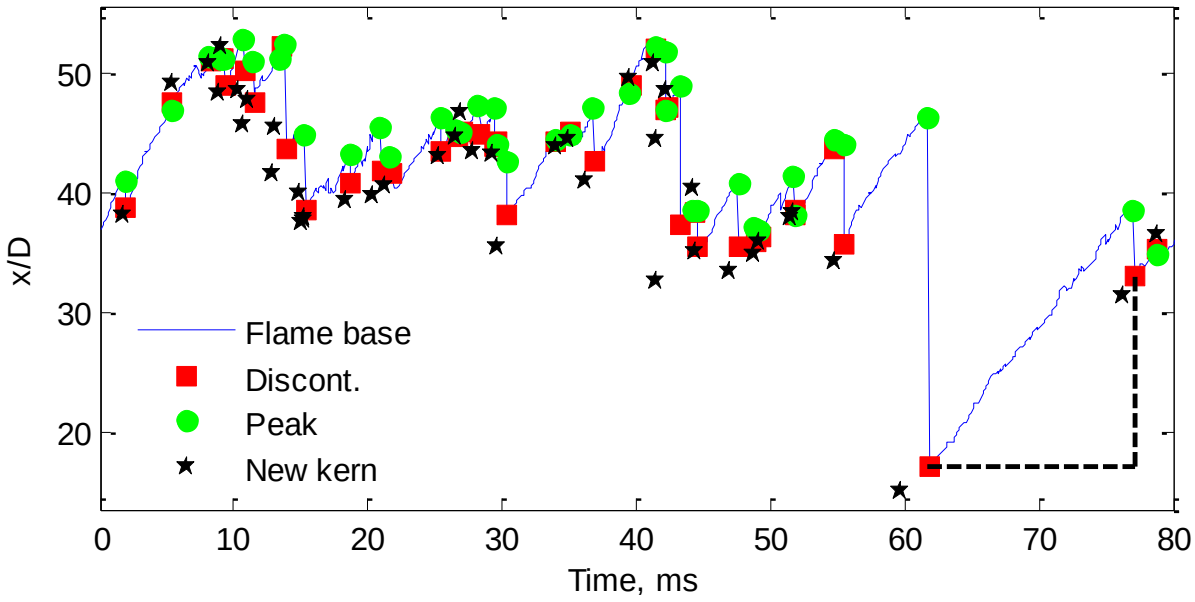

Fig. 4-12 Temporal flame base kernel interaction over a 80 ms period (800 images) for a H_2:N_2 = 1:3 at T_C = 1040 K, including kernel merging (Discont.), the flame base advection peak and kernel formation (New kern).

The advection of the flame base can be calculated by two methods, either, by determining the average gradient for the flame base downstream displacement between large consumption events with time (dL_H/dt) given by the dashed-line (rise/run) between 62 - 78 ms. The second method is to determine the flame base displacement between each new kernel consumption event, noting both methods yielded very similar results.

A pictorial diagram of the kernel base (FB) advecting down-stream with an ignition kernel (K) growing to merge with it, is given below in Fig. 4-13 for two times: t_1 and t_2, where the velocity flow field is given by grey arrows (V^{FL}). The velocity of the flame bodies is described as: Flame base (*FB*), kernel (*K*), kernel leading edge (*Le*), kernel centroid (*C*) and kernel trailing edge (*Tr*). The velocity of each flame body is represented based on the flame description and velocity components. That is, the velocity is described by: $V_{Body,\ description}^{Velocity\ components}$, where the velocity components include the local flow field velocity (*FL*) and the flame propagation (*FP*). As such the kernel leading edge (*K*,

Le) velocity is made up from the flow field velocity plus the flames propagation speed: $V_{K,Le}^{FL+FP}$.

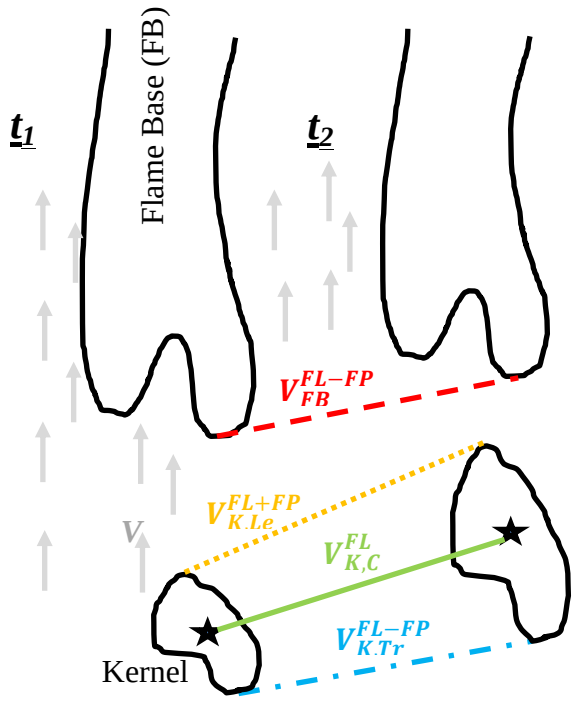

Fig. 4-13 Pictorial diagram describing the: flame base advection (V_{FB}^{FL-FP}) , the kernel leading edge velocity ($V_{K,Le}^{FL+FP}$) , kernel centroid velocity ($V_{K,C}^{FL}$) and the kernel trailing edge velocity ($V_{K,Tr}^{FL-FP}$).

For the H_2 example in Fig. 4-12, for a coflow temperature of T_C = 1040 K, the flame base advection velocity shown as the dashed red line in Fig. 4-13 is ~7 m/s, seen in Fig. 4-14 (*FB*). The advection velocity for all fuels are calculated in the same manner and are also displayed in Fig. 4-14; the hydrogen flame is seen to have the largest advection speed for the highly lifted flames.

Kernel-leading and trailing edge velocities are calculated on a shot to shot basis for growing kernels indicated previously by lines in Fig. 4-9b. The kernel velocities (leading and trailing) are found to be similar across all growing kernel samples for a given fuel and coflow temperature. Therefore, the average leading and trailing edge kernel velocities are given in Fig. 4-14.

By making assumptions that the leading and trailing kernel edge propagate into the same mixture and that the flow field is similar between both points (up and down-stream of the kernel), a flame propagation speed can be determined.

Kernel propagation speed and flame propagation speed is described in Eq. (4.1) and (4.2) Eq. respectively.

$$V_k^{FP} = \frac{(V_{K,Tr}^{FL-FP} - V_{K,Le}^{FL+FP})}{2} \quad (4.1)$$

$$V_{K,Le}^{FL+FP} - V_k^{FP} = V_k^{FL} \quad (4.2)$$

The velocities and the flow components such as: the flame base velocity, kernel leading edge, kernel trailing edge, flame propagation, kernel centroid and flow field velocity are given in Fig. 4-12. The velocities are plotted versus the average lift-off heights (Fig. 4-2) for each fuel. The lift-off height is used opposed to the coflow temperature to identify if there are common characteristic velocities across all fuels despite the various fuel sensitivities to coflow temperature.

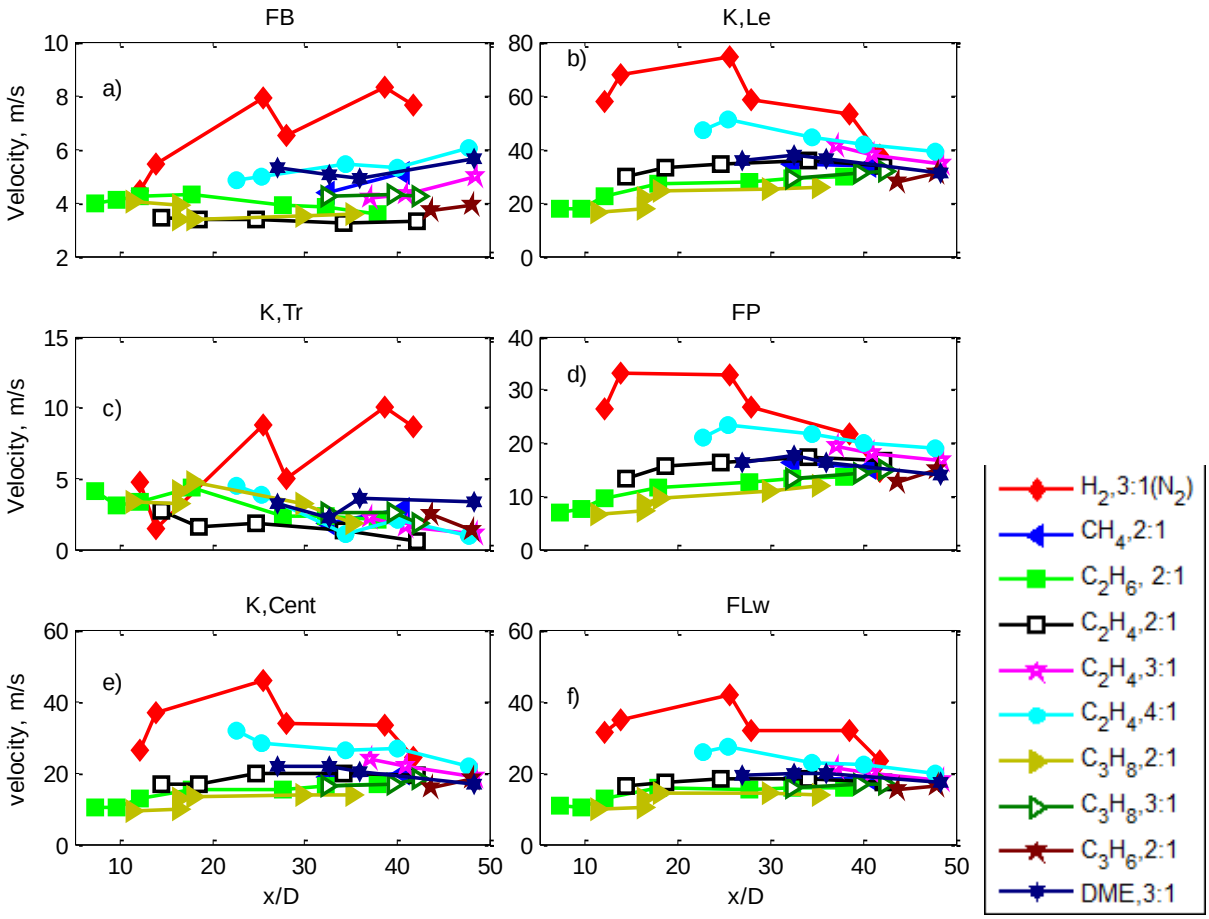

Fig. 4-14 Results for the: Flame base advection velocity (a), kernel leading edge velocity (b), kernel trailing edge velocity (c), flame propagation speed (d), average experimentally measured centroid velocity (e) the calculated centroid velocity (f).

All hydrocarbons have similar flame base advection speeds (6- 3 m/s) seen in Fig. 4-14, where increased flame advection velocity indicates increased dependence on kernels to be stabilised. That is, the faster the flame base advects, the lesser is the ability of upstream flame propagation to overcome the flow field velocity. All flames studied have a constant flame base always existing less than 60 *D*, i.e., the flame is never 'blown-off'. Therefore, the kernel leading edge velocity needs to be great enough to join the flame base prior to blow off. As such, the leading-edge velocity is also plotted in Fig. 4-14. As expected the flame with the fastest flame base advection velocity (7 m/s, H_2) has correspondingly the fastest kernel leading edge velocity of ~ 50 m/s. Hydrogen, additionally, is

found to have the largest calculated propagation velocity of ~ 30 m/s for low lifted flames with high coflow temperatures and propagation speeds up to ~ 20 m/s for higher lifted flames. The hydrocarbons have closer propagation velocities between 10- 20 m/s with ethylene being the fastest. The analysis based on kernel velocities is similar to the work by Oldenhof et al. [50], who identified the front and back velocities of a 'flame pocket' (kernel), for two coflow temperatures using natural gas. It was identified increased back (trailing-edge) velocity increased the lift-off height, whilst kernel formation rate decreased it.

The flame base advection speed for increasing ethylene premixing (2:1 to 4:1) increases the flame base advection velocity for a given average lift-off height. In turn, the flames propagation speed is seen to increase to achieve the same equivalent lift-off height. It is further noted that for an equivalent lift-off height, increased premixing leads to an increased new kernel formation rate (Fig. 4-4). Therefore, the average lift-off height location isn't solely dictated by the kernel formation rates and advection and flame propagation rates have a large effect.

The ratios between relative: kernel, flame base and flame propagation speeds are seen in Fig. 4-15. It identifies that, as seen visually, the kernel trailing edge has a similar velocity to the flame base velocity (ratio = 0.4 - 1.4). Identifying that both the flame base and the kernel trailing edge experience a similar mixing field, flow/velocity field and mixture fraction space. The flow velocity is like the flame propagation velocity (ratio = 1.1 - 1.6), this emphasises that whilst the flame base advects downstream, somewhat slowly (3 - 7m/s) for a decaying 100 m/s fuel jet, the flow velocity always exceeds the propagation velocity, for all coflow temperatures and all fuels.

Finally, for all fuels, the kernel leading edge is much faster than the flame base advection velocity (ratio 6 – 10, between L_H = 15-50 *x/D*). This ratio identifies again that the relatively slow flame base advection velocity enables ignition kernel events to grow to relatively large sizes before

merging into the flame base. The growing and faster kernel leading edge is what enables stabilisation for all fuels issuing into the hot coflow burner.

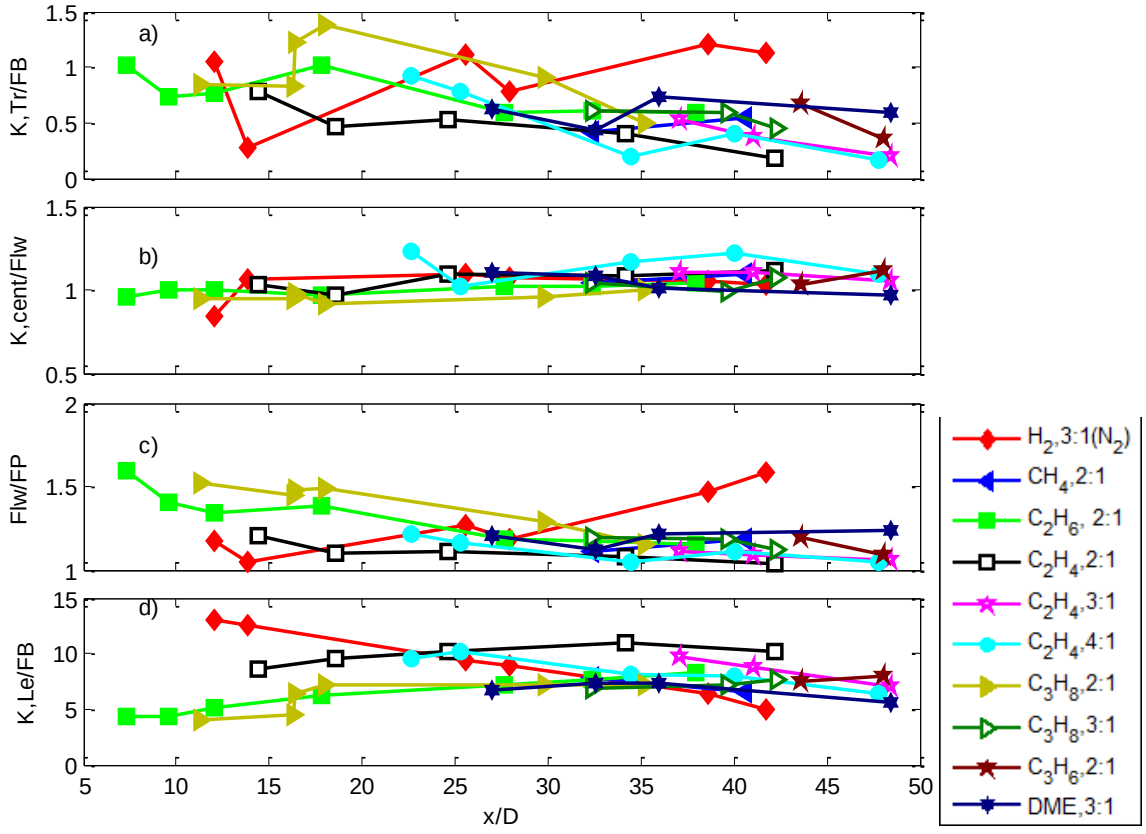

Fig. 4-15 Ratios between velocities for the: flame base advection and kernel trailing edge (a), Kernel centroid and the flow field velocity (b) the flow field and the flame propagation velocity (c) and finally the kernel leading edge velocity and the flame base advection velocity (d).

The similar velocity ratios of all the fuels studied, between the flame base and ignition kernels, indicates that despite the range of coflow temperatures, the dynamics for stabilisation is somewhat similar. That is, all flames and fuels are well described by the interaction of the kernel feeding into the advecting flame base. Moreover, kernel autoignition (average location) relative to the flame base is proportional to the flame propagation rate of the ignition kernel and flame base, for flames to have an average lift-off heights less than 60 *D*'s.

4.5 **Flame acoustic emission**

As the formation of ignition kernels and their interaction with the flame base is an inherently transient process it follows that it would contribute to the flame acoustic emission. The flame acoustic emission for all the fuels studied is presented in Fig.. 2. All flames exhibit a strong sensitivity of acoustic emission to coflow temperature above a lift-off height of x/D = 10, as shown in Fig.. 2a) and b). The L_{10} value, that is the sound pressure level that is exceeded 10% of the time is used to characterise the global flame sound level. In addition, sound levels that exceed the L_{10} level indicate significant acoustic events. These large sound emissions may correspond to autoignition or large kernel/ flame base merging events, where this is explored in the following sections.

The methane flames are found to produce the lowest L_{10} values, approximately 60%, lower than the other hydrocarbon flames, as for a given lift-off height, the ethylene flames produce the largest L_{10} values. For the ethylene flames at high levels of partial premixing (3:1 and 4:1) there exists an intermediate lift-off height, corresponding to an intermediate coflow temperature, that is well within the shroud of the hot coflow where the L_{10} sound emission peaks. This peak in sound emission, whilst not as pronouced, exists for other hydrocarbon flames, such as: DME and propane.

It is seen that for ethylene flames the trend of lift-off height with the L_{10} value (Fig. 4-16 b) doesn't have a linear correlation. Noting there was a linear correlation between lift-off height and the flames fluctuation (Fig. 4-16 b), as such, the sound production is not entirely attributed to the fluctuations in the flame base height at least for the ethylene cases. For the propane cases, however, the correlation of L_{10} sound emission and $\sigma(L_H)$ is stronger and flame base fluctuation may be a larger contributor. It is further hypothesising that the level of sound for each fuel is proportional to: the level of sound production correlating with the fluctuation in the rate of heat release rate per unit volume.

The hydrogen flame is a relatively quiet flame and indeed has somewhat different sound characteristics and as such it is analysised separately. The H_2 flames at the lifted cases, > 18 *x/D*, emits a series of 'popping' sounds, whilst not directly correlated to new kernel formation, the intermittent sound effects the global sound emission, and induces a peak in sound for a relatively low lift-off height (18 *x/D*).

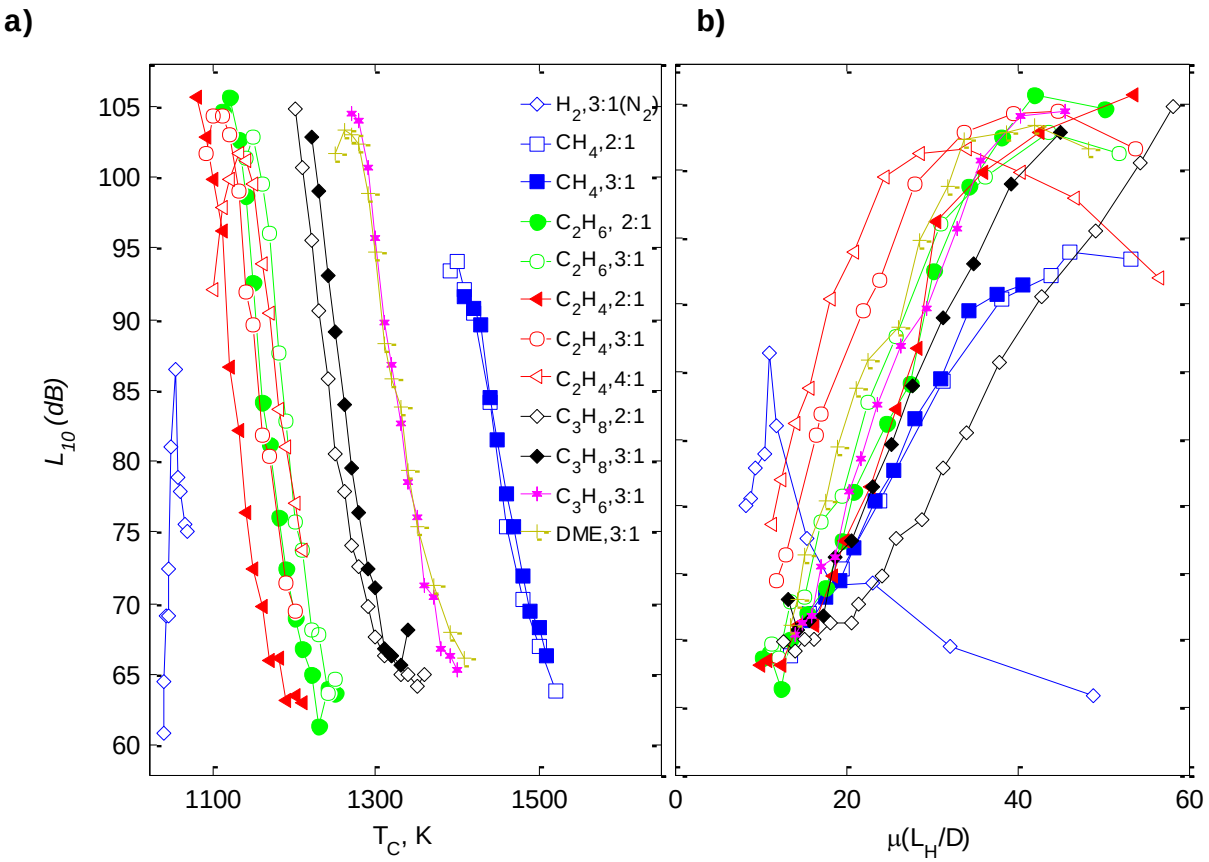

Fig. 4-16. L_{10} sound emission vs. coflow temperature a), and mean lift-off height b) for a range of fuels types and premixing ratios.

4.5.1 **Temporal correlation of sound and chemiluminescence**

The temporal evolution of sound emission, flame lift-off height and kernel formation are shown in Fig. 4-17 for the 3:1 ethylene jet case. The sequences in Fig. 4-17 shows how kernel formation events (shown as red dots) do not correlate with large acoustic emission events; this is

illustrated by the four kernel initiation events between 40-70 ms which contain no peak sound emission events for the T_C =1090 K case. However, the four high pressure peaks for the T_C =1090 K case do correlate with large jumps in the flame base height. These jumps are attributed to large kernels merging with the flame base, as illustrated in Fig. 4-17 for the case with T_C = 1090 K, where the vertical dashed lines mark such instances (a more pronounced example is highlighted by arrows at 18 ms). Irrespective of the intermittent high acoustic emission events, the background sound pressure level is much larger for the T_C = 1090 K than the T_C = 1190 K flames. The high coflow temperature, T_C = 1190 K, flame has a low lift-off height, indicating that despite a high kernel formation rate, the sound emission mechanism is not correlated to kernel initiation.

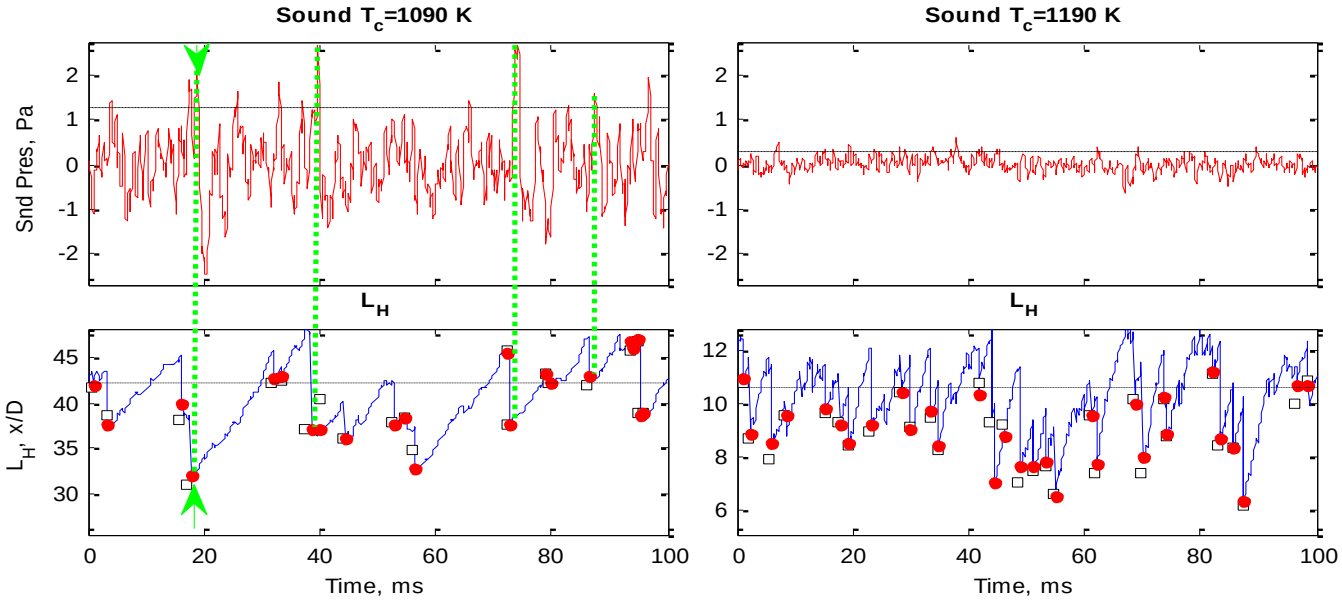

Fig. 4-17. Ethylene temporal sound and Lift-off heights: T_C = 1090 K and T_C = 1190 K. New kernels and kernel consumption events are the open squares and closed circles respectively. The horizontal dashed line in the sound plot indicate the L_{10} value, the vertical dotted line correlates the sound data to the temporal lift-off heights.

To determine the temporal correlation of kernel merging events and the larger sound emissions, the events are identified in both the chemluminescent images and sound sequence seen in

Fig. 4-18, it shows three coflow temperatures for an ethylene 2:1 case. The red circles indicate the large sound emission events and the green triangles indicate the extreme ‘flame-base’ jumps.

The 100 kHz sound data was processed by sampling it at the same rate as the 10 kHz high speed measurement, then only the positive sound emissions were processed. The extreme peaks were identified using the in built *findpeaks* matlab function, this function identifies all local peaks within the data. Further, conditioning based on the extracted data peaks standard deviation was applied to identify the large sound peaks.

The large merging events for the chemiluminescence data was obtained by identifying the lift-off height temporal gradients (dL_H/dt). The extreme gradients, those that were four standard deviations ‘away’ from the mean upstream flame base ‘jumps’ were identified as the large merging events given in 4-18. The large ‘jumps’ identified by the green arrowsindicate the large kernel merging events, they are distinct from the smaller merging events, where all merging events are given by the black dots.

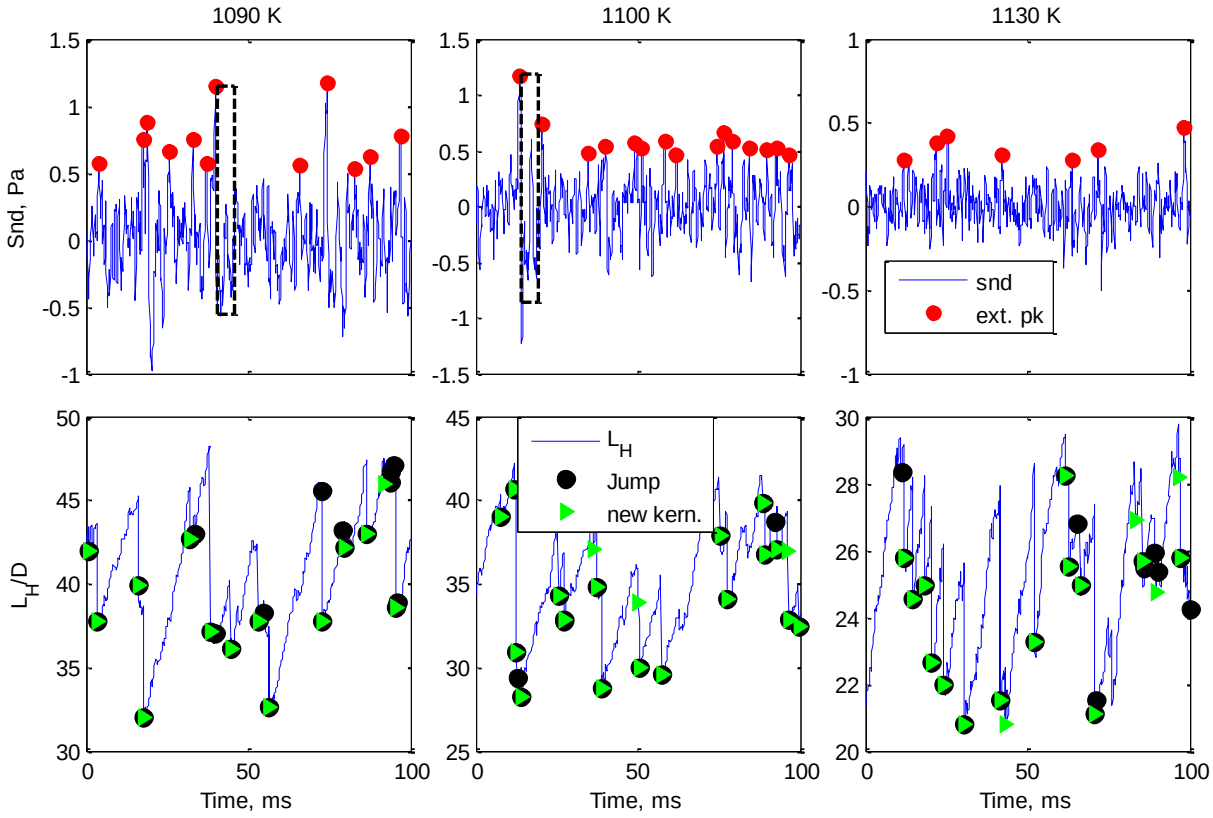

Fig. 4-18 Temporal sequences (100 ms) for the sound emission and flame lift-off heights for three coflow temperatures: T_C = 1090 K, 1100 K and 1130 K. The red dots indicate extreme positive sound/ pressure peaks, the green triangles identify extreme flame base jumps, whilst black dots indicate all kernel merging events. The dotted box indicates the time window for which large ignition events correlate to sound.

The extreme sound events (red dots) were temporally correlated to the large flame base jumps (green arrows) by restricting the two events to within a 1 ms 'time window' (dashed box in Fig. 4-18). The correlation was normalised by dividing the number of extreme merging events that temporally (within 1 ms) overlaped onto the extreme sound events, by the number of extreme merging events. The correlation is seen in Fig. 4-19; a correlation of one indicates perfect temporal correlations between the extreme merging events and the extreme sound peaks.

The data in Fig. 4-19 is presented versus the mean lift-off height as there is a large temperature range between fuel cases. However, a high lift-off height corresponds to a relatively low coflow

temperature, seen previously in Fig. 4-2. As such, it can be seen for hydrogen there is a good correlation (C > 0.4) for high lift-off heights, ~40 *x/D* – 15 *x/D* or correspondingly a coflow temperature range of *T*c= 1040 – 1050 K. The Ethylene 2:1 case also has a reasonable correlation (C > 0.5) for low coflow temperatures, with DME having a poorer correlation (C<0.4). All other fuels presented in Fig. 4-19 exhibit no real correlation, with a correlation constant less than 0.3. This identifies that for more than 70 % of large ignition kernel merging events no peak sound events occur. Furthermore, whilst the global sound level (Fig. 4-16) is a good indication of the flames instability for all fuels, the temporal sound fluctuation is not.

It has been hypothesised previously that the 'popping' noise made from the H_2 flames for low coflow temperatures, T_C < 1050 K, is from kernel ignition events. Whilst this is true to a certain extent, it is from large kernel events merging/ growing quickly into the flame base, opposed to all ignition events. Furthermore, it is highlighted here that the kernel formation rate is of the order of 600 kernels per second (Fig. 4-4) which would be difficult to detect as 'popping' noises.

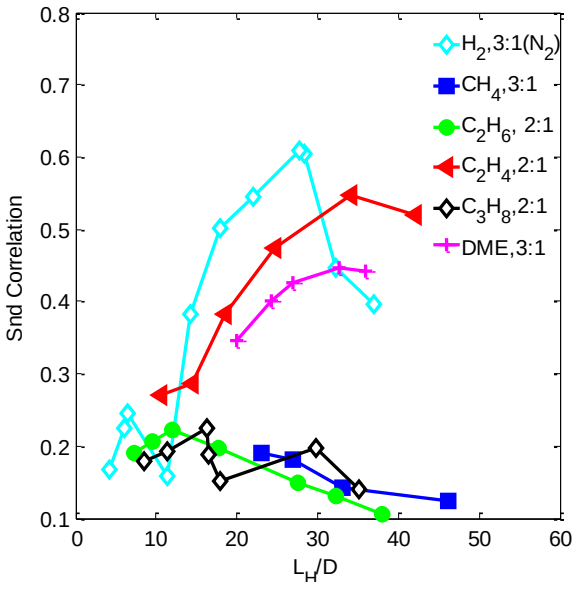

Fig. 4-19 The correlation coefficient for the extreme sound and lift-off height jumps versus a mean flame lift-off height for a range of fuels.

Despite there not being a strong temporal correlation for all fuels, between the peak sound and merging events, there is a reasonable correlation between the number of extreme sound events and the number of extreme merging events (Fig. 4-20). This figure presents the number of extreme sound events divided by the number of extreme merging events, versus the number of merging events. A ratio of one indicates that the number of extreme sound events matches the number of merging events per second. A negative linear slope is identified for increased temperature, the temperature is given for the propane (T_C = 1240 – 1350 K) and H_2 (T_C = 1038 – 1056 K) case in text, in Fig. 4-20.

The relative number of large upstream events increases for higher coflow temperatures, noting, this does not necessarily correlate to kernel merging events. Whilst the upstream propagation increases for high coflow temperatures the number of sound events doesn't increase at the same rate, hence the negative slope. This further identifies that the sound large emissions can better represent low coflow temperatures not higher temperatures. It was determined that the number of extreme lift-off height events was approximately half the kernel formation given in Fig. 4-4, this is for the definition of lift-off height 'jumps' used here.

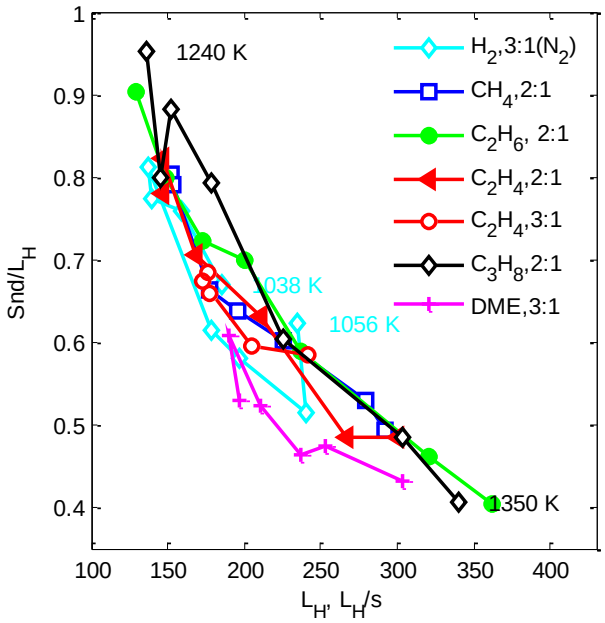

Fig. 4-20 The ratio between the number of extreme sound events and lift-off heights versus the number of extreme lift-off height events per second.

4.5.2 **Kernel formation with sound**

The PDF of new kernels and their respective *x/D* is presented below in Fig. 4-21 for two premixed ethylene flames and a single propane flame with the lift-off height PDF for a given fuel case and coflow temperature, where relatively high and low coflow temperatures are presented. The three cases plotted in Fig. 4-21 highlight that C_3H_8 has the highest kernel formation rate (given as ks^{-1} in each respective figure) for the high coflow temperature, T_C =1350 K. However, this high formation rate corresponds to a low sound level seen in Fig. 4-16, again ruling out kernel formation as the primary sound generator. Increased premixing of C_2H_4 to 4:1 leads to a greater formation rate for both a low and high coflow temperature, where the highest formation rate is for the lower coflow temperature. Ethylene premixing reduces sound levels for an equivalent lift-off height seen in Fig. 4-16 so formation rate does not explain the difference in sound generation.

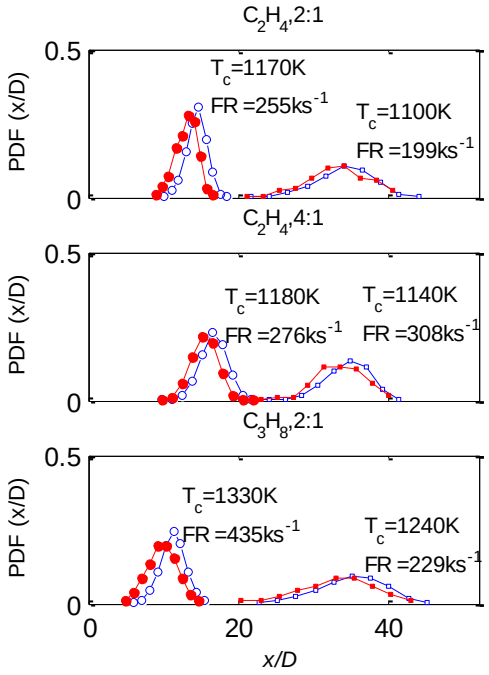

Fig. 4-21. Two C_2H_4 flames and one C_3H_8 flame is given, indicating: kernel formation (closed circles) and lift-off height (open circles) PDF's with total kernel formation rate (FR) per second given (ks^{-1}) for relatively high and low coflow temperatures.

4.5.3 **Kernel growth rates and sound correlation**

Fig. 4-22 shows the projected chemiluminescence kernel area and its respective growth as a function of time, for propane and ethylene at various premixing ratios and coflow temperatures. It is observed that C_2H_4 kernels grow faster than C_3H_8 kernels for the same relatively high or lower coflow temperature (same lift-off height). Since the formation rates of these flames do not indicate any correlation to sound generation and large kernel consumption producing peak sound generation, it is prudent to examine kernel growth rates. In other words, the rate with which a kernel grows/merges into the main flame body may be the cause of large flame front annihilation and pressure/ sound wave generation.

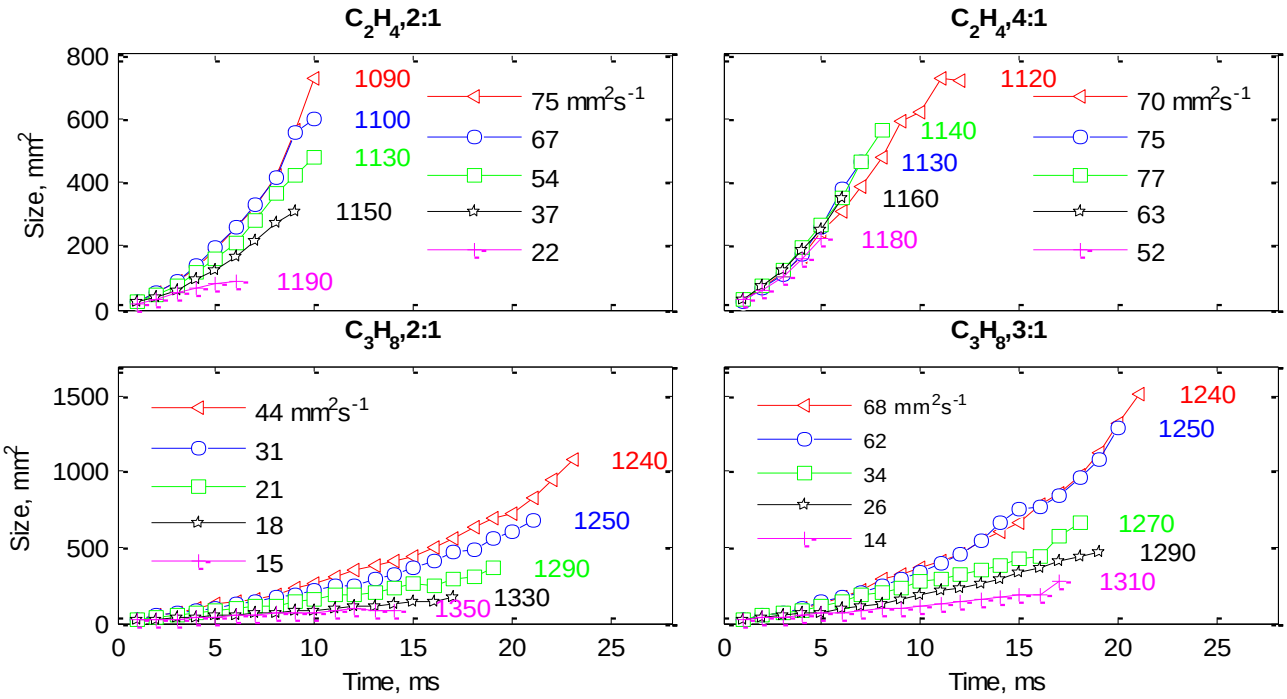

Fig. 4-22. 2-D projected kernel size with time for two fuels (C_2H_4 and C_3H_6) and two premixing ratios. Kernel growth rates (legend) are presented for different coflow temperatures (text).

The propane flames shown in Fig. 4-22 show consistent trends for growth rate and sound: a reduction in coflow temperature increases the global sound generation and growth rate. Furthermore,

increased premixing of propane leads to both faster growth rates and larger flame noise generation. This correlation of kernel growth and sound is further emphasised for C_2H_4 between both premixing cases. For reduced premixing, 2:1, there is a linear correlation between reduced coflow temperature leading to increased sound and growth rates. The increase in premixing of 4:1 has an optimal temperature for growth rate identified before as T_C =1140 K, this also matches the peak sound level. It is hypothesised that kernel growth rate is somewhat indicative of the turbulent flame speed, therefore growth rates may be strongly linked to sound generation, this assertion however needs investigating.

4.6 **Fuel parametric study discussion**

This chapter implemented a range of gaseous hydrocarbons, both alkanes and alkenes, including a diluted hydrogen jet (diluted with N_2) issuing into the vitiated hot coflow burner. Digital movies were used to capture slow modes of the flame base oscillation, to construct lift-off height correlations with coflow temperature. The high-speed (10 kHz) chemiluminescence set up was used to capture new and growing auto igniton events, to identify their interaction with the flame base.

The PDF's for the height of formation of ignition kernels above the burner were compared to the average lift-off height PDF locations. The relative overlap of the two PDF's was identified irrespective of fuel types (Fig. 4-5), where the peak formation versus the peak lift-height locations are given in Fig. 4-23. The strong linear correlation for all hydrocarbons indicates that all fuels behave in a similar manner. That is, an ignition event forms upstream of the flame base and due to the large difference in the flame base advection and kernel leading edge velocity (Fig. 4-15) it merges quickly into the flame base, such that the new flame base is close to the location of the new kernel. The strong correlation for the lift-off height with autoignition events raises the question as to

whether there is relationship between ignition delay times and the experimental lift-off heights. The comparison between delay times and lift-off heights is given in the final thesis discussion chapter.

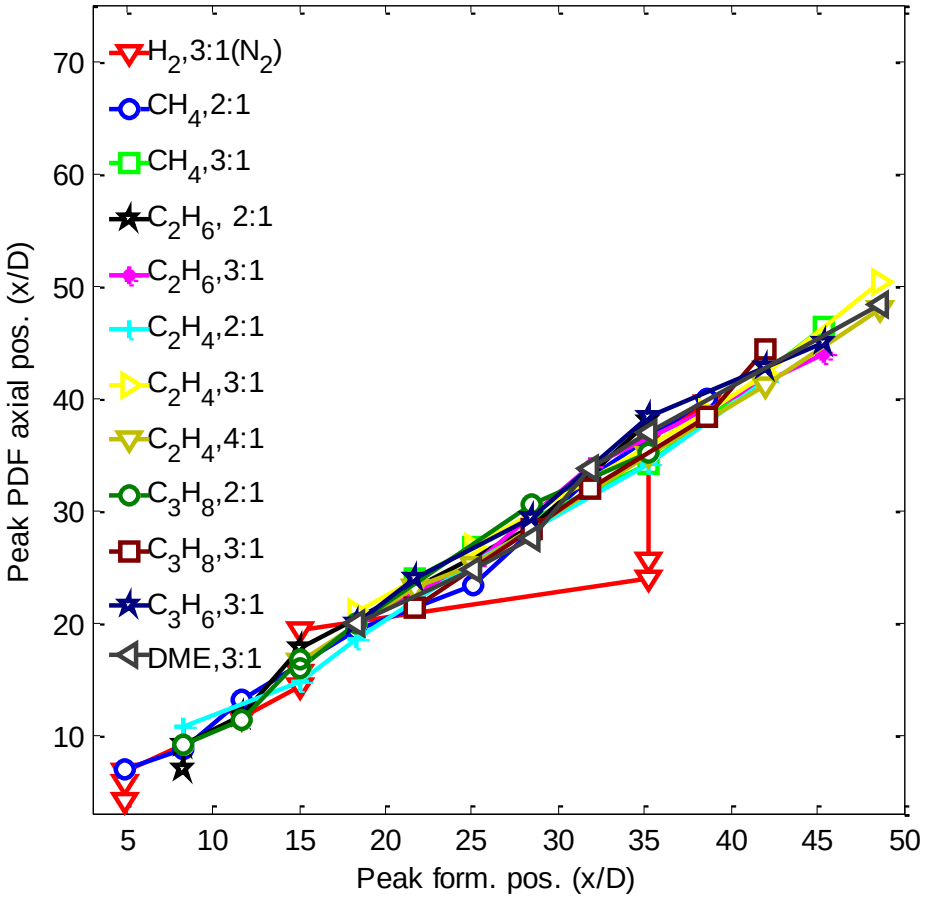

Fig. 4-23 Results for the peak axial location above the burner for the PDF of lift-off heights and formation rates, for all fuels and premixing cases studied.

The only fuel that slightly deviates from this linear correlation given in Fig. 4-23 is H_2 at two coflow temperatures: T_C = 1040 K and T_C = 1042 K, leading to the average lift-off heights of 24 and 26 *x/D* respectively. There are in fact two major peaks for the location of new kernels, seen in Fig. 4-24, for the coflow temperatures of T_C = 1042 K. The two formation peaks arise despite of a single peak location in the lift-off height PDF, for the relatively low lift-off height at 26 *x/D*. The largest

formation peak at 36 *x/D* is further downstream of the peak lift-off height at 26 *x/D*, causing the divergence from linearity of H_2 in Fig. 4-23.

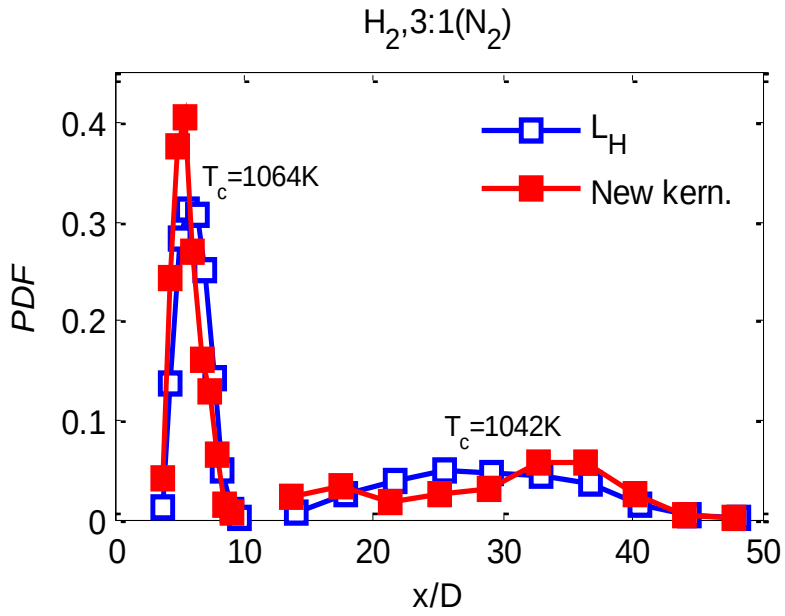

Fig. 4-24 H_2 kernel formation and lift-off height PDF's for two temperatures: T_C = 1064 K and T_C = 1042 K.

The two peaks for the formation of kernels (Fig. 4-24) are believed to be due to new ignition kernels forming over a large axial window above the burner (10 - 50 *x/D* or 45 – 220 mm). Therefore, the new kernels may have different leading-edge velocities, noticeable for the extremes in formation location, as they are subjected to different jet velocity fields. The ratio for the flame base (V_{FB}) velocity for the kernel leading-edge ($V_{K,Le}$) close to the nozzle (upstream) and further downstream are presented in Fig. 4-25 as U_{Strm} and D_{Strm} respectively. As expected, kernels that form further up-stream experience a faster velocity field and have faster leading edge velocities relative to the flame base. However, kernels forming further down-stream are slower and hence merge with the flame base slower. This is believed to be the cause of the two peaks in formation location, while the lift-off heights PDF only has one. This however needs further investigation using velocity-based

measurements within the burner. These results were not observed to such a significant degree for the hydrocarbons.

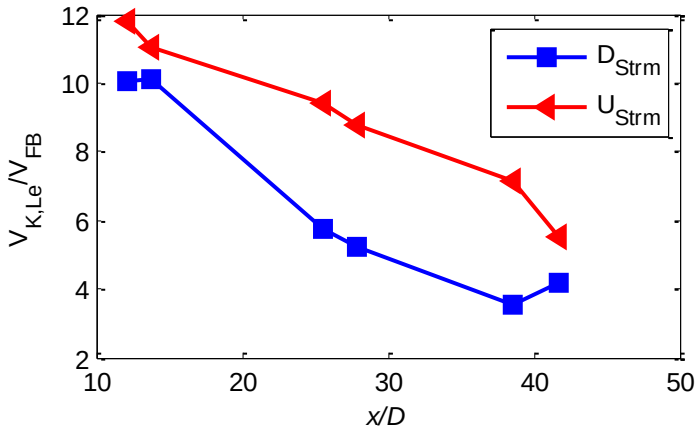

Fig. 4-25 Ratios for the flame base advection velocity (V_{FB}) and kernel leading edge velocity ($K_{,Le}$), kernels are conditioned based on their formation location, either: upstream, close to the nozzle (U_{Strm}) or further downstream (D_{Strm}).

The parametric study of gaseous fuels identified the importance of kernels to 'feeding' the advecting flame base, however, it doesn't identify the relative importance of autoignition kernels for differing coflow temperatures. Therefore, the kernel composition, i.e., heat release measurements are analysed in the following section. These heat release measurements will be able to ascertain, as seen with the kernel flame base merging interaction, whether high coflow temperature flames have reduced dependence on kernels for stability.

Chapter 5. **High-speed (10 kHz) OH/CH_2O PLIF setup and heat release verification**

This chapter presents the high-speed, 10 kHz, PLIF setup of: OH and CH_2O, and the out of plane chemiluminescence camera. This setup is used to perform diagnostics on JHC flames; where the results are presented in the following chapters. The OH PLIF results are presented for H_2 and CH_4, while both OH and CH_2O results are given for DME. This chapter presents the correction process used for the beam profile and laser absorption of the OH and CH_2O PLIF signals. Furthermore, it verifies the OH beam profile correction, since 'shot to shot' measurements of the flat flame were not performed in the experiment, and the beam slightly drifted throughout daily experiments. This chapter identifies that there is an abundance of CH_2O signal in DME flames, where this is an order of magnitude greater than CH_4. The abundance of CH_2O in these flames enables the use of high-speed (10 kHz) and further the imaging of heat release (OH x CH_2O)

This chapter additionally identifies that the spatial product of OH and CH_2O is a good marker of heat release in DME autoignition flames. The theoretical heat release measurements and the CH_2O and OH species are obtained from multiple transient counter-flow simulations, at a range of strain rates. These signals are converted to a theoretical PLIF signal by correcting for species quenching and the ground-state Boltzmann fraction at the CH_2O excitation wavelength of 355 nm. The theoretical signals are then calibrated to an experimental DME Bunsen flame, where species concentrations are known.

5.1 **PLIF OH and CH_2O setup**

The experimental setup is presented in Fig. 5-1. It showcases the setup for the high–speed (10 kHz) planar laser-induced fluorescence (PLIF) of OH and CH_2O, combined with out of plane chemiluminescence imaging. This setup enables the investigation of spatiotemporal dynamics from OH, CH_2O and visible broadband chemiluminescence fields, with respect to kernel ignition and growth. The PLIF experimental setup diagram, in Fig. 5-1, illustrates the orientation of the three cameras employed relative to the laser beams and flame.

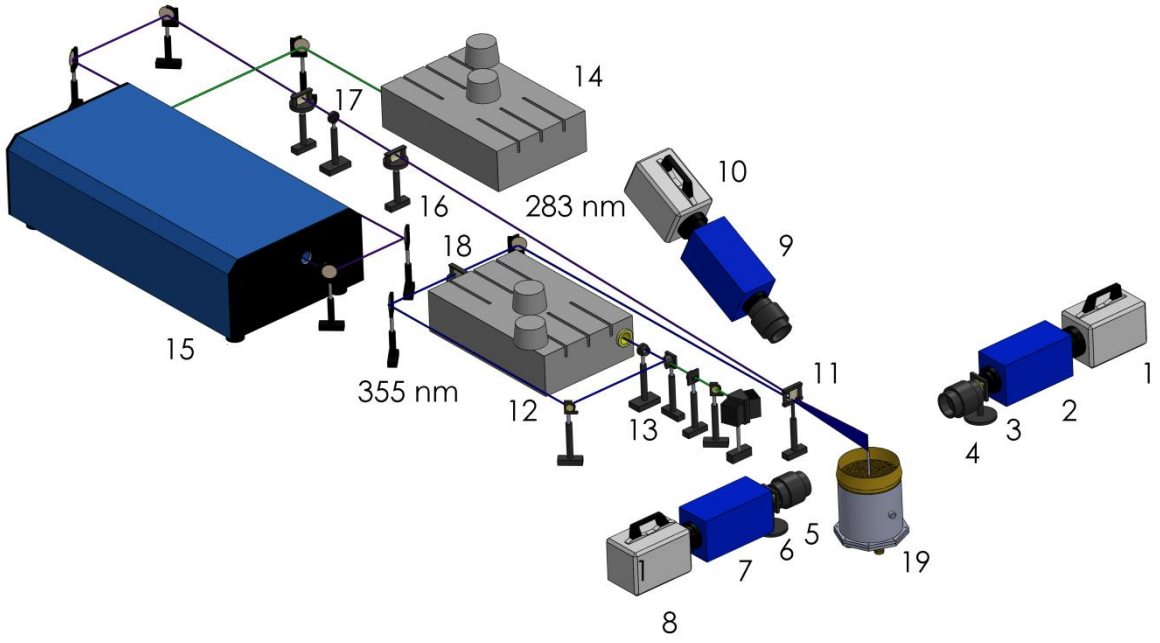

Fig. 5-1 10 kHz experimental setup: (1) OH PLIF camera (2) OH Intensifier (3) Semrock FF01-315/15-50 (4) OH UV collection lens (5) 85 mm $f_{\#} = 1.2$ lens (6) Semrock FF02-409/LP-25 (7) CH_2O Intensifier (8) CH2O PLIF camera (9) CH^* IRO (10) CH* camera (11) Cylindrical lens (12) CH_2O Edge wave laser (13) Dichroic mirror (14) OH Edge wave laser (15) OH Dye laser (16) Keplerian telescope (17) Galilean telescope (18) JHC burner.

The OH radical was fluoresced using an Edgewave Nd-YAG laser (Edgewave IS8II -E) that pumps a tuneable dye laser (Sirah Credo). This system produced a wavelength of 283 nm that overlapped onto the strong $Q_1(6)$ transition for $A^2\Sigma^+ \leftarrow X^2\Pi(1,0)$ excitation, the laser energy was measured at 0.14 mJ/pulse. The OH PLIF signal was collected with a 150 mm focal length, $f_{\#}$=1.65, six element UV lens (2 of CVI LAPQ-300.0-60.0-PM+APMQ-300.0-60.0-PM), it resulted in a mapped pixel resolution of 56 µm/pixel. Interferences were blocked using a 15 nm FWHM band pass filter, centred at 315 nm (Semrock FF01-315/15-50) and a coloured glass filter (1 mm, UG-11), combined with a short intensifier gate time of 200 ns. The OH signal was captured perpendicularly to the laser sheet using a CMOS camera, after a dual stage intensifier (LaVision HS-IRO s-20).

Excitation of the CH_2O PLIF was achieved using the third harmonic at 355 nm from an Nd:YAG (Edgewave HD30II-E) laser. Excitation at 355 nm probes the weaker rotational transitions within the $\tilde{A}^1A_2 - \tilde{X}^1A_1 4_0^1$ vibronic state. The 355 nm beam was measured to be 25 mm high and 350 µm wide at the probe volume with an energy of 3.3 mJ/pulse. The CH_2O PLIF signal was collected with an 85 mm $f_{\#}$ = 1.2 lens, resulting in a mapped pixel resolution of 56 µm/pixel. A combination of a 409 nm longpass filter (Semrock FF02-409/LP-25), the 355 nm beam being p-polarised and a short intensifier gate time of 200 ns removed interferences. The CH_2O signal was also captured perpendicularly to the laser, using a CMOS camera with a dual stage intensifier (La Vision HS-IRO s-25). Beam expansion telescopes were utilised to match the focal point of the 283 nm and 355 nm beams at the probe volume, as well as to expand the beams in the vertical direction.

A third camera collecting, visible chemiluminescence was oriented in line with the laser beam at 20, whilst perpendicular to the other two PLIF cameras. The signal was collected with a visible 50 mm $f_{\#}$ = 1.2 Nikon lens, this includes broadband chemiluminescence. A separate spectroscopic analysis confirmed that chemiluminescence from these DME non-sooting flames is mostly due to CH^*. The image size was 77 mm x 77 mm and had a mapped pixel resolution of 56 µm/pixel.

The spatial mapping, needed to achieve the overlap between the CH_2O and OH cameras was achieved using a metal plate with uniformly spaced 1 mm holes, after which a polynomial warping and correction was applied. The image mapping, between the OH and CH_2O PLIF camera's, was achieved with a mean pixel mapping error of 0.4 pixels, and a maximum error of 0.8 pixels, which is acceptable for the calculation of the product $[CH_2O]$ x [OH], minimising the spatial overlap error.

Cross-talk interferences between the CH_2O and OH PLIF signals were eliminated by delaying the 355 nm beam from the 283 nm beam by 200 ns. The beam energy fluctuations for both the 355 nm and 283 nm were acquired using photodiodes (Thorlabs DET10A), recorded using a digital storage oscilloscope (Tektronix DSA70404C). The spatially overlapping region for both OH and CH_2O PLIF signals was 20 mm (height) x 43 mm (width). The signal to noise ratio, (SNR: the ratio of a mean signal to the RMS) for OH and CH_2O PLIF is around 11 if the mean signal is around 300 counts for both. However, the peak count levels for this setup of OH and CH_2O are ~1100 and ~320 respectively, at these signal levels, the SNR's are 20 and 11 respectively.

The PLIF measurements of CH_2O, with relatively low laser energies, obtained from the third harmonic of a high-repetition Edgewave style Nd:YAG laser at 355 nm is applicable for DME, however, this not the case for CH_4 flames due to the high concentration of CH_2O produced in a DME flame. The increased CH_2O signal, above the background, collected by this system, for a DME Bunsen flame with different equivalence ratios, is compared to CH_4 in Table 5-1. The yields are based off an unquantified comparison, excluding population density and quenching for a 355 nm laser, for the corresponding fuels. For comparison, 1-D premixed flames for CH_4 and DME at stoichiometric values gave a mole fraction of $9.5x10^{-4}$ and $8x10^{-3}$ respectively. The close to an order of magnitude difference in mole fractions is consistent with the difference in fluorescence signals obtained for these two fuels. The change in CH_2O profile for a DME Bunsen is given in appendix B.1.

Table 5-1 Maximum CH_2O signal yield from a Bunsen flame for varying equivalence ratios using DME and CH_4 fuels.

DME	
Equivalence ratio (φ)	CH_2O signal
1	240
2	512
5	912
CH_4	
3	27

5.1.1 **PLIF-OH beam profile correction**

Before processing the OH images, to extract ignition kernel dynamics, the images need to be corrected for the system's variations due to the: camera, intensifier and laser. The correctional process from the unprocessed image (R_{IMG}) to the processing stage is as follows: the cameras 'noise' (dark image, D_{IMG}) is subtracted from the unprocessed image. Then a flat flame (FF_{IMG}) image (beam profile) is used to correct for the laser energies fluctuation across the OH laser sheet. The beam profile further includes the camera noise (which is subtracted), the lens through put image, the intensifiers noise and variation, and finally laser absorption, which hasn't been corrected for. The corrected image (C_{IMG}) is depicted below in Eq. (5.1).

$$C_{IMG} = \frac{Raw_{IMG} - D_{IMG}}{FF_{IMG} - D_{IMG}} \qquad (5.1)$$

The flat flame produces a uniform field of OH, the OH uniform field is produced by burning a premixed, mixture of DME mixed with air, at ratio of: 12 SLM of DME to 80 SLM of air (CH_4 can also be used, with varying flow rates). The flat uniform field of OH species is produced over the beam height, ~ 20 mm, seen in Fig. 5-2. The beam profile is typically Lorentzian in nature across the

height of the beam (20 mm). The flat flame, in Fig. 5-2, shows the OH beam variation, in addition to the Lorentzian profile, the beam additionally has striations that initiate within the laser. The laser energy from the PLIF setup is such that the OH signal is within the linear regime, whereby an increase in laser energy proportionally increases the OH signal. The average, 'dark' image identifies the cameras inherent pixel noise. The intensifier response is also incorporated into the beam profile correction, the intensifier image is taken for a uniform white light, giving a count level of 1000.

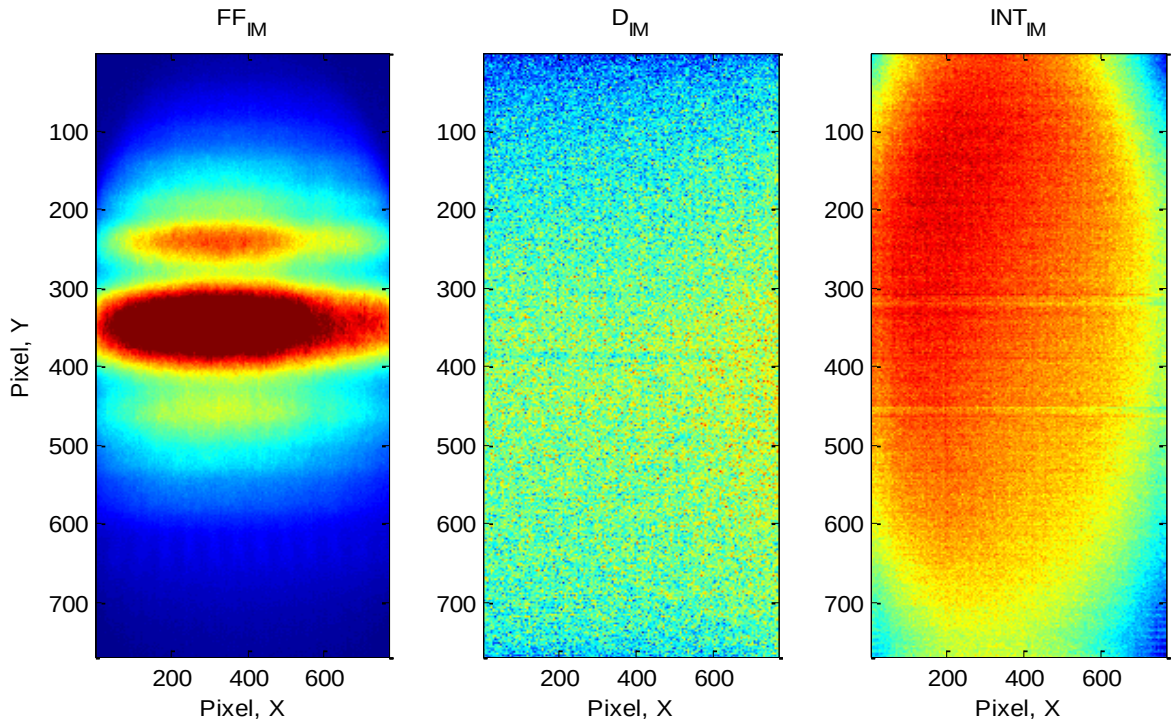

Fig. 5-2 Average OH flat flame (Flat flame), OH camera dark pixel noise, intensifier response (~ 1000 counts).

The average OH beam profile (an average of 5000 images) was taken, typically, in between each large set of flame data collection, i.e., at the start middle and end of the day. However, it was found that the OH laser profile was found to drift, not 'shot to shot' but consistently within a single day for the experiments done in this study, seen in Fig. 5-3. This in turn slightly effects the image correction, and as such, a method to identify the influence of the beam profile of OH and its spatial correlation with CH_2O and therefore the average heat release (for DME) was devised. It is mentioned

prior to the imposed corrections that the variation in the beam profile had minimal effect on the OH signal and hence the DME heat release results.

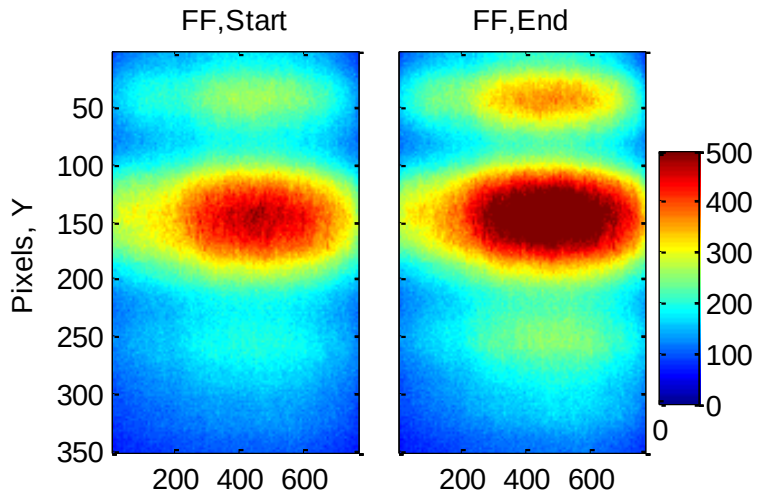

Fig. 5-3 Two OH beam flat flame profiles (FF) over a 5 hour time period (start and end), given in counts.

5.1.2 **Imposed OH beam profile correction**

To reconstruct an OH profile and verify the flat flame image, the individual components of the flat flame image are required, including the: optical focus, intensifier response and beam absorption. The optical focus of the OH image was deemed to be the most difficult to ascertain, a few assumptions were required to obtain it, using the flat flame image. A key assumption and deemed to be valid for the fluorescence wavelength of OH used (283 nm), is that the beam absorption is minimal. Once this assumption was made it is identified that the horizontal variation across a uniform flat flame image of OH, after the dark image and intensifier correction, is due to the camera focus, seen in Fig. 5-4.

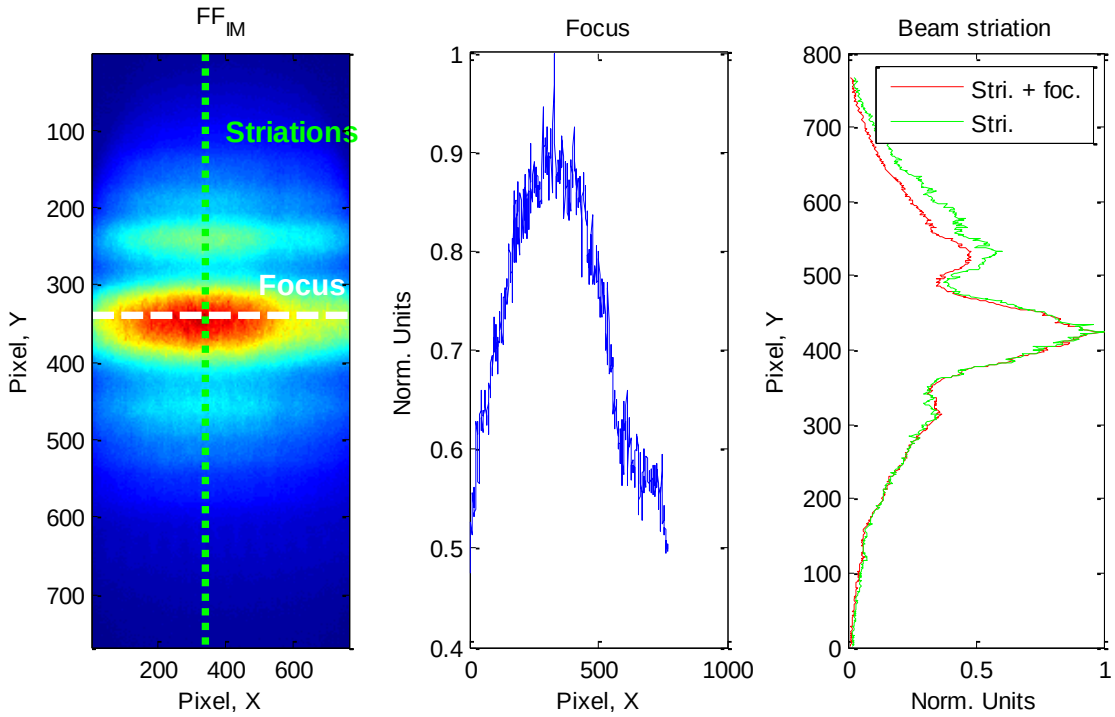

Fig. 5-4 OH flat flame profiles: OH flat-flame (FF_{IM}), horizontal optical focus, vertical beam striation with optical correction.

The 1-D OH profile given by the vertical striation line in Fig. 5-4 is corrected using the optical focus, given by the horizontal focus line. Therefore a 1-D beam profile can be constructed, which can be repeated to form a 2-D imposed correction seen in Fig. 5-5. The imposed 2-D OH profile is then used on the original flat flame image to obtain the optical focus.

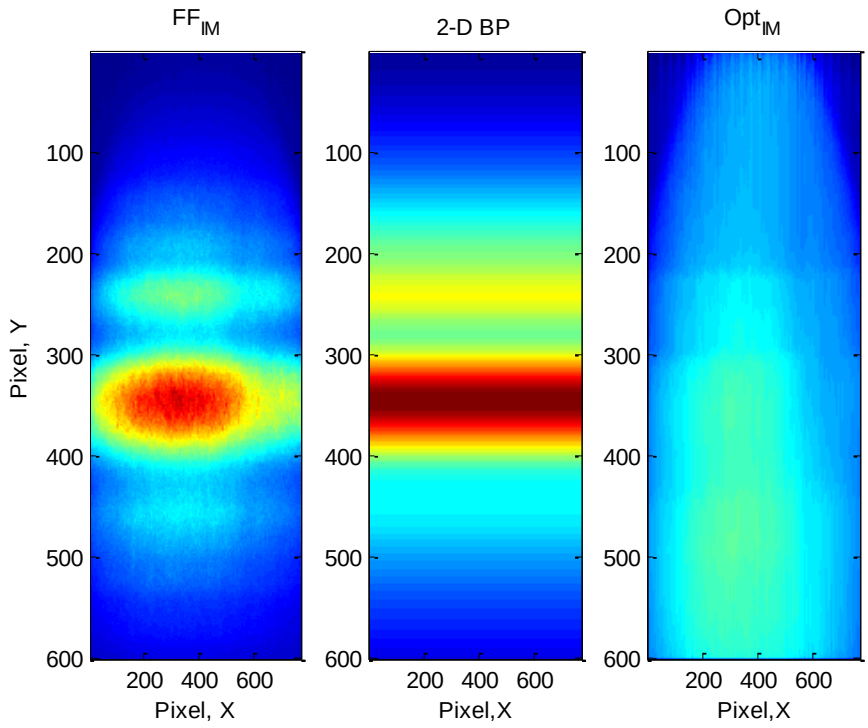

Fig. 5-5 Results for the OH beam profile: Flat flame image (FF_{IM}), corrected imposed 2-D OH beam profile with no throughput (2-D BP) and the calculated OH cameras optical throughput (Opt_{IM}).

5.1.3 **Flame brush correction**

Since simultaneous, 'shot to shot', OH Flat flames were not performed simultaneously to the JHC flame PLIF, and since the profile drifted slightly throughout the day, a new beam profile was constructed. An OH beam profile (Fig. 5-6) was based on the average OH flame brush from the JHC experiment, seen in Fig. 5-5, since the average OH signal is deemed to be at steady state. The average flame brush was then used to verify the flat OH beam profile from the flat flame. It was determined that across the 20 x 20 mm shot (camera FOV), a uniform, average, OH flame brush existed for positions further downstream (circled in Fig. 5-5). The OH average image is based on approximately 10 000 images. This flat/ uniform OH flame brush (F_{Br}) was used to generate the beam profile, where the lens focus was obtained from the flat-flame image (as per Fig. 5-5). The

imposed correction is based on a vertical 1-D profile taken across the downstream flame brush, the correction was such, as to make this signal flat and uniform, as was done in Fig. 5-5.

The imposed flame brush beam profile is created as follows: the average uniform flame brush (Br_{IMG}) is corrected for the camera dark noise (D_{IMG}) which is then corrected for by the camera optical throughput (Opt_{IMG}) and intensifier response (Int_{IMG}). From this the beam profile is generated across the vertical corrected flame brush (L_{BP}) by creating flat flame profile, this is then repeated across the image size and recorrected for the optical throughput and intensifier response image. A flow diagram of the process to produce a OH beam profile is shown in Fig. 5-6 where the flame brush correction is obtained from Fig. 5-7. After creating the imposed beam profile, a 'raw' OH image is corrected as previously done in Eq. (5.1).

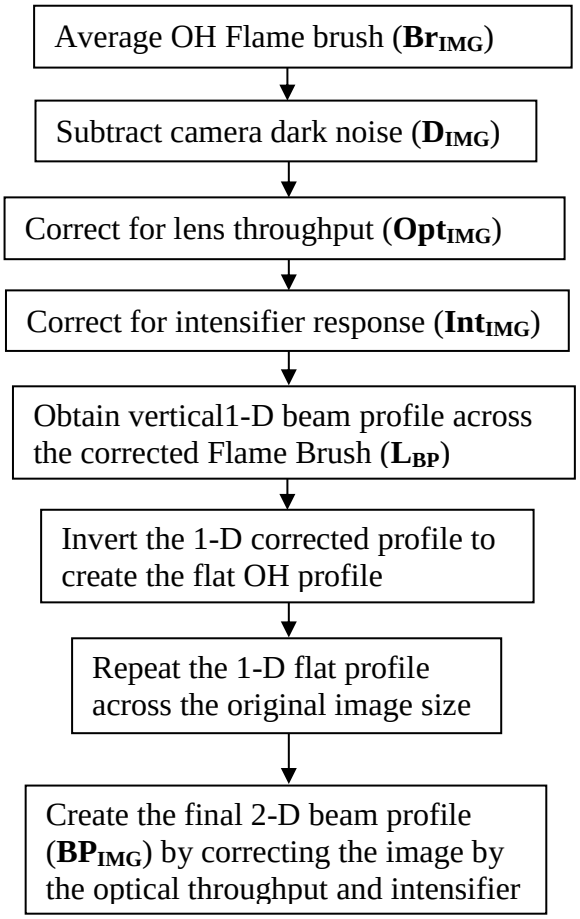

Fig. 5-6 Flow diagram to create a OH beam profile from the uniform OH flame brush.

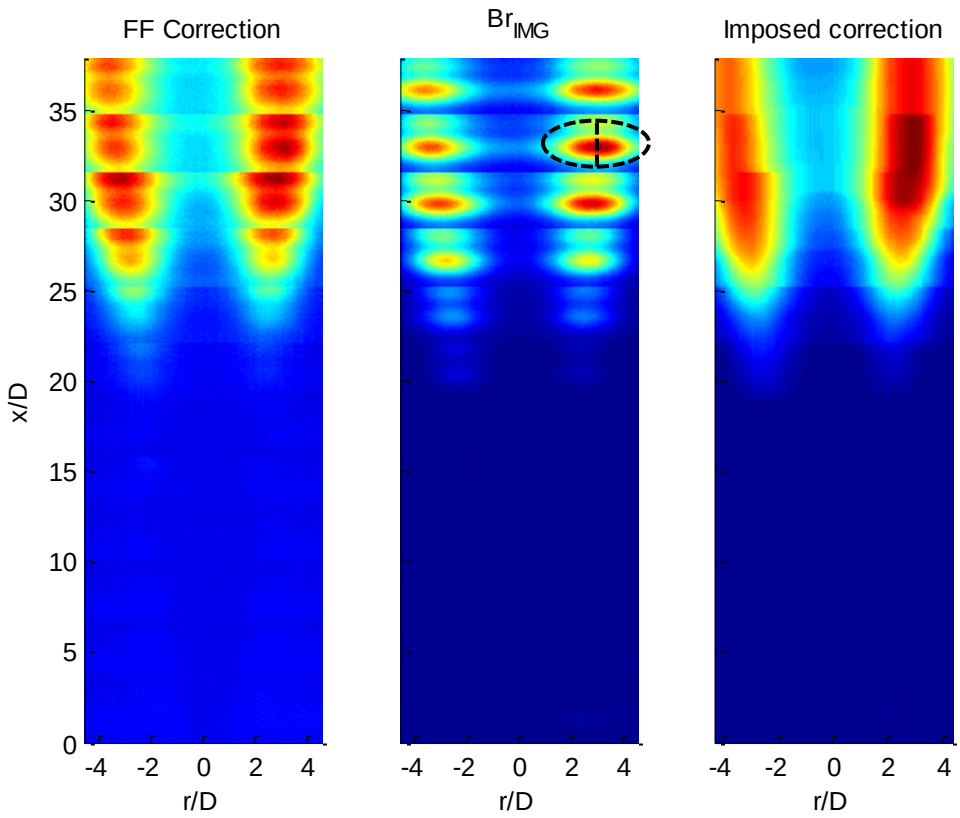

Fig. 5-7 Stacked OH average flame corrections for a hot coflow flame. Results include: an average flat flame (FF) correction, Stacked uncorrected flame (middle) and imposed correction (right, focal and beam striation correction). The OH flame brush correction is circled ($\boldsymbol{Br_{IMG}}$) and the vertical line indicates the 1-D beam profile ($\boldsymbol{L_{Br}}$).

5.1.4 CH_2O PLIF correction

The CH_2O image is corrected in a similar fashion to the OH PLIF correction as above. The CH_2O correction process is simpler compared to the PLIF OH since the stability of the CH_2O laser was improved (signal didn't drift). The raw CH_2O image has the camera noise subtracted, afterwards the signal is normalised by the CH_2O beam profile. To obtain a flat uniform CH_2O profile is somewhat more complicated, compared to the flat flame OH profile (Fig. 5-3). The CH_2O profile is created using a rich DME Bunsen flame (φ = 2), the rich Bunsen flame presents a near vertical CH_2O branch

on the rich side of the Bunsen flame, seen in Fig. 5-8. Therefore, the 1-D CH_2O Bunsen profile (Fig. 5-8) is obtained from the vertical CH_2O formation and repeated across a 2-D array. The CH_2O camera doesn't have a significant optical through put, and therefore no optical correction was required. By using this correction for stacked entire length flames, and their downstream uniform flame brush of CH_2O, it was determined that this correction was valid and therefore it is used in this study.

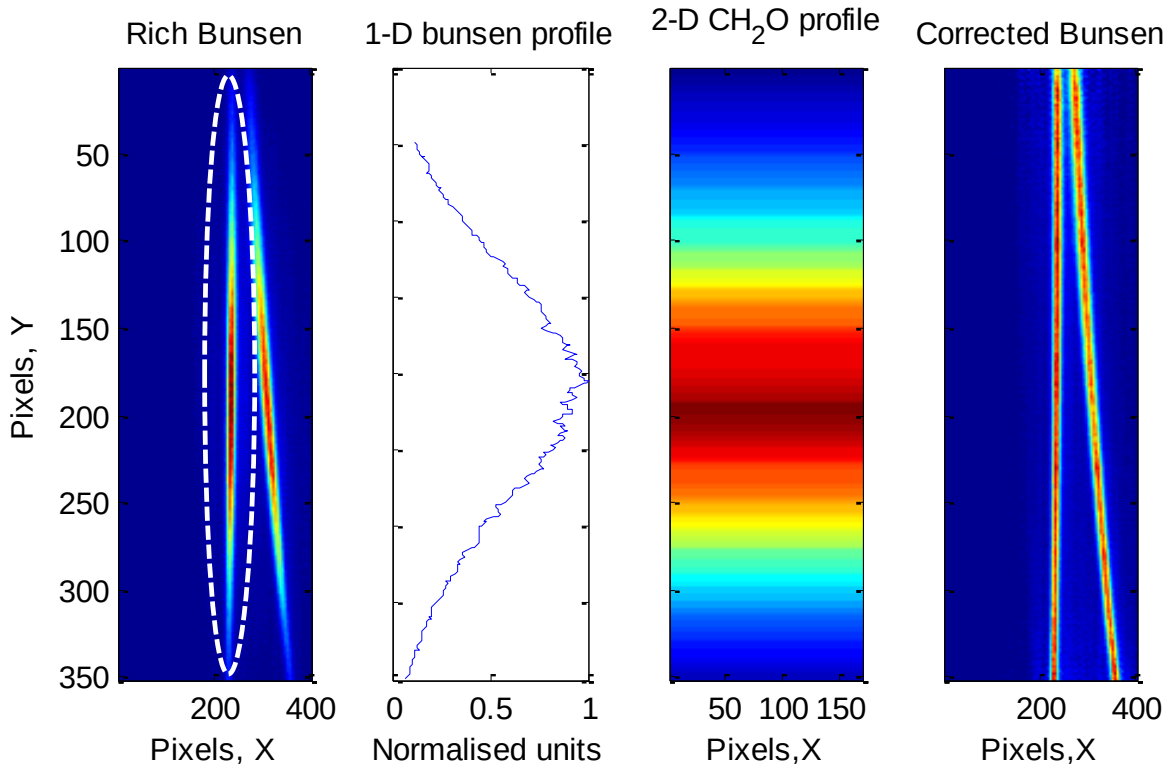

Fig. 5-8 Rich Bunsen CH_2O corrections and profiles, including: the rich Bunsen image, 1-D vertical CH_2O rich Bunsen profile, 2-D CH_2O correction profile and the corrected Bunsen.

5.1.5 **Relative OH and CH_2O PLIF Bunsen formation**

A slightly rich Bunsen flame, φ = 1.2., is shown in Fig. 5-9, for both OH and CH_2O. The two images have been corrected using the OH and CH_2O methods outlined previously. After the images are

corrected, the spatial correction/overlap between the images is created using the warping algorithm. The bunsen profile, in Fig. 5-9, shows that the CH_2O signal forms on the inside of the OH region, where low-temperature reactions are taking place. The OH signal forms later in the combustion process and hence forms on the outside on the CH_2O profile, where the flame front is present. The product indicates the region of high reactivity and potential heat release. The correlation of heat release and the product (OH x CH_2O) is presented below in section 5.1.1, for an unsteady opposed flow measurements, not for a premixed flame.

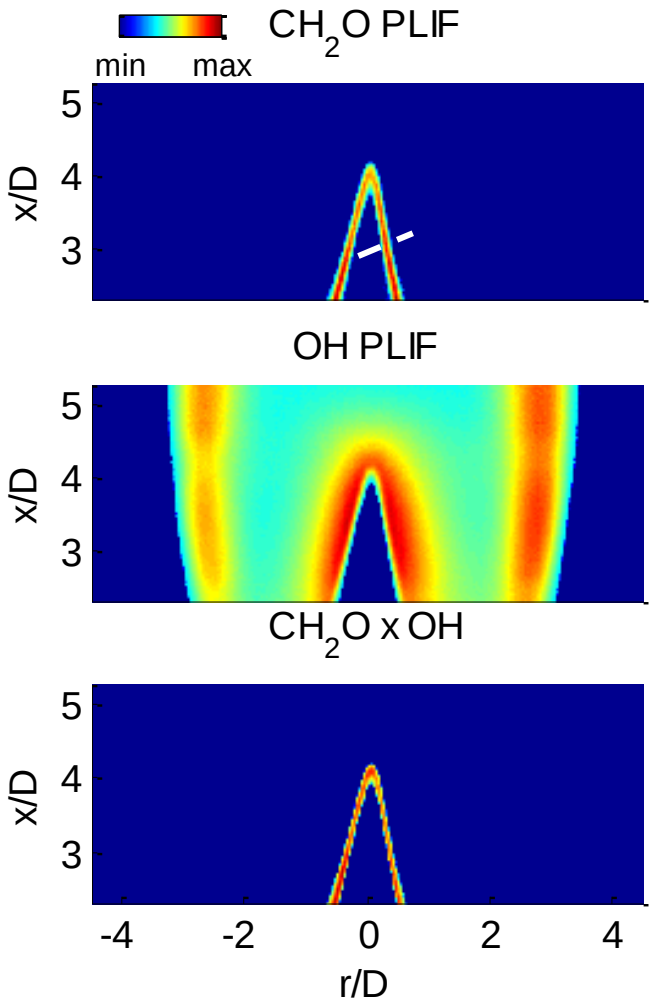

Fig. 5-9 Experimental PLIF results for a Bunsen flame, φ=1.2 for: CH_2O (top) and OH (middle) and their respective product, CH_2O x OH (bottom). The dashed line is given normal to the front in the CH_2O image.

5.1.5.1 Normal OH/CH_2O Bunsen profiles

A 1-D profile is taken from the Bunsen flame in Fig. 5-9 across the Bunsen flame front to indicate the separation between the signals and their respective peaks. The separation and relative spatial overlap is given below in Fig. 5-10 for two Bunsen flames (φ = 1.2 and φ = 2), taken across a line normal to the flame front (dashed white line, Fig. 5-9). It is evident that the overlap is large between the CH_2O and OH for the leaner Bunsen, φ = 1.2, with approximately a 1 mm separation between the signal peaks.

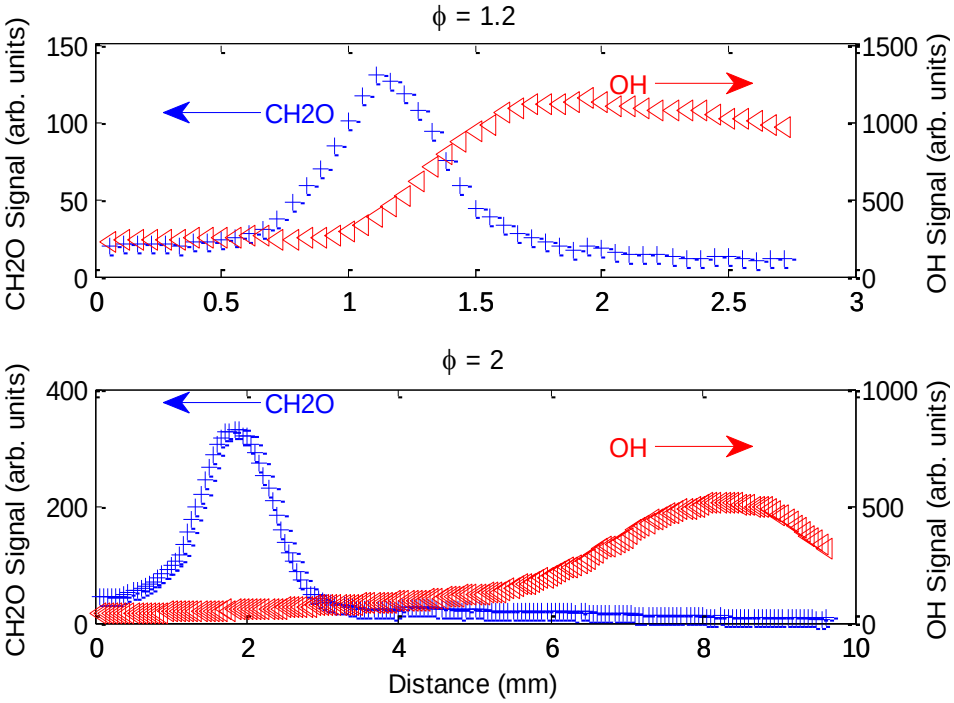

Fig. 5-10 Normal flame front projections for the separation between the OH and CH_2O for two experimental Bunsen flames: φ = 1.2 and φ = 2.

For the richer and more diffusive flame, φ = 2, the separation becomes very large between the signals, approximately, 6 mm between the peak signals. Indicating that the product may not be an indication of heat release in diffusive flames, also observed numerically by Popp et al. [181]. However, it is mentioned that autoignition is known to occur is lean mixture for the JHC burner;

where the comparison of heat release and the product, OH x CH_2O, is presented below for an autoignition counter -flow reactor.

5.1.1 DME correlation of OH xCH_2O with heat release

Prior to measuring the overlap of OH and CH_2O and determining them as a marker of heat release, the correlation of OH x CH_2O with heat release was identified using a counter-flow reactor. The results from multiple unsteady opposed flow simulations are presented in Fig. 5-11 (the unsteady solver is described further in Chapter 8). The flow configuration corresponds to opposed streams of pure DME on one side, opposed against combustion products from a premixed H_2/air flame at an equivalence ratio of φ=0.4 (T_C = 1400 K). The Cantera code [152] with an unsteady Ember solver [203, 204] is employed, using multicomponent diffusion and the reduced Pan mechanism for DME. The Pan mechanism [74, 76, 77] consists of 29 species and 66 reactions [55]. Twenty simulations are repeated for strain rates spanning the range a = 2-500 s^{-1}, the results of heat release (HR in kW/m^3) versus the 'expected LIF counts' from the product of CH_2O x OH are plotted. The counts presented in Fig. 5-11 are an arbitrary unit, they are specific to the quantum yield in this PLIF system. Samples of these results are shown in Fig. 5-11 for strain rates of: a = 2 s^{-1}, 50 s^{-1} and 250 s^{-1} at 300 μs post autoignition. For the case of a = 250 s^{-1}, two additional profiles are also shown for times before (*) and during ignition (**).

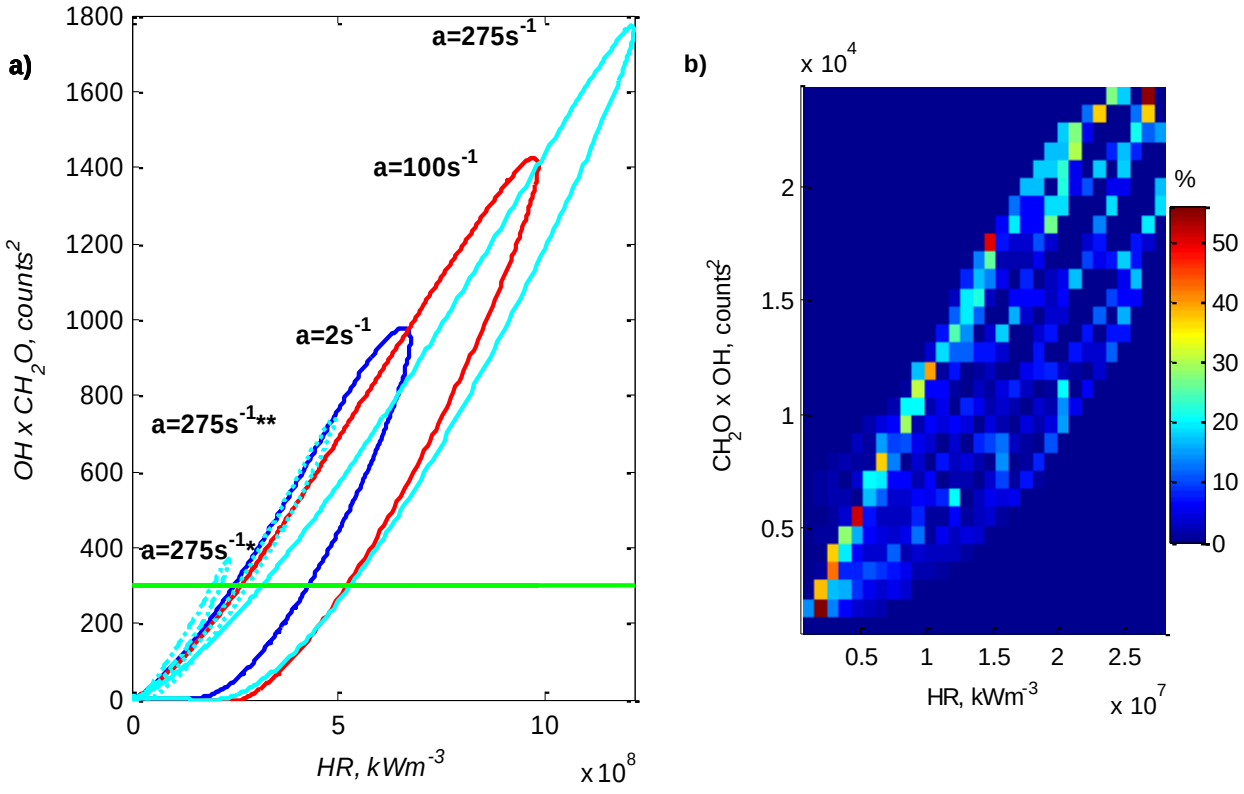

Fig. 5-11 Results for heat release (*HR*) and the product, CH_2O x OH, computed for a pure DME jet opposing hot coflow products from a premixed H_2/air flame at T_C = 1400 K (φ = 0.39). (a) Profiles of the product CH_2O x OH vs. *HR* plotted for strain rates of a = 2 s^{-1}, 50 s^{-1} and 250 s^{-1} at 300 µs post autoignition (solid lines). For the case of a = 250 s^{-1}, two additional profiles are also shown for times before (*) and during (**) ignition. The horizontal line shows a sample value of the product CH_2O x OH for which a histogram for the computed values is determined (b) Colour contours of the probability of the correlation between the product CH_2O x OH and *HR* is obtained from the entire set of 20 simulations.

The 'expected LIF counts', from the product of CH_2O x OH, is representative of the PLIF signal that would have been obtained from the experiment. To determine this, the computed OH and CH_2O concentrations are corrected for quenching and Boltzmann population distribution as follows. The OH PLIF correction is well understood and has been performed in accordance with Kamura et al. [165]. However, the quenching properties of the polyatomic molecule, CH_2O, is not as well

understood and multiple groups have approximated the quenching characteristics using a temperature based correlation, $Q \propto T^{-0.5}$, [179-182]. In this thesis, an approximate species-based correction is applied, using temperature quenching cross sections of N_2 and O_2 from Yamasaki et al. [186]. The study shows that both the more passive quencher, N_2, and aggressive quencher, O_2, (which is approximately 8 times greater than N_2) have very similar negative linear gradients for an Arrhenius fit with temperature. That is, the decay time for CH_2O in a 'bath' of N_2 and O_2 at room temperature and atmospheric pressure is $\tau^{-1} = 10x10^{-2}$ $ns^{-1}$and $2x10^{-2}$ ns^{-1}, where the temperature based quenching constant varies linearly. This linearity for the two extreme quenchers justified the assumption that the other known room temperature (~300 K) quenchers (DME, CO_2, CO, NO and CH_2O) behave in a similar way, with the room temperature quenching cross sections [186, 187] used for the intercept on the Arrhenius fit. The Arrhenius species quenching (σ_i) effect is given in Eq. (5.2), the fit is dependent on: the universal gas constant I and temperature (T) for species (i), where the individual quenching cross section is given as A.

$$\sigma_i(T) = Ae^{RT} \qquad (5.2)$$

The compiled CH_2O species quenchers are given in Table 5-2, where individual species quenchers/intercept, A, is listed. The Boltzmann correction for a 355 nm excitation of CH_2O was used from the work of Kyritsis et al. [188] and Clouthier et al. [189]. This correction is majorly shifted due to the significant low temperature population density of the 355 nm fluorescence of CH_2O (Fig. 5-12).

Table 5-2 Compiled quenching cross sections.

Species	Quenching cross section
N_2	1*
CO_2	0.932
DME	0.466
O_2	8.9
NO	2.8
CO	1.32

$^{*}N_2$ room temperature quenching constant 1.18

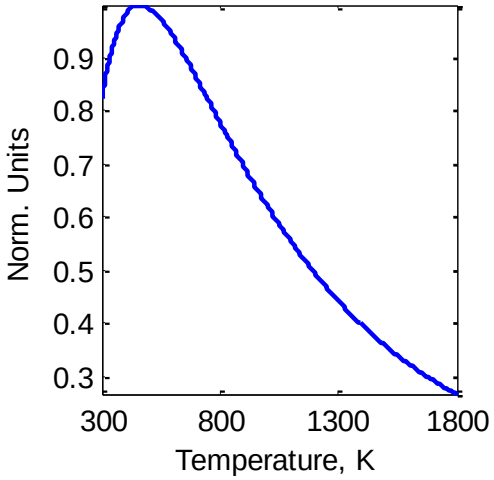

Fig. 5-12 Population density for the 355 nm fluorescence of CH_2O [188].

The LIF correction for the mole fractions of OH and CH_2O species, from a 1-D laminar flame Chemkin simulation, is given in Fig. 5-13 The correction uses the species quenching corrections and the Boltzmann population correction (Fig. 5-12). As expected there is a strong low-temperature 'shift' for CH_2O, this shift is predominantly controlled by the Boltzmann fraction. The LIF-OH correction, however, is small and it is attributed to the fluorescence of OH at 283 nm.

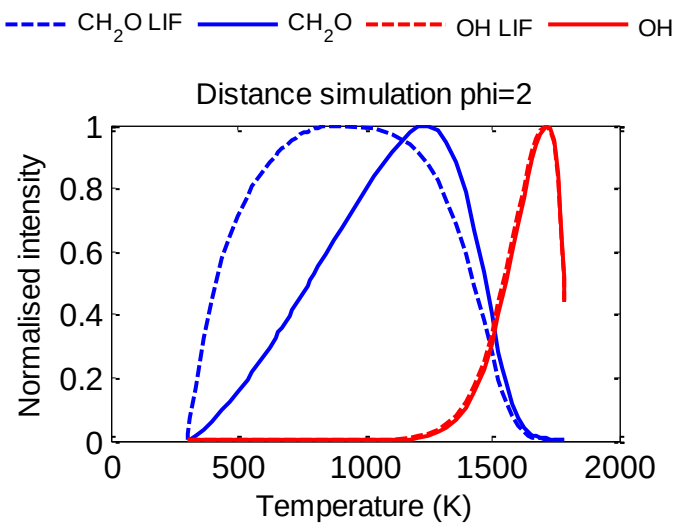

Fig. 5-13 1-D laminar simulation, quenching and population density correction for LIF signals of CH_2O and OH, for a 355nm and 283 nm excitation respectively.

Using the LIF correction similar to Fig. 5-13, the correlation of heat release and the product, given in Fig. 5-11 is obtained. Fixed vertical binned values for the LIF corrected product, CH_2O x OH, as illustrated by the horizontal line of Fig. 5-11 (a) are used to create a histogram of *HR*. Along these binned horizontal lines, the histogram of *HR* is created, based on the intersection of the 20 simulations. This process is repeated to extract the correlation between *HR* and the 'expected LIF counts' for the product of CH_2O x OH as shown in Fig. 5-11 (b). The colour bar shown on the right-hand side of Fig. 5-11 b marks a probability density for the joint correlation between *HR* and the product CH_2O x OH. The data has been presented by normalising each row to form a colour map that produces the most probable heat release values for a given CH_2O x OH product. That is, for a given product CH_2O x OH of ~6000 counts^2, there is 50 % confidence that this produces $5x10^6$ kW/m^3 of heat, while 20 000 counts^2 has a more uniform probability of ~20 % for an interval: 1.8-$2.5x10^7$ kW/m^3.

The lean branch (upper bound) from the simulation has a better correlation of CH_2O x OH to heat release. Furthermore, solutions from the unsteady solver were collected at ~10 µs intervals post

autoignition. Autoignition is defined when the OH signal exceeds ~100 counts (after LIF correction) as per the experiment. While the correlation between heat release and the product of CH_2O x OH seems to break down for steady diffusion or partially premixed flames [180, 181], it remains valid for the transient state where autoignition is occurring as relevant to the flows considered here.

Chapter 6. OH-PLIF results for H_2 and CH_4 JHC flames

This chapter presents results for the planar imaging of H_2 and CH_4, using only OH PLIF; focus is given to the OH imaging of ignition kernels below the main flame body. Since H_2 flames are carbonless, they do not have any CH_2O emission, whereas, the CH_2O yield from CH_4 at high-speed is too 'weak' to be measured, with reasonable SNR (presented in Table 5-1). The OH-PLIF results gives details about the radial position of ignition kernels, relative to the centreline, that the previous, H_2 and CH_4, volumetric chemiluminescence results could not.

The OH method to process and detect OH ignition kernels are given in this chapter; where the same method is used for DME kernels in the following chapter. The centroid location for new kernels is placed in a 2-D map relative to the jet exit plane and centerline, creating a 2-D formation map. The 2-D kernel formation maps are given in this chapter for both CH_4 and H_2 flames, the same 2-D map is given for DME in the following chapter. The 2-D formation map is used to interpret the mixture with which kernels ignite, indicating they are lean for high coflow temperatures. These 2-D formation maps are further discussed and compared to the 1-D chemiluminescence formation plots.

6.1 OH PLIF: CH_4 and H_2

The previous measurements, in Chapter 4, were based on volumetric line-of-sight chemiluminescence for both the CH_4 and H_2 JHC flames. Since they are line-of-sight, they cannot identify the radial formation rates, relative to the jet centreline. The chemiluminescence measurements were successful to identify the flame base and kernel interaction, indicating autoignition kernels being fundamental to providing flame base stability. This section, however, describes high-speed (10 kHz) OH-PLIF measurements of H_2 and CH_4 flames, focused on ignition kernels, identifying a 2-D formation map relative to the average lift-off height and jet centreline.

The OH-PLIF laser setup up substantially increases the camera resolution (from 4 to 56 pixels/mm) as the focus is solely upon the flame base and ignition events. The OH-PLIF measurements can further identify kernels forming close to the flame base, for higher coflow temperatures, this was difficult for the chemiluminescence setup. Furthermore, the SNR is substantially increased for H_2 flames as the chemilumescence signal of these flames was relatively low.

Previous 10 Hz species measurements on CH_4 and H_2 flames were performed by Cabra et al. [39, 205]. The focus was to identify ignition and extinction, of these hot coflow flames, based on temperature and mixture fraction scatter plots. Therefore, this setup, for the imaging of CH_4 and H_2, at high-speed, provides new temporally resolved kernel formation maps.

6.1.1 **OH-kernel tracking and processing**

An example of an instantaneous: OH and CH^* image is shown in Fig. 6-1 after the OH correction, given in section 5.1.1. The OH signal that forms upstream of the instantaneous flame base is defined as an ignition kernel (given by the green arrow). Since the measurements are planar there are two distinct OH 'branches' defined as the flame base (Fig. 6-2). Any kernel (OH island, disconnected from the main flame) that forms downstream of either branch is not defined as a kernel (indicated by the two red arrows). The image (Fig. 6-1) is compared to the CH^* volumetric projection, where no two distinct flame branches exist. Therefore, these separate OH islands above the flame branches could be in fact be due to the flame 'folding' upon itself and may not be true ignition events. As such, an ignition kernel, in Fig. 6-1, is defined as an OH event, found upstream of the two main OH branches, where the centroid of the identified kernel is indicated by a star (*).

The dashed horizontal lines in the CH* image, mark the bounding region of interest that OH camera sees, where the two cameras' FOV and resolutions are different. The vertical dashed line marks the laser beam that creates the OH sheet, noting the CH* camera is placed perpendicular to the OH laser sheet (Fig. 5-1).

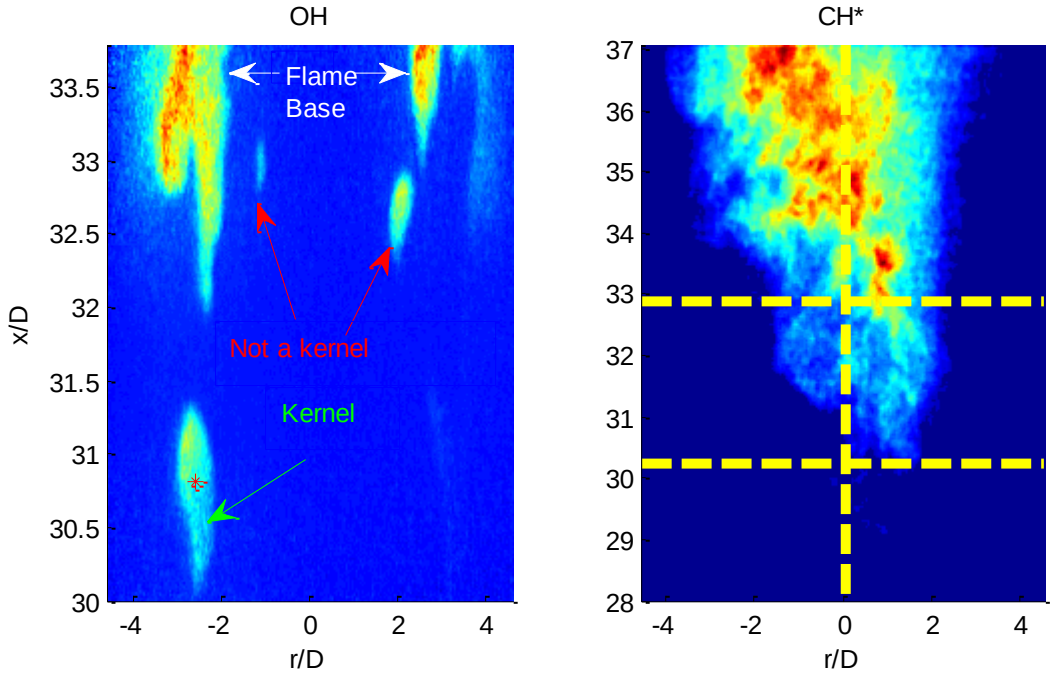

Fig. 6-1 Raw images from single frames of OH and CH*, operating at 10 kHz. The OH 'island' upstream of the two distinct flame branches (flame base) is identified as a kernel (green arrow).

It is evident that there is a distinct OH edge/boarder for both the OH flame base and OH-kernel in Fig. 6-1, as such, minimal processing was required to extract the features of interest. Various filtering techniques were applied, such as: an edge sharpening technique (gradient sharpening), Gaussian and median filter, where negligible differences to the noise filtering were identified. Therefore, a [5x5] Matlab median filter was applied, this was before a simple pixel tolerance, which was used to further extract the distinct OH features.

The kernel image was binarised as seen below in Fig. 6-2, the third image (200 µs) corresponds to Fig. 6-1. At time 000 µs, a new ignition kernel is observed, deemed 'new' since it is

the first occurrence of this OH island upstream of the main flame body. At 400 µs it has merged with the flame base indicated by the solid magenta line, indicating upstream flame tip propagation. The ignition events can be tracked because the centroid moves predictably along a vertical stream line, with the kernel growing somewhat symmetrically around it (as observed previously in the chemiluminescence results). The kernel centroid advects down-stream, indicated by the dashed red line, at a similar rate to the kernel trailing edge (given by the blue dotted line). The evolution of the kernel and its somewhat circular growth are investigated within the DME results section.

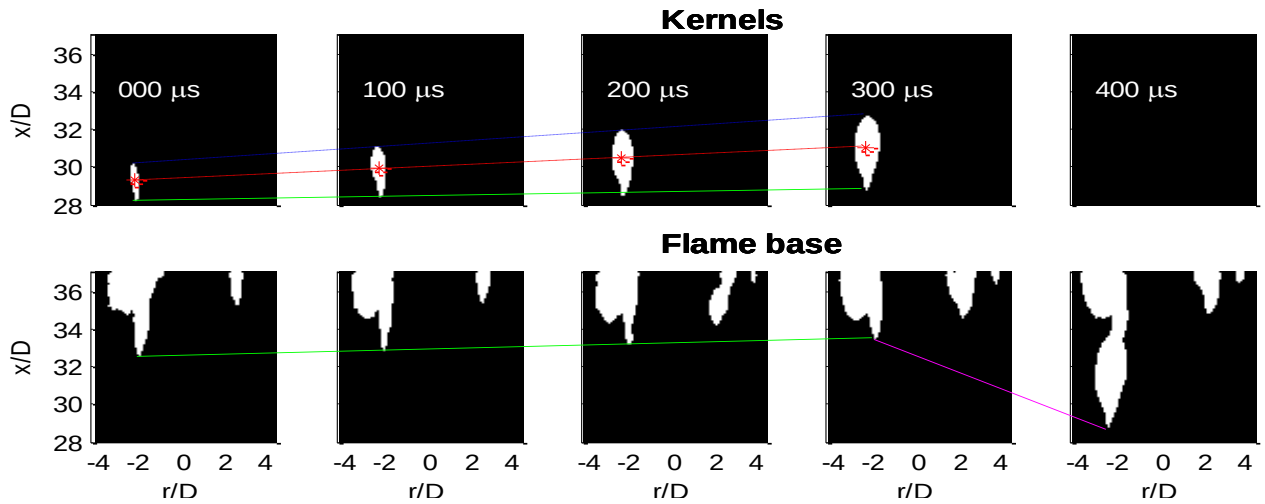

Fig. 6-2 Consecutive (500 µs) binarised OH images presenting an ignition kernel with its kernel centroids (*, top) and the Flame base (bottom). Kernel propagation lines are given: dotted blue indicates the kernel leading edge, dashed red indicates the centroid and the solid green line highlights the kernel trailing edge. The flame base lines indicate the: flame base advection (green) and kernel merging (magenta).

6.1.2 H_2 formation map

Using the above processing method for each OH PLIF image and the kernel tracking method (Fig. 6-2), the centroid location for new kernels is determined. By binning the centroid positions in the

axial and radial directions a formation map based on their position is determined, seen below in Fig. 6-3. Based on approximately 10000 images for a given flame position, the formation rates can also be determined; the formation density is given in the colorbar as kern/mm^2*s.

Two coflow temperatures, a high (T_C = 1070 K) and low-temperature (T_C = 1045 K), with their corresponding formation map is presented in Fig. 6-3, these temperatures correspond to a stable and lifted flame respectively, for hydrogen diluted flames with N_2 (H_2:N_2=1:3). It is evident for a higher coflow temperature, T_C = 1070 K, the flame base doesn't fluctuate much axially, observed by the high density of ignition kernels forming near the mean lift-off height (dotted green line). The minimal fluctuation was seen previously for the chemiluminescence results in Fig. 4-2. The small fluctuation is indicated here by the relatively small axial kernel formation fluctuation range of 10 *x/D* (Fig. 6-3). The small kernel fluctuation range further corresponds to the relatively small lift-off height RMS, presented previously in Fig. 4-2, for high coflow temperature H_2 flames. Furthermore, the radial kernel formation is distinctly forming either side of the centreline, indicated by the vertical dashed line, and therefore seen to form closer to the coflow shear layer, where mixtures are thought to be leaner.

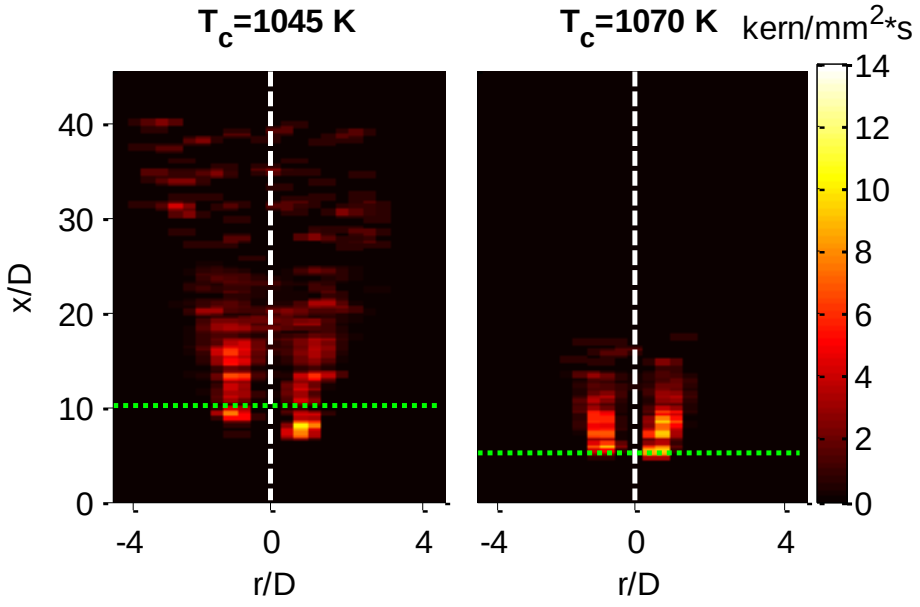

Fig. 6-3 N_2:H_2 = 3:1, OH 2-D formation maps for a high (T_C = 1070) and low (T_C = 1045 K) coflow temperature, corresponding to a stable and lifted fluctuating flame. The vertical dashed line indicates the centreline, while the horizontal dotted line marks the mean lift-off height.

The decrease in coflow temperature, to T_C = 1045 K, vastly increases the axial formation range, between –6 - 40 *x/D*, this corresponds to nearly the full length of the flame, where full flame H_2 lengths are seen in Fig. 6-4 for temporally averaged chemiluminescence images. The formation range has a similar range to the flame length, indicating that the downstream advection of the flame base (given in Fig. 4-14) nearly matches the delay time/ formation rates of new kernels. That is the flame base constantly advects downstream and the flame base is nearly blown off, when a new kernel forms to merge with the flame, creating the new flame location. Furthermore, this large axial range, in particular, the upstream formations, indicates that ignition events are somewhat governed by mixing, that is, if the fuel jet mixes to the correct degree with the coflow it ignites in a rapid succession.

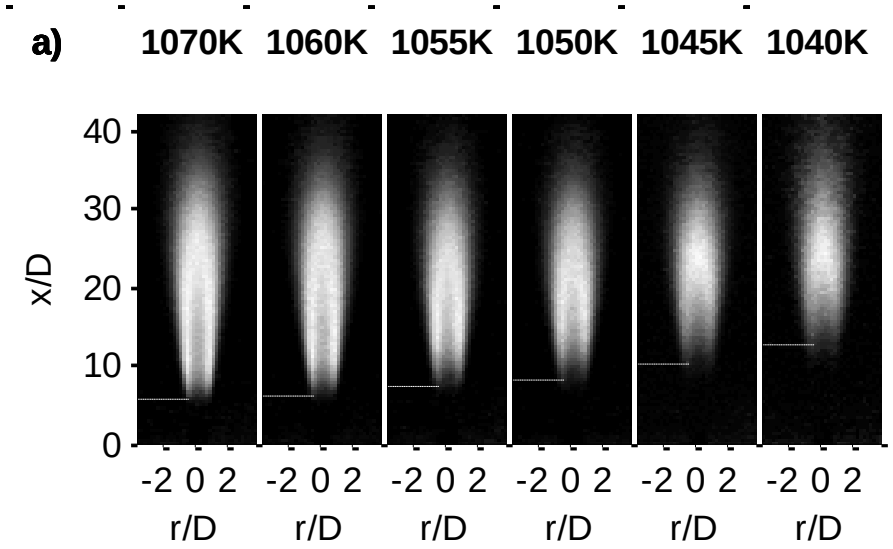

Fig. 6-4 Average H_2 flame lengths for varying coflow temperatures. The horizontal line markers the average lift-off height.

The lower coflow temperature, T_C = 1045 K, has increased the radial formation range, ignition events form along the centreline exceeding 15 *x/D*. It is hypothesised, that this corresponds to increased mixing of the jet with the coflow, where the coflow is further entrained into the centre of the jet. These premixed centre-line ignition kernels don't exist at higher temperatures as the mixture ignites prior to the mixing timescales. Furthermore, for downstream locations greater than 20 *x/D*, ignition kernels have a large radial range, along the centreline, 0 - ± 4 *r/D*. This larger axial range corresponds the proposed jet dispersion and the turbulent integral scales of the fuel jet at U_J = 107 m/s.

6.1.3 CH_4 formation map

The CH_4 jet formation maps are seen in Fig. 6-5 for two temperatures, in addition to two premixing ratios (2:1 and 3:1). Like H_2, a higher coflow temperature forms kernels further upstream with reduced range, seen in Fig. 6-5, T_C = 1520 K. This is the case for both premixing ratios with air (2:1 and 3:1), noting kernels form either side of the jet centreline. The increase in premixing with air (2:1 to 3:1), hasn't significantly shifted the initial location for ignition events for T_C = 1520 K, it has, however, slightly increased the kernel axial formation range.

For a reduction in coflow temperature, T_C = 1420 K, the formation range has increased, kernels are now forming along the centreline. For additional premixing, air:CH_4 = 3:1, the initial kernel formation location has increased, by ~ 5 *x/D*, from 37 *x/D* to 42 *x/D*. This increase in the initial formation of kernels agrees with the increase in the average lift-off height, given by the dotted horizontal line in Fig. 6-5, further agreeing with mean lift-off heights in Fig. 4-2.

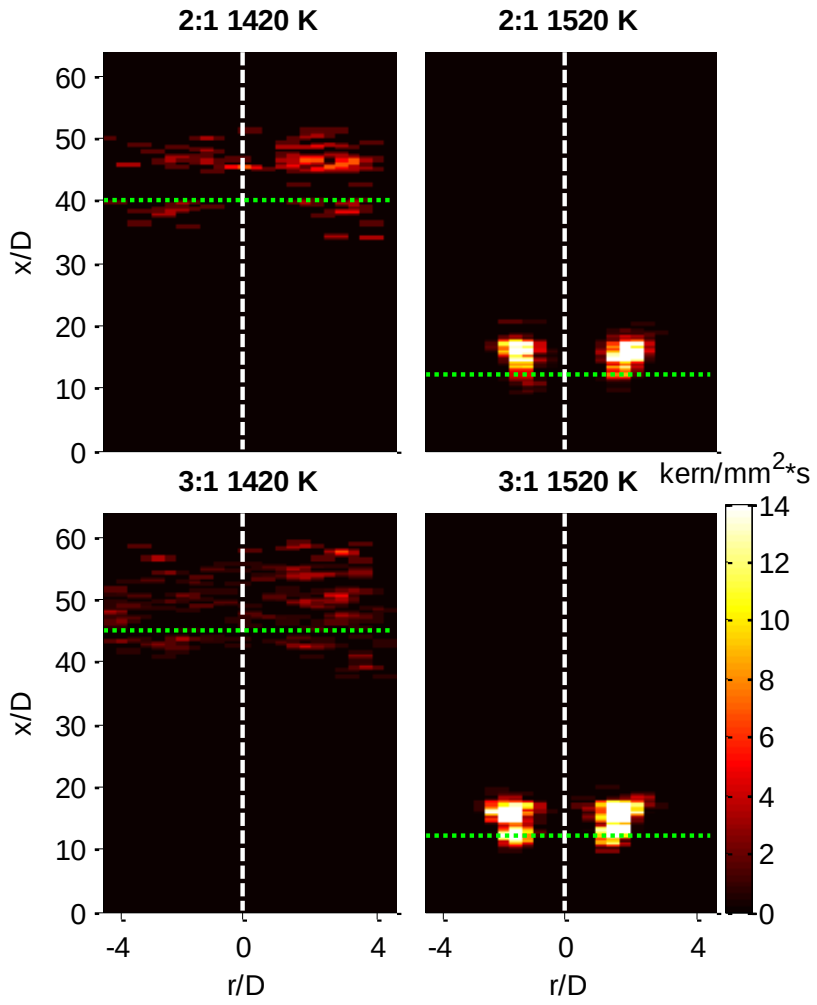

Fig. 6-5 2-D formation map (kern/mm^2*s) of CH_4, for two premixing ratios with air, 2:1 and 3:1, relative to the jet centreline (vertical dashed line). Relatively high and low coflow temperatures are given, *T*c = 1520 and 1420 K respectively. Lift-off heights are marked by the horizontal dotted line, the vertical dashed line marks the jet centreline.

6.1.4 H_2 and CH_4 PLIF summary

The 2-D kernel formation maps constructed for H_2 and CH_4 provide additional information to those from the 1-D formation rates in Fig. 4-4. The planar imaging of PLIF OH enables a greater understanding of where the kernels form relative to the jet centreline, which the volumetric chemiluminescence results were unable to identify. It is concluded that for both H_2 and CH_4, as found

previously in Fig. 4-4, kernels form further downstream as coflow temperatures are decreased. However, the OH-PLIF data highlights, which were not possible from the chemiluminescence, that in addition to forming further downstream the kernels have a wider axial ‘spread’, potentially matching the jet dispersion. The radial distribution of the PLIF data shows for higher coflow temperatures kernels form distinctly either side of the jet centreline. With decreasing coflow temperatures, the kernels form closer to the jet center line, and occasionally on the jet line, also potentially matching the jet dispersion and downstream mixing between the coflow and fuel jet.

Chapter 7. High-speed (10 kHz) results: CH_2O/OH PLIF

This chapter presents work from the high-speed (10 kHz) PLIF experiment, imaging OH and CH_2O, with simultaneous out of plane chemiluminescence for DME JHC flames. The focus of this chapter is to determine high-speed kernel heat release (OH x CH_2O) for DME flames, at a range of coflow temperatures. The kernel heat release is used to identify the relative importance of ignition kernels at relatively high and low coflow temperatures. The OH radical is used to indicate the flame front, while the CH_2O intermediate indicates low temperature chemistry leading to autoignition.

The final section discusses the PLIF results of OH and CH_2O, focusing on their relative formation and overlap within ignition kernels. The overlap is used as a heat release marker, seen to be a good marker given previously in section 5.1.1. Mixtures that are measured in this experiment include: partial premixing of DME with air and partial dilution with N_2, for two coflow temperatures, at two jet velocities. The coflow temperatures selected are based on a highly lifted flame (low coflow temperature) and a low lifted flame (high coflow temperature), selected based on chemiluminescence results.

7.1 Dimethyl Ether (DME)

The use of DME (CH_3OCH_3) within the hot vitiated coflow burner is applied here, due to a variety of reasons. Firstly, it provides an abundance of CH_2O within JHC burner conditions, compared to other fuels such as CH_4 (shown in Table 5-1), this enables the use of high-speed (10 kHz) PLIF CH_2O measurements and therefore high-speed heat release (OH x CH_2O) measurements. Secondly, DME would be a viable replacement for diesels in compression ignition (CI) engines [52] owing to its high cetane number, where this burner replicates autoignition conditions. Furthermore, it can potentially replace compressed natural gas (CNG) and liquefied petroleum gas (LPG) as a cleaner fuel [206] in

land-based gas turbines. Finally, due to DME's low-temperature [207] and more complex chemistry, compared to CH_4, it also makes DME interesting to study in an autoignition burner, analysing low-temperature species, in particular CH_2O.

7.1.1 DME chemiluminescence and PLIF flame selection

This section determines how DME flames, coflow temperatures, are chosen. Since only a select number of flames can be imaged owing to the number of positions (noting the image FOV is 20 mm x 20 mm) and images taken for a flame. Since different premixing of DME with air provide different lift-off heights, the coflow temperatures were chosen based on similar lift-off heights from chemiluminescence images. Furthermore, the RMS of the flame base fluctuation identifies the 'window' for which a significant number of images show be taken.

7.1.1.1 Lift-off heights

The chosen DME flames for further PLIF diagnostics were based on: a single, low and high coflow temperature, for a range of air premixing cases (U_J = 50 m/s), a single dilution case (N_2, U_J = 50 m/s) and a higher velocity case, U_J = 100 m/s. The chosen high and low lift-off heights were based on 30 second digital movie sequences, seen in Fig. 7-1. The movie series (as was done for Fig. 4-2) determines both the flame fluctuation and mean flame base position (lift-off height), both important quantities to measure prior to the larger PLIF experiments.

Diluting with N_2 has similar effects as with air, where increased N_2 levels increases the lift-off height. Furthermore, for the same volumetric ratio of N_2 to air, with a constant coflow temperature, the lift-off heights slightly increase. Finally, increased jet velocity (Fig. 7-1), from U_J = 25-100 m/s, has a somewhat small impact on the lift-off height, where increasing jet velocity only slightly

increases the lift-off height (not proportional to jet velocity). For comparison, previous measurements on a preheated DME jet at 433 K at U_J = 43.7 m/s, had a coflow temperature range of T_C = 966-1149 K [208], for a seated stable flame to a lifted flame. This is compared to the range, T_C = 1250-1400 K found here for a fuel jet temperature of 298 K.

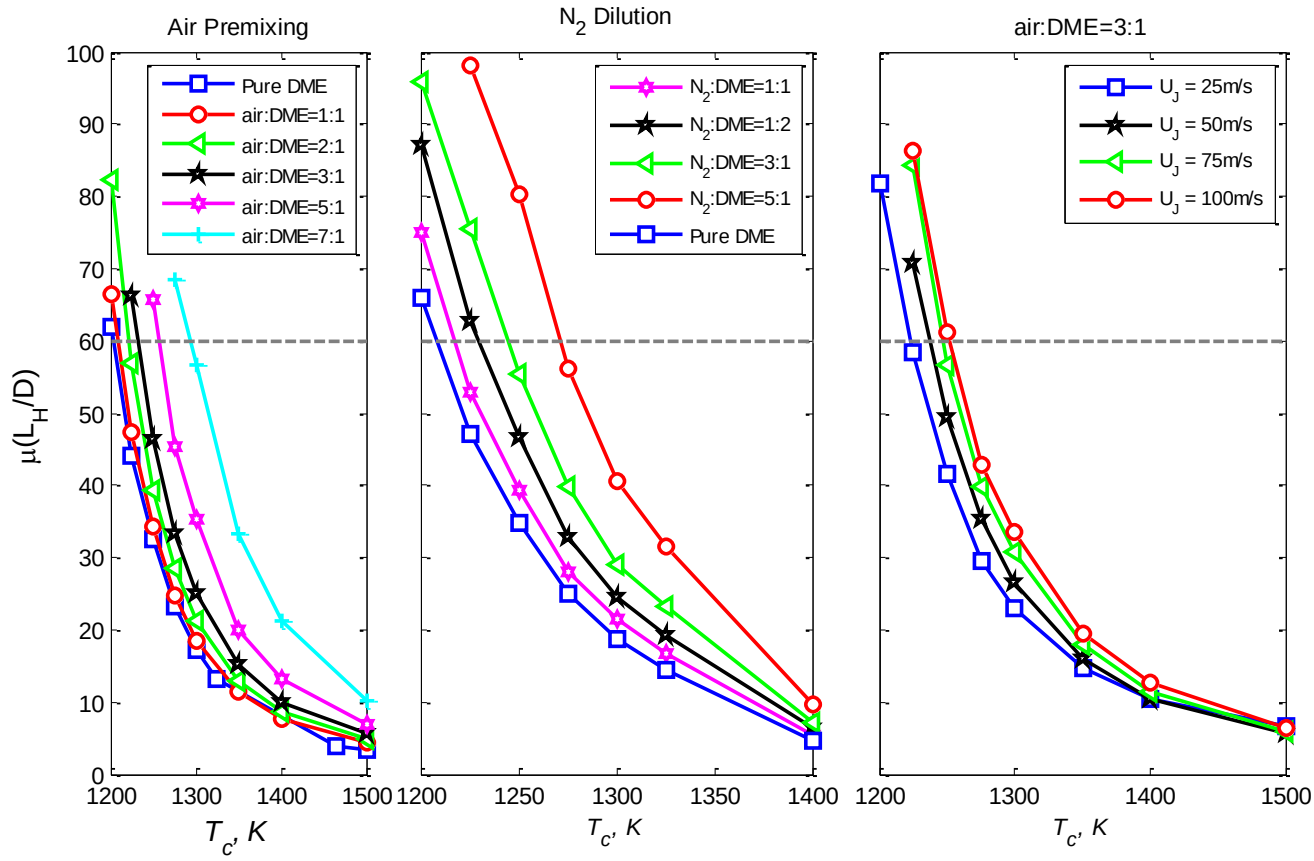

Fig. 7-1 DME lift-off heights for varying levels of: air premixing (left), N_2 dilution (middle), jet velocities for a fixed 3:1 air premixing (right). The dashed horizontal line indicates the valid cone of 60 *D*.

It was found by Oldenhof et al. [209] increased jet Reynolds number, and therefore the increased momentum ratio between the jet and coflow, in fact increases coflow entrainment and early onset of jet reactions. This may explain the U_J = 50 m/s jet having a higher lift-off than the U_J = 100 m/s for high coflow temperatures, T_C = 1500 K. It must also be noted that the jet exit is 70mm

downstream of the coflow exit and hence more preheat occurs for a slower jet. This would, in theory, increases the lift-off height of the increased jet velocity relative to the lower velocities, where a small variation in lift-off height is seen in Fig. 7-1

Other than mean lift-off heights, the flame base range (*RMS*) is important to identify prior to doing high speed measurements, seen in Fig. 7-2, for the air premixing cases. It is seen that increased premixing increases the lift-off height for a given coflow temperature as seen in Fig. 7-1, where, a decrease in coflow temperature has a linear increase in flame base oscillation (RMS). The lift-off height RMS provides the 'window' for which a large number of PLIF images are to be taken in the JHC experiment, since the lift-off heights closely match the location of new kernels (Fig. 4-6).

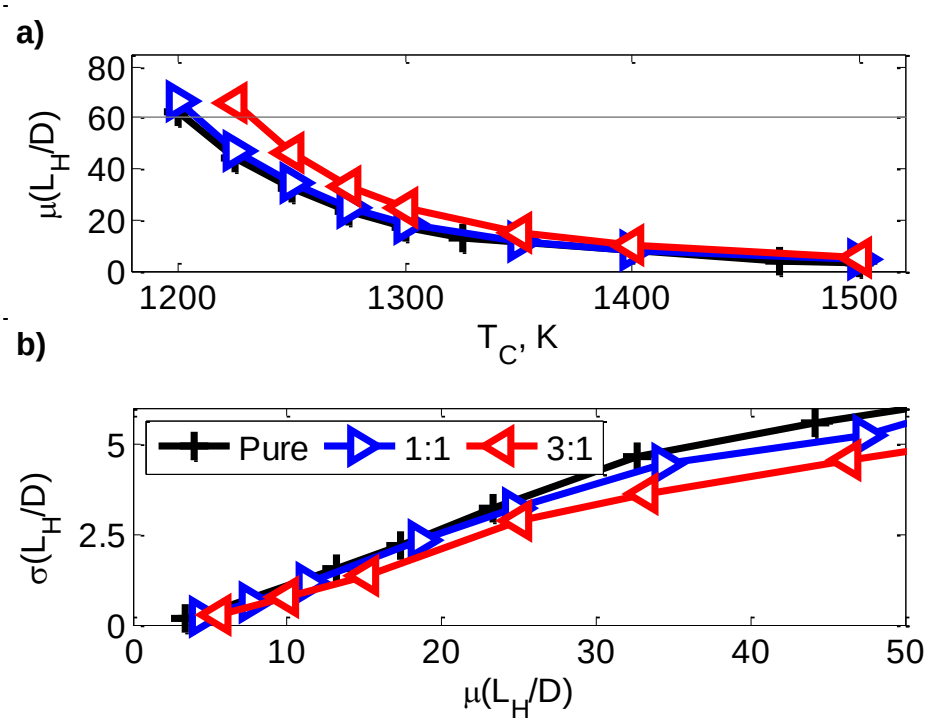

Fig. 7-2 DME mean flame lift-off heights (a) and flame fluctuation (b).

7.1.1.2 Formation rates

The focus of the PLIF study was to measure both flame base stability due to kernel interaction, and further kernel-based evolution/growth. Therefore, it is important to identify the axial range for which the kernels are forming and the frequency of formation prior to embarking on a larger campaign; these closely match the lift-off height RMS range. The kernel formation rates and the axial range of formation for DME flames are seen in Fig. 7-3, measured in the same manner as the fuel parametric study (Fig. 4-4). The kernel formation range indicates which axial position, within the flame, requires more PLIF imaging as to measure 'enough' kernel ignition events, noting the camera-PLIF FOV is ~20mm.

It was seen that previously from the kernel formation and lift-off height PDF's, in the Parametric fuel study (Fig. 4-4 and Fig. 4-5); statistically the flame base oscillation and kernel formation range overlap. Therefore, imaging in the formation region will encompass, both the flame base and new kernel formation/ growth. Differentiating the flame base from ignition kernels is defined in the OH tracking section, where the flame base here is not the focus of this PLIF study.

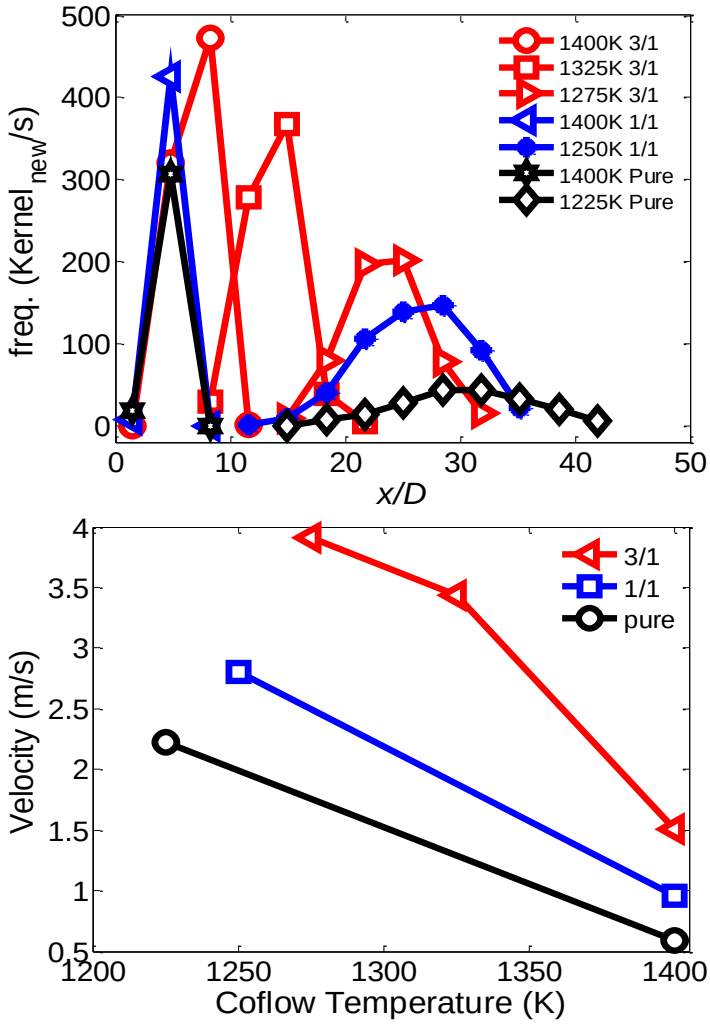

Fig. 7-3 DME kernel formation rates (top) and flame base advection velocities (bottom) for various DME to air partial premixing ratios.

The kernel formation rate in pure DME flames (Fig. 7-3) is lower than premixed DME flames despite the lift-off height being lower for a given coflow temperature, seen in Fig. 7-2. This is explained by the average downstream advection velocity of the flame base, excluding any kernel merging events seen in Fig. 7-3. A pure DME jet has almost half the downstream advection velocity for the same lift-off height, indicating that the kernel formation does not entirely characterise these flames' stability. It highlights that a higher coflow temperature has a lower advection velocity and indicates increased stability by flame propagation. This identifies that the investigation of radical

pooling such as CH_2O, upstream of the flame base, is of interest to determine the stabilisation properties of a high and low coflow temperature.

7.1.2 Selected DME coflow temperature cases

A lower coflow temperature (around T_C = 1250 K) was chosen between the premixing cases, as it led to a high average lift-off height of $x/D \approx 29$, resulting in coflow temperatures ranging from T_C = 1225 K to T_C = 1275 K for the fuel mixtures outlined in Table 7-1. The higher coflow temperatures were set to T_C = 1400 K, this provided a constant temperature between cases, producing a lower lift-off height of $x/D \approx 7$. The jet velocity of U_J = 50 m/s is selected such that the flame base remains, for all cases, within the valid cone, while the jet Reynolds number (Re_J) is sufficiently high. The partially premixed case of air:DME = 3:1 is also studied at a higher jet velocity of U_J = 100 m/s to report the effects of higher mixing rates. Table 7-1 also shows the stoichiometric mixture fraction (ξ_{st}), which increases slightly with decreasing coflow temperature, due to a slight change in the composition of the hot coflow.

Table 7-1 Selected premixed and diluted DME flames for further PLIF study.

Jet mixing	Pure DME		air:DME = 1:1		air:DME = 3:1		N_2:DME = 3:1		air:DME = 3:1	
U_J (m/s)	50		50		50		50		100	
Re_J	38610		22990		16650		16683		33293	
T_C (K)	1225	1400	1250	1400	1275	1400	1275	1400	1275	1400
ξ_{st}	0.06	0.06	0.11	0.11	0.21	0.20	0.17	0.16	0.21	0.20

7.2 OH/CH_2O-PLIF results

Select mean and instantaneous LIF-OH and LIF- CH_2O structures of flames listed in Table 7-1 are reported in the following sections with a particular focus on the upstream region close to the stabilisation point. Full flame mean images are given for the premixing of air:DME = 3:1, U_J = 50

m/s, T_C = 1400 K and T_C = 1275 K. While instantaneous images obtained from both the PLIF as well as chemiluminescence are given for the pure DME jet cases. The final sections analyse kernel dynamics: formation rates, growth rates, aspect ratios and kernel heat release.

7.2.1 **Mean flame signals, CH_2O and OH: 3:1 = Air:DME, U_J = 50 m/s**

There are notable differences in both the OH and CH_2O fields, and their spatial correlation between the high and low coflow temperature case. It is observed in Fig. 7-4 that the OH initiation occurs at $x/D \approx 8$ and $x/D \approx 25$ for the T_c = 1400 K and T_C = 1275 K cases respectively, agreeing closely with the chemiluminescence lift-off heights presented in a previously in Fig. 7-2. The lift-off height is defined by the axial position for which OH has a peak gradient (*d(OH)/dx*), along a vertical line that intersects with the peak OH signal.

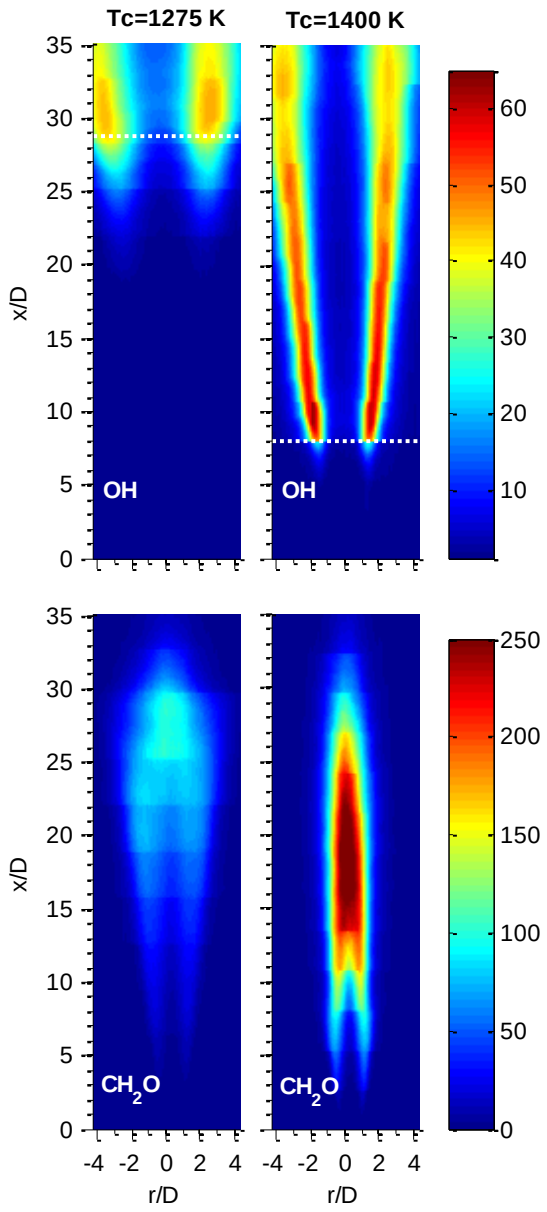

Fig. 7-4 Average stacked OH and CH_2O PLIF results for partial premixing, air:DME = 3:1 U_J = 50 m/s with coflow temperatures of T_C = 1275 K (left column) and T_C = 1400 K (right column). Colour bars describe the signal counts and correspond to each OH and CH_2O row respectively. The horizontal line indicates the mean OH lift-off height.

The radial OH signal width for the lower coflow temperature case (T_c = 1275 K) is much broader for all *x/D*'s compared to the higher 1400 K coflow case, this is despite the stoichiometric mixture fraction (ξ_{st}) being very similar. The low-temperature coflow case for T_C = 1275 K, has a peak in OH signal near the flame base, whilst at higher temperatures (T_C = 1400 K) the signal

remains high for almost the full length of the flame with a peak signal closer to the jet centre. For the lower coflow temperature, T_C = 1275 K, the flame base (marked by the horizontal dashed line in Fig. 7-4) is not only much further downstream than that of T_C = 1400 K but appears to have a spatially wider OH profile. This is because at this downstream location of x/D ~ 28, and for the same mixture fraction band, OH covers a broader spatial range because of the shallower gradients. It is evident that as the flame stabilization region transitions to a downstream axial location, it experiences different flow and mixing fields. However, the key factor remains that these transitions are induced by the co-flow temperature which changes the ignition delay times significantly but also influences the most ignitable mixture and the tolerable scalar dissipation rates. These trends are also consistent with unsteady laminar flame calculations for auto-igniting mixtures (presented in the discussion chapter of this thesis).

The initial formation of the CH_2O signal seen in Fig. 7-4, occurs in similar axial locations of $x/D \approx 6$ for both the high and low coflow temperatures, this is much earlier than the region of OH initiation. The location of the CH_2O relative to OH indicates that CH_2O is forming in richer regions where entrainment of the coflow is relatively small, also indicating lower temperatures.

The centreline containing unreacted fuel is indicated by the absence of LIF-CH_2O. The region of unreacted fuel is shorter for T_C = 1400 K, extending to $x/D \approx 12$, whereas no CH_2O signal occurs until $x/D \approx 17$ for the low coflow temperature, T_C = 1275 K. The axial distance over which the entire CH_2O signal may be detected is somewhat similar between the coflow cases, extending to $x/D \approx 30$, which can be attributed to the comparable jet momentum of both flames.

At higher coflow temperatures, T_C = 1400 K, CH_2O forms in the centre of the OH branches for the axial locations where it is detected. In these regions the spatial overlap in the radial direction is minimal. A build-up of CH_2O for the lower coflow temperature (T_C = 1275 K) occurs directly below the flame base highlighting its importance before the formation of OH, an axial and radial spatial

overlap is observed compared to T_C = 1400 K. The accumulation of CH_2O upstream of the flame base and OH is indicative of it being a low temperature species, therefore, highlighting CH_2O's importance to the lead up to autoignition and hence stabilisation to the flame. There is seemingly less dependence on the build-up of CH_2O below the OH flame base for T_C = 1400 K. The reduced axial distance between the formation of OH and CH_2O, for T_C = 1400 K, indicates that an increased coflow temperature has reduced the time between the conversion/reaction of CH_2O into OH.

7.2.2 Instantaneous Kernel Structure

Samples from the time evolution of PLIF OH and CH_2O images collected from a pure DME jet with coflow temperatures: T_C = 1225 K and T_C = 1400 K is seen in Fig. 7-6 and Fig. 7-7 respectively, they present kernel formation and growth for 100 μs intervals. This sequence highlights the formation of a kernel, its growth and the varying perspective that the chemiluminescence camera observes. A kernel refers to an island of LIF-OH (OH-kernel) or an island of chemiluminescence (CL-kernel), with overlapping LIF-OH and LIF- CH_2O termed a *HR*-kernel. Kernels produced from a pure fuel jet compared to the increased premixed cases have been found to grow at a slower rate, which is further explored in Section 7.2.6 of this chapter.

7.2.3 Lifted jet flame (no coflow): CH_2O/OH PLIF

A sequence of laminar lifted (no hot coflow) DME flames are presented below in Fig. 7-5 for five consecutive (500 us) images, these are for comparison to the mean OH and CH_2O JHC signals above. For this example, the fuel jet (D_J = 4.45) is one-part air to one-part DME for a jet velocity, U_J = 10 m/s. It can be observed that CH_2O forms as expected on the outer edge of the OH signal, in lower temperature regions. Furthermore, it forms a narrow boarder that traces the edge of the OH,

this structure and signal distribution is seen to be entirely different from the heated coflow case (Fig. 7-4), which forms in a sheet. The CH_2O structure observed is slightly wrinkled, however, owing to the low velocity, the flame is laminar, and the structure doesn't significantly change within 500 us.

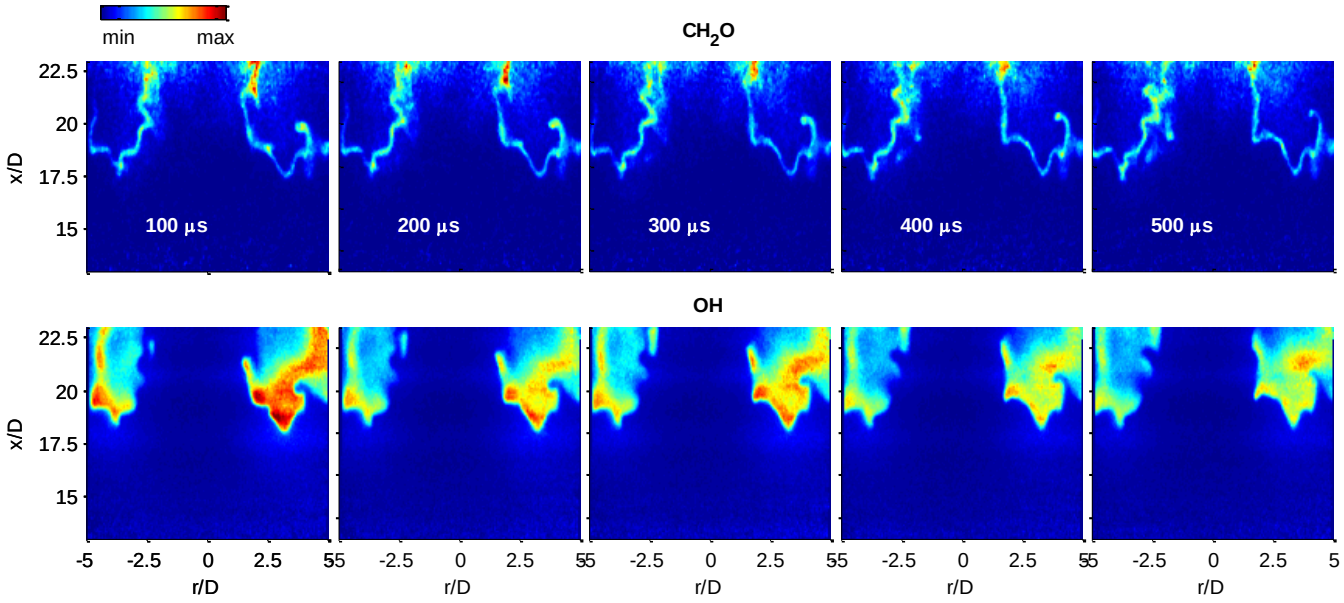

Fig. 7-5 Lifted, unpiloted DME jet flame PLIF results for CH_2O (top) and OH (bottom) over five consecutive images at 10 kHz.

7.2.3.1 Instantaneous images: pure DME Jet: T_c = 1225 K

The evolution of an autoignition event, OH-kernel, is defined by the number of OH pixels below the flame base exceeding a signal threshold above the background as described in section 6.1.1. The CH_2O kernel signal is the projected signal that overlaps onto the given OH-kernel. With this definition, the OH-kernel is forming in the first and second image of Fig. 7-6 and continues to grow in the following images.

The 2-D projected OH-kernel growth is somewhat spherical whilst advecting downstream with no upstream kernel centroid propagation. The OH-kernel is predominantly on the outside of the

CH_2O sheet, two diameters from the jet centreline as observed in Fig. 7-6 a-b. Having captured the signals simultaneously with sub-pixel spatial alignment, between the OH and CH_2O camera's, the product of the two signals given in Fig. 7-6 (c) marks the overlap, where it is indicative of the heat release for the kernel. Heat release occurs from the first image, in row c of Fig. 7-6, and this is defined as kernel initiation. Furthermore, initially the heat release distribution within the kernel is uniform until about 300 µs. After this time, the distribution changes, and the intensity becomes progressively stronger on the kernel's edge, closest to the CH_2O sheet, toward the centre of the jet. The pattern and trends in heat release are discussed in more detail later in this chapter.

The chemiluminescence images shown in Fig. 7-6 d capture a larger field of view than the PLIF images. Therefore, the lines B-B and A-A are the boundaries for the PLIF camera, while line C-C marks the location of the laser sheet. The OH kernel initiates in the first image (row a), the product CH_2O x OH indicates uniform heat release from it (row c) but the chemiluminescence camera fails to show any signal until 900 µs later (last frame of row d). It was noted earlier that the chemiluminescence observed here is largely due to CH^* and its delayed appearance is most probably due to a lower sensitivity in the camera although a mismatch between the production of CH^* and the product CH_2O x OH may also be a contributor. This latter aspect cannot be confirmed here and may be the subject of further investigations. Other cases have been found where a kernel forms in the chemiluminescence camera and not until it grows and crosses the laser sheet C-C does it appear on the PLIF camera. However, there are multiple occasions where an OH-kernel is observed in the PLIF OH image but not on the chemiluminescence camera.

7.2.3.2 Instantaneous images: pure DME Jet: T_C = 1400 K

Increasing the coflow temperature, from T_C = 1225 K to T_C = 1400 K, for the same pure DME jet changes many characteristics of the flame, as shown in the sample sequence of images presented in Fig. 7-7. Kernels are forming much closer to the flame base, where the flame base is observed in the

chemiluminescence images (row d) and appears in the LIF-OH frame as it cuts the line B-B. A similarly sized kernel to the low coflow temperature, T_C = 1225 K, forms in the first to the second image but the formation is much further upstream and closer to the flame base. Since the kernel forms so close to the flame base, it is consumed within 300 µs.

The OH-kernel forms further outside the CH_2O sheet relative to the lower, T_C = 1225 K coflow case, forming closer to the shear layer between the coflow and jet. The centre of the CH_2O sheet has a region of no signal, this is due to the fuel jet having no low-temperature reactions taking place at this upstream axial location. Furthermore, since the ignition kernel is further outside of the CH_2O layer, the overlap is identified to be smaller and this is explored in more detail later in the paper.

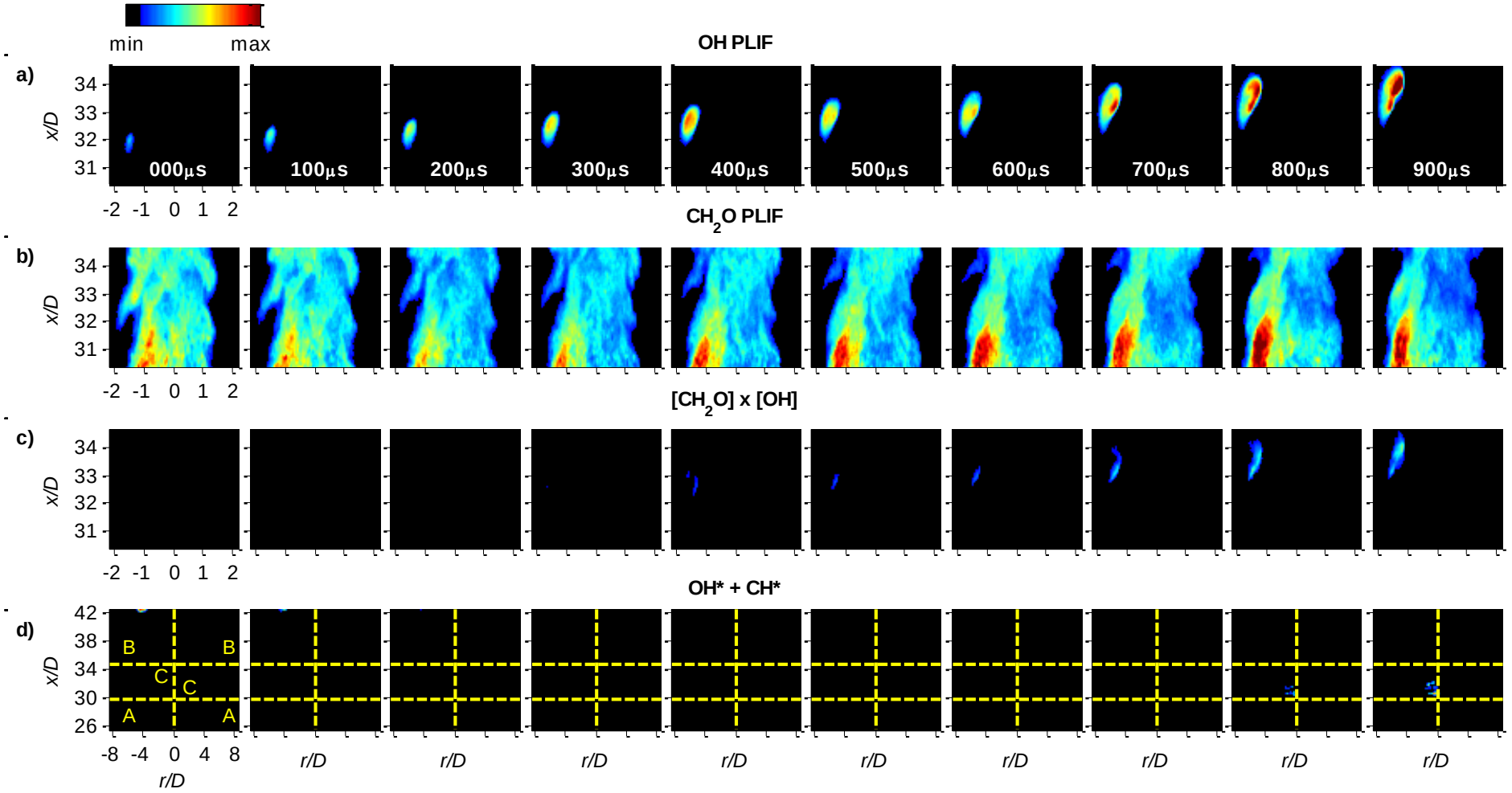

Fig. 7-6 Consecutive 10 kHz imaging for a T_c = 1225 K coflow igniting a pure DME fuel jet: OH PLIF (a) CH_2O PLIF (b) CH_2O x OH product (c) Perpendicular OH* CH* chemiluminescence (d).

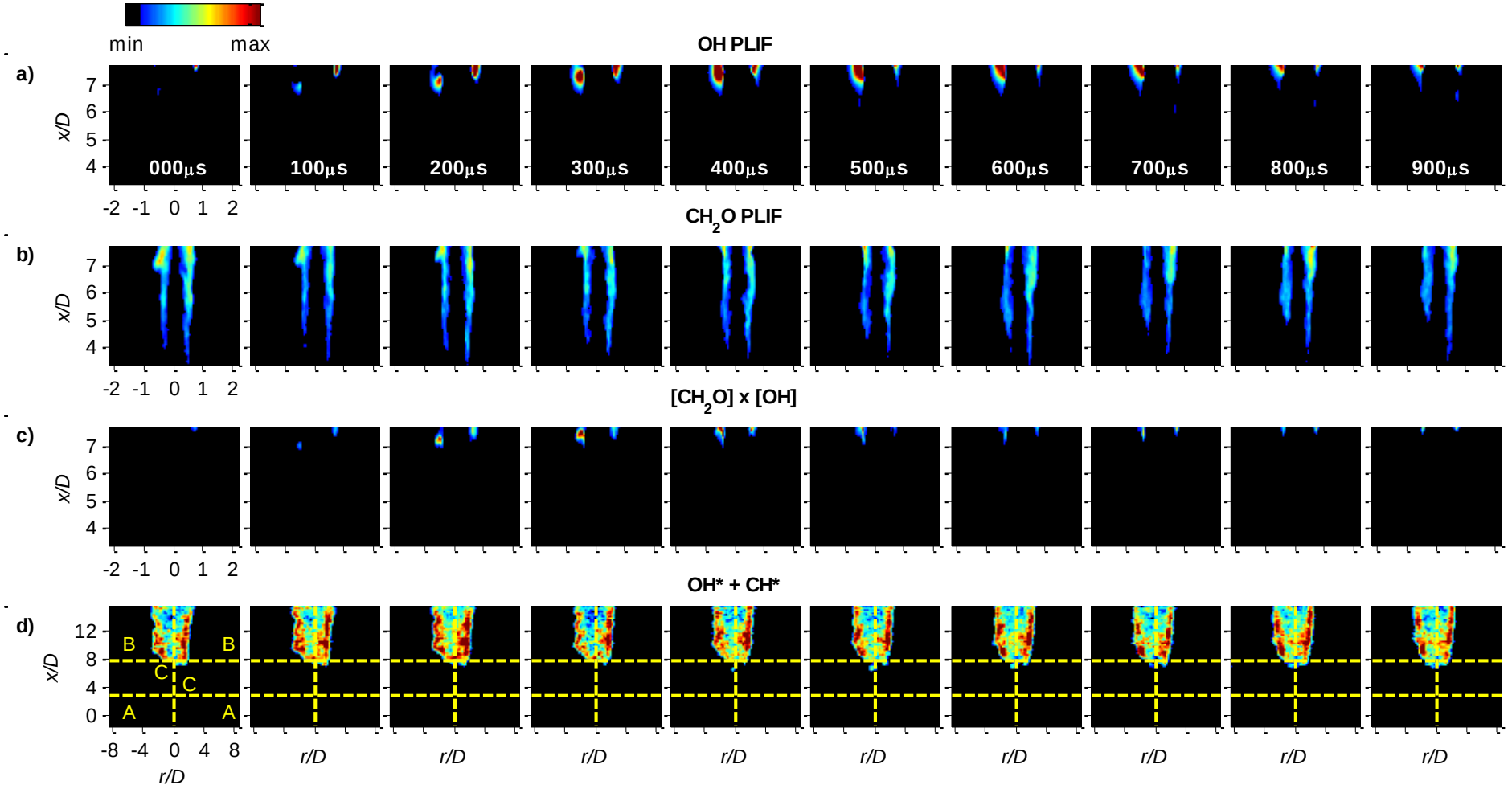

Fig. 7-7 Consecutive 10 kHz imaging for a T_C = 1400 K coflow igniting a pure DME fuel jet: OH PLIF (a) CH_2O PLIF (b) CH_2O x OH product (c) Perpendicular OH* CH* chemiluminescence (d).

7.2.4 **Formation of OH-Kernels**

This section tracks the formation and evolution of OH-kernels as markers of autoignition events. It is acknowledged here that initiation of kernels would have occurred upstream in fluid parcels populated by other species, such as CH_2O, before OH is produced, however, they cannot be conditioned appropriately for accurate diagnostics or are not measured (such as HO_2). For convenience, the centroids of OH-kernels are tracked in consecutive images, and the OH-kernel centroids are binarized, creating a 2-D formation map as seen in Fig. 7-8. The colour bars indicate the rate of OH-kernel formation (kern/mm^2*s) at the relevant location; formation rates can be measured since the since the formation of kernels is temporally resolved at 10 kHz. Heat release kernels (*HR*-kernels) as marked by the product of CH_2O x OH are discussed in a subsequent section of this chapter.

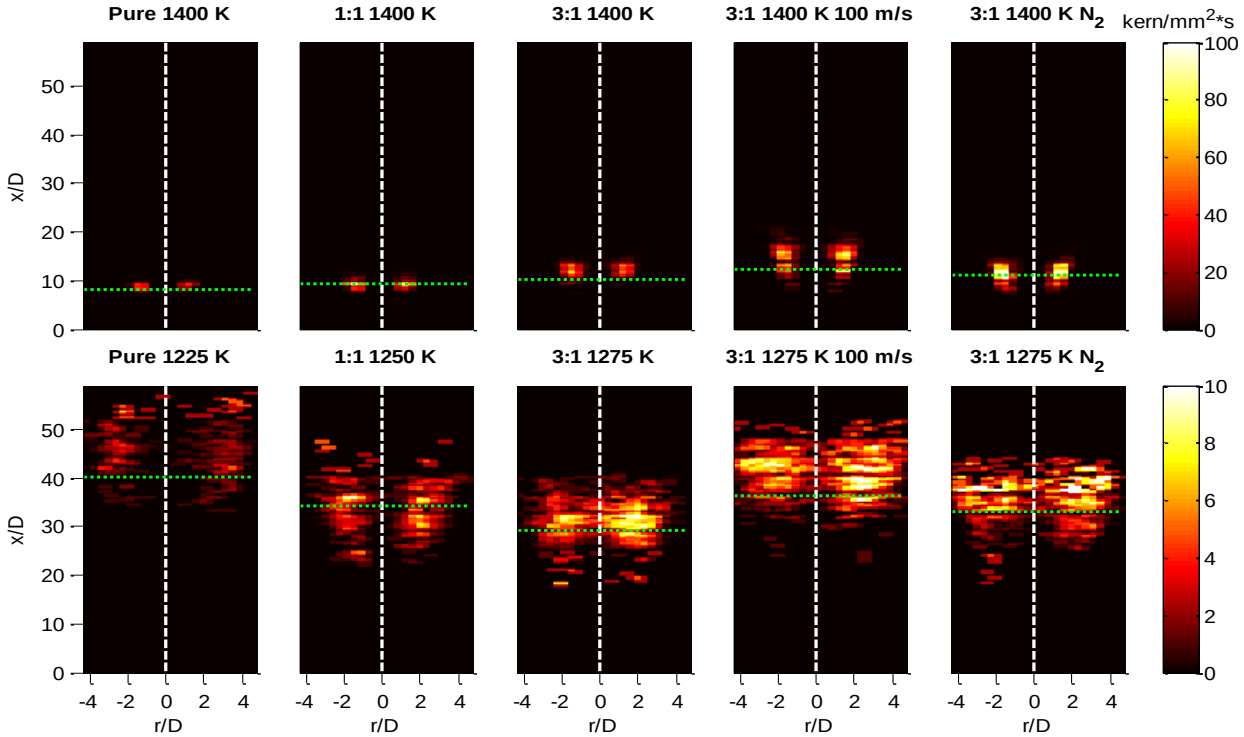

Fig. 7-8 OH-Kernel formation map for all flames studied: premixing ratios, velocity and dilution with N_2. Colour bars are given for an entire row, and they indicate spatial formation rates (kern/mm^2*s).

From the formation map in Fig. 7-8 a higher coflow temperature of T_C = 1400 K produces ignition OH-kernels at higher localised frequencies, where they form much closer to the exit nozzle and shear layer of the fuel jet. A decrease in coflow temperature, from T_C = 1400 K for U_J = 50 m/s drastically increases the downstream location and axial range, for OH-kernel formation, albeit with a lower peak formation frequency. For a common coflow temperature of T_C = 1400 K, OH-kernels from a pure fuel jet form further upstream and have a reduced axial and radial formation range. Coflow temperatures lower than T_C = 1400 K produce, for the pure DME jet, OH-Kernels well outside of the centreline. However, with increasing premixing, such as the case with air:DME = 1:1, kernels move closer inwards. For the air:DME = 3:1 case with T_C = 1275 K, OH-kernels form along the centreline with increased probability of formation moving radially outwards.

The 2-D formation rate map for a third, intermediate, temperature of T_C = 1325 K for air:DME = 3:1 is presented in Appendix B.2. It shows for this intermediate coflow temperature, the ignition rates and formation location sit between the higher and lower coflow temperature bounds, T_C = 1400 K and T_C = 1275 K respectively. That is, the radial and axial formation range is greater than the T_C = 1400 K coflow, whilst the local formation rate density (kern/mm*s) is less. On the contrary, the lower, T_C = 1275 K coflow, has a smaller axial and radial formation range, with a higher local formation density than the T_C = 1325 K coflow.

Increasing the jet velocity to U_J = 100 m/s with air:DME = 3:1 moves the formation of OH-kernels further downstream for both the T_C = 1400 K and T_C = 1275 K coflow. Additionally, the axial range and formation rate of OH-kernels increase for increased jet velocity for both the high and low coflow temperatures. Finally, by analysing the spatial map of OH-kernels for high and low coflow temperatures, it is evident that at high-temperatures,

T_C = 1400 K, kernels form further upstream in regions with potentially steeper mixture fraction gradients. Even though the low-temperature kernels are more spread axially and radially, they could be potentially across similar mixture fraction iso-contours as they are further downstream.

7.2.5 **OH-Kernel Formation Rates**

The axial formation rates of OH-kernels are binned into increments of three jet diameters, based on new OH-kernel centroids and are presented in Fig. 7-9. Formation rates are presented based on: air premixing and jet velocity, dilution or premixing and increased jet velocity (U_J = 100 m/s). The radial dimension has been 'collapsed' from the 2-D formation map presented previously in Fig. 7-8. The findings are summarised in bullet points below in regards to how varying partial premixing, coflow temperature and jet velocity effects OH-kernel formation: rates, location, and axial range.

- A reduction in coflow temperature is found to produce OH-kernels further downstream for all partial premixing cases. Additionally, the axial range is larger but more intermittent, such that the temporal integration of formation rates is similar between, high and low coflow temperatures for a given premixing case.
- Increased partial premixing for a common coflow temperature induces higher OH-kernel formation rates. The explanation for the increased formation rate is identified in Fig. 7-8, where kernels are forming with increased radial and axial range in the fuel jet, identifying that ignitable mixtures are more prevalent.
- A reduction in partial premixing is found to increase the axial range of kernel formation, noting that coflow temperatures between premixing cases were chosen

based on similarity between lift-off heights. The axial broadening in formation rates is an attribute of the slower formation rate of reduced premixed jets, a slower formation rate, in fact, creates a spatially broader formation range. This was identified previously in Fig. 7-3 where the advection velocity of a pure DME fuel jet flame base is a lot slower than premixing of air : DME = 3:1, excluding kernel merging events. This decreased advection velocity explains how the formation rate can be slower while the lift-off height is similar.

- Results for OH-kernels at U_J = 100 m/s, ar:DME = 3:1, indicate formation rates and the axial location for new OH-kernels increase for both high and low coflow temperatures. The increased rates may be due to the improved mixing induced by the higher shear between the fuel jet and coflow, further measurements are needed to ascertain this speculation.
- Jet dilution with nitrogen, for the N_2:DME = 3:1 case, seen in Fig. 7-9 leads to an increase in OH-kernel formation rates, for both the T_C = 1400 K and T_C = 1275 K coflow. However, the peak formation rate shifts downstream, with this being more pronounced for the T_C = 1275 K coflow. The downstream shift in the formation rate is expected as the addition of an inert diluent reduces the reactivity of the mixture and hence increases the delay time for autoignition.
- Formation rates have previously been presented from chemiluminescence measurements in Fig. 7-3 and these were found to be five times lower than those btained from the OH PLIF measurements in Fig. 7-9. The reduced formation rate emphasises the finding in Fig. 7-6, where OH-kernels form well before chemiluminescence. In some instances, OH-kernels are detected from PLIF measurements but not from chemiluminescence of CH^*. Laminar calculations using a

1-D isobaric reactor and the NUIG Mech_56.54 mechanism [73] confirm that the initial formation of OH form slightly earlier than detectable levels of CH^*.

- Biasing of kernel formation rates from planar OH measurements may occur as a kernel that forms out of plane may then grow into the plane. The inter-plane growth would be registered as a new event increasing the formation rate: indicating that volumetric OH-LIF measurements are required to diagnose between out plane formation and inter-plane growth.

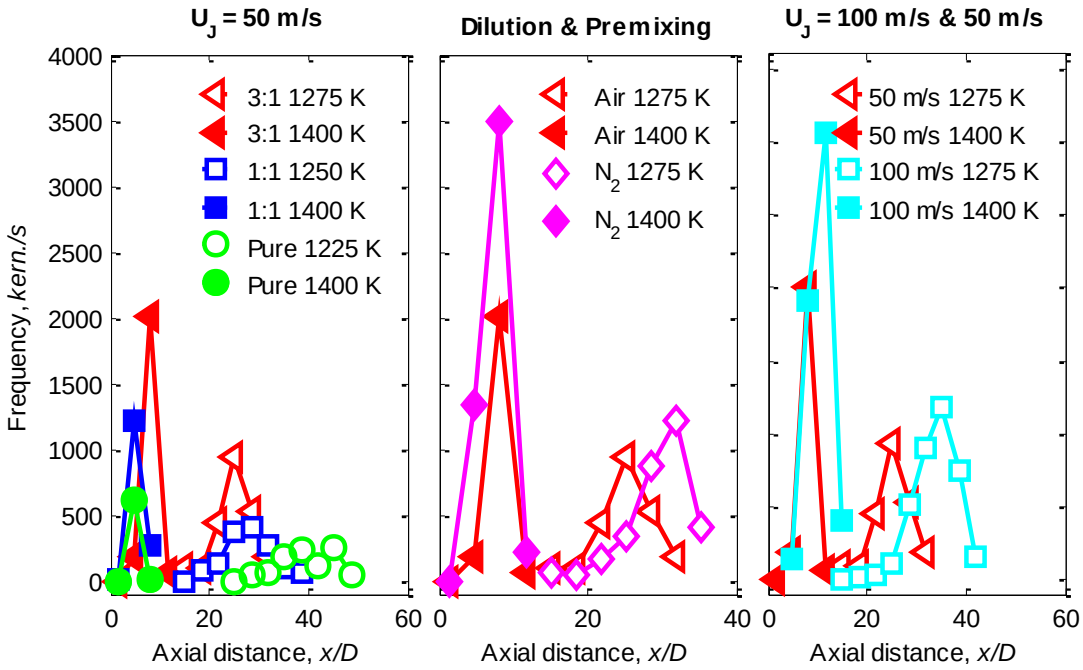

Fig. 7-9 New OH-Kernel formation rates for various coflow temperatures and diluents: Constant jet velocity (U_J = 50 m/s), varied dilution with constant 3:1 mixing (Dilution & Premixing) and varied jet velocity with constant air:DME = 3:1 premixing (U_J = 100 m/s and 50 m/s).

7.2.6 **OH-Kernel Growth**

Mean OH-kernel growth rates are presented in Fig. 7-10 a based on one second of consecutive images collected at 10 kHz. The kernel size is defined by the OH-kernel projected onto the laser sheet, where the number of OH-kernel pixels is converted to mm^2 using the cameras pixel resolution. The OH-kernels grow larger than what is presented here of ~25 mm^2 for lower coflow temperatures (less than T_C = 1400 K). However, owing to the small OH-PLIF camera field of view, these kernels are excluded for further analysis and the reader to the previous chemiluminescence measurements Fig. 7-3. In this plot, chemiluminescence from low coflow temperature kernels grow up to 180 mm^2 for pure DME, 150 mm^2 for 1:1 and 130 mm^2 for 3:1 before merging with the flame base.

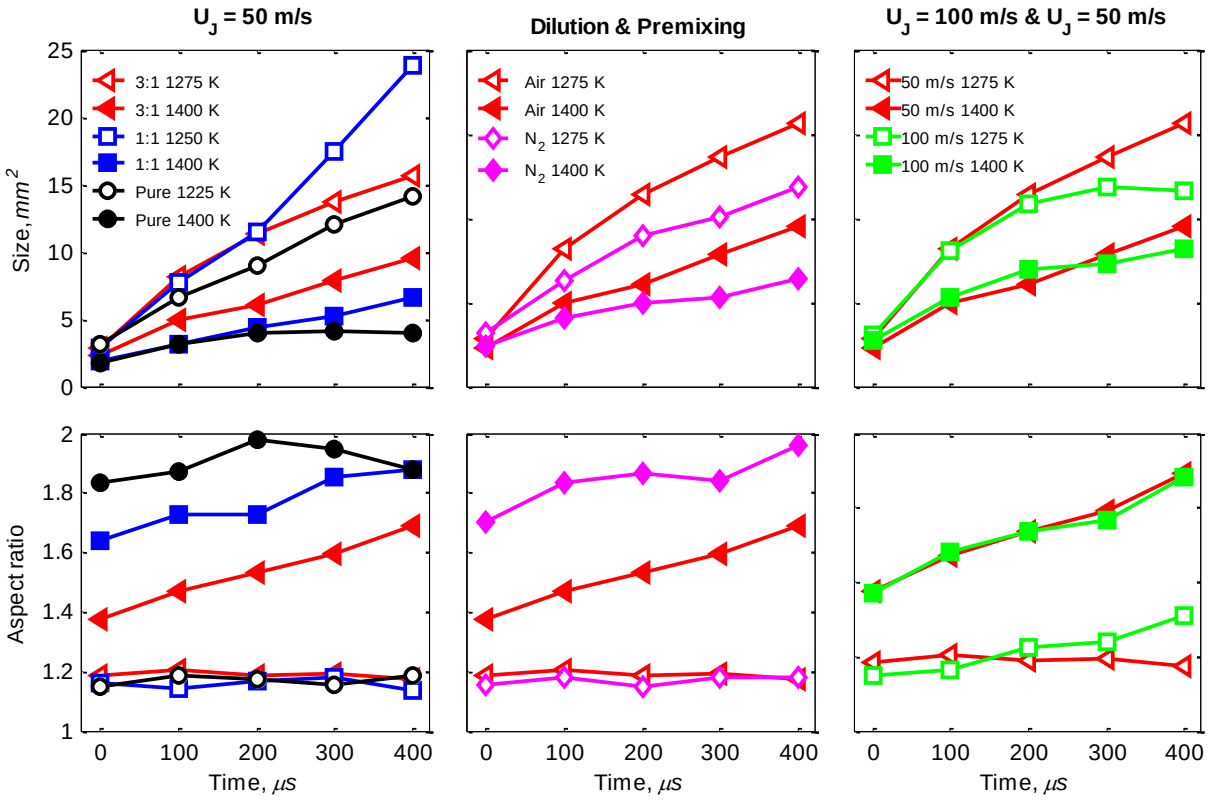

Fig. 7-10 OH-kernel growth with respect to time, based on size and aspect ratio: Row a) indicates size (mm^2). Row b) displays aspect ratios (kernel axial length divided by width).

Columns separate constant jet velocity (U_J = 50 m/s), varied dilution with constant 3:1 mixing (Dilution & Premixing) and varying jet velocities for constant air:DME = 3:1 premixing (U_J = 100 m/s and 50 m/s).

Growth rates are affected by in- and out-of-plane motion. However, mean values are presented here and these are found to be not affected by out-of-plane motion, as confirmed by Meares et al. [210] for a non-premixed piloted burner.

In Fig. 7-10 a) there exists a linear relationship between size and evolution duration since the initiation of an OH-kernel. However, for all premixed and diluted cases studied here, the lower coflow temperatures yield OH-kernels that are growing faster. The duality in growth behaviour between coflow temperatures can be explained by analysing Fig. 7-10 b where the aspect ratio of a kernel (axial length/ width) for a given evolution time is presented. Again, there is a separation between the aspect ratio from lower and higher coflow temperatures for a given premixing ratio, dilution and fuel velocity. Lower coflow temperatures (~T_C = 1250 K) all exhibit near unity aspect ratios identifying, as is observed visually in Fig. 7-6, the kernels are circular in shape. However, higher coflow temperatures (T_C = 1400 K) have increased aspect ratios, indicating that they are no longer circular but elongated in the axial direction. For an intermediate temperature, T_C= 1325 K, the growth and aspect ratio are like the lower temperature T_C = 1275 K (appendix B.3). The temperature of T_C= 1325 K coincides with the transition between the low (T_C = 1400 K) and highly lifted flame. These lower temperature flames, T_C = 1275 K and T_C= 1325 K, therefore may have similar dependency on kernels for stability, and as such, it may explain why the kernels exhibit similar growth and shape characteristics.

It is of interest that the aspect ratio of the OH-kernel with time or correspondingly with respect to size is not significantly changing, indicating they are growing preferentially along contours of similar mixture fractions. That is, the higher coflow temperature kernels form in an elongated manner and grow around its centroid, elongating slightly. This preferential growth of kernels along major axis is further seen in the results of Pareja et al. [211] who used tomographic OH-LIF to capture three dimensional kernel formation and growth. Since the lower coflow temperature leads to the formation of OH-kernels further downstream, the spherical nature and growth could indeed be along similar contours of mixture fractions as the spatial mixture fraction gradients are not as steep. This implies that at such high-temperature conditions, ignition and kernel growth could be occurring across a wider mixture fraction range.

Finally, the aspect ratios further indicate that for a constant premixed ratio at air:DME = 3:1 with varied injection velocities (U_J = 50 m/s to U_J =100 m/s), kernels are forming and growing with a similar shape. The similar aspect ratio implies that while the mixture fraction field is constant between fuel jet velocities, similar turbulence levels or scalar dissipation rates are required for the initiation of kernels. It is worth noting for increased velocity, U_J = 100 m/s, kernels are forming slightly further downstream as seen in Fig. 7-9.

7.2.7 **Kernel Signal Intensities**

Before analysing the average heat release from autoignition events, a definition of the integrated heat release is required. The heat release reported hereon is based on the product between an OH-kernel defined in Fig. 7-11 (OH Kernel) and the corresponding CH_2O signal that is projected onto it, Fig. 7-11 (CH_2O Kernel). Furthermore, the integrated kernel heat

release is determined by the pixel sum from the product CH_2O x OH, Fig. 7-11 (CH_2O x OH), across the entire OH-kernel and their corresponding signal intensities.

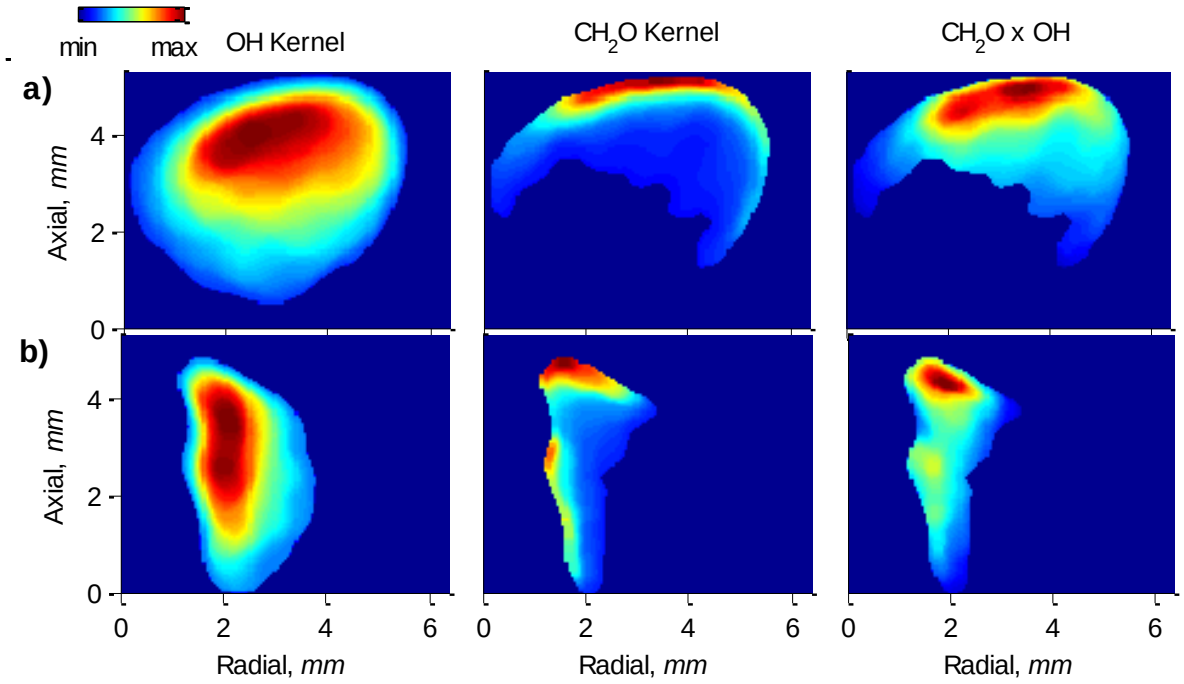

Fig. 7-11 A single autoignition event for a high and low coflow temperature: *Tc* = 1225 K a) and *Tc* = 1400 K b), for a Pure DME jet. Displayed is an OH-kernel, the CH_2O overlap (projection) and product CH_2O x OH (*HR*-kernel).

An example of an ignition event for a high and low coflow temperature is seen in Fig. 7-11. It highlights for a low coflow temperature Fig. 7-11 (a), the peak OH signal is predominately in the centre of a kernel, whilst the peak CH_2O signal is toward the OH-kernel edge. The product of the two signals, i.e., the heat release, moves relative to the OH and CH_2O signals, and peak heat release occurs towards the upper region of the OH-kernel. A

pixel threshold was selected for the CH_2O signal, such that it just exceeds the background, therefore, zero CH_2O counts are observed, and correspondingly zero heat release occurs. In Fig. 7-11 b the higher coflow temperature, T_C = 1400 K, the kernel is elongated axially, where the distribution of the OH signal from T_C = 1225 K and T_C = 1400 K cases are significantly different for these kernel samples. The low-temperature has a somewhat uniform OH gradient across both axes of the kernel, while the high-temperature has a radial OH gradient.

The signal distribution presented in Fig. 7-11 was for a single OH and *HR*-kernel, the distributions and intensities vary for different samples (seen in the scatter plots below), this leads to fluctuating heat release levels. Furthermore, the signal intensities and spatial overlap vary for differing fuel mixtures and coflow temperatures. A summary of the peak signals and the average overlap of CH_2O onto OH are given in Table 7-2 for each fuel mixture based on the entire set of kernel events. The percentage of overlap relates to how much of the OH-kernel is overlapped by CH_2O above the threshold. A decrease in coflow temperature was found to increase the overlap, seen for the air:DME = 3:1 case between T_C = 1275 K and T_C = 1400 K given by 5 % and 75 % respectively.

Table 7-2 Spatial overlap of CH_2O onto an OH-kernel and their peak signals for all OH-kernels observed for varying: coflow temperatures, premixing and jet velocities.

Mixing ratio (U_J)	Pure DME (50 m/s)		air:DME = 1:1 (50 m/s)		air:DME = 3:1 (50 m/s)		N_2:DME = 3:1 (50 m/s)		air:DME = 3:1 (100 m/s)	
T_C (K)	1400	1225	1400	1250	1400	1275	1400	1275	1400	1275
Peak CH_2O (Counts)	433	907	433	563	481	574	509	647	518	617
Overlap (%)	50	99	30	95	75	95	40	60	60	92
Peak OH (Counts)	1028	2096	1028	1988	772	1069	1748	2116	2187	961

Peak OH and CH_2O signals were found to be indicative of signals within ignition kernels (measured in the region of overlap) for various fuel mixtures. A decrease in coflow temperature somewhat surprisingly increases the signal strength for both OH and CH_2O within the kernel region for U_J = 50 m/s. The contrary is observed for the air:DME = 3:1 case with U_J = 100 m/s where the peak OH signal occurs for higher coflow temperatures.

7.2.8 **Scatter Plots: Heat Release, OH and CH_2O**

While Table 7-2 presented the peak signals within kernels and the mean spatial overlap of OH onto CH_2O, it does not show the correlation between these species, nor does it provide any information about the heat release that occurs during various stages of kernel evolution. Having defined the spatial overlap in Fig. 7-11 of OH and CH_2O and how it affects the distribution of heat release within kernels, scatter plots for OH, CH_2O and *HR* signals are now presented in Fig. 7-12 for the case of air:DME= 3:1, and for two temperatures T_C = 1275 K and T_C = 1400 K. Two stages in the kernel evolution are given, for kernel initiation (triangles) and for 300 μs after initiation (circles). The scatter plots for all fuel mixtures and temperatures studied are given in the appendix (B.5, B.6 and B.7).

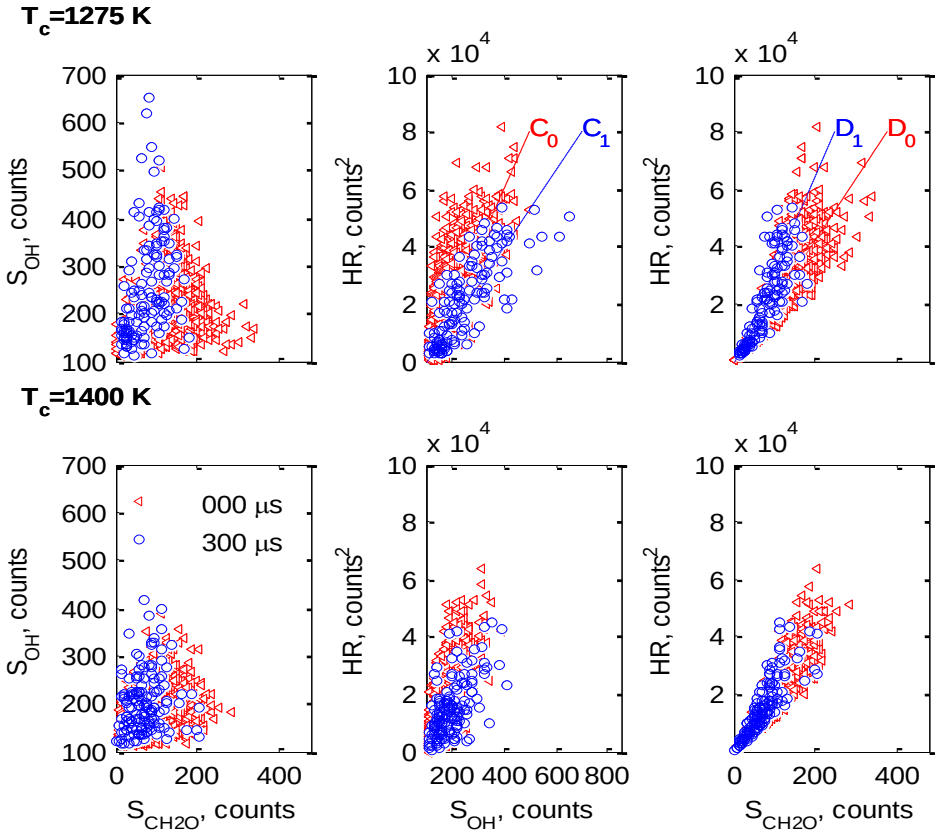

Fig. 7-12: Scatter plots for OH, CH_2O and *HR* signal counts for the case of air:DME= 3:1, and for two temperatures T_C = 1275 K (top row) and T_c = 1400 K (bottom row). Left: correlation of signals S_{OH} vs. S_{CH2O}, middle: correlation of *HR* vs. $S_{OH,}$ right: correlation of *HR* vs. S_{CH2O} Each plot shows two stages in the kernel evolution, for kernel initiation (triangles) and for 300 µs after initiation (circles). The dashed lines shown are the slopes C_0, D_0 are for kernel initiation and C_1, D_1 for 300 µs after initiation.

The correlation of S_{OH} vs. S_{CH2O} is not monotonic for these kernels, that is, a kernel with large S_{OH} does not correspond distinctly to a low S_{CH2O}. However, as kernels grow over 300 µs, the average CH_2O signal can be seen to decrease, whilst the OH signal increases. The change in these signals with kernel evolution is expected as the low-temperature build-up of CH_2O is consumed, leading to higher temperature reactions involving OH. For the heat release (S_{CH2O} x S_{OH}) vs. S_{OH}, a somewhat monotonic correlation is observed, where increasing OH levels lead to increased heat release. The slopes for the *HR* vs. S_{OH} plots

shown in Fig. 7-12 (middle column) are labelled C_0 and C_1 respectively for the times during kernel initiation and 300 μs after. It is evident that the gradient of the scatter has decreased as ignition progresses ($C_1<C_0$). The decreasing gradient indicates that as a kernel grows, the *HR* doesn't correlate to increasing OH levels, and therefore, CH_2O and its overlap has a somewhat larger influence on the heat release.

For *HR* vs. S_{CH2O} the scatter is further decreased, compared to S_{OH}, and the near linear relationship is improved. The slopes for the for the *HR* vs. S_{CH2O} plots are shown in Fig. 7-12 (right column) and are labelled D_0 and D_1 for the two times during kernel initiation and 300μs after. The slopes of *HR* vs. S_{OH} have reversed trends, such that the gradient for 300 μs after ignition is now higher with $D_1>D_0$ (instead of $C_1<C_0$ as observed earlier for *HR* vs. S_{OH}). Therefore, as described in Table 3 the overlap and CH_2O intensity has a large influence into the heat released from a kernel. Reduced scatter for S_{CH2O}, whilst indicating a stronger correlation to heat release, could be an artefact of the kernel being defined by the OH kernel contour. That is, the low-temperature intermediate, CH_2O would occur upstream of OH being present leading to a reduction in the correlation between *HR* vs. S_{CH2O}.

The lower coflow temperature, T_C = 1275 K, compared to T_C = 1400 K, has a larger OH signal for all time intervals, whilst CH_2O is similar for both temperatures. The increase in signal levels, in addition to the increased signal overlap as described in Table 7-2, leads to increased heat release levels for the lower coflow temperature. However, the correlation (monotonic relationship) between *HR*-OH and between *HR*-CH_2O (reflected in the slopes C_1, C_0 and D_1, D_0) in Fig. 7-12 is similar for the high and low coflow temperatures, including the varying correlation with kernel growth. The trends observed here for the air:DME=3:1 between the low and high-temperature case are comparable to the other premixing and jet

velocity cases, where the CH_2O, OH and *HR* plots are given in the Appendix (B.6, B.7 and B.8).

7.2.9 Integrated Kernel Heat Release with Size

The average integrated heat release for varying *HR*-kernel sizes is displayed in Fig. 7-13 for all cases listed in Table 1, where a linear relationship between kernel size and time was shown in Fig. 7-10.

Kernel heat release was normalised with size to indicate that heat release is growing proportionally to kernel size, shown by the horizontal lines in Fig. 7-13. The linear correlation between heat release and size indicates that whilst heat release forms on part of a kernel edge, seen in Fig. 7-10 c, it grows proportionally to the kernel area. Note that a quadratic relationship would exist if the heat release were to be uniform across a growing kernel.

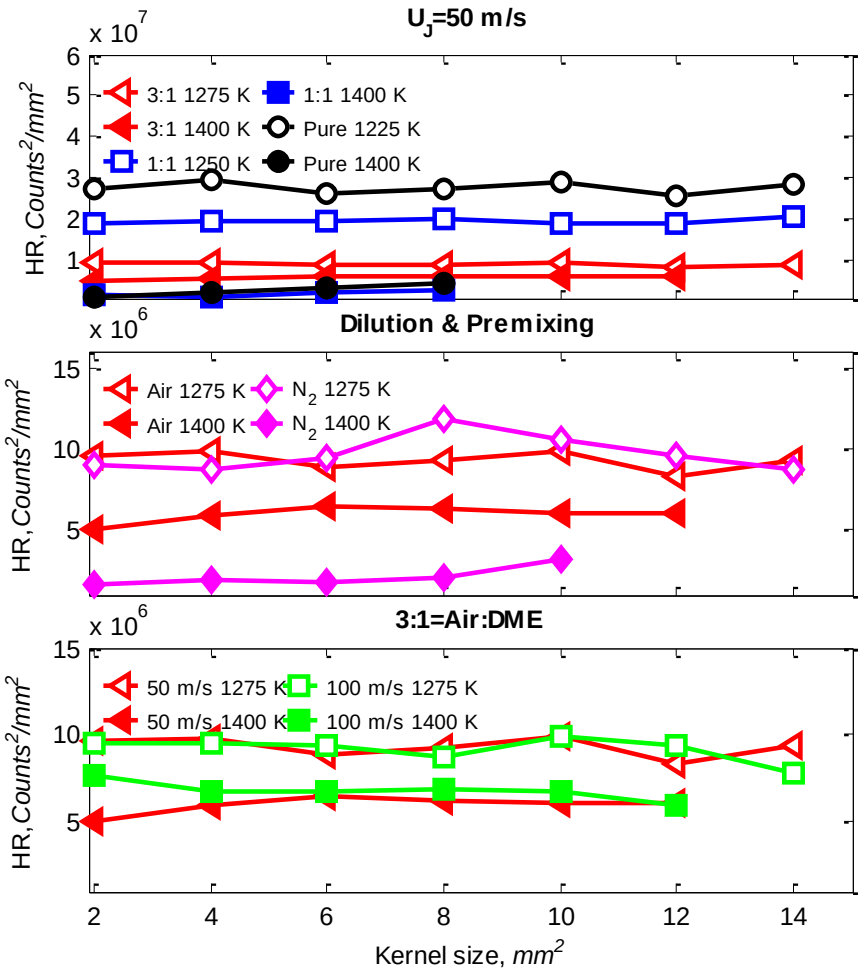

Fig. 7-13 Average integrated heat release normalised heat release ([CH_2O] x [OH]) for kernel sizes at 1 mm^2 bins. Rows describe: constant jet velocity (U_J = 50 m/s), varied dilution with constant 3:1 mixing (Dilution & Premixing) and varying jet velocities for constant Air:DME = 3:1 premixing (U_J = 100 m/s and 50 m/s).

A distinct finding is the degree of difference between the high and low coflow temperatures, increased coflow temperature, in fact, decreases the heat release. The difference in heat release is predominately attributed to lower coflow temperatures having a larger spatial overlap of CH_2O onto an OH kernel as observed in Table 7-2. The increased

spatial overlap is in addition to higher OH and CH_2O signal intensities for lower coflow temperatures.

It is seen in Fig. 7-13 that the heat release increases with reduced partial premixing for coflow temperatures less than T_C = 1400 K. Pure DME for T_C = 1225 K produces more integrated heat release than air:DME = 1:1 at T_C = 1250 K followed by air:DME = 3:1 at T_C = 1275 K. Whilst the air:DME = 3:1 cases are bimodal between high and low coflow temperatures, the degree of bimodality is reduced. The heat release from the 3:1, coflow temperature case of T_C = 1325 K is given in the Appendix, B.4. This intermediate temperature has almost the same heat release observed from the lower coflow temperature of T_C = 1275 K.

The effect of N_2 dilution has increased the separation of heat release between the high and low coflow temperature seen in Fig. 7-13 (Dilution). The high coflow temperature (T_C = 1400 K) has increased occurrences for low heat releasing kernels which are a direct correlation of the reduction in CH_2O and OH. The distribution between OH and CH_2O for T_C = 1275 K, N_2:DME =3:1 is similar to that of air:DME = 3:1, leading to the similar levels of heat release. Increased velocity, U_J = 100 m/s, has done very little to change the heat release levels for a high and low coflow temperature despite T_C = 1400 K kernels producing more OH signal.

The observed linearity of average integrated heat release with increased kernel size indicates the signal distribution and intensities do not vary significantly during growth. That is, the average CH_2O signal decreases slightly across an OH-kernel while the average OH signal increases slightly for an increase in size. Indicating, size or amount of overlap has a larger influence on the integrated heat release.

There is a relatively strong correlation between the kernel aspect ratios observed in Fig. 7-10 and the heat release profiles from Fig. 7-13 For example, in the pure DME jet case the high-temperature coflow, T_C = 1400 K, has a large kernel aspect ratio (~1.9) and corresponding low heat release. While the low temperature coflow, T_C = 1225 K, has a small aspect ratio (~1.2) and a relatively high heat release. If the aspect ratio is indicative of the spatial mixture fraction gradient of a kernel as mentioned in Section 7.2.6, the heat release is also proportional to the relative ignitable mixture fraction. Therefore, this potentially means the higher coflow temperature kernels are igniting in leaner regions than low coflow temperatures (still igniting in lean mixtures) which would lead to lower heat release.

7.2.10 Integrated Heat Release Fluctuations

There are numerous occasions for all fuel cases listed in Fig. 7-13 where there is up to two orders of magnitude difference for the integrated heat release for a given kernel size. The PDF of heat intensities are presented in Fig. 7-14 for two kernel sizes, 1 mm^2 is deemed to be kernel formation and increasing size indicates different stages of kernel propagation.

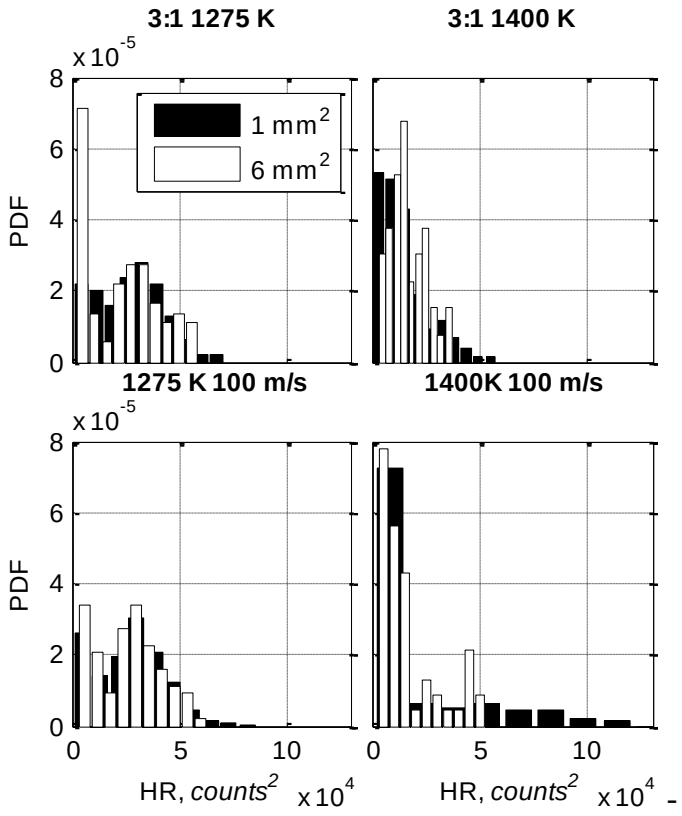

Fig. 7-14 Size normalised heat release (CH_2O x OH) PDF for varying diluents and coflow temperatures. A 1 mm^2 kernel represents kernel initiation.

The variation in the integrated heat release for differently sized kernels is attributed to fluctuating levels of OH and CH_2O overlap, their respective signal intensities and distribution throughout an OH-kernel. Therefore, it is identified that there are instances where a kernel is burning intensely and is providing significant heat to the flame base. However, there are other occasions where they are seemingly less fundamental to the heat released into the flame base and hence to the stabilisation process. Normalising with kernel size has produced overlapping PDFs for differing kernel sizes, verifying that kernel size is attributed to increased integrated heat release opposed to varying overlap or signal strength as a kernel propagates. Furthermore, there are occasions where the 1 mm^2 kernel can be burning more intensely than larger kernels.

For high coflow temperatures (T_C = 1400 K), the pdf is strongly ‘skewed’ to the right i.e., reduced heat release, verifying why the integrated average heat release in Fig. 7-13 is smaller for increased coflow temperature. Stabilisation due to autoignition is theorised to produce kernels that are significant to stabilisation and have high reactivity/heat release, where this is observed for low coflow temperatures. Higher coflow temperatures have minimal heat releasing kernels and therefore it is theorised to be stabilised by flame propagation in addition to autoignition events.

The PDF’s for all other premixing cases are given in Appendix, B.8, where the same distribution between the higher coflow temperature being ‘skewed’ to the right is observed. The increased probability for high coflow temperatures producing less heat release is more pronounced for pure DME. Furthermore, the ‘flattening’ of the PDF for lower coflow temperatures is further emphasised for the pure DME case. For high coflow temperatures, for reduced premixing, kernels don’t grow up to 6 mm, and as such, are not observed in the PDF’s.

The PDF makes it possible to identify how the increased velocity (U_J = 100 m/s) for air:DME = 3:1, T_C = 1400 K can have instances where a kernel has larger peak OH (Table 7-2) and heat release intensities (Fig. 7-14) than the T_C = 1275 K, U_J = 50 m/s case, while the overall average heat release is less given by Fig. 7-13. The smaller average heat release for increased velocity is due to an even greater left skew for T_C = 1400 K, with more occurrences of kernels having minimal heat release. The range in heat release for increased velocity may be due to increased turbulence producing both higher scalar dissipation and similar dissipative levels to the lower U_J = 50 m/s case, however, this requires further investigation.

7.3 Conclusion: DME OH/CH_2O PLIF experiment

This DME PLIF experiment presented results for the study of autoignition characteristics of DME using a jet in a hot vitiated coflow burner. Focusing on the kernel ignition events with high camera resolution to identify the heat release and growth of kernels before the merging to the flame base. A range of jet dilution and partial premixing ratios are studied for high (T_C = 1400 K) and low coflow (T_C = 1225 K-1275 K) temperatures corresponding to a low stable flame and a lifted flame respectively.

The following conclusions are drawn:

- The lift-off heights and hence regions of OH formation is further downstream when the coflow temperature is low. Formaldehyde forms upstream of OH, and significant levels occur upstream of the flame base for relatively low coflow temperatures. The pooling of CH_2O upstream of OH agrees with other studies with simpler fuels such as CH_4 [46] for the same hot vitiated coflow burner.
- By using high-speed imaging, kernel formation events could be identified, where kernels occur upstream of the main stabilisation zone at both low and high coflow temperatures. The kernels occur further downstream with increased axial range at lower coflow temperatures.
- The product of CH_2O x OH LIF signals was used as a heat release marker for DME where its use was validated from transient opposed flow simulations. Therefore, the spatial overlap between the OH and CH_2O LIF images was used as a surrogate for heat release in ignition kernels.

- Within a given autoignition kernel a large range of CH_2O signals was found, correlating with a multitude of OH levels. However, for increasing CH_2O levels, there was a broad correlation of increasing heat release, this correlation was found to be much stronger than that of OH and heat release.
- The amount of integrated heat release has a linear correlation with kernel size, which indicates the relative overlap and intensities of OH and CH_2O do not vary significantly during kernel evolution. That is heat release is predominantly produced on a single kernel edge and grows at a proportional rate to the kernel area.
- Lower coflow temperatures produced kernels with greater heat release relative to the high coflow temperatures. The OH and CH_2O signal levels vary slightly between high and low coflow temperatures, however, spatial overlap of CH_2O onto OH varies the greatest, with lower coflow temperatures having a larger overlap.
- The relatively small heat release for a high coflow temperature is seemingly correlated with the large aspect ratio of a kernel (axial elongation). If the aspect ratio is indicative to local mixture fraction gradients, the larger aspect ratio of kernels from hotter coflow temperatures means the kernels in regions of steeper mixture fraction gradients.

The novel heat release measurements obtained, at high-speed, for DME in the JHC burner, under autoignition conditions, identifies that kernels are more fundamental to the stabilisation of these flames at relatively low coflow temperatures. This assertion agrees with the high-speed chemiluminescence imaging whereby the flame base only propagates upstream when a new ignition kernel merges into the flame base.

The results presented in this chapter have explored kernel evolution and heat release exclusively for DME. The use of DME as a fuel in this study allows the sustained high-speed PLIF of CH_2O at relatively low laser energies (3.3 mJ/pulse) with high SNR.

The influence of, or lack thereof, NTC behaviour and the relative formation of species is analysed in the final discussion chapter. Furthermore, the varying heat release from high and low coflow temperatures is discussed in relation to laminar unsteady calculations.

Chapter 8. Laminar Calculations: Unsteady counter-flow and premixed reactor

This chapter studies the transient autoignition of CH_4 using a counter-flow and premixed unsteady solver. The setup and application of these solvers is discussed in relation to the conditions, strained and diffusive conditions, experienced in the hot coflow burner. Typically, homogeneous reactors are used to identify if these experimental JHC flames are dictated by simple autoignition delay time kinetics (explored in the next chapter). Homogeneous reactors can identify the relationship between: coflow temperature, delay times and low temperature chemistry build-up before ignition and thermal runaway. However, the homogeneous reactors neglect diffusional effects, which are large in hydrogen auto-igniting flames [47, 149] and less so in hydrocarbon flames. Furthermore, homogeneous simulations don't provide a sensitivity analysis of strain rate. They impose a mixture fraction prior to the reactor and hence don't allow a true determination of the ignition mixture fraction. This chapter, therefore, analyses the influence of both diffusion and strain rate effects on the most reactive mixture fraction, using unsteady premixed and counter-flow flames. The influence of diffusion and strain rate on delay times is in addition to determining if the transient counter-flow reactor can capture the sensitivity of lift-off height, found in the previous JHC experiments.

Typically, these numerical simulations solve steady state conditions to determine steady flame speeds and species concentrations. Therefore, flame propagation speeds cannot be obtained from the premixed reactor for temperatures exceeding the autoignition temperature. Furthermore, because no steady species balance exists, in this now transient process, no delay time can be determined from steady counter-flow flames. The unsteady solvers investigated

here, do not approximate steady state conditions and therefore time stepping occurs in real time (not pseudo time stepping). Previous studies have used unsteady solvers to look at autoignition [153, 154]. These studies, however, do not examine what promotes or suppresses ignition, such as an investigation on transport budgets for certain species. The studies don't investigate an analysis of species: convection, diffusion and reaction in the lead-up to ignition, hence this is also the focus of this chapter.

Finally, whilst homogeneous 0-D isobaric reactors indicate the dependence of delay times, to approximate the average experimental position of the flame (lift-off height), they don't identify the relative importance of ignition kernels. Such as, what caused the variation in kernel heat release as seen for the DME PLIF experiment for a change in coflow temperature. Whether, strain rate or the most reactive mixture fraction indicates why lower coflow temperature kernels produce higher heat release. Therefore, the effect of strain rate and coflow temperature on 'kernel heat release' will be investigated for DME counter-flow flames.

8.1 **Methodology**

Most steady state, counter-flow and premixed solvers are found in packages such as Chemkin [151] or Cantera [152]. The unsteady solver used in this chapter is Ember, a solver that is coupled onto Cantera. The solver and code was developed by Speth et al. [203, 204], it uses a rebalanced splitting scheme to march in time with high accuracy. Calculations are performed here for CH_4, using the Gri30 mechanism (similar to Gordon et al. [46]), with 53 species and 325 reactions [212], with multicomponent diffusion and the Soret effect.

The unsteady counter-flow and premixed simulations solve the governing equations (8.1) - (8.4): momentum, continuity, energy and species conservation. Certain assumptions have been made to simplify the equations, including: no body forces and the second coefficient of viscosity being zero (8.1), incompressibility is assumed and as such the pressure variation with time is zero, finally viscous work is assumed to be negligible (8.3). The divergence term is represented in each equation by ∇, applied in the stress tensor matrix (T), direction velocity component ($\boldsymbol{v}$), heat flux ($\boldsymbol{q}$) and mass diffusion flux (j), for the: momentum, continuity, heat flux and species equations respectively. The governing equations are 'closed' using the state equation of an ideal gas assumption (8.5).

$$\rho \frac{D\boldsymbol{v}}{Dt} = \nabla \cdot T \tag{8.1}$$

$$\frac{\partial \rho}{\partial t} + \nabla \cdot (\rho \boldsymbol{v}) = \tag{8.2}$$

$$\rho \frac{Dh}{Dt} = -\nabla \cdot \boldsymbol{q} \tag{8.3}$$

$$\rho \frac{DY_k}{Dt} = -\nabla \cdot j_k + \dot{\omega}_k W_k \tag{8.4}$$

$$pV = nRT \tag{8.5}$$

A large focus of this chapter is the investigation of: the convective, diffusive and production balance of CH_2O, given by the species conservation equation (8.4). The species conservation equation can be divided into three parts: the convective ($\rho \frac{DY_k}{Dt}$), diffusion ($-\nabla \cdot j_k$) and production component ($\dot{\omega}_k W_k$). The convective term is driven by the domain

velocity, that is, physical movement of species into that node within the computational domain. Species diffusion, j_k, is determined by local species concentration gradients. Finally, species are either added to the species balance by consumption or production, $\dot{\omega}_k$, where k is the species of interest, given by CH_2O in this study. The analysis largely focuses on the transient evolution of CH_2O which is recognized as the key species that populates the species pool leading to ignition.

8.2 **Vitiated coflow burner**

To best replicate conditions promoted by the JHC, counter-flow and premixed configurations are applied. The reactors identify that ignition kernels are subjected to both: premixed flame propagation (as the kernel grows) and to varying degrees of strain and diffusion between the coflow shear and jets, due to varying degrees of turbulence. Furthermore, it has been proposed that ignition kernels are premixed pockets burning at the centre of vortices with low strain/scalar dissipation [130]. It is, however, identified that for higher coflow temperatures ignition kernels are seemingly forming in the shear layer between the jet and coflow (observed in Fig. 6-5), where the kernels remain partially premixed. That is, the kernels in the shear layer may have significant diffusion from the coflow, and these conditions are better represented by an opposed flow setup. Therefore, it is proposed here that early stage kernel initiation is represented by the counter-flow simulations and kernel growth is replicated by premixed free flame propagation.

Results from the unsteady simulations are cross-referenced with previous autoignition hot vitiated coflow burner (JHC) experimental results for CH_4 given in Fig. 4-2. The JHC flames were identified to be stabilised by autoignition since new autoignition kernel events are

feeding into the constantly advecting flame base. Therefore, the numerical results obtained from this study are aimed to replicate the sensitivity of lift-off heights (using ignition delay times) with coflow temperature. As such, the domain temperatures for the simulations are selected to represent those obtained experimentally, for CH_4, issuing into the JHC (Fig. 4-2).

8.3 **Opposed flow setup**

The equilibrated products from a H_2/air mixture at the required equivalence ratio, to achieve a specific temperature (like the JHC experiment), are used as the oxidant in the opposed flow simulation. These products at three temperatures are opposed against different CH_4-air mixtures, the stoichiometric mixture fraction (ξ_{st}) and temperatures are listed in Table 1 for the different CH_4-air ratios studied. Varying coflow temperatures alters the O_2 and H_2O mole fractions (Fig. 3-4) and hence slightly alters the stoichiometric mixture fraction. A step profile in the domain, from H_2/air coflow products at the equilibrated temperature to the fuel at 300 K was used for the initial conditions, where no ignition source is required. Relatively low (T_C = 1300 K) and high (T_C = 1500 K) coflow temperatures are listed in Table 8-1 with an additional medium temperature (T_C = 1400 K), used for the counter flow study. The chosen temperatures are slightly lower than those given in the JHC experiment, for methane, since they gave similar sensitives to delay times compared to the experiment (lift-off heights). The coflow temperatures in the numerical counter-flow setup are potentially lower to match the experiment since the experiment experiences thermal loses and as such adiabatic temperatures are not experienced.

Table 8-1 Inlet boundary conditions for the counter flow parametric study with stoichiometric mixture fractions for different air premixing ratios (CH_4:air).

High temp (K)	Med temp (K)	Low temp (K)	ξ_{st}@0:1	ξ_{st}@1:1	ξ_{st}@2:1
1500	1400	1300	0.059	0.1	0.14

The temperatures selected for the heated opposed flows are chosen to be comparative to the hot coflow experimental measurements, while the strain rates were varied from $a = 2s^{-1}$ to extinction. Ignition was defined by a temporal evolution of temperature (dT/dt) threshold such that once this threshold was exceeded, the time step was classified as ignition. For this chosen time step the most reactive mixture fraction was then defined by the peak temperature within the reactor domain. The discretised domain has a species flux balance as defined by Eq. (8.4); the peak production value within the domain at given time step is used for the species balance analysis. The equivalent convection and diffusive fluxes for this given peak production flux are used to calculate flux ratios, seen in the following section.

8.4 **Premixed flame setup**

Temperatures exceeding autoignition can be used for the Ember solver, since no steady state boundary conditions are applied. An inflow of unburnt products is ‘fed’ into the premixed reactor domain, the velocity is increased until the flame front remains fixed spatially, that is, when the inflow velocity matches the propagation speed. On the contrary to the counter-flow simulation, a defined mixture is required as the initial conditions prior to ignition, this was chosen based on the most reactive mixture fraction from the counter flow simulation of φ = 0.4. This equivalence ratio (φ = 0.4) was fixed across all premixed ratios and coflow

temperatures, this is despite the most reactive mixture fraction varying slightly for different coflow temperatures and premixing ratios. A range of equivalence ratios, φ = 0.4 – 1, was also used for fixed premixed temperatures, to analyse the relationship of premixed and autoignition temperatures with the flame propagation speed.

8.5 Numerical results

8.5.1 Opposed flow simulation

Results from the opposed flow solver are given here, describing a single CH_4 case, including the temporal evolution of temperature, reactive mixture fraction, CH_2O mole fraction and CH_2O species flux. The following sections describe the effects of varying strain rates for the three temperatures studied, and for three premixing cases with air. The final section describes the variation in delay times using the CH_2O production budgets.

8.5.2 Evolution of a CH_4 counter flow-jet: a = 160 s^{-1}, T_C = 1300 K

A single counter-flow simulation, with a strain rate a = 160 s^{-1} is presented in Fig. 8-1. It presents a pure CH_4 jet opposed against the products of H_2/air at a temperature of T_C = 1300 K. Six plots (a - f) are shown and ordered as follows: the top plot indicates the temporal evolution of temperature (a), followed by the mole fraction (b) of CH_2O and then its corresponding transport budgets/fluxes for: convection (c), production (d) and diffusion (e). The final plot presents the mixture fraction (f), equivalent to the maximum temperature within the domain for a given time step. All variables are plotted in correlation to the distance within the reactor domain, the left side describes the fuel inlet, whilst the right is the oxidant

(coflow) inlet. The five different symbols indicate different time steps for the solution, extending from pre-ignition (45.9 ms), ignition (46.45 ms) and steady state (49.8 ms).

It is evident from the top plot that temperature slowly evolves, until ~ 45.9 ms, a rapid rise in temperature occurs at 46.45 ms (indicated by the dashed arrows), this is defined as autoignition for this coflow temperature and strain rate. The peak temperature at autoignition leads to a most reactive mixture fraction of ξ = 0.03 (ξ_{st} = 0.059) given in Fig. 8-1 (f), it indicates the mixture is igniting at a very lean composition of ~ φ = 0.5. In the next section, it is seen that varying coflow temperatures and strain rates alter the delay time and ignition mixture fraction.

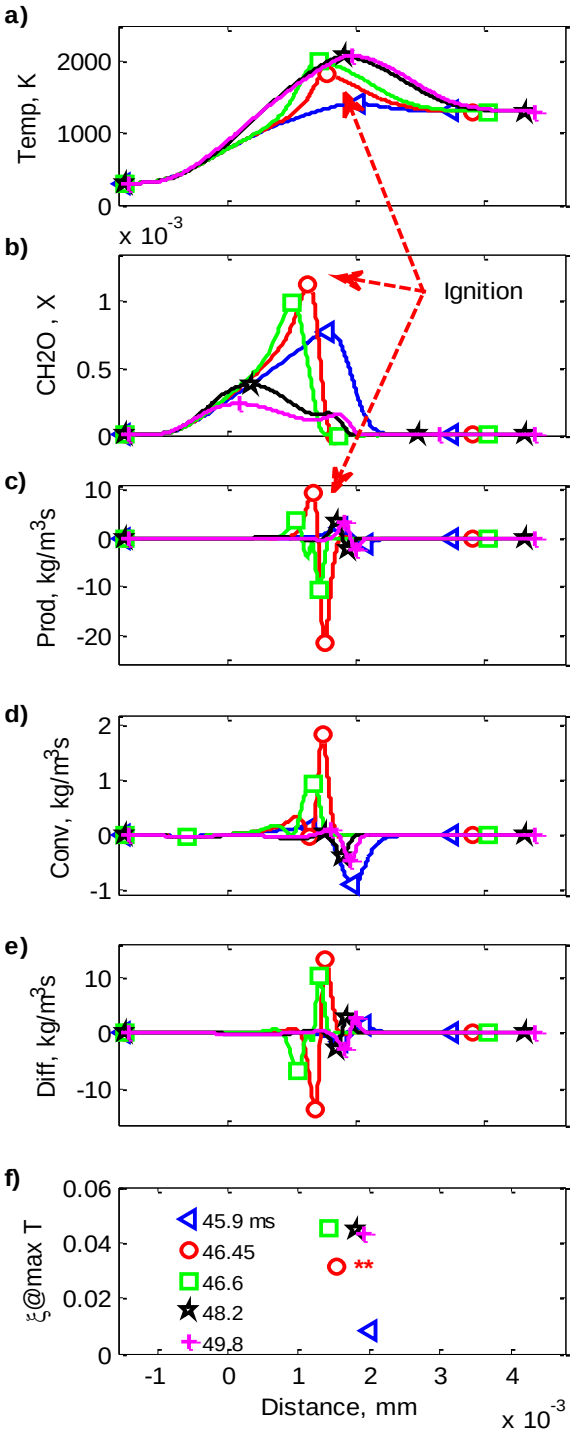

Fig. 8-1 Temporal evolution results of: temperature (a), CH_2O mole fraction (b), transport budgets (c-d) and mixture fraction (ζ, f) for a single counter flow simulation of a pure CH_4 fuel jet with strain rate a = 160 s^{-1} opposed against a T_C = 1300 K coflow. Five different time step contours (from pre-ignition to steady state) are indicated by symbols, ignition is given at τ = 46.45 ms (**), indicated by the dashed arrows for: temperature, CH_2O and the production flux.

The next four plots, after temperature in Fig. 8-1, describe the evolution of the mole fraction, CH_2O (b), and its flux budgets for: production (c), convection (d) and diffusion (e). The build-up prior to autoignition (time step, 45.9 ms) is evident from the increasing mole fraction of CH_2O in cool regions less than 800 K. This lower temperature also corresponds to a richer mixture, where the spatial peak for CH_2O in the domain doesn't match the peak in temperature (given by the dashed arrow). The peak in CH_2O closely corresponds temporally to autoignition at τ = 46.45 ms, where soon after this time (46.6 ms) the peak value drops and other high-temperature species such as OH begin to rise in concentration (not shown here).

The balance of the CH_2O fluxes in the lead up to ignition (45.9 ms) indicates a positive production being balanced by the removal of species, through diffusion and convection. The CH_2O fluxes, like the species mole fraction, peaks near ignition (τ = 46.45 ms). The peak in the production flux is given by the dashed arrow at ignition (Fig. 8-1), the fluxes decrease as steady state is approached (48.2 - 49.8 ms). Furthermore, as steady state is approached, positive production is balanced almost entirely by the diffusion out of CH_2O. The peak productive fluxes for different time steps are summarised in the following sections, for variations in strain rates.

The ignition mixture fraction in Fig. 8-1 (f) corresponds to the maximum temperature at a given time step, with ignition occurring at ξ = 0.03. The plot further highlights how the ignition mixture evolves as the reactor approaches steady state (45.9 - 48.2 ms). That is, autoignition occurs in very lean mixtures and as steady state is approached the mixture becomes richer, burning with an increasing diffusive/production balance, seen in the next section. Following a slightly richer mixture just prior to ignition at 46.6 ms, the peak temperature at steady state (48.2 ms) corresponds closely to the stoichiometric mixture fraction of ξ_{st} = 0.059.

8.5.3 **Strain dependence of CH_4 for: delay times and most reactive mixture fractions**

Fig. 8-1 shows the variations of ignition delay times (a) and the most reactive fraction (ξ_{mr}, b) presented versus strain rate. Calculations are reported for three fuel compositions being: pure CH_4, air:CH_4 = 1:1 (by volume) and air:CH_4 = 2:1 (by vol.) for three opposed flow temperatures each: T_C = 1300 K, 1400 K, and 1500 K.

It can be seen for higher coflow temperatures (triangles) the mixture ignites faster for all equivalent strain rates, with increased resistance to strain/ scalar dissipation. That is, for pure CH_4 opposed against a T_C = 1500 K coflow the extinction strain rate is a = 1500 s^{-1}, whilst for T_C = 1300 K, the extinction strain rate is a = 160 s^{-1}. This leads to the assumption that within the coflow experiment, under turbulent autoignition conditions, the higher coflow temperature has a lower lift-off height due to a lower delay time but additionally from increased resistance to scalar dissipation. That is, ignition for low lifted flames (high coflow temperatures) may be occurring in upstream locations, where the velocity field is greater. This sensitivity of ignition delay times to strain rate agrees with DNS studies, which identify autoignition events are occurring at lean mixtures, with low scalar dissipations [47]. The same phenomenon of increased coflow temperatures being more resistant to strain is found for H_2 and propane given in the appendix (C.1.and C.2), and further found for DME, given in the follow Chapter.

It is further observed in Fig. 8-2 that for increased coflow temperatures, T_C = 1500 K, the mixture ignites leaner, leaner than T_C = 1300 K, for all common strain rates. Furthermore, for higher coflow temperatures, T_C >1400 K, larger strain rates force the mixture to ignite in richer mixtures. This is also observed for a steady state counter-flow solver with a methane

jet (2:1) opposed against a T_C = 1500 K coflow (H_2/air), given in the appendix, C.3. It identifies that for a coflow temperature, T_C = 1500 K, the mixture has a peak in temperature for a richer mixture. The mixture fraction for a peak in temperature also gets richer as the strain rate is increased, which was observed for Fig. 8-2.

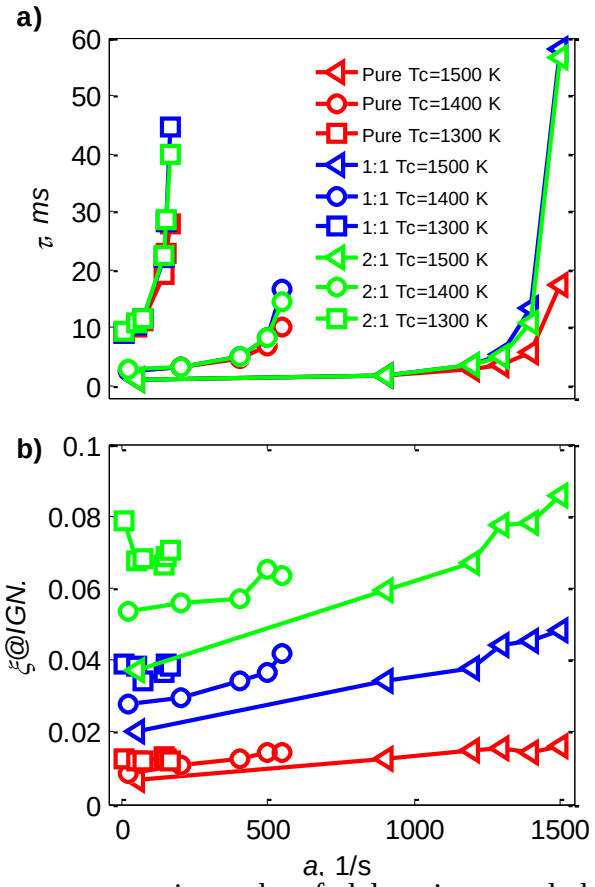

Fig. 8-2 Results from a parametric study of delay times and the most reactive mixture fractions (ξ_{st}@IGN.) for variations in strain rates and coflow temperatures for CH_4 at three premixed ratios with air. The maximum strain rates and corresponding ξ_{st}@IGN for each premixing and coflow tempreature indicate the extinction strain rate.

The plots in Fig. 8-2 also show that for increased premixing, from pure CH_4 to one (1:1) and two parts air (2:1), increases the delay time for an equivalent strain rate (less sensitive between 1:1 and 2:1). This increased delay time with additional air premixing agrees with previous experimental results Fig. 4-2, where premixing with air increased the

lift-off height. Furthermore, increased premixing reduces the mixtures resistance to strain rate, i.e., for T_C = 1400 K at a = 1500 s^{-1} the delay time for 1:1 premixing is τ = 60 ms, whilst for pure CH_4 it is τ = 19 ms.

The effect of premixing is further seen in Fig. 8-3 b which plots the most reactive equivalence ratio (φ_{mr}) over a range of counter flow temperatures for four fuel mixtures. The mixture includes: pure CH_4, air:CH_4 = 1:1 (by vol.) air:CH_4 = 2:1 (by vol.), and air:CH_4 = 3:1 (by vol.). The ignition delay times for the same conditions were performed at a constant and low strain rate of a = 2 s^{-1}. The most reactive mixture fraction for which ignition occurs was converted to an equivalence ratio; it was found that increased premixing leads to richer ignition mixtures, whilst still leaner than stoichiometry. This increase in equivalence ratio for increased premixing implies that the reactivity and ignition of a CH_4 mixture is driven by the fuel content.

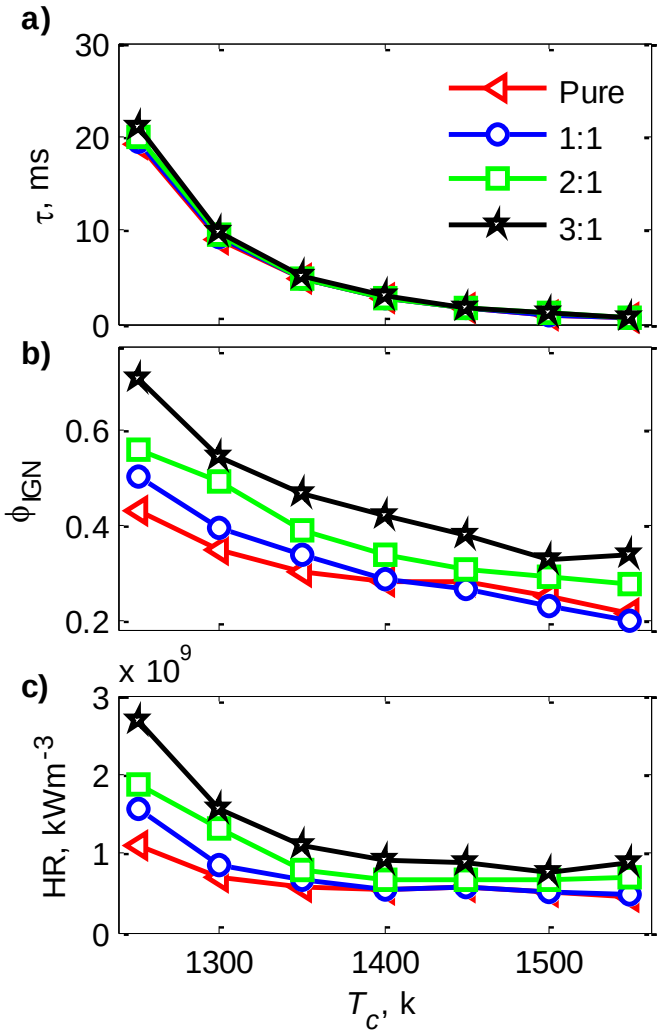

Fig. 8-3 Counter flow results for: delay times (a) for a fixed low strain rate, a = 2 s^{-1}, the most reactive ignition equivalence ratios (b) and heat release (c) for four premixing ratios of CH_4 and air for a range of coflow temperatures (T_C).

Finally, increased temperature is leading to leaner ignition mixtures, implying hotter coflow temperatures increase the fuels reactivity and hence increasing the flammability limit. Whilst ignition is faster and leaner for hotter coflow temperatures the heat released is smaller seen in Fig. 8-3c. This decrease in the ignition equivalence ratio is also observed for propane (C.1) and DME (following chapter). However, the mixture fraction remains somewhat

unchanged for hydrogen as the coflow temperature is increased, this is believed to be due to the highly diffusive nature of H_2 and the H radical (appendix C.2).

From Fig. 8-3, the heat release varies almost linearly with the ignition most reactive mixture fraction (not plotted here). This indicates ignition kernels from the coflow experiment, for higher coflow temperatures, form further upstream in leaner mixtures. However, the kernels are 'weaker' with less heat feeding into the flame base. This agrees with heat release results for a DME jet (Fig. 7-13), where hotter coflow temperatures produce ignition kernels with lower heat release (CH_2O x OH), this is discussed specifically for DME in the next chapter. Despite increased premixing leading to richer ignition mixtures, the delay time is longer (small difference for this low strain rate). In these simulations and in the hot coflow burner experiment, leaner mixtures require increased mixing or diffusion of the fuel stream into the oxidant (coflow).

8.5.4 **Transport budgets: Pure CH_4 jet, T_C = 1300 K**

Fig. 8-4 shows the transport budgets for CH_2O for the maximum production flux and the corresponding convection and diffusion flux computed for a single strain rate a = 160 s^{-1} given in Fig. 8-1. Four time steps were presented in Fig. 8-1, for the enitre domain, where Fig. 8-4 presents all maximum production fluxes leading to ignition and steady state. Results are plotted versus time, where time 0 ms correponds to the first simulation time step and 46.45 ms, indicated by the dashed lines, corresponds to the ignition delay time as seen in Fig. 8-1.

The first plot in Fig. 8-4 shows the maximum production flux ($Prod_{MAX}$)., the maximum production flux at ignition is approximatly 9 kg/m^3s, also given by the dashed

arrow in Fig. 8-1 (c). This maximum ignition flux corresponds to the value indicated by the horizontal dashed line in Fig. 8-4 ($Prod_{MAX}$). The corresponding diffusive ($Diff@Reac_{MAX}$) and convection fluxes ($Conv@Reac_{MAX}$) at this maximum production flux are seen in Fig. 8-4 (dashed lines), given as: -8 kg/m^{3}s and -0.7 kg/m^{3}s respectively (also seen in Fig. 8-1). The ratio between the maximum production flux and the corresponding convective/ diffusive fluxes are given in column two, from the values given in column one. Positive production or species creation by forward reactions is balanced by removal of species through negative diffusion and convection. The contrary is also true, that is, the consumption of species is balanced by positive diffusion and convection.

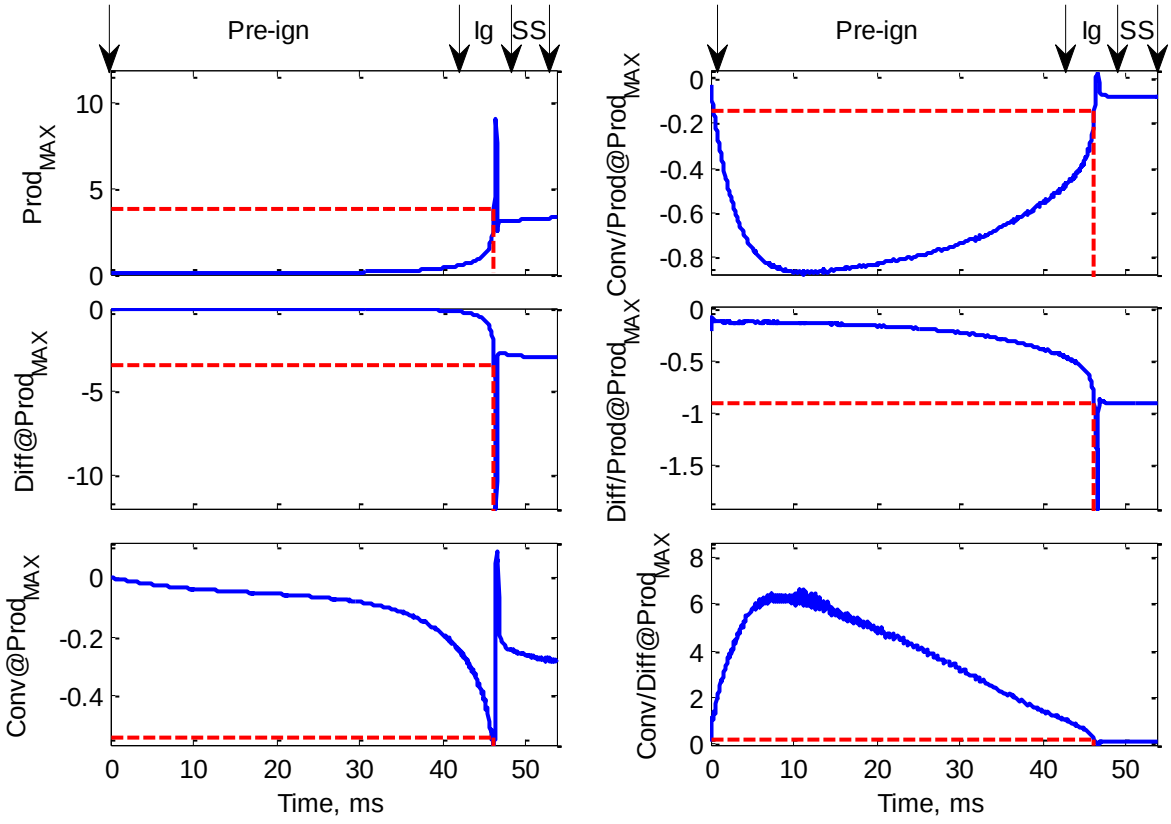

Fig. 8-4 Results for the maximum production flux of CH_2O and the equivalent diffusion and convective flux (left-hand-side, LHS) at a single strain rate, a = 160 s^{-1}, for pure CH_4 opposed against a coflow temperature T_C = 1300 K. Ratios between the production, diffusion and

convection flux are given for the corresponding maximum production flux within the reactor domain (right-hand-side, RHS). The dashed lines indicate the ignition values and a corresponding delay time. Arrows mark the intervals for the lead up to ignition (pre-ign), ignition (Ig) and steady state (SS).

The ignition delay time is indicated by the red vertical dashed line in each respective plot in Fig. 8-4, so the time steps leading up to ignition identifies the flux balance leading to ignition (interval marked Pre-ign). The times steps after ignition indicate the balance leading to steady state (interval marked SS). By analysing the left column in Fig. 8-4, it can now be identified that in the lead up to ignition, diffusion and production are near zero, whilst the convection flux is non-zero. A peak in fluxes for the: production (positive), diffusive and convective fluxes (both negative) all occur temporally close to autoignition. The non-zero convective flux in the lead up to autoignition can be seen to be responsible for delaying the process. That is, the negative convective flux removes CH_2O from the reactive pool leading to species production and chain brancing, limiting thermal run away and hence ignition.

The ratio between: convective, species production and diffusive flux corresponding to the domains peak production flux is seen in Fig. 8-4 (right column). It identifies the charecteristic balance of CH_2O in the lead up to: ignition (Pre-ign) and steady state (SS). In the lead up to ignition, convection dominates diffusion (Conv/Diff@$Prod_{MAX}$), since the ratio is greater than unity, hence species production is being balanced by convection. Not until the ratio between convection and diffusion is approximately zero, does ignition occur; this identifies that a strong correlation between convection and diffusion is dictating the ignition delay. Correspondingly as the convection/diffusive flux balance approaches zero the flame is balanced sololy by a unity ratio of production/diffusion, with the convection/production ratio also balancing near zero at steady state.

A comparison of the ratio between convection and diffusion is presented for two additional strain rates: a = 10 s^{-1} and 100s^{-1}, in Fig. 8-5. It can be seen that for all strain rates the same phenomenon occurs, where ignition doesn't occur until the balance of convection to diffusion is zero, or the diffusion to production ratio approaches unity (given in the appendix, C.4). However, for increased strain rate, a = 160 s^{-1}, the convective/ diffusive balance is larger, noting this strain rate is close to extinction for this coflow temperature. The convective diffusive balace for a higher temperature, T_C= 1500 K, is given in the appendix, C.5. It is observed that whilst the maximum peak value in the ratio, between convection to diffusion (Conv/Diff@$Reac_{MAX}$), is different between increased strain rates, the temporal location of the peak is very similar occuring at ~8 ms for all strained cases. The delay times, however, are significantly different between the strain rates, given by the flux ratio approaching zero for eeach case. That is the ignition delay times are: τ = 10 ms, 13 ms and 46 ms for strain rates of a = 10 s^{-1}, 100 s^{-1} and 160 s^{-1} respectively.

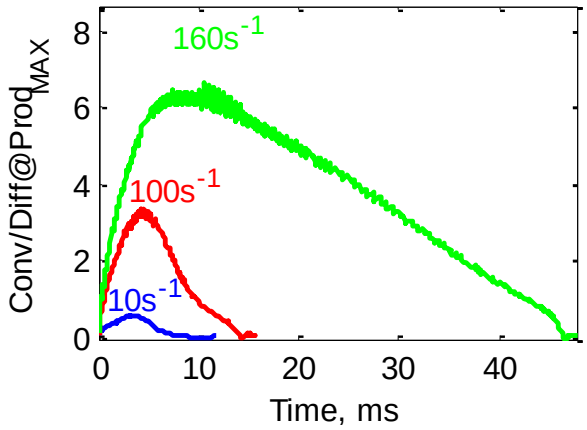

Fig. 8-5 Counter-flow results for a pure CH_4 jet opposed against a T_C = 1300 K coflow for the convection/diffusion ratio at the maximum production flux within the domain, for three strain rates: a = 10s^{-1}, 100s^{-1} and 160 s^{-1}.

The lead up to ignition being dominated by convection over diffusion is consistent with work from Gordon et al. [135], where convection and production was dominant at autoignition conditions. The peak flux magnitude and temporal flux evolution vary for different coflow temperatures and premixing ratios for CH_4, given in the appendix, C.5. The flux balance varies in accordance to their respective delay times (Fig. 8-2), however, the flux balance charecterisitcs are similar to those in Fig. 8-4.

8.6 Varied unburnt temperatures for CH_4 freely propagting flames

Flame propagation velocities (a) and the ratios of transport budgets (b): production/diffusive, convective/diffusive and convective/reactive (bottom) are presented in Fig. 8-6 versus domain temperature (T_C). The results are presented for a range of coflow temperatures for four fuel mixtures: pure CH_4, air:CH_4 = 1:1 (by vol.), air:CH_4 = 2:1 (by vol.) and air:CH_4 = 3:1 (by vol.). It is emphasised again that the propagation velocity is not calculated by the typical steady state Eigenvalue solution. The mixture propagation velocity (denoted here as V_L) is calculated by increasing the speed of the unburnt mixture 'fed' into the domain until the burnt mixture can no longer propagate into it. This is different from the steady burning velocity, S_L, which is normally characterized by the production/ diffusive balance, although at steady state conditions and within the relevant mixture fraction range V_L and S_L converge.

The calculations in Fig. 8-6 are performed for an equivalence ratio of φ = 0.4. Therefore, the premixed flame propagation velocities computed here correspond to a premixed ignition kernel that has ignited near the most reactive mixture fraction, continuing to burn to steady state conditions. At that steady state condition, a balance is established

either between diffusion and production or between convection and production, whether the flame is stabilised by premixed or autoignition stabilisation respectively.

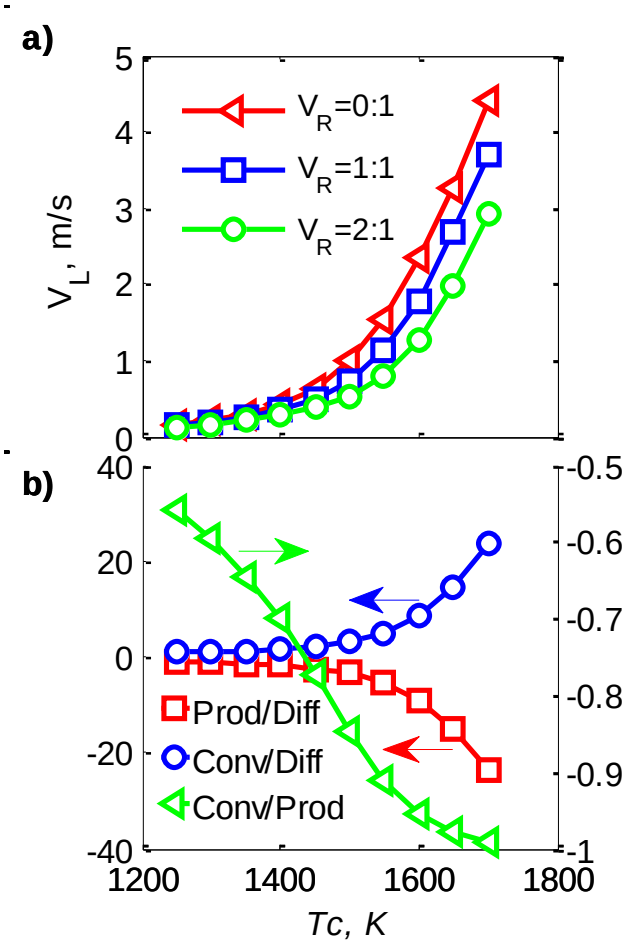

Fig. 8-6 Propagating velocities (V_L) for three premixing cases with varying coflow temperatures (T_C) for a fixed stoichiometric ratio, φ = 0.4 (a). Diffusive ratios correspond to the left axis: Convection/diffusion (circles) and production/diffusion (squares). Convection balance (triangles), convection/production, corresponds to the right axis (b).

The coflow temperature range presented is similar to those from the lift-off heights with coflow temperature, from the JHC experiment Fig. 4-2, additional temperatures of T_C = 1250 K up to T_C =1700 K are also given. It can be seen there is a strong sensitivity to coflow

temperature within this range, for T_C = 1250 K the flame velocity is V_L = 15 cm/s and for T_C = 1700 K the velocity is V_L = 450 cm/s, both velocities correspond to a pure CH_4 jet. It is further seen that for increased premixing, the flame speed is slower for the same given temperature, i.e., for T_C = 1600 K, with pure CH_4, the propagation speed is V_L = 220 cm/s, whilst for 2:1 air premixing V_L = 100 cm/s. Ignition indeed occurs at richer mixtures seen in Fig. 8-3 for increased premixing, from φ = 0.4 to φ = 0.5, however, this has negliable effect on the propagtion velocity, seen below in Fig. 8-7. This increase in flame velocity and reduction in ignition delay time for reduced premixing further indicates why reduced premixing leads to lower lift-off heights from the JHC experiment (Fig. 4-2).

Similar to the balance of fluxes from Fig. 8-4 the ratio of the maximum convection/diffusivion, production/diffusion and convection/production flux ratios are given in Fig. 8-6. The flux balance indicates that for lower temperatures (T_C = 1200 K - 1400 K) the diffusion of CH_2O is non-negliable, it is larger than than the convective term, with a convective/diffusive ratio close to zero. Furthermore, the species flux balance up to ~ T_C = 1400 K is that of a conventional premixed flame propagation, the production within the flame is a balance by species diffusion. This production diffusive balance is dictating both the flame width and flame speed (the eigenvalue solutions for a steady state solver).

As the temperature is increased, the balance between convection and diffusion shifts, where convection becomes ~18 times greater than diffusion at T_C = 1700 K. The converse is also true between the convection/production flux at lower temperatures, diffusion is prevalent and production is relatively small (half the convection flux). However, at higher temperatures the balance between production and convection is close to unity and hence species production is balanced solely by convection. This balance between convection and production for high-

temperatures agrees with DNS studies, where this unity ratio (unity Damköhler number) occurs as autoignition is dominant [128]

To potentially identify where auto ignition becomes dominant in these premixed flames, the intersection point near T_C = 1580 K is highlighted (Fig. 8-6 b). This intersection describes the point where diffusion becomes minimal (the convection/diffusion gradient becomes large) and the flame has transitioned to an autoignition, production/convection balance. Furthermore, this intersection identifies the temperature for which the production/diffusion ratio divergence from a unity balance. For comparison, a mixture between heated air and fuel was performed and the same flux ratios and balances occur at higher temperatures (not displayed here).

It is again noted that for added premixing, ignition is forming in richer mixtures seen in Fig. 8-2, ignition occurs at φ = 0.4 for pure CH_4 and at φ = 0.5 for 2:1 premixing of CH_4 with air. Therefore, propagtion velocities for varying equivalence ratios for three coflow temperatures is presented in Fig. 8-7. An interesting phenomenon is observed between the three coflow temperatures for all premixing cases, at a relatively low-temperature where production is balanced by diffusion (Fig. 8-6) the flame velocities vary in a conventional manner. That is, for these relatively low temperatures, lean mixtures have a low velocity (approxiamtely half the peak velocity) with increasing velocities for increasing stoichiometry, with a peak in flame propagation velocity at φ = 0.9-1. For a medium unburnt temperature, T_C = 1400 K, there is a small variation between flame velocities for a variation in the mixture equivalence ratio. Finally at a high-temperature, T_C = 1600 K, the flame velocity decreases rapidly with increasing equivalence ratio. The decrease in flame velocity for increased equivalence ratio at higher temperatures agrees with kinetic autoignition delay times, where leaner mixtures correspond to fastest delay times.

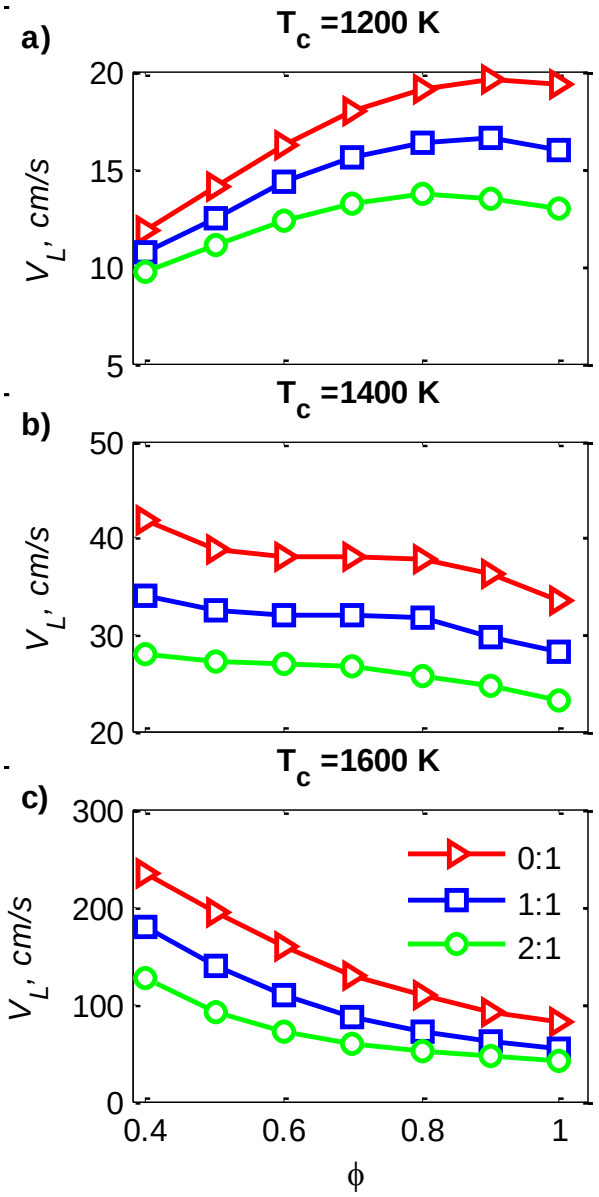

Fig. 8-7 Flame velocity dependence for three coflow temperatures (T_C = 1200 K, 1400 K and 1600 K) for a range of equivalence ratios (φ = 0.4 -1) at three premixing ratios.

8.7 **Conclusion, unsteady calculations**

The implementation of unsteady solvers to investigate turbulent auto-igniting flames was verified using CH_4, creating transient autoignition under strained conditions. The numerical solvers included both the counter-flow and premixed reactors, to capture the effect of coflow temperature on transient auto ignition. It was found that for the counter-flow solver, that increased coflow temperatures decreased delay times and increased the resistance to strain, where ignition occurred as the convective/diffusive balance of CH_2O approached zero. The counter-flow reactor was able to capture similar sensitivities of reduced delay time for increased coflow temperature, like the experimental results of lift-off height. The premixed solver was further able to identify that at lower coflow temperatures premixed flame propagation is more prevalent, and as coflow temperatures are increased autoignition dominants the CH_2O species balance.

The mixture fraction gradients imposed by the counter-flow solver are used to identify compositional space for which ignition occurs, with ignition occurring in lean compositional space for higher coflow temperatures. The leaner ignition mixtures for increased coflow temperature help to explain why the kernels produced in the JHC experiment, in the previous chapter, had reduced heat release for increased coflow temperature. The temporal evolution of species in compositional space is used, in the following chapter, to replicate the hot coflow burner conditions required for ignition in relation to the DME kernel heat release/ PLIF experiment.

Chapter 9. **Discussion**

This chapter discusses the experimental results from the hot coflow burner, comparing the findings between the two major experiments: the chemiluminescence study for all fuels and the OH/CH_2O PLIF study, both done at high-speed, in a temporally resolved manner at 10 kHz. The results of these studies are further discussed in relation to laminar 0-D isobaric calculations and unsteady counter-flow numerical results.

Testing a range of fuels verified the similar dependence of autoignition kernels being fundamental to 'supporting' and feeding the main flame base, for all fuels studied. The autoignition PDF of ignition kernels nearly overlapped the axial location of the lift-off height PDF. Since autoignition kernels match the axial location of the lift-off heights closely, a transient study can be implemented to verify if these flames are characterised by ignition delay times. Therefore, delay times are discussed, in this section, to determine if simple autoignition kinetics can capture the sensitivity of different fuels with coflow temperature.

Imagining of chemiluminescence, parametric study identified the more 'global' effect of kernels stabilising the flame base. While the DME heat release measurements indicated the energy/ heat release of kernels, impacting the flames stability for different coflow temperatures. Therefore, unsteady flames, using DME, are explored here to indicate if the heat release measurements, with less heat release occurring for higher coflow temperatures, can be determined. As such, the unsteady reactors are tailored to identify conditions for which ignition occurs with respect to strain and compositional/mixture fraction space.

9.1 Ignition delay times: 0-D homogenous reactor

Ignition delay times are a simple (computationally inexpensive) and effective way to identify conditions for which the experimental coflow temperatures may operate within. Furthermore, if the ignition delay times strongly represent the experimental lift-off height sensitivity with coflow temperature, it is an excellent indication that the flames are driven by kinetic stabilisation, opposed to free flame propagation. There were multiple fuels used in the previous chemiluminescence study, given previously in Table 3-1. Each fuel has its own chemical mechanism to describe the: thermodynamic properties, reaction rates and transport properties. The mechanisms include: GRI-30 (CH_4), San Diego (C_3H_8), AramcoMech 1.3 [70] (C_2H_4), AramcoMech 2 [213] (C_4H_8), AramcoMech 1.3 (C_2H_6) and Burke [73] (DME).

9.1.1 Reactor conditions

The 0-D isobaric homogenous reactor used here is from Cantera. The initial conditions used the products and temperature from the H_2/air coflow, at equilibrium, with the fuel jet (containing pure or mixed fuel with air). As seen in the Burner setup and flow conditions chapter, Fig. 3-4, the residual oxygen levels are less than 15% for all coflow temperatures, where increased temperature and equivalence ratio further decreases the O_2 concentration. As such a small comparison between a heated air coflow, a H_2/air coflow and for reference a CH_4/air coflow is given in Fig. 9-1. The heated air coflow, comparable to Markides et al. [123], has the shortest delay time, whilst H_2/air and CH_4/air are similar. This similarity is despite the addition of CO_2 in the CH_4/air coflow; the similarity can be attributed to the temperature and the O_2 and H_2O equilibrated products being similar, this is seen by

comparing the O_2 concentrations found in Fig. 3-4 for a H_2 coflow to those of the CH_4 coflow in Appendix D.1.

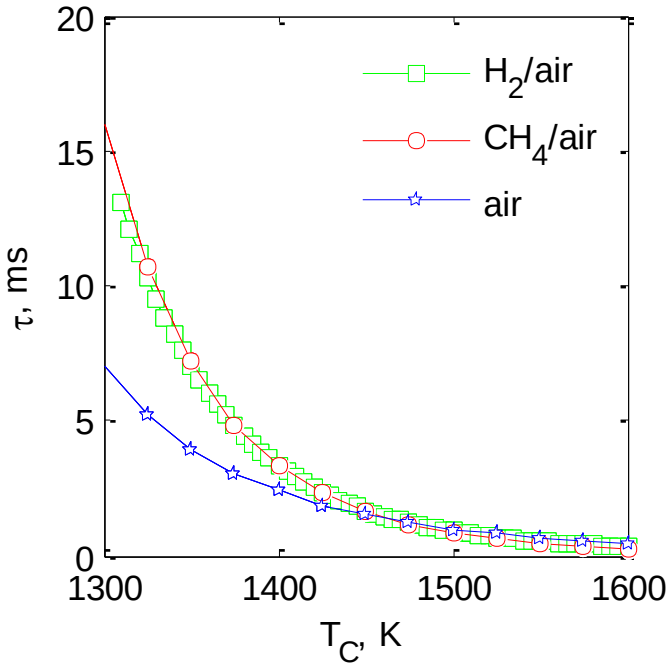

Fig. 9-1 Delay times for a H_2/air, CH_4/air and preheated air coflow for a CH_4 pure fuel jet.

The effect of O_2 concentration in the coflow is seen Fig. 9-2. The air coflow with 21% oxygen has the faster ignition delay times, with a decrease in O_2 levels having a near linear increase in the delay times, similar to the findings for MILD combustion from Medwell et al. [145, 214]. The reduced O_2 levels in the coflow increases the delay times, however, it also increases the residual OH radical (~200 ppm) which slightly reduces the delay time, given in the appendix D.2. It is mentioned that the reduction in O_2 levels increases the delay times more than the OH radical decreases them.

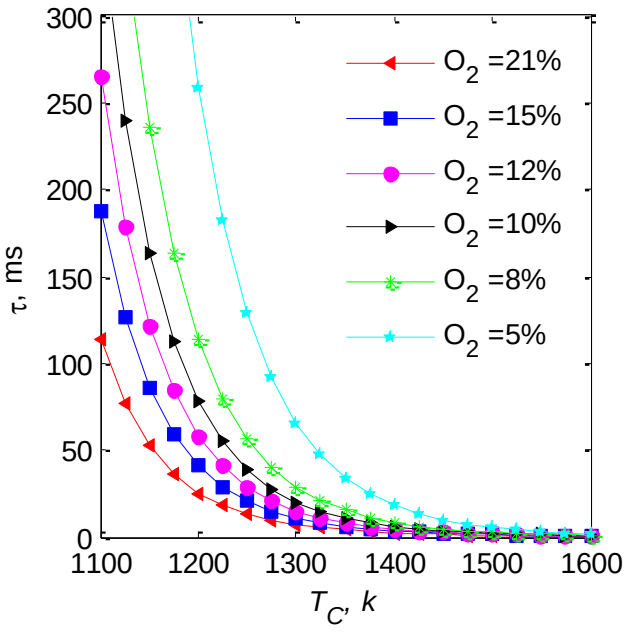

Fig. 9-2 Ignition delay times for a preheated air coflow with reduced O_2 concentration for a pure CH_4 fuel.

The coflow study above indicates that there is a strong sensitivity of the coflow to O_2 concentration, however, for the entirety of the experiments a H_2/air coflow was implemented. As such for all following laminar delay times calculations the products from a H_2/air equilibrium solver, and the residual temperature, is used as the initial conditions. The temperature presented in each of the following Figures is the coflow temperature not the mixture temperature of cold (298 K) fuel and the hot H_2/air products. The initial coflow temperature for the reactor was chosen based on the experimental coflow temperature (auto ignition temperature), that is the temperature that gave the highest lift-off height (Fig. 4-2) that remained within the 'valid cone' ($L_H < 60\ x/D$) given in Table 9-1.

Table 9-1 Experimental autoignition temperatures of fuels.

Fuel	Autoignition temperature (K)
H_2	1040
C_2H_4	1090
C_2H_6	1140
C_4H_8-1	1190
C_3H_8	1220
DME	1250
C_3H_6	1280
CH_4	1410

Since the mixture fraction at which ignition occurs is not confirmed and potentially varies due to different strain rates and local temperatures, seen in the previous counter-flow section the choice for the mixture fraction used for the 0-D reactor is difficult to ascertain. As such, a sensitivity study based on mixture fraction/equivalence ratio for the reactor is given in Fig. 9-3. All fuels have a minimum delay time for a very lean mixture of approximately φ = 0.2, however, the rich mixture sensitivities of the fuels are vastly different. For H_2, the delay time is very sensitive to the initial mixture, a mixture richer than ~φ = 0.2, has a steep rise in delay time, and a mixture near stoichiometry has a delay time exceeding 1 second (not displayed). For C_4H_8-1, the delay time is less sensitive to the reactor mixture, such that, an equivalence ratio of 2 still has a delay time less than τ = 30 ms.

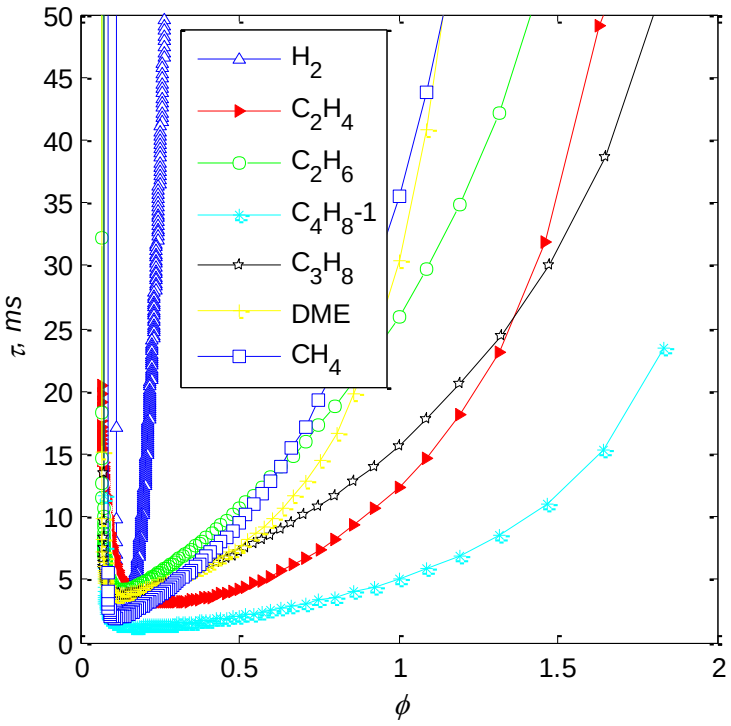

Fig. 9-3 Delay times (τ) from the 0-D isobaric reactor, for a range of fuels with varying equivalence ratios (φ) ignited at experimental autoignition temperatures.

If coflow temperatures lower than those in Table 9-1 were used in the reactor, minimum delay times less than τ = 5 ms cannot be obtained. Temperatures lower than the experimental autoignition temperatures do not achieve lift-off heights that match a representative delay time, from the JHC experiment. The delay times are converted to a lift-off height by multiplying it by the average flow velocity (U_J = 100 m.s), giving an upper bound for the lift-off height conversion.

Since all fuels have different sensitivities of ignition delay times with coflow temperature for different equivalent ratios (Fig. 9-3), a fixed equivalence ratio of approximately $\varphi \approx 0.2$ is used in Fig. 9-4. This equivalent ratio corresponds closely, as seen in Fig. 9-3, to the minimum ignition delay time for all fuels and therefore is the fixed value

chosen. Furthermore, this equivalence ratio produces delay times that correspond well to the lift-off height sensitivities obtained from the JHC experiment, seen in Fig. 4-2. It is further noted here that the coflow and jet velocities are, whilst, similar between the hydrocarbon fuels and H_2 they are different, given in Table 4-1. The chosen equivalence ratio therefore assumes that the mixing process due to shear layer velocity ratios is less sensitive in the experiment compared to the rapid ignition delay times.

This fixed equivalence ratio between fuels enables a comparison of delay times versus coflow temperature, seen in Fig. 9-4. It indicates that H_2 is most sensitive to coflow temperature, operating within a small temperature range (T_C = 1040 – 1070 K). Furthermore, H_2 is igniting with a reasonable delay time of τ = 2 m/s at a low-temperature of T_C = 1040 K, corresponding to Table 9-1. It is noted that different fuels may be igniting at different equivalence ratios. However, $\varphi \approx 0.2$, for all fuels, lead to reasonable delay time sensitivities with coflow temperature, compared to the JHC experiment.

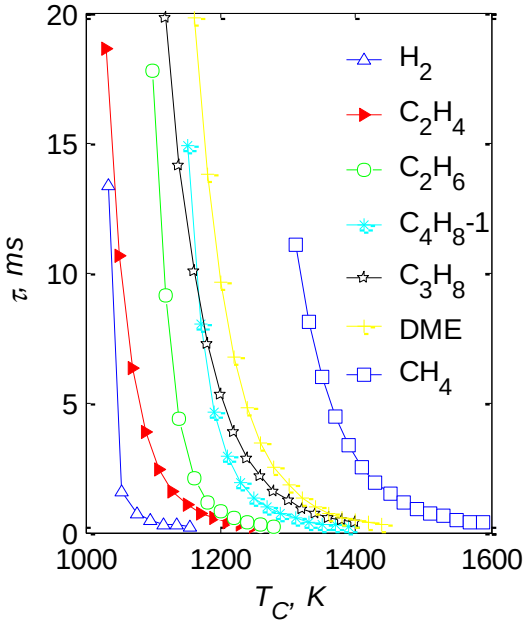

Fig. 9-4 Ignition delay times (τ) for pure fuel jets from an isobaric reactor for different ccoflow temperatures (T_C), φ = 0.2.

9.2 Varying N_2 dilution ratio for H_2 (JHC)

It was observed for the sensitivity of H_2, with equivalence ratio in Fig. 9-3, an initial equivalence ratio greater than $\varphi = 0.2$ significantly increased the delay time. Indeed, ignition can be deemed not to occur for $\varphi > 0.3$, since the delay time is too large and the autoignition event would exceed the valid coflow cone (60 D_J), for an inlet jet velocity of $U_J = 107$ m/s. The sensitivity of H_2 with the ignition mixture warrants experimental investigation, where a small study was conducted. The study varied the nitrogen content in the jet, in turn altering the stoichiometric mixture fraction, where the relatively large molecular weight of N_2 compared to H_2 increases the stoichiometric mixture fraction, seen in Fig. 3-5. The increased mixture fraction 'forces' the ignition to move further inward into the fuel jet. As such, to achieve a similar equivalence ratio the lift-off height would increase, as more mixing is required with the coflow. Furthermore, whilst the stoichiometric mixture fraction is changed, the mixing and chemistry is also changed, results for the variation of nitrogen dilution are presented in Fig. 9-5.

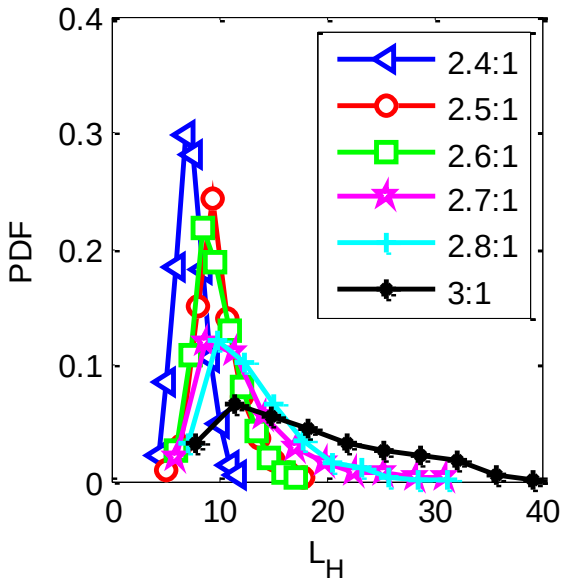

Fig. 9-5 Varied dilution of H_2 jet with N_2 for a fixed coflow temperature, $T_C = 1040$ K.

The results in Fig. 9-5 show the lift-off height PDF's for varying N_2 dilution, 2.5 - 3 parts N_2 with H_2, within the fuel jet for a fixed coflow temperature of T_C = 1040 K. The data is presented as a PDF to indicate the varying lift-off height range between dilution levels. Reduced dilution of H_2:N_2 = 2.4:1 has the lowest lift-off height at ~ 7 *x/D*, whilst H_2:N_2=3:1 has the highest lift-off height of 12 *x/D*. The highest dilution of 3:1 has the highest lift-off height and at the same time has the greatest range, indicating it is the least stable flame.

It is proposed that the increase in lift-off height for a small increase in partial dilution is due to the stoichiometric mixture fraction increasing, where the variation in the stoichiometric mixture fraction for H_2 was given in Fig. 3-5. Therefore, for ignition to occur, additional mixing is required to achieve the same equivalence ratio and mixture temperature that leads to ignition. A richer mixture has a significantly larger delay time (Fig. 9-3), therefore, it is believed that mixing is controlling the lift-off height and not ignition delay times, for H_2.

9.2.1 **Laminar calculations sensitivity to experimental temperatures**

It is seen in Fig. 9-3 and Fig. 9-4 that the ignition equivalence ratios and ignition delay times of various gaseous fuels are more sensitive to coflow temperatures than others, with H_2 igniting at the lowest coflow temperature and CH_4 at the highest. The temperature range measured in the experiment and the calculated delay times makes it possible to identify whether the two results have similar sensitivities, that is, a comparison between experimental and theoretical resutls. Since the: jet velocity, burnt coflow velocity and premixing ratio for a given fuel, in the experiment are fixed, the lift-off height is solely driven by the variation in

coflow temperature. Therefore, it is determined here whether the reactor delay times and experimental lift-off heights have the same dependence on coflow temperatures.

It is hypothesised that if the JHC flames are stabilised/dependant on autoignition, the sensitivity of experimental lift-off heights and the calculated delay times would be similar. Noting the lift-off height PDF matches closely the autoignition formation PDF (Fig. 4-6) and hence these flames are seemingly stabilised by autoignition. If the delay times do not correlate well to the lift-off heights, the flames have another dominant stabilising property, such as free flame propagation being dominant, or further, could be driven by mixing dynamics.

Like the previous delay times in Fig. 9-4 the calculated delay times in this section for each fuel uses a constant equivalence ratio. The equivalence ratio used in this section for all fuel delay times are based on the equivalence ratio that produces a converted numerical lift-off height ($L_H = U_J \times \tau$) of approximately 60 *x/D*. The temperature from the experiment that corresponds that corresponds to this lift-off height is used for the laminar calculation temperature, defined previously as the autoignition temperature (Table 9-1). That is, for CH_4 the equivalence ratio that leads to a lift-off height of 60 *x/D* at the temperature of 1410 K is φ = 0.25, this is held constant for all calculated delay times of CH_4. The same process is repeated for all fuels, measured in the JHC experiment, and the delay times versus the experimental lift-off heights are given in Fig. 9-6. The ignition delay times of the simulations were converted to an equivalent lift-off height by multiplying the calculated delay times by the average jet velocity, U_J = 100 m/s. This is an approximate velocity, it does not account for the jet velocity decaying exponentially along the centre line, where the velocity is potentially lower at the location where kernel ignition occurs.

It can be seen in Fig. 9-6 that there is a strong linear correlation between the experimental lift-off height and the calculated delays, i.e. $\tau \propto L_H$. This linear correlation varies from the work from Choi et al. [89], for laminar auto-igniting flames, where lift-off heights were proportional to delay times squared $\tau^2 \propto L_H$. An additional constant could be used to better collapse all the hydrocarbon and hydrogen curves based on the laminar flame speed. However, this term requires significant investigation, including what temperature kernel ignition occurs and propagates, as such, it isn't including here.

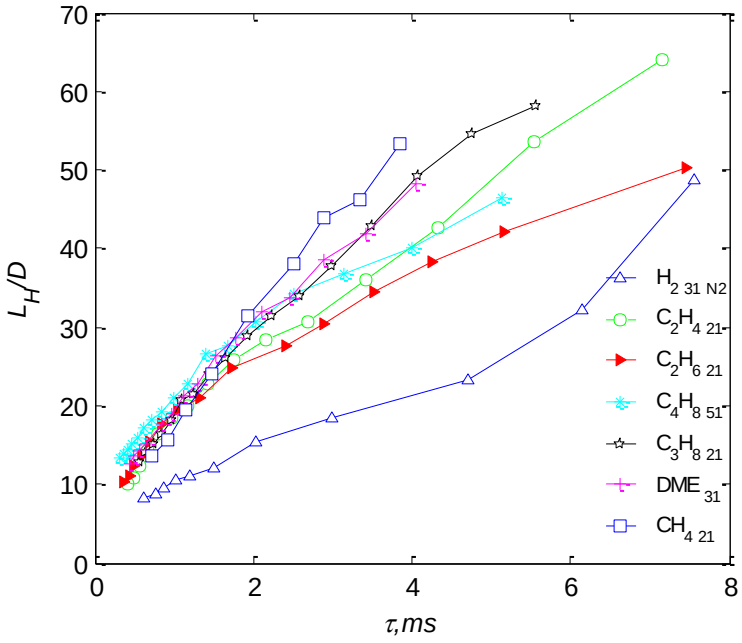

Fig. 9-6 Lift-off heights vs. laminar calculated delay times. For all fuels given the mixture 0-D equivalence ratio is given by, φ = 0.2.

It can be seen in Fig. 9-6 that H_2 has a shifted linear correlation, relatively slower delay times, compared to the other hydrocarbons. If the equivalence ratio is decreased, the H_2 delay time decreases for the same equivalent coflow temperature, this indeed improves the overlap onto the hydrocarbon cases. However, if the delay times are corrected by the difference in laminar flame speeds between H_2 and the hydrocarbons, it also improves the overlap with the

hydrocarbons. The correction involving the laminar flame speed and its importance to the lift-off height was discussed in relation to the flame base advection speeds in Fig. 4-14. It was identified that ignition formation rates were not enough to completely describe the flame lift-off height, and the flame base advection velocity (flame speed) has an influence on the average flame base location, this observation however needs further investigation.

A further comparison between lift-off height and delay times is done by comparing the converted calculated ignition delay times to an equivalent lift-off height. The comparative lift-off heights verify if the temperature range from the calculations, match the experimental coflow temperature range and sensitivity. By plotting both the experimental lift-off heights and the ignition delay times in an Arrhenius fashion (Fig. 9-7 a-b), the relative separation between ignition delay times of fuels is consistent with experimental observations. That is, for the CH_4, case, a long delay time of τ = 10 m corresponds to the high experimental lift-off height (50 *x/D*), for a common temperature of T_C = 1420 K (0.72, K^{-1}). Additionally, the 'short' delay time, of τ = 0.6 ms, corresponds to a low experimental lift-off height of 12 *x/D*, corresponding to a common temperature of T_C = 1540 K (0.65, K^{-1}). Furthermore, the gradients of the simulation delay times appear to match those of the experimental lift-off heights for the Arrhenius fit. It is seen that for both the calculations and experiment the high-temperature region for hydrogen (T_C = 1070 K) is not represented well by an Arrhenius fit.

To identify the relative sensitivity between the experimental lift-off heights and the laminar delay times the coflow temperatures corresponding to the same lift-off heights are normalised together. That is, the coflow temperature that corresponds to the experimentally determined lift-off height is divided through by the equivalent coflow temperature that corresponds to the calculated lift-off height ($L_H = U_J \times \tau$). This produces binary values of zero to one, one identifies that the same coflow temperature produces a calculated lift-off

height equivalent to the experiment. These binary values are multiplied by the 'auto ignition temperature' from Table 9-1 to aid in the visual presentation in Fig. 9-7c.

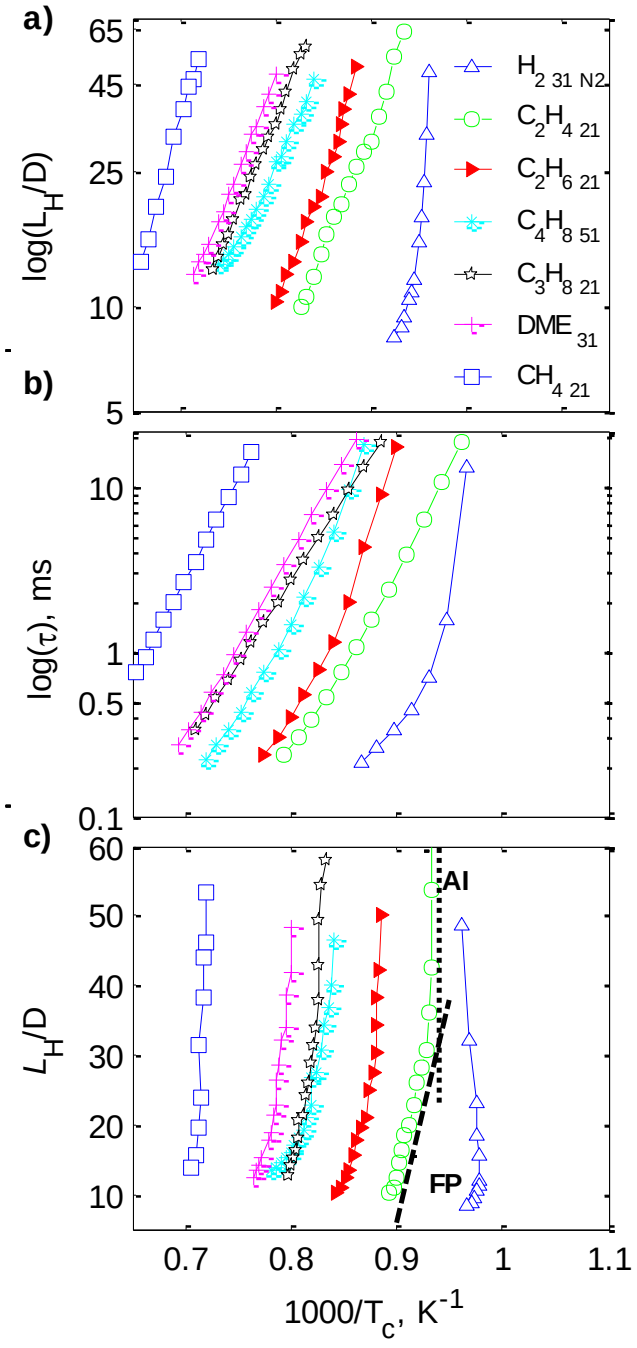

Fig. 9-7 0-D reactor Isobaric results with lift-off heights: a) Experimental lift-off heights (Arrhenius fit) b) simulated delay time (Arrhenius fit). (c) Experimental lift-off heights corrected by delay times, the vertical dotted line indicates autoignition (AI) stabilisation, dashed line highlights free flame propagation (FP) modes.

The vertical proportion, in Fig. 9-7 (c) given by AI (Autoignition) from the curves, indicate that the numerical simulations, in that region, are well represented by the temperature sensitivity of the experiment. As the experimental coflow temperature is increased the deviation from vertical, indicated by the dashed line FP (Flame Propagation), identifies that the flame is not well represented purely by delay times. The deviation of the curve from the vertical AI-line is particularity evident for C_2H_4, at the three temperatures: T_C = 1080 K, 1090 K and 1100 K; these temperatures are proposed to be highly dependent on autoignition for stability. However, as the temperature exceeds T_C = 1100 K, the curve trends toward the FP-line, and stabilisation characteristics is deemed a combination of ignition delay time and free flame propagation. This finding of higher coflow temperatures being stabilised by flame propagation agrees with the assertion from Arndt et al. [119] for CH_4 flames.

It is however noted that these simulations are based on a constant equivalence ratio for each fuel, the hotter coflow temperatures may in fact be igniting in leaner mixtures, this is explored for the unsteady simulations. Furthermore, using just the ignition delay times to characterise the fuel lift-off heights identifies that mixing is negligible. However, since higher coflow temperatures are igniting further upstream, they are subjected to different flow and strained fields. These differing flow fields may additionally affect the results between the high to low coflow temperature seen in Fig. 9-7, whereby, the lower coflow temperatures are better represented by the ignition delay times. The effect of strain rates is further explored using the unsteady counter-flow simulations with DME.

9.3 DME kernel heat release and ignition precursors

The previous DME heat release PLIF experiment was based on the product and integrated kernel signals from OH and CH_2O. Therefore, the temporal and compositional formation of species including, OH and CH_2O are discussed here, identifying what influences the different heat release levels between coflow temperatures; where a higher kenrel heat release was determined for a lower coflow temperature. The compositional space and heat release for DME autoignition kernels are analysed using laminar unsteady flame calculations. It looks at the different heat release levels observed in the experiment, from high to low coflow temperatures, in relation to unsteady heat release results. Species precursors leading to the autoignition of DME are also observed to determine low and high-temperature pathways leading to ignition (NTC behaviour). Further identifying if low-temperature chemistry is observed in the experiment, whether the low-temperature (low-temperature pathways) pooling of CH_2O in the lead up to ignition is observed in the region where OH occurs.

9.3.1 Autoignition species: markers and precursors

The OH radical was used in the PLIF experiment to identify the early stages of autoignition events, whilst CH_2O is used as a low-temperature marker. As such, it is important to identify how the concentration of these species temporally evolve from: before, during and after autoignition. Therefore a 0-D isobaric reactor was implemented at a somewhat low coflow temperature of T_C = 1200 K, seen in Fig. 9-8, where T_C = 1400 K is considered the high coflow temperature, that led to low stable DME flames (Fig. 7-2).

The reactor mixture temperature (before ignition) is defined from the 'mixing triangle', between the 300 K pure DME fuel with the products from the equilibrium of H_2/air, leading to the coflow temperature of T_C = 1200 K. The delay time is defined here by the vertical dashed-line in Fig. 9-8, it is based on a rapid temperature rise, dT/dt > 3000 K/ms. A lean equivalence ratio, φ = 0.5, was used as the initial mixture, between the fuel and coflow products, ignited in this simulation. The value of φ = 0.5 was determined based on an investigation using the counter-flow solver with DME, in the following section. Furthermore, all equivalence ratios were investigated, however, the relative formation of species in Fig. 9-8 were similar even though their formation rates were different (delay time).

As expected, the CH_2O signal builds up early within the combustion process, that is CH_2O forms before ignition, where ignition is defined here as τ = 16.05 ms (Fig. 9-8, vertical dashed line). This early pooling before ignition indicates that CH_2O is a low-temperature marker, occurring early in the ignition process, as DME 'breaks-down'. The OH radical, however, is forming at higher temperatures, temperatures greater than 1600 K. After the initial ignition occurs, the CH_2O decreases significantly, and it approaches zero as the OH radical peaks.

The relative temporal pooling of species (CH_2O, OH and species) scale with the delay times presented in the previous section in Fig. 9-4, however, the mole fractions vary. Other low-temperature species such as: CH_3, HCO and H_2O_2 radicals are presented, they additionally form before ignition, in varying levels, where the CH_3 and HCO peak closer to ignition. The H_2O_2 radical is like CH_2O, forming early before auto ignition and approaching zero as ignition occurs, while the HO_2 radical peaks.

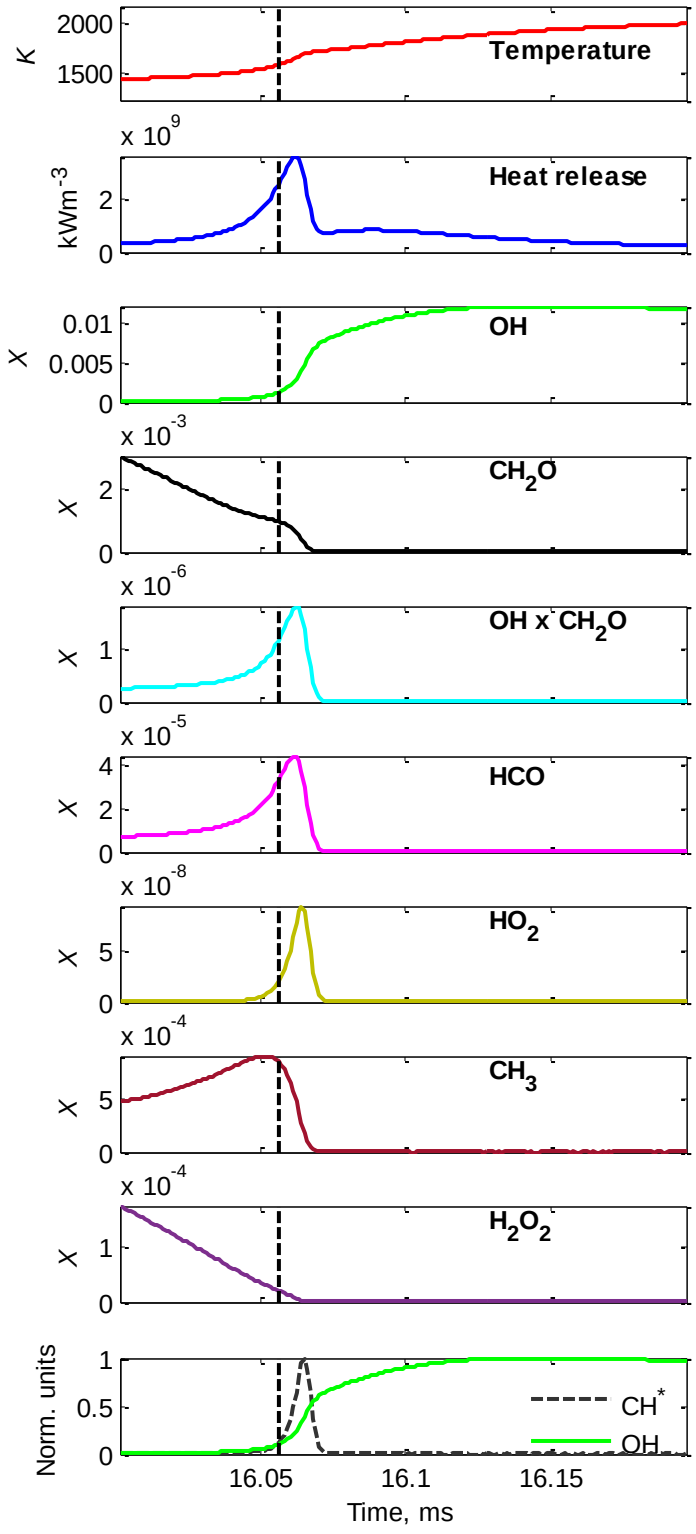

Fig. 9-8 Temporal evolution of: Temperature, heat release and species: OH, CH_2O, OH x CH_2O, HCO, HO_2, CH_3, H_2O_2, CH^* for a pure DME jet mixed with a T_C = 1200 K coflow. The ignition delay time is marked by the vertical dashed line, τ = 16.05 ms.

The OH radical was used as a marker of autoignition, and as a flame front marker in the PLIF study, as it can be used to distinguish both the flame front and ignition events. Furthermore, it was utilised since the fluorescence signal level is high and the fluorescence band is readily available. However, as seen in Fig. 9-8, OH does not coincide directly with autoignition, τ = 16.05 ms. The CH_3 or HO_2 radical would be better suited for identifying ignition, since these species peak near ignition, however, they are not imaged in this experiment. Therefore, it is acknowledged that autoignition events would occur upstream of the OH detection within the coflow burner PLIF experiment. These markers may be better suited to identify ignition than CH_2O, since CH_2O has a peak before ignition. This low temperature build-up of CH_2O before ignition was seen in the experiment, where a CH_2O sheet was observed across the entirety of the jet (Fig. 7-6 b) irrespective of the ignition OH event.

Normalised values of CH^* and OH^* are also given, they form close, temporally, to each other, however, there is a small delay between where measurable quantities of OH and CH* occur. Therefore, within the experiment, the inability to detect early kernels (Fig. 7-6 d) by the CH^* camera, whilst the OH camera identifies them, is potentially due to both: the camera's quantum efficiency, the camera's resolution and time to detect the required signal level of CH^*. The relative experimental, temporal formation of OH relative to CH^* needs further measurements to identify this phenomenon.

The temporal formation of the heat release marker between the CH_2O and OH product corresponds well to the temporal formation of HCO and heat release for this simulation. This good temporal correlation of OH x CH_2O with heat release is given in Fig. 9-9, it is similar to the heat release and OH x CH_2O correlation from the unsteady simulations from Fig. 5-11.

Therefore, despite OH not being an excellent marker for ignition it provides a good marker for heat release, using its product with CH_2O.

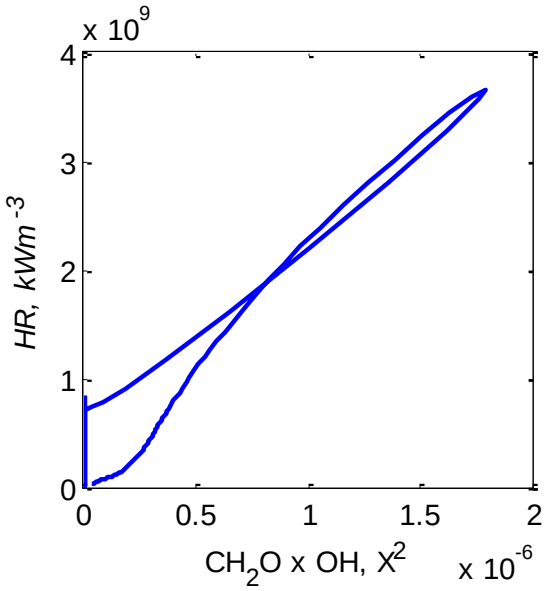

Fig. 9-9 Heat release (*HR*) correlation with the product, CH_2O x OH, for a coflow temperature, T_C = 1200 K, reacted in a 0-D isobaric reactor.

9.4 DME chemical pathways and CH_2O formation

Since DME presents mild NTC, or dual stage ignition behaviour, it is important to analyse both the, low and high-temperature pathways that lead to ignition. That is, does CH_2O originate from low or high-temperature reactions, and does NTC behaviour effect ignition dynamics from the DME experiments.

There are two competing pathways leading to the formation of CH_2O for DME, seen in the chemical equations below, and the reaction diagrams in Fig. 9-10. These reaction diagrams are from a 0-D isobaric reactor, using the Burke mechanism [73] for high and low-temperature coflow temperatures. A low coflow temperature, of 800 K, predominantly

induces reactions that go down the low-temperature path, leading to $CH_2OCH_2O_2$ [207, 215, 216]. The higher temperature (1200 K) diagram has minimal formation of $CH_2OCH_2O_2$, and most of the reactions go through the formation of the methyl (CH_3) radical (high-temperature pathway). Additionally, both reaction pathways are leading to the formation of CH_2O which is directly relevant to this PLIF setup. The low-temperature (9.1) pathway leads to two moles of CH_2O, whilst the high-temperature pathway (9.2) leads to a single mole of CH_2O.

$$CH_2OCH_2O_2H = OH+2CH_2O \tag{9.1}$$

$$CH_3OCH_2 = CH_2O+CH_3 \tag{9.2}$$

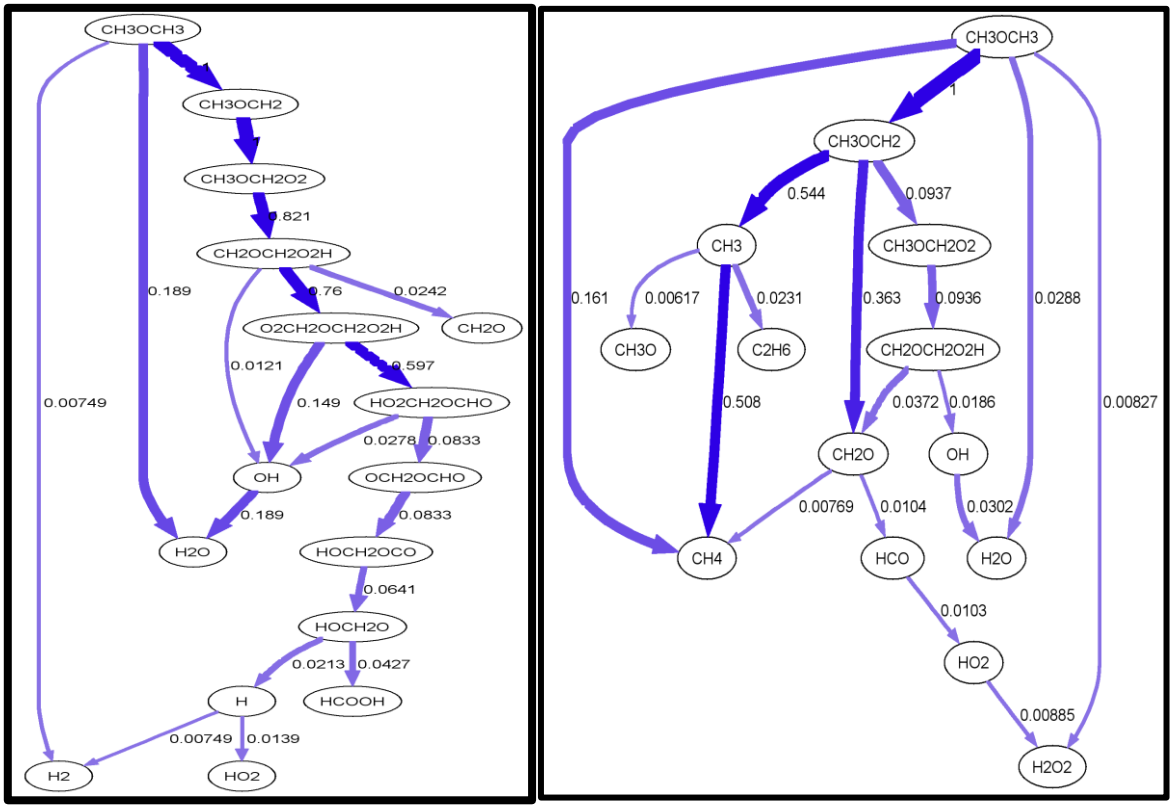

Fig. 9-10 Reaction pathway diagrams for two coflow reactor temperatures: 800 K (low-temperature, left) 1200 K (high-temperature, right) from a 0-D isobaric reactor. Arrow widths and number ratios identify the amount of hydrogen (H) flux leading to a given species.

The question becomes how to identify whether the CH_2O is being produced, by low or high-temperature reactions within the experiment, and whether NTC behaviour is occurring. The competing normalised reaction pathways, both high and low-temperature, are shown in Fig. 9-11 a, they trace the hydrogen (H) elemental flux (production rates), based on 0-D isobaric simulations at ignition. It traces the pathways leading to CH_3 (high-temperature reactions) and $CH_3OCH_2O_2$ (low-temperature reactions) from the CH_3OCH_2 reaction. The CH_3OCH_2 reaction is where the low and high-temperature pathways diverge, seen in Fig. 9-10. The greater the flux of elemental hydrogen leading to the production of $CH_3OCH_2O_2$, the greater amount of low-temperature reactions occurring. The opposite is also true, the more hydrogen flux leading to the CH_3 reaction, the increased number of high-temperature reactions that are occurring.

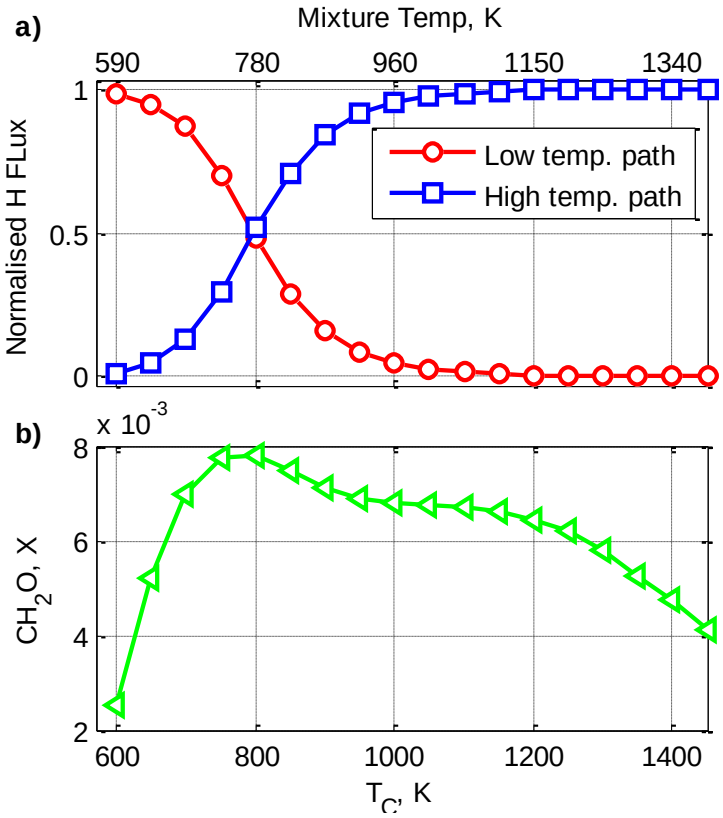

Fig. 9-11 Results for the autoignition of DME for a 0-D isobaric reactor, including: normalised competing low and high-temperature pathways and the CH_2O mole fraction at ignition (a). The coflow temperature (T_C) and equivalent mixture temperature (top x-axis), obtained from the mixing of a jet at coflow at φ = 0.5, is given (b).

The mole fraction of CH_2O at autoignition is given in Fig. 9-11 b, it shows that there is a peak in CH_2O mole fraction occurring as the balance between the high and low-temperature reaction pathways are occurring, i.e. T_C = 800 K. This identifies that as expected, two moles of CH_2O are produced during low-temperature reactions, twice what is produced during the high-temperature pathway reactions. However, as the coflow temperature is increased, CH_2O production rates increases, this leads to an optimal/ peak CH_2O production at ~ T_C = 800 K or a mixture temperature of 780 K seen in Fig. 9-11.

Fig. 9-11 (a) shows that low-temperature reaction pathways are dominant for low-temperatures between 600 - 800 K. After 800 K, the plots insect and the higher temperatures, leading to the CH_3 formation are more dominant. Furthermore, after 1000 K the formation of CH_2O is due to high-temperature chemical pathways, where this JHC experiment operates with coflow temperatures exceeding T_C = 1225 K. Therefore, it has been assumed that all CH_2O signal in the PLIF experiment are produced due to reactions containing the CH_3OCH_2 radical (high-temperature pathway) and NTC behaviour doesn't influence ignition kernels. The correlation with OH and the low or high-temperature CH_2O formation is further analysed, using the counter-flow reactor, in the next section.

The reactor mixture temperature is given on the top x-axis, this identifies the mixture temperature from the mixing of a giving coflow temperature (T_C), with the fuel at an equivalence ratio of φ = 0.5. The mixture temperature is given to identify the reactor temperature that affects the chemical kinetics of DME, opposed to the coflow temperature that is relevant to the JHC experiment.

The lack of influence of NTC behaviour is also identified from the lift-off height response to coflow temperature or kernel formation rates from the JHC experiment. If NTC behaviour were to be evident in the JHC burner, a variation in lift-off height would deviate from the smooth curve, the correlation of lift-off height and coflow temperature, for low to high coflow temperatures in Fig. 7-1. Furthermore, there would be a sudden deviation in formation rates or formation location in the chemiluminescent formation rates plots (Fig. 4-4). The potential NTC behaviour is seen in Fig. 9-12, where for a given temperature the chain termination reactions dominant chain branching and ignition delay times increase, resulting in increased lift-off heights.

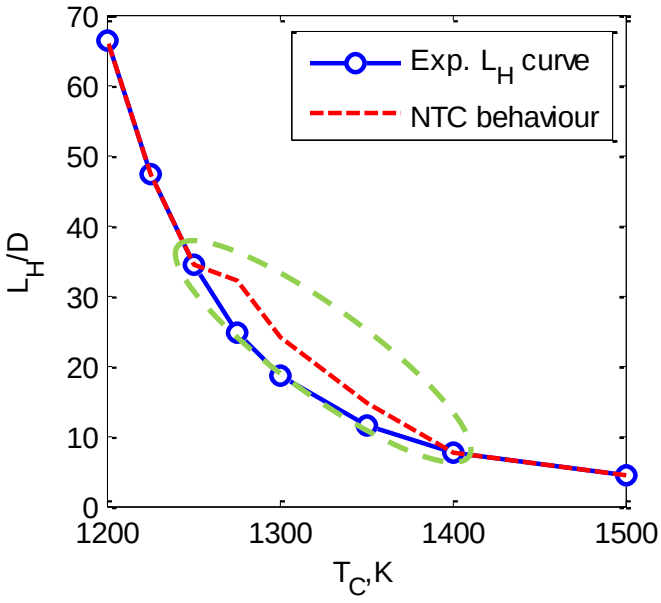

Fig. 9-12 The potential effect of NTC behaviour on the experimental (Exp.) lift-off heights. The proposed NTC region is indicated by the dashed ellipse.

9.5 1-D unsteady reactor: species build-up

A 1-D unsteady counter-flow reactor was used here for DME, as was used in Chapter 8 (for CH_4), it uses Ember [203, 204] to identify the DME species temporal and composition evolution. The reduced Pan [75] mechanism was used for the unsteady reactor as it vastly reduced computational costs. A comparison [77] between delay times and major OH and CH_2O species have shown good agreement with the parent Burke [73] mechanism. The Zhao DME mechanism [217] was also tested, it gave similar results with a small reduction in sensitivity of ignition delay times to strain rate.

The simulations oppose equilibrated coflow products from H_2/air against a room temperature (298 K) fuel jet with pure DME. It has a step in the domain from the coflow

species to the fuel jet, as seen in Fig. 9-13. For this single simulation pure DME is opposed against a coflow temperature of 1400 K at a strain rate of a = 50 s^{-1}.

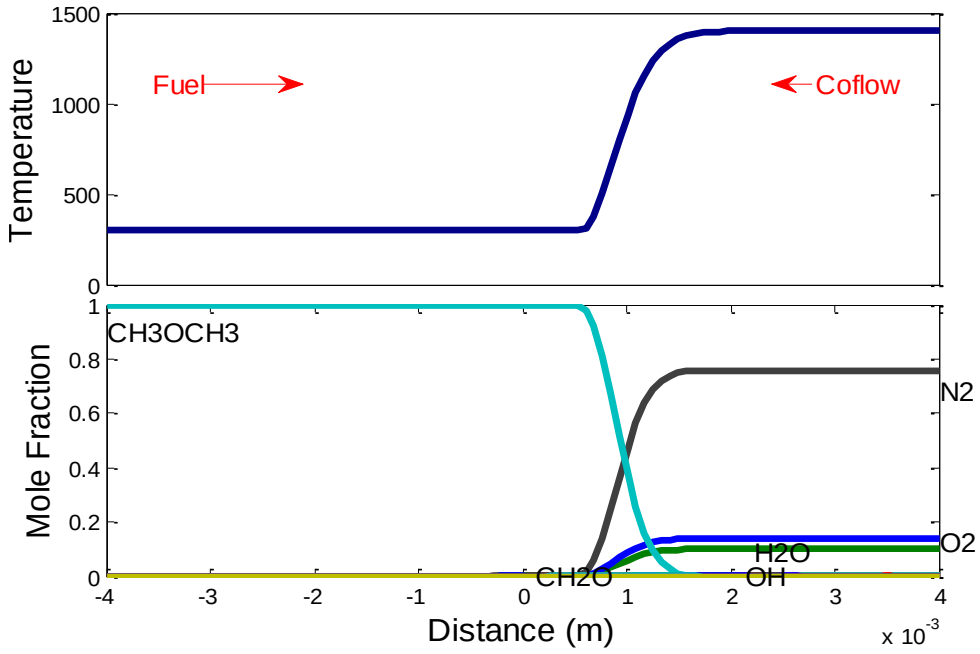

Fig. 9-13 Unsteady opposed flow solver domain prior to temporal evolution of the simulation. Hot coflow H_2/air equilibrated products at T_C = 1400 K opposed against a pure DME jet. The domain consists of a step-in temperature (top) and step-in products (bottom).

The compositional space given in Fig. 9-13 is ignited and the: temperature, heat release and species profiles are given in Fig. 9-14, for time steps leading up to and including ignition. Since the counter flow reactor has diffusion and mixing, it doesn't require a previously chosen mixture fraction input, like the isobaric reactor, seen in Fig. 9-8. A most reactive mixture fraction, as seen for CH_4 can be identified, noting it was defined by the mixture fraction corresponding to the peak temperature at the ignition time step.

The most reactive mixture fraction is determined to be ξ_{MR} = 0.018, for this example (Fig. 9-14, vertical dashed line). The stoichiometric mixture fraction is also given, ξ_{st} = 0.06

(vertical dotted line), identifying ignition to be lean, φ = 0.3, the ignition delay time is also given (τ = 0.9 ms). Species temporal formation are given by the colour bar, and their relative formation in mixture fraction space is identified, relative to the stoichiometric mixture fraction (vertical dashed line). Therefore, species forming on either side of ξ_{st} = 0.06 are lean or rich, and species forming either side of ξ = 0.015, are determined to be richer or leaner than the most reactive mixture fraction. Furthermore, the leaner mixtures (ξ) correspond to higher temperatures as verified by the temperature plot in Fig. 9-14.

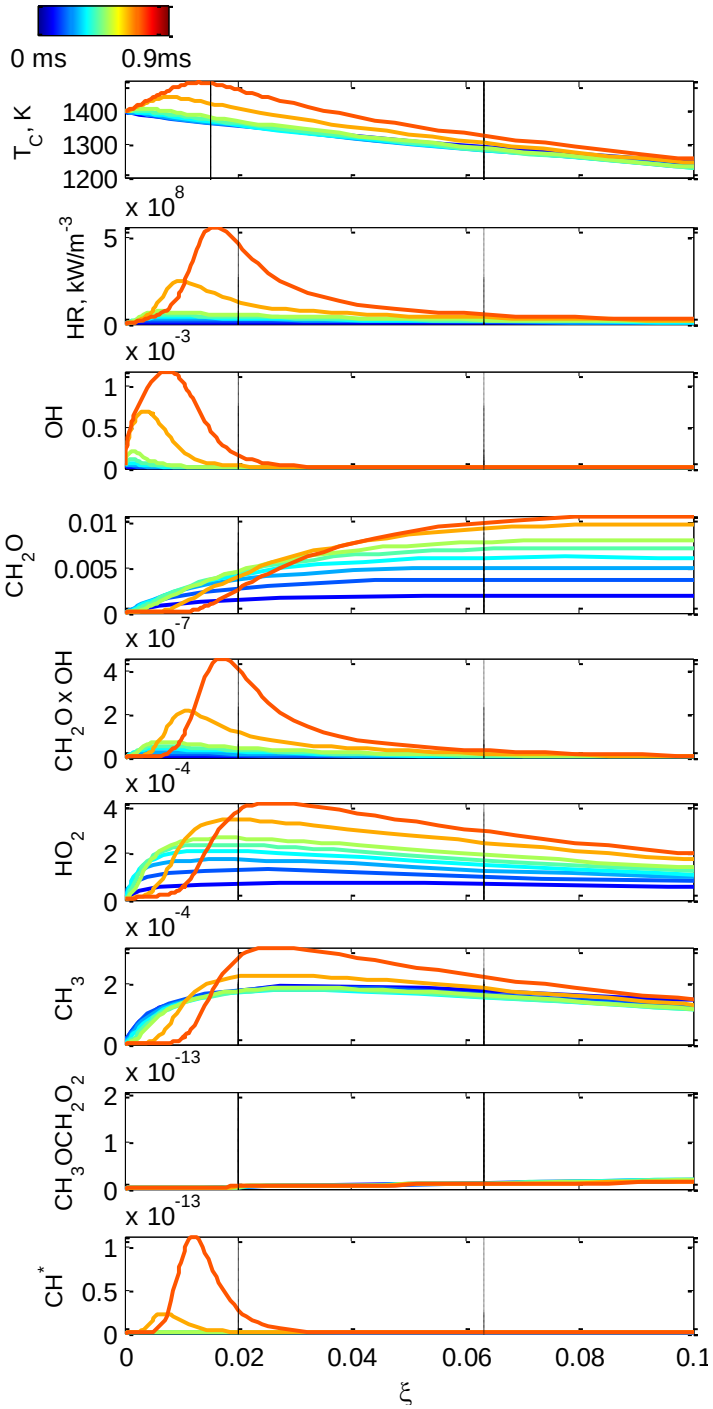

Fig. 9-14 Counter flow results for a T_C = 1400 K coflow, with coflow products opposed against a pure DME jet. Results include, temporal evolution of temperature and species: OH, CH_2O, CH_2O x OH, HO_2, CH_3, $CH_3OCH_2O_2$ and CH_3. The colour bar indicates the temporal evolution from 0-1.13 ms. The vertical line indicates the stoichiometric mixture fraction, where ignition is occurring at τ = 0.97 ms, at a very lean mixture fraction of ξ_{st} = 0.025. The mixture fraction domain is restricted to ξ = 0 – 0.1.

The simulation identifies that the onset of OH occurs in leaner mixtures, on the left side of the dashed, most reactive mixture fraction line, occurring for relatively high domain temperatures. The peak heat release (*HR*) as expected corresponds closely to the most reactive mixture fraction (dashed line). The peak CH_2O is occurring in much richer regions, in correspondingly lower temperatures, where the peak value occurs richer than stoichiometry, not presented in Fig. 9-14. The CH_2O mole fraction approached zero in the isobaric, purely autoignitive reactor, as ignition was reached. However, for the counter-flow reactor the overlap at ignition is significant, this is similar to the experimental findings where significant overlap was observed.

The low and high-temperature pathway precursors, $CH_3OCH_2O_2$ and CH_3 respectively, are also shown in Fig. 9-14. The high-temperature pathway radical, CH_3, is forming in lean compositions, like the formation of CH_2O. The low-temperature pathway species marker, $CH_3OCH_2O_2$, is forming richer than $\xi = 0.1$ (peak not shown). This doesn't correspond to OH reactions, or where maximum heat release occurs. Therefore, for the PLIF experiment, where the OH autoignition marker occurs and overlaps CH_2O, high-temperature pathway reactions occur, with no NTC behaviour. Furthermore, where the overlap of CH_2O x OH (heat release) is given no NTC behaviour exists, occurring in lean mixtures (ξ =0.02), τ = 0.9 ms.

To further identify the potential formation of CH_2O, whether it is in low or high-temperature regions within the experiment, the 1-D unsteady reactor was used, implementing two DME mechanisms. One mechanism contained two pathways leading to the formation CH_2O (high and low-temperature pathways) i.e., the Burke mechanism [73], and another that contained a single pathway (high-temperature) Pan [74].

It can be seen in Fig. 9-15, for the Burke mechanism there are low-temperature reactions, leading to CH_2O, occurring in very rich mixtures, $\xi > 0.5$, corresponding to temperatures less than 700 K. These low-temperature pathway reactions lead to the formation of CH_2O, from the reaction: $CH_2OCH_2O_2H = OH+2CH_2O$, described above in section 9.4.. In addition, there are the higher temperature reactions, $CH_3OCH_2 = CH_2O+CH_3$, from the CH_3 reaction leading to the formation of CH_2O, $\xi = 0.02 - 0.03$.

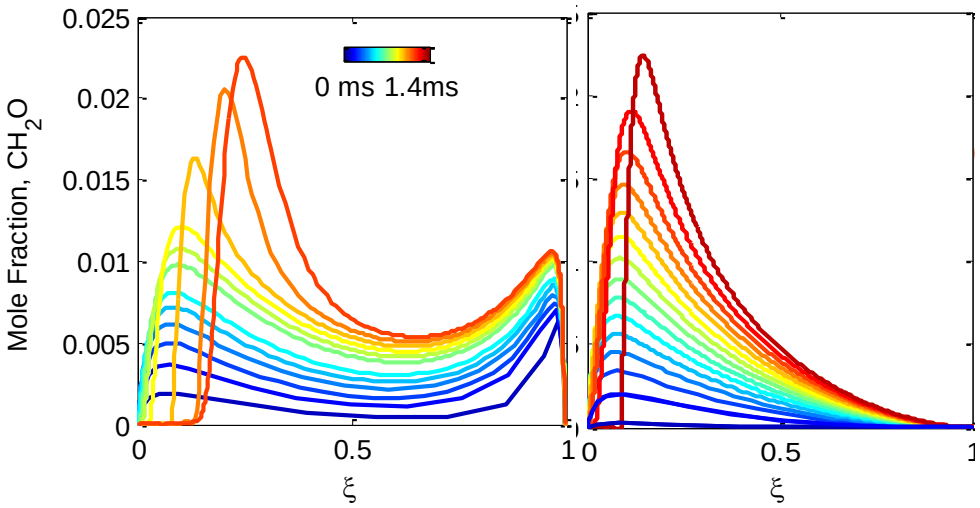

Fig. 9-15 Unsteady counter-flow solver results for the formation of CH_2O, *T*c=1400 K, using two mechanisms: the Burke Mechanism (left) and the Pan mechanism (Right). The colour bar identifies the temporal evolution, ignition occurs at $\tau = 0.9$ ms.

The Pan mechanism [75], doesn't have these low-temperature reactions, since it is an optimised version of the Burke mechanism, and as such doesn't have the formation of CH_2O in very rich regions (Fig. 9-15, right). Hence, it is further identified for the experiment, where lean ignition occurs the only possible CH_2O signal is from high-temperature reactions. Furthermore, it was identified that this low-temperature reaction pathway was responsible for NTC behaviour, as such, NTC behaviour is not predicted to impact upon kernel formation.

9.6 **DME strained ignition and kernel heat release**

The previous section identified that the formation of CH_2O that overlaps onto OH must occur in high-temperature locations, where high-temperature pathway reactions are occurring (Fig. 9-14). It however, doesn't identify why higher coflow temperatures lead to higher heat release and overlap (CH_2O x OH), seen in the experiment (Fig. 7-13). It is proposed that owing to the elongated nature of higher coflow kernels (Fig. 7-10), kernels are forming in different compositional space, in steep mixture fraction regions. Therefore, the counter-flow simulations are used here to identify how coflow temperatures effect delay times and composition, with the added complexity of diffusion and strain.

Fig. 9-16 indicates, as was seen previously for CH_4 (Fig. 8-2), that the higher coflow temperatures for DME at a given premixing ratio, not only ignite faster but has increased resistance to strain. Furthermore, the higher temperature reactors are igniting leaner, where increased strain rates cause the mixture to ignite richer with increased robustness and heat release.

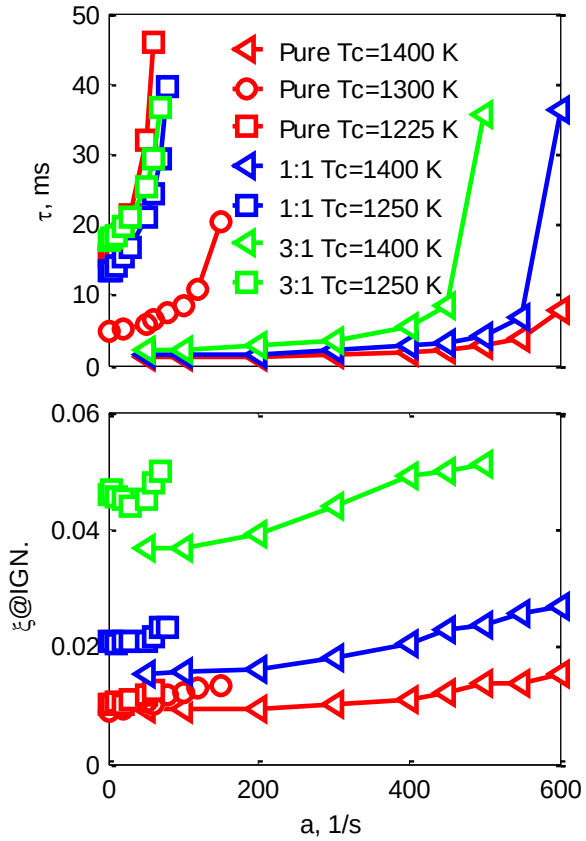

Fig. 9-16 Results from a counter-flow simulation with DME for two premixing ratios (1:1 and 3:1) and a pure jet opposed against three coflow temperatures: T_C = 1250 K, 1300 K and 1400 K. Delay times (τ) and ignition mixture fraction ($\zeta_{@IGN}$) are given for a range of strain rates (a).

9.6.1 **Isobaric reactor release**

The average integrated kernel heat release seen in Fig. 7-13, indicates that, higher coflow temperatures have reduced overlap (CH_2O x OH) and therefore heat release. For the standard 0-D isobaric reactor, seen in Fig. 9-17, if a mixture is ignited at the same equivalence ratio, for a high to low coflow temperature, the higher coflow temperature leads to greater heat

release. This is seen in Fig. 9-17, where for all equivalence ratios, the higher temperature (T_C = 1400 K) produces more heat release (*HR*). However, if the higher coflow temperature (T_C = 1400 K) were to ignite leaner, i.e., φ = 0.3 than the T_C = 1250 K (φ = 0.6) case, the lower coflow temperature would produce more heat release. It is noted that the lower coflow temperature case must still ignite lean (φ < 0.6, dashed line) to have an ignition delay time that would lead to a plausible mean lift-off height from the JHC experiment. Imposing a leaner mixture fraction onto the isobaric reactor for increased coflow temperature can verify the experimental heat release difference from Fig. 7-13.

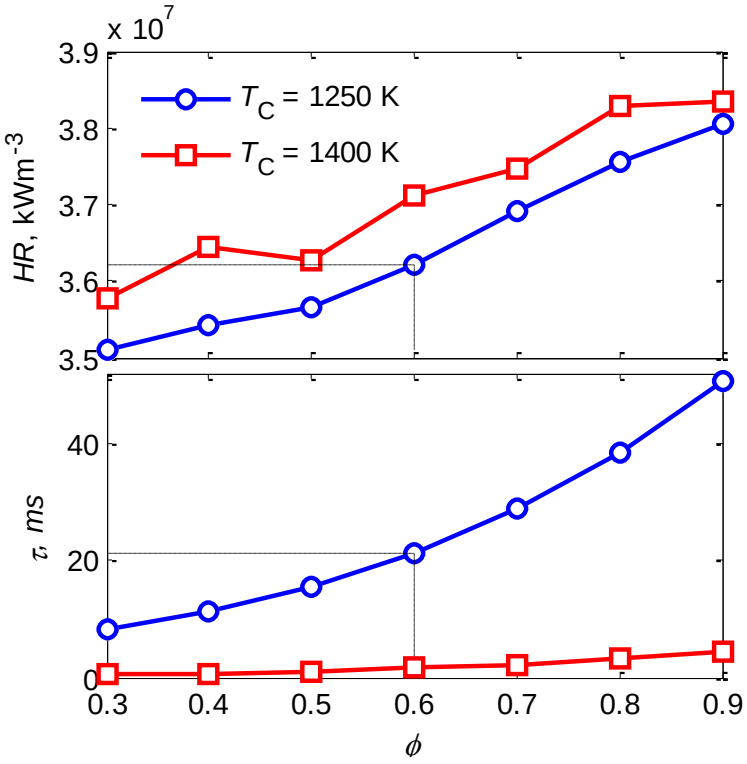

Fig. 9-17 Maximum heat release (*HR*) and delay times (τ) from a 0-D isobaric reactor for two coflow temperatures: T_C = 1250 K and T_C =1400 K, for a range of equivalence ratios (φ). The dashed line indicates the equivalence ratio and corresponding heat release for a delay time of τ = 20 ms.

Heat release quantities, in Fig. 9-17, are for the maximum heat release at ignition, whilst, the experimental values are for the kernels integrated heat release. Therefore, the small difference in maximum heat release values from the isobaric reactor between the high and low coflow temperature will be ‘amplified’ when integrated across a larger 2-D kernel. This increased heat release level matches the difference between coflow temperatures, seen in Fig. 7-13.

9.6.2 **DME counter-flow heat release**

As mentioned previously, the counter-flow reactor doesn’t enforce an equivalence ratio, unlike the 0-D reactor (Fig. 9-17). The counter-flow simulation, in Fig. 9-18, opposes hot coflow products (for multiple temperatures) against varying DME mixtures with air, at a constant strain rate, a = 2 s^{-1}. Ignition occurs when the convective/ diffusive flux reaches zero and the diffusive/reactive balance is close to unity, as described in the previous laminar calculation chapter for CH_4. As such, it can be seen in Fig. 9-18, for increased coflow temperatures, mixtures are igniting leaner, this is particularly evident for 3:1 premixing. This corresponds to reduced heat release levels, as seen for the experiment (Fig. 7-13).

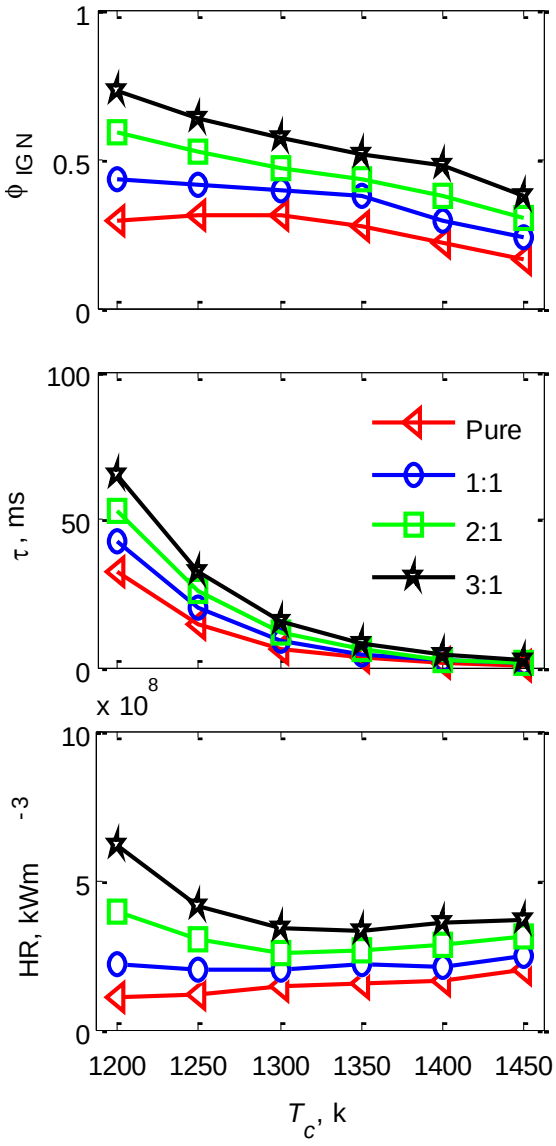

Fig. 9-18 Results from a counter-flow simulation of DME with three premixing ratios (1:1, 2:1 and 3:1) and a pure case. The ignition equivalence ratio (φ_{IGN}), delay times (τ) and heat release (*HR*) are given for a range of coflow temperatures (T_C).

The difference in heat release between a high to low coflow temperature corresponds directly to the differences in equivalence ratios. Therefore, it can be seen, for pure DME, the difference in heat release for the low the low to high coflow temperature (T_C = 1225 – 1400 K) is small, corresponding to the small difference in equivalence ratio (Fig. 9-18). However, with reference to Fig. 9-16, despite the high coflow temperature producing more heat release

for a pure DME jet (not agreeing with Fig. 7-13). The higher coflow temperatures may be experiencing different strain rates in the experiment leading to potentially leaner most reactive mixtures as further less heat release.

The differences in the most reactive ignition mixture fraction, leaner for increased coflow temperature, seems to explain the difference in the heat release (CH_2O x OH) levels from the PLIF experiment. However, ignition mixture fractions measurements need to be obtained to verify this hypothesis.

9.7 **Nitrous oxide addition**

To determine the relative importance of autoignition and potentially the heat release of kernels, in comparison to free flame propagation speed for the flame base location/stability, a catalyst, such as NO_X can be used. The oxidant, NO_X, additive is known to drop the ignition delay times [218] and ignition temperatures for counter-flow flames [79], shock tubes [219] and reacting flows [220], without significantly changing the flame speed. The NO_x, increases the hydrogen chemistry reactions [219] for H_2 and has a catalytic effect on low temperature reactions for CH_4 [28, 221], leading to autoignition. Therefore, if the flame base location decreases with the catalyst addition, the flame is strongly linked to autoignition. The effect of NO_X upon low-temperature chemistry in chemical mechanisms is still under investigation. For a variation in the NO_x mechanism, ignition delay times are significantly affected, where the catalytic effect of NO_x as an oxidant varies [70, 222, 223].

Nitrous Oxide (NO_2) was added to fuel jets in this thesis, including: H_2, CH_4 and DME flames, by substituting some of the diluent or air for equal parts of NO_2 in the fuel stream. The results were somewhat inconclusive, the NO_2 addition seemingly decreases the DME

delay times, lowering the lift-off heights, however, this needs to be confirmed. The results for the fuels tested using NO_2, for: DME, H_2 and CH_4 are given in the Appendix, D.3. Nitric oxide (NO) would have been a better catalyst, as it has improved oxidant properties. However, in high purity, it is difficult to get in a laboratory setup, so its addition to the fuel jets was not tested here.

9.8 Concluding remarks

The counter-flow simulation identifies that for varying levels of heat release, between a high and low coflow temperature (as for the PLIF experiment), the ignition mixture fractions are different, and in fact the higher coflow temperature kernels ignite leaner. This is despite ignition kernels for a high coflow temperature having a similar formation rate, for a given DME premixing case. The different formation rates are seen for OH PLIF results, Fig. 7-9, and for chemiluminescence results, Fig. 7-3. The reaction pathway analysis in Fig. 9-10 and Fig. 9-11 indicates, for DME, that ignition and CH_2O production is due to high-temperature reaction pathways, with no NTC behaviour.

For higher coflow temperatures, the impact of kernels (heat release) is not as important to joining and stabilising the flame base as lower coflow temperatures. That is, for higher coflow temperatures, particularly, for pure DME jets (T_C = 1400 K), ignition kernels form near the flame base, merging quickly into the flame base. However, the flame base is held somewhat ‘fixed’ axially, with minimal downstream advection irrespective of kernel merging, seen by the slower flame base advection velocity in Fig. 7-3. Therefore, for higher coflow temperatures, stabilisation is thought to be a combination of mechanisms, such as, a relatively fast upstream flame propagation velocity in addition to autoignition. This assertion

agrees with the 0-D isobaric delay time sensitivity study from Fig. 9-7. That is, high coflow temperature cases diverged from the ‘Auto ignition’ line/boundary, indicating they have weaker autoignition dependency for stabilisation.

Chapter 10. **New actively cooled burner**

This chapter looks at a new application of the hot coflow burner, it resolves the problem of jet preheat due to the fuel issuing into the coflow 70 mm downstream of the coflow exit. This distance of the jet exiting into the coflow stream creates different preheat between fuels and fuel injection velocities within the old burner setup. The new burner design has an actively cooled jet, which insulates it from the heated coflow environment.

This chapter discusses the previous burner jet preheat, using FLUENT simulations, comparing the old burners preheat temperatures to the new burners preheat. New experimental results are also given here, using a: CH_4, DME and H_2 jet to determine the new burner's lift-off height sensitivity to coflow temperature. These results are compared to the results from the previous burner's coflow sensitivity (Parametric fuel study chapter). An additional fuel mixture was also measured here, H_2/CH_4:N_2=3:1, to determine the effect of H_2 addition to a CH_4 jet.

10.1 **Old burner preheat fuel jet**

The current jet burner design (given in Fig. 3-1) has the jet mixing with the coflow, 70 mm above the coflow (H_2/Air) exit from the bass plate. Therefore, prior to the mixing of the jet into the hot environment, there is a degree of preheat within the jet as seen in Fig. 10-1. The temperature profile results are from an ANSYS FLUENT simulation, using a k-epsilon turbulence model with standard wall functions, with an energy model containing no radiation. The jet is at U_J = 50 m/s, where the temperature profile across the steel tube and fuel jet are presented in Fig. 4-21.

The jet in Fig. 4-21 is simulated to be injected into a T_C = 1500 K coflow with a bulk velocity U_C = 4 m/s. The steel tube has a steady state temperature on the fuel side of ~ 650 K. This generates a radial temperature gradient across the outlet of the fuel from the nozzle, seen in Fig. 10-2 for three jet velocities, U_J = 50, 100 and 150 m/s.

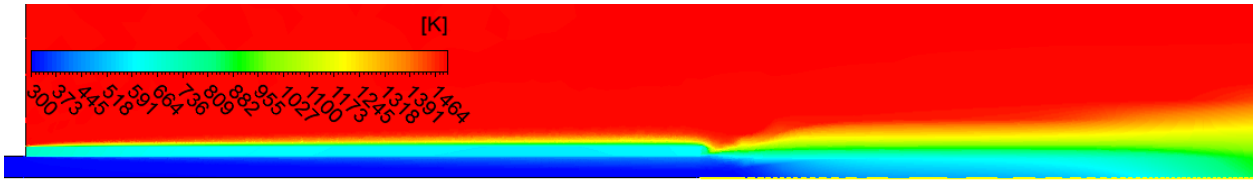

Fig. 10-1 Temperature profile results for an ANSYS simulation, for the original burner fuel jet preheat, with a jet velocity, U_J = 50 m/s. The jet is issuing into a coflow T_C = 1500 K, with a burnt velocity, V_C = 4 m/s.

There are different levels of preheat, for the varying jet velocities seen in Fig. 10-2, ranging from: 300 K to 480 K, for a jet velocity of U_J = 50 m/s and U_J =150 m/s respectively. This range of preheat means that measurements for this burner at varying jet velocities will be altered by preheat. As such, the outlet temperature is not strictly controlled, this alters the downstream axial mixture temperature (mixing between the coflow and fuel jet) prior to ignition (Fig. 10-2). The varying jet preheat with injection velocity warrants the design and manufacture of an actively cooled jet with an insulated ‘sleeve’, seen in section 10.2.

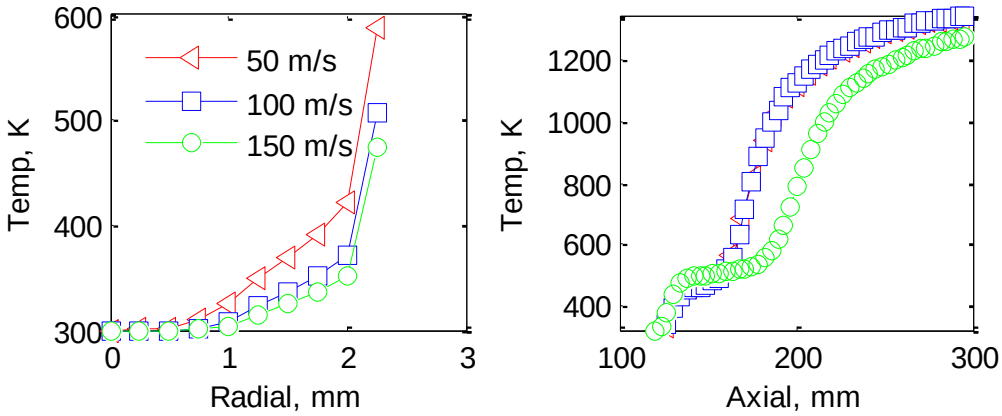

Fig. 10-2 Jet preheat for three velocities: U_J = 50 m/s, 100 m/s and 150 m/s, for radial temperature profiles across the nozzle exit (left) and the axial temperature profile along the centre-line up to 200 mm from the nozzle exit.

10.2 Insulated Jet: Ceramic and active cooling

The modified burner, that includes active cooling, is seen in Fig. 10-3. The modifications include a copper cooling water jacket, the jacket has a constant water supply that runs through the burner up to the copper heat sink (Fig. 10-4). The heat sink is further shrouded by a machinable MACOR ceramic (a detailed view is given in Fig. 10-5), this ceramic prevents large heat conduction from the heat sink into the hot coflow. A larger hole has been drilled through the base plate to accommodate the jet cooling (1 inch, 25.4mm), as such, ~ 30 holes have been removed from the brass plate compared to the old burner (Fig. 3-1).

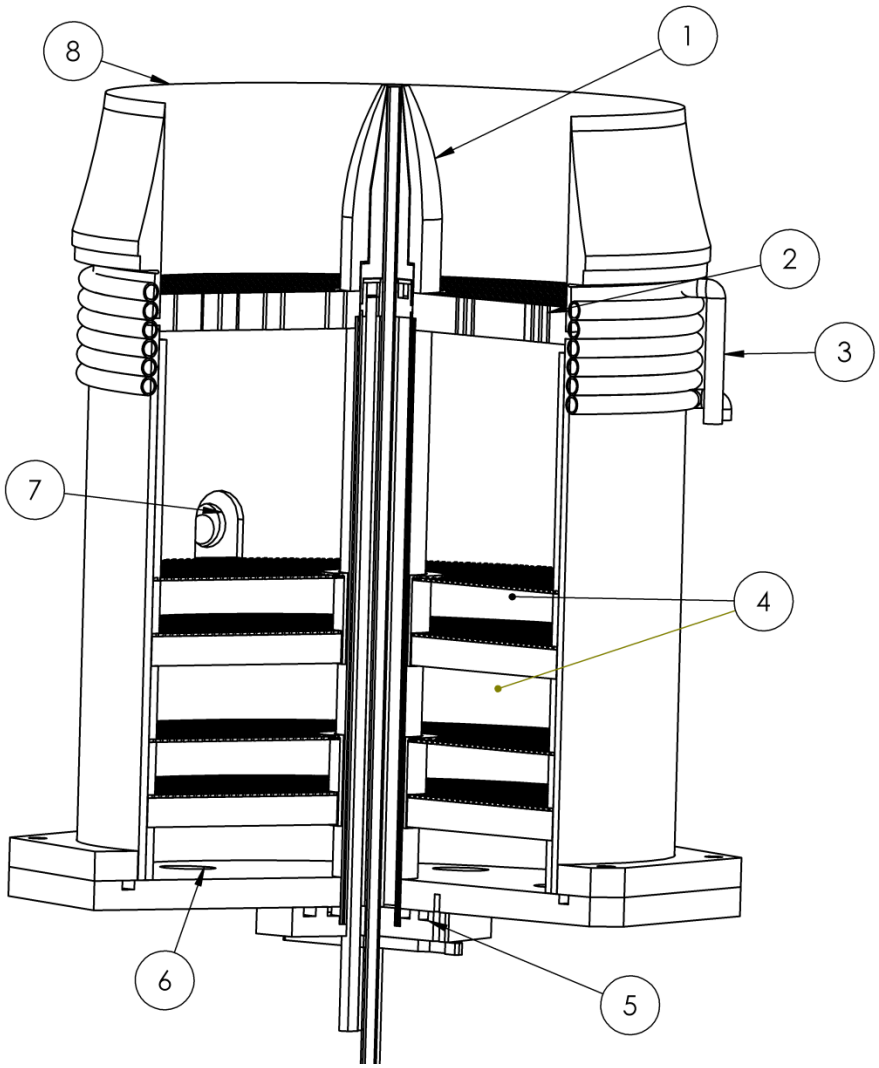

Fig. 10-3 Model of the new burner with active cooling: Actively cooled jet with ceramic shroud 1) Coflow brass plate 2) Body cooling coil 3) Glass bead spacers 4) Jet seal 5) Coflow inlet port 6) Pressure sensing port 7) Coflow shroud 8).

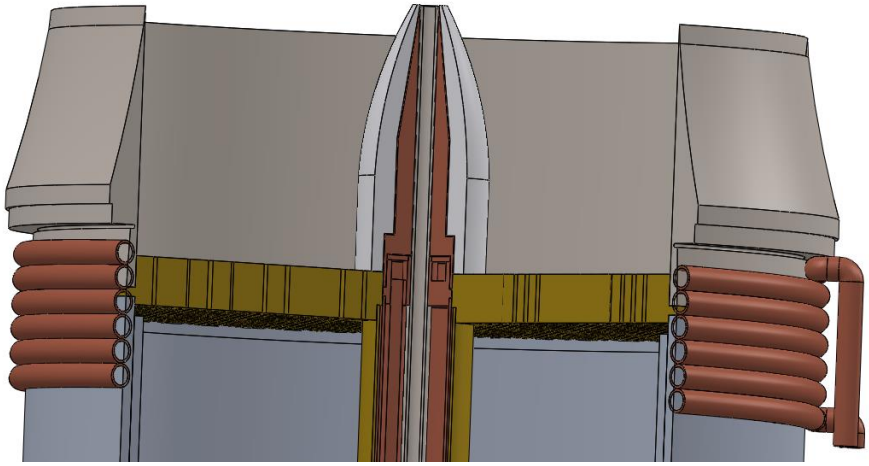

Fig. 10-4 Closer view of the actively cooled jet exit within the coflow brass base plate, including the: copper heat sink and ceramic shroud.

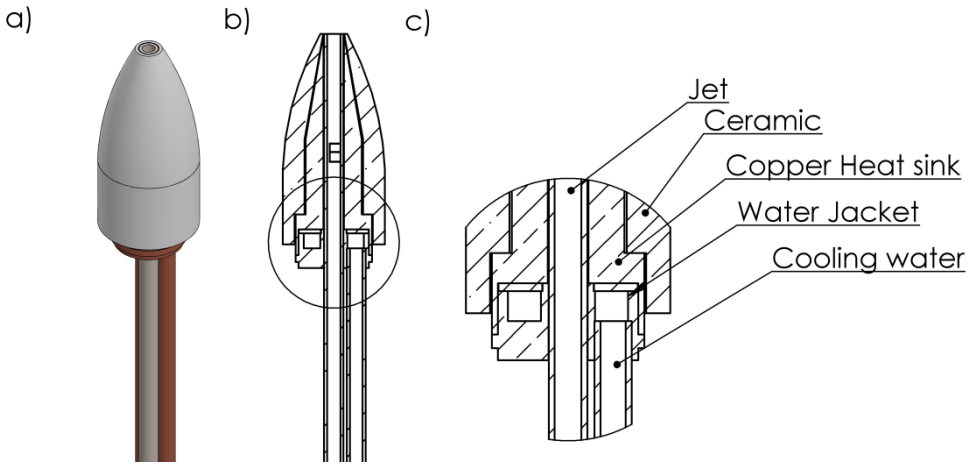

Fig. 10-5 Actively cooled jet and ceramic: a) 3-D view b) Cross section of ceramic and heat sink c) detailed actively cooled jet view with description.

The centering of the jet is achieved by maintaining a small (~0.1-0.2 mm) gap between all concentric tubes: the coflow base plate, burner body and actively cooled jet. Due to the addition of the cooling water running through the burner, the sealing was the largest complication. The top of the burner (Fig. 10-4) was sealed by soldered (or in future press fit) a fixed brass tube into the coflow base plate, this tube runs through the burner, sealing the

fuel jet from the H_2/Air mixture, within the body of the burner. The tube is sealed at the base of the burner by an O-ring and additional sealant (if required) seen in Fig. 10-6. Furthermore, Fig. 10-6 shows the copper tube that runs through the burner to fix the heat sink height. The sealing plate is fastened into the coflow base with 6 x M5 bolts.

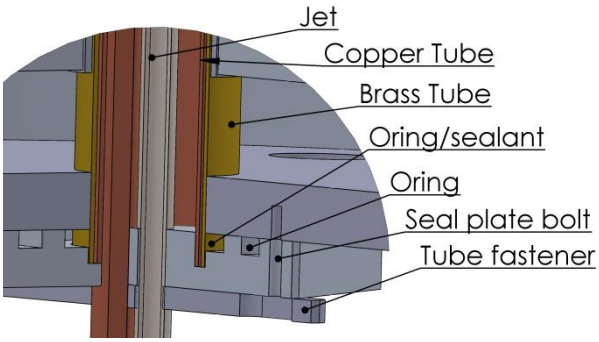

Fig. 10-6 Burner base seal with sealed bass plate.

10.3 **Actively cooled jet, thermal simulation: ANSYS**

A simulation from ANSYS for the new actively cooled burner is seen in Fig. 10-7. It shows that the ceramic heats up significantly more than the copper heat sink, to approximately 800 K, the small air gap between the ceramic and heat sink, has the largest temperature gradient. The coflow is influenced slightly by the new active cooling, forming a small temperature profile close to the ceramic. The new temperature profile for a jet velocity, U_J = 50 m/s, is seen in Fig. 10-8, where almost no preheat occurs: only about 5 K preheat for the U_J = 50 m/s jet and 3 K for a U_J = 100 m/s jet (not displayed).

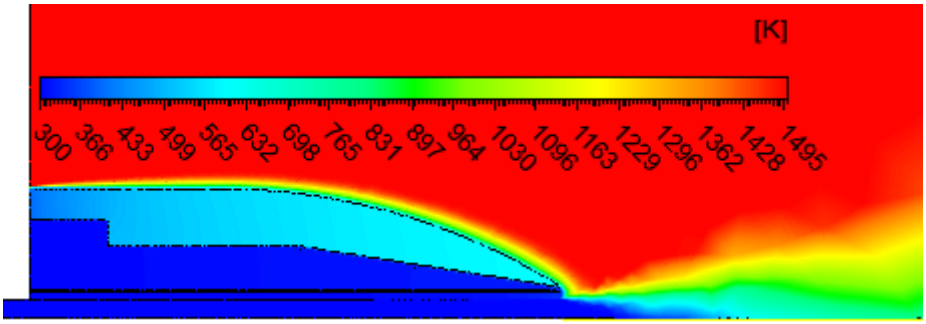

Fig. 10-7 Actively cooled jet temperature profile. The jet velocity is U_J = 50 m/s, issuing into a coflow temperature of T_C = 1500 K with a velocity of V_C = 4 m/s.

A comparison between the previous fuel jet with no insulation and the new actively cooled jet is seen in Fig. 10-8. There is a significant difference between the level of preheat for the two jets, approximately 300 K for a jet velocity of U_J = 50 m/s and a coflow temperature T_C = 1500 K. Furthermore, the axial temperature mixing is also presented, where for the same downstream distance of 180 mm, the uninsulated jet is ~ 100 K hotter.

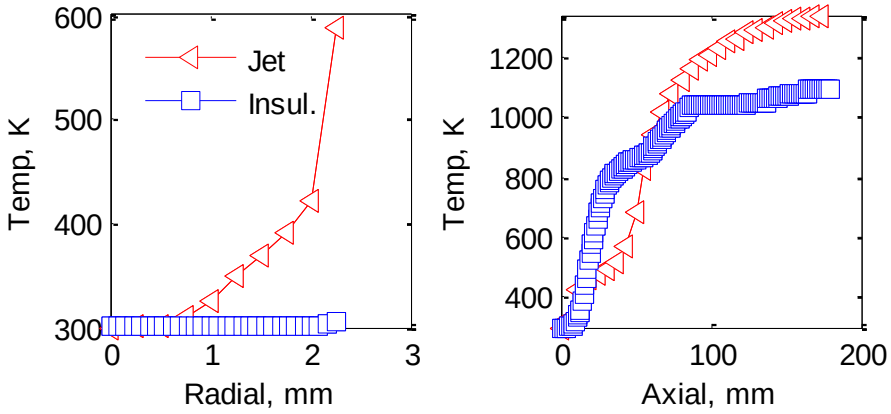

Fig. 10-8 Comparison between the old jet with no insulation and the new insulated/ actively cooled jet.

10.4 Experimental jet preheat effects

With the introduction of the new actively cooled jet tests were done to determine if the coflow temperature range, and its sensitivity with lift-off height has changed or shifted when compared to the old non-insulated nozzle. The comparative cases used were based on older measurements of: air:DME=3:1 and air:CH_4=2:1 (Fig. 4-2). These two cases are of interest to test as they offer a varying sensitivity of lift-off height with coflow temperature (dL_H/dT_C).

DME previously operated between a temperature of, T_C = 1250 K and T_C = 1400 K for a lifted and stable flame, and a low lifted flame respectively. The new burner lift-off heights for DME, seen in Fig. 10-9, has a similar temperature for the unstable, low coflow temperature case, T_C = 1250 K. However, the sensitivity with temperature (dL_H/dT_C) has reduced and the stable coflow temperature has increased to approximately T_C=1430 K, an increase of 30 K. This reduction in sensitivity of the coflow temperature to lift-off height is expected, as at higher coflow temperatures, the temperature difference between the injected fuel and the coflow has increased. Therefore, the conduction through the steel, and the preheat to the jet, for the old burner, is much greater than the cooled jet, particularly, at these higher temperatures.

The influence of higher temperatures and the effect of active cooling, with reduced coflow temperature sensitivity to lift-off height, are further highlighted by the CH_4 fuel jet. The old burner operated between ~ T_C = 1400 – 1520 K, however, the new burner has shifted the unstable flame coflow temperature to ~T_C = 1410 K (a 10 K increase). The new burner like the DME flames has reduced the coflow temperature sensitivity, where the high stable temperature is extrapolated to be ~ 1570 K (a 50 K increase). Higher temperatures were not

tested for CH_4, as the heat conduction through the brass plate and coflow shroud starts to become very large.

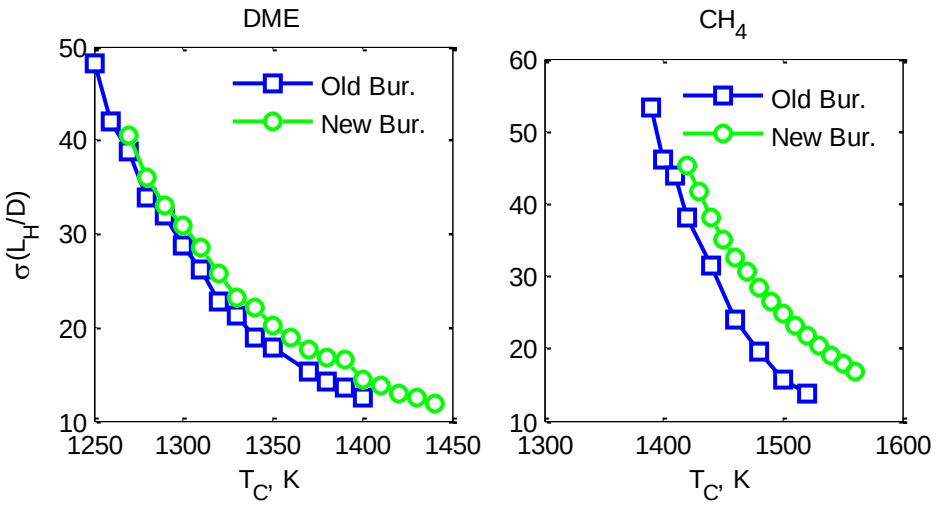

Fig. 10-9 Results for the old burner with preheat and the new burner with active cooling for: DME (left) and CH_4 (right).

The two results for both DME and CH_4, both indicate there is an increasing influence for higher coflow temperatures, this is because the conduction effects through the steel pipe for a non-insulated nozzle has increased. This preheat dependence on coflow temperature is further seen for the hydrogen case (not shown here), where minimal difference between the new and old burner is detected. That is, the lift-off heights with coflow temperature (T_C = 1040 – 1070 K) for the old and new burner are within the precision error of the coflow temperatures and flow meters of the setup ±6 K.

10.5 Methane and hydrogen fuel jet mixing

New measurements for fuel mixing between hydrogen and methane (50/50) with three parts N_2 dilution (H_2/N_2:N_2=0.5/0.5:3) are presented in Fig. 10-10. The lift-off height results are

obtained from the new burner measurements, however, for the coflow temperature range presented, T_C = 1090-1220 K, this would see minimal difference compared to the old burner. The minimal difference is because the coflow temperature is relatively low, and therefore, minimal heat conduction to the uninsulated fuel jet would occur, seen in the above section.

The results presented in Fig. 10-10, is for the mean lift-off heights from the H_2/CH_4:N_2=1:3 case compared to the pure fuel jets: CH_4 and H_2 for three parts dilution with N_2. It is seen that the coflow temperature for which a seated and lifted flame occurs, has been reduced compared to the CH_4 coflow temperature range. That is the temperature range for CH_4 was T_C= 1400 – 1560 K, whilst for the combined jet, H_2/CH_4, the range is: T_C= 1090 – 1220 K, this is closer to the H_2 temperature range of T_C= 1040 – 1070 K. Furthermore, the sensitivity with coflow temperature has been increased (dL_H/dT_C). However, when analysing the flame fluctuation with lift-off height, the new H_2/CH_4 jet is like the methane jet, that is the maximum lift-off height minus the minimum lift-off height is relatively small compared to the pure H_2 jet (Fig. 10-10).

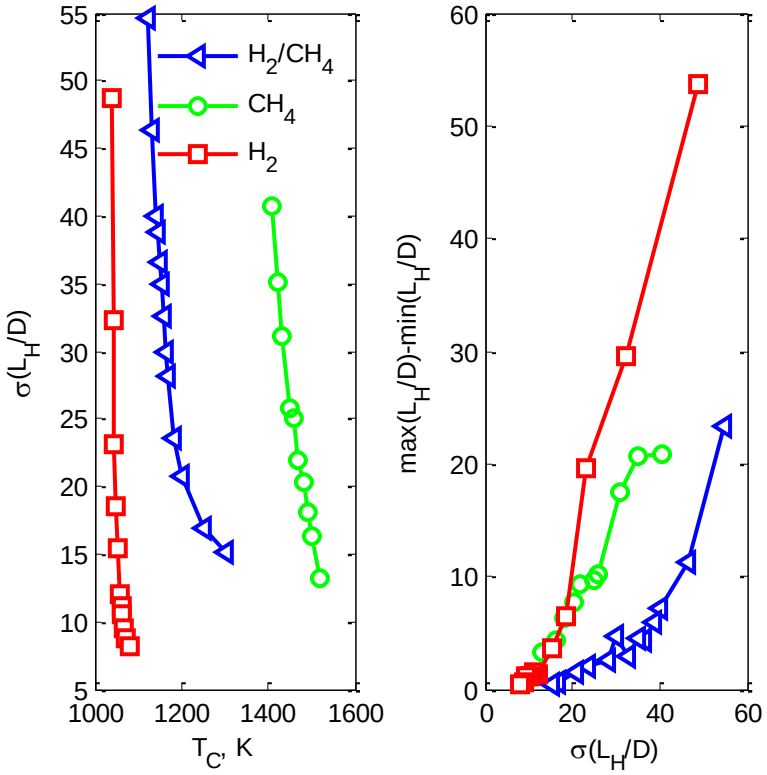

Fig. 10-10 Coflow dependant results for the mean lift-off heights (left) and flame base fluctuation (max – min, right) for the mixing of fuels: H_2 and CH_4, with three parts N_2 dilution.

10.6 **New burner discussion**

This chapter discussed the implications of jet preheat occurring in the old burner due to the jet nozzle exiting 70 mm into the coflow stream. Varying levels of preheat were determined for different fuel velocities in the old burner, where the new actively cooled jet did not have these issues. A comparative study between the sensitivity of lift-off heights and coflow temperature was done between the old and new burner. It is determined that fuels operating under higher coflow temperatures have increasing preheat effects in the old burner.

It is concluded, that the new burner minimises the effects of preheat for fuels issuing into the coflow burner. Therefore, steady temperature boundary conditions can be determined for the inlet of the fuel jet. Furthermore, the sole effect and understanding of lift-off height vs. coflow temperature can be determined, without jet preheat temperature as an uncontrolled variable.

Chapter 11. **Conclusion**

This thesis presented a comprehensive study of autoignition and stabilisation of turbulent lifted flames in the jet in hot coflow burner (JHC). A large range of fuels were investigated using high-speed (10 kHz) flame chemiluminescence imaging with simultaneously acquired acoustic emission measurements. A second experimental campaign utilising high-speed (10 kHz) PLIF measurements of OH combined with volumetric chemiluminescence imaging determined out of plane motion, in H_2 and CH_4 fuelled flames was conducted. In the second experimental campaign for DME fuelled flames, a third high-speed camera and corresponding laser system was added to obtain CH_2O PLIF measurements and obtained simultaneously with the OH PLIF/chemiluminescence measurements. The large CH_2O signal from DME flames combined with the OH PLIF provided high-speed planar heat release results. Laminar flame calculations were employed to interpret and explain the measurements and phenomena observed in the JHC experiments. The following conclusions and observations are drawn from the work presented in this thesis:

- For all conditions and fuels studied, a "high coflow temperature flame" was stabilised near the jet exit plane of the JHC burner, featuring small temporal axial fluctuation in the flame base's leading edge. A decrease in the coflow temperature produced the "low coflow temperature case", it featured a high mean lift-off height with large axial oscillations in the flame base.
- For a given jet velocity, flames utilising H_2 and CH_4 as fuels were found to have the greatest and least sensitivity to coflow temperature respectively. To achieve the same mean lift-off height of other hydrocarbons studied, including DME, temperatures within the coflow temperature bounds of H_2 and CH_4 were required. It was found that

the RMS of the flame lift-off height increases approximately linearly with increasing mean lift-off height, however, the rate of increase of the RMS flame lift-off height with mean lift-off height was found to be fuel dependent.

- For all fuels, particularly at low coflow temperatures, the similar axial location of the mean and similar distribution shape of the kernel formation PDF and the flame base PDF indicates that all flames are stabilised by ignition kernels. The dominant stabilisation mechanism in these flames is due to an ignition kernel forming upstream of the flame base that is constantly advecting downstream, the kernels grow quickly and merge with the flame base, hence moving the new the flame base to be upstream. The higher coflow temperature cases, however, are less dependent on this mechanism, with premixed stabilisation seemingly more important.
- Sound measurements indicated that increased sound levels were emitted for high lift-off flames that feature autoignition. The most significant finding that was only obtainable though joint high-speed chemiluminescence measurements, was that for all of the fuels studied sound emission was not due to autoignition kernel formation. Even the distinctive 'popping' sounds produced from the H_2 flame were found not to correlate with the formation of new ignition kernels. The intermittent large acoustic emission events generated by the low coflow temperature flames were found to correlate with flame front annihilation events, produced from the merging of large ignition kernels with the main flame base.
- To verify that all fuels are predominantly stabilised by autoignition, particularly at low temperatures, autoignition delay times were calculated and compared to experimental lift-off heights. A linear correlation between the delay times and experimental lift-off height, for a given coflow temperature, was observed, confirming that autoignition is a strong mechanism that controls the stabilisation of

these lifted flames. At higher coflow temperatures the correlation between the delay time and lift-off height is not as ‘strong’, and potentially free flame propagation is more prevalent.

- Utilising DME as a fuel and performing simultaneous PLIF of OH and CH_2O, planar measurements of heat release were measured at high-speed. The measurements verify that at high coflow temperatures, flames have reduced dependence on ignition kernels for stabilisation. The lower coflow temperature cases produced ignition kernels with greater heat release, for all kernel sizes, this indicated a greater influence of kernels for the overall flame stabilisation.
- Using counter-flow simulations, the different heat release levels between high and low coflow temperatures, from the DME PLIF experiment, were identified. Greater heat release was measured for the lower coflow temperature due to the kernels igniting in richer mixtures (still leaner than stoichiometry).
- The numerical studies show for the DME flames studied, at the coflow temperatures investigated, that no NTC behaviour occurred. The formation of OH and the overlap onto CH_2O only occurs in regions with high-temperature chemical pathways, without competing low-temperature reactions.
- A separate unsteady study, on CH_4, using counter-flow and premixed flames was found to be an excellent tool to study autoignition. In addition to detailed chemical kinetics, this reactor captures two important phenomena: gradients of velocity and scalars, as well as allowing diffusion as a transport mechanism. The analysis of transport budgets of CH_2O identifies that convection and reaction fluxes are dominant in the lead up to ignition, with a unity balance of diffusion and production established at ignition. Increased strain rate increases delay times, due to an increase in species convection. The premixed flame study agrees with previous DNS and numerical

studies, where convection and production fluxes are dominant when autoignition temperatures are exceeded.

- Finally, this thesis introduced a new actively cooled vitiated coflow burner, where the fuel jet is actively cooled and insulated from the coflow. The new burner prevents significant heat transfer to and from the hot coflow to the central jet and minimises the jet preheat variations for different jet velocities and coflow temperatures. Testing using the new burner identified that the effect of preheat was larger for fuels that required higher coflow temperatures, such as CH_4.

Through the comprehensive experimental and numerical investigations on the turbulent coflow burner, in this thesis, a greater understanding on the universal nature of autoignition based stabilisation for fuels was determined. However, despite all fuels being stabilised through autoignition kernels, there are varying degrees of the dependence between high and low-coflow temperatures. This observation needs further examination as described in the following future work section.

Chapter 12. **Future work**

The findings from this thesis were focused on exploring kernel ignition evolution and the dynamics of the ignition kernel and flame base interaction. However, during these studies inevitably many potential areas for further investigation were uncovered. Some ideas for further study are briefly outlined below.

For all of the studies employed in this thesis the hot coflow temperature was varied by adjusting the equivalence ratio of the hydrogen-air premixture, thereby varying the concentration of O_2 in the hot coflow products with coflow temperature. A worthy area of further study would be to hold constant the O_2 content within the hot coflow when the hot coflow temperature is varied. By controlling the O_2 level in the hot coflow it would be possible to delineate the influence of temperature and O_2 concentration on the flame lift-off height and flame dynamics observed in the measurements reported in this thesis. Simultaneous control of the O_2 levels and temperature of the hot coflow could be achieved by adding an additional O_2 or N_2 stream to the existing hydrogen-air premixed stream used for the hot coflow.

One of the primary tasks of this thesis was the analysis high-speed imaging results with a significant finding that chemiluminescence alone could be used to identify the importance of ignition kernels to feeding into the flame base. Flame base and kernel dynamics were analysed with reference to a stationary global reference frame in both the: chemiluminescence and planar imaging campaigns with no information of the local velocity fields. The kernel leading edge velocity was found to be greater than the flame base advection velocity in a global reference frame, with knowledge of the local velocity fields the true local

flame speed of the flame base and kernel could be determined which would be very valuable. The necessary velocity measurements could be obtained using stereoscopic or tomographic PIV combined with chemiluminescence imaging or multiplane OH imaging.

The kernel tracking and ignition of kernels in the high-speed PLIF study were based on the imaging of OH, whereas numerical simulations indicate that precursor radicals such as HO_2 or CH_3 would be complementary indicators of early-stage autoignition. Therefore, it would be beneficial to image these radicals in addition to the already imaged CH_2O radical. Furthermore, it was not possible to conclusively identify ignition kernels using only CH_2O, since the entire jet produces some level of CH_2O, owing to low-temperature reactions. Therefore, time resolved velocity measurements that would allow identification of turbulent mixing structures may prove useful to indicate and track, in addition to CH_2O, early stage ignition.

The high spatial resolution and sensitivity of the OH-PLIF measurements compared to the chemiluminescence measurements could identify small ignition kernels, however, the new kernel formation rate from the OH-PLIF was found to be greater than that from the chemiluminescence measurements. As such, it is necessary to further analyse the effect of camera sensitivity, for ignition kernels and further the correlation for the formation of OH with chemiluminescence (CH^*, OH^*, H_2O^* and HO_2^*), their relative temporal and spatial formation. The increased formation rate from the OH-PLIF is biased to some degree from kernels forming outside the laser plane, advecting or growing into the sheet and hence positively biasing the formation rate. Therefore, multi-planar OH or volumetric OH LIF followed by tomographic OH reconstruction, as done by Pareja et al. [211], could be used to construct 3-D kernels, thereby verify the kernel shape, origin and further the absolute unbiased formation rate of kernels.

The lower heat release for higher coflow temperatures is believed to be due to the kernels igniting in leaner mixtures, as such, detailed multi-scalar measurements to determine mixture fraction are required to verify this hypothesis. Such multi-scalar measurements such as line based Raman-Rayleigh-CO/OH LIF would also be invaluable for the determination of composition, scalar gradients and scalar dissipation in many regions of the flame as well as between the high and low coflow temperature flames.

An initial scoping study on the effect of N_2O on flame lift-off heights was investigated in this thesis. However, a larger study on the effect of other sensitisers such as N_2O, NO, H_2O_2 and O_3 would be of interest, this would identify the impact of varying autoignition delay times without significantly altering flame speeds.

Another parameter of interest would be to investigate further the effect of significantly and systematically increasing or decreasing the stoichiometric mixture fraction, using heavier fuels (liquid fuels at room temperature). Furthermore, an area for further investigation is the effect of Reynolds number upon kernel formation and lift-off heights. It was mentioned in this thesis that CH_4 has a small change in Reynolds number for increased premixing, investigating this phenomenon would help identify how these flames are affected by a change in stoichiometry, without significantly altering the turbulence levels. An additional study on the effect of turbulence for this burner is to vary the nozzle diameter or induce turbulence by the addition of a grid/swirl.

Finally, the new actively cooled burner is proposed to be the focus of measurements in the future since it provides stable temperature boundary conditions for fuel jets entering the coflow stream. This new burner provides well defined temperature and in turn velocity

boundary conditions and profiles for both: numerical modelling and experimental investigations that explore large ranges of jet velocities and hot coflow temperatures.

Chapter 13. **Appendix**

A.1

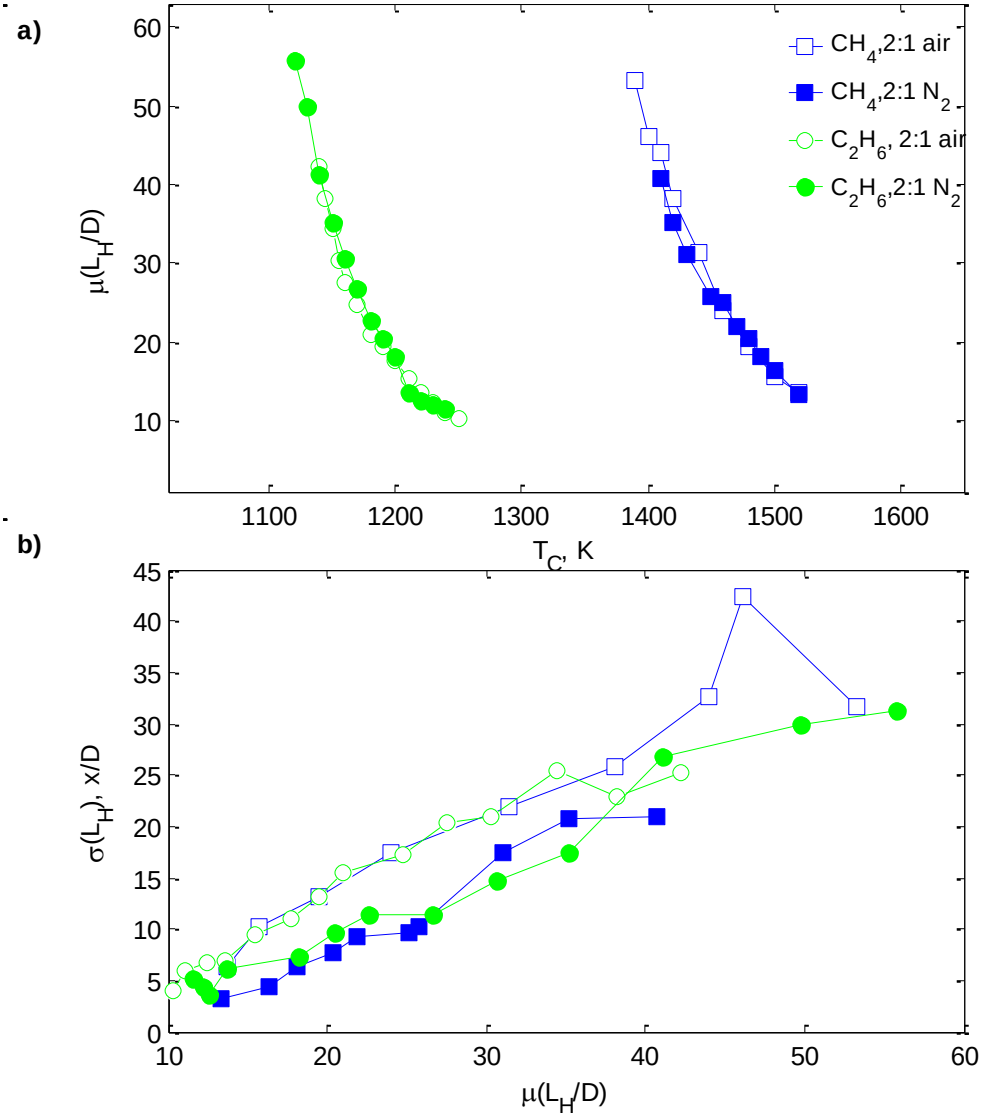

A. 1 Mean lift-off heights (L_H) vs. coflow temperature (a) and lift-off height standard deviation vs. mean lift-off height (b). Fuels and the degrees of nitrogen dilution is shown in the legend for each case.

B.1

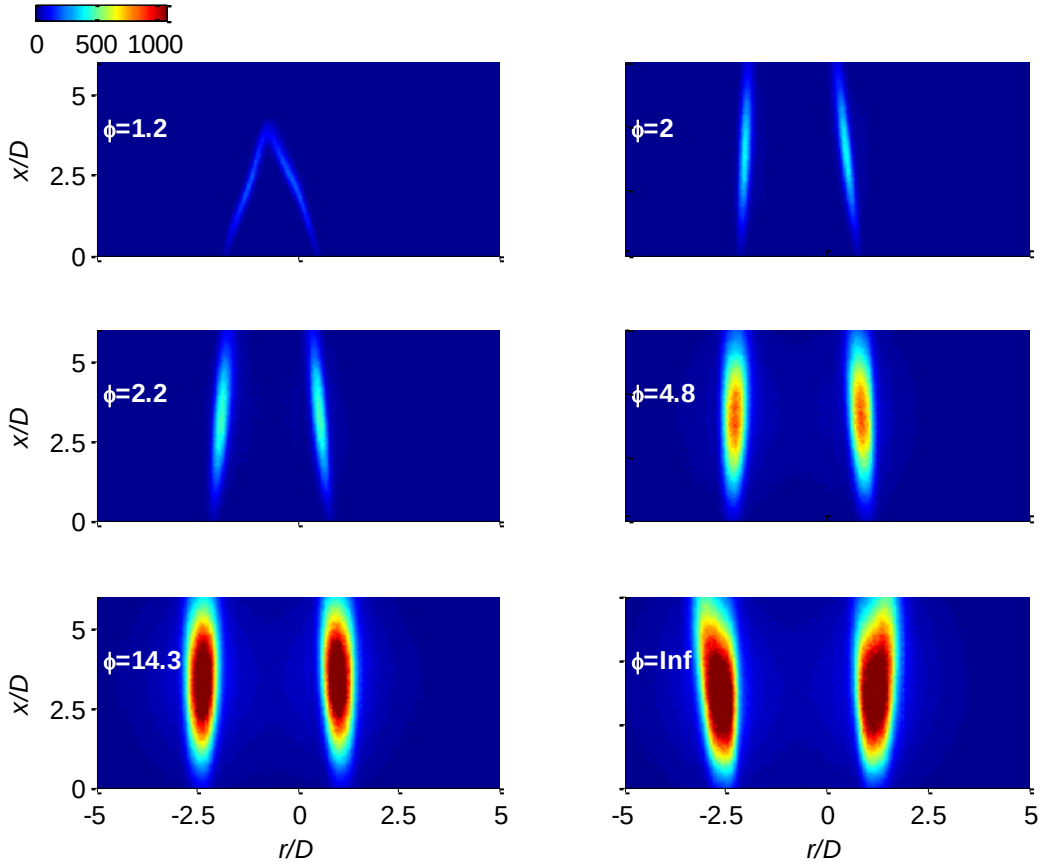

B. 1 CH_2O fluorescence signal (counts) for various Bunsen equivalence ratios for DME flames with air mixing. The colour map intensity is common between all profiles; a pure DME flame has the highest CH_2O signal.

B.2

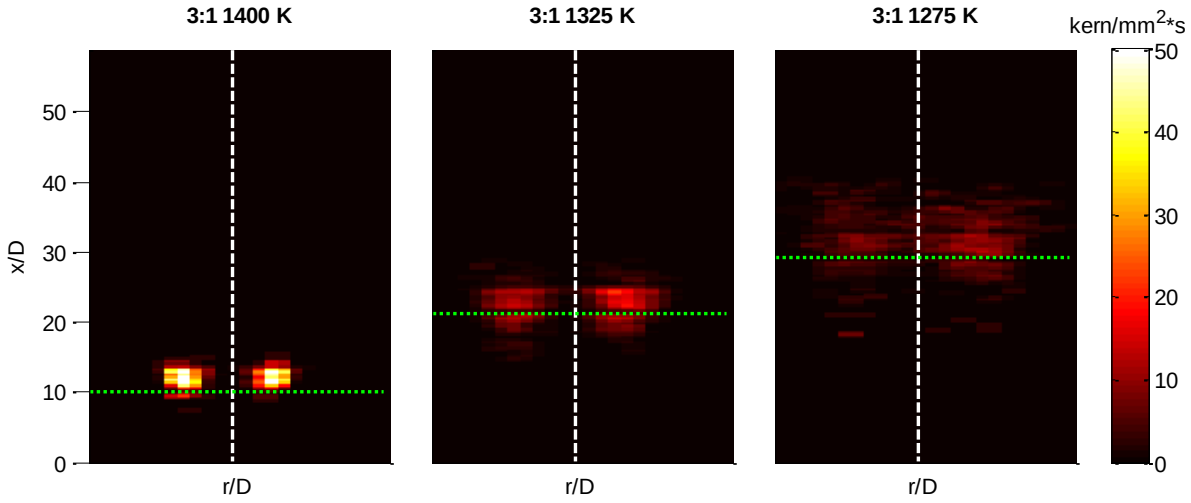

B. 2 2-D OH-Kernel formation map for air: DME =3:1 flames, for three coflow temperatures: T_C = 1400 K, 1325 K and 1275 K. The colour bar indicates spatial formation rates (kern/mm^2*s). The horizontal dotted line marks the mean lift-off height and the vertical dashed line indicates the jet centre-line.

B.3

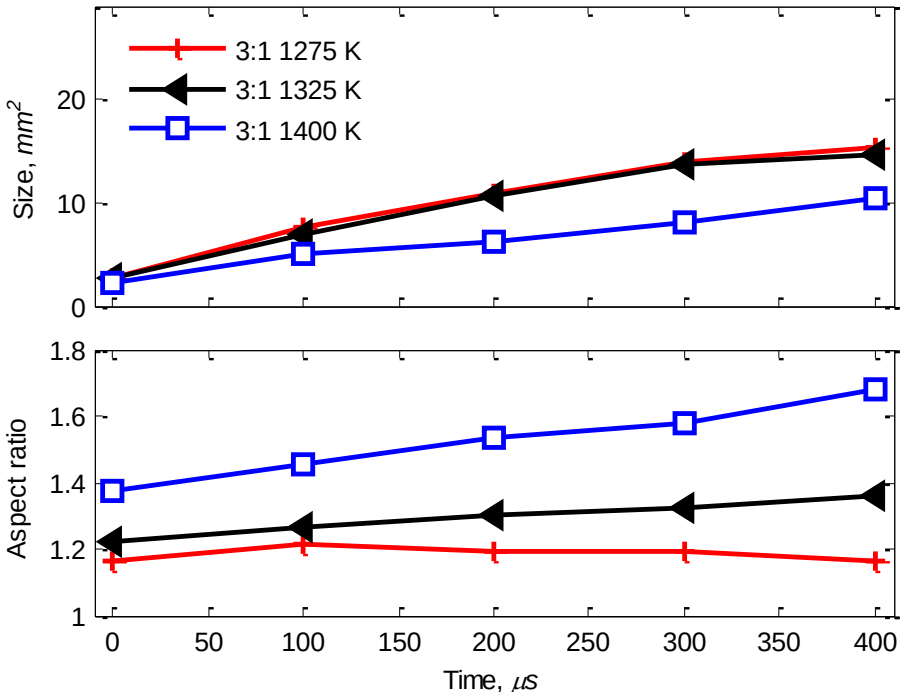

B. 3 2-D kernel growth of size (top) and aspect ratio (length/width) with respect to time from kernel initiation, for premixing of air:DME = 3:1. Three coflow temperatures are presented: T_C = 1275 K, 1325 K and 1400 K.

B.4

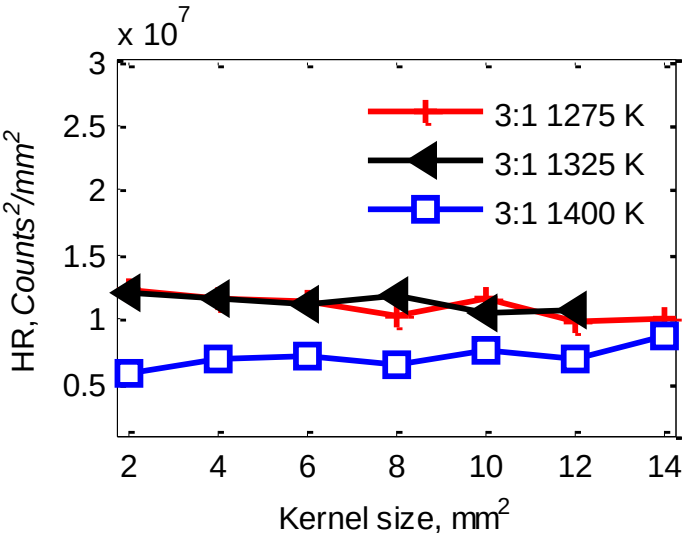

B. 4 Normalised kernel heat release with kernel size versus kernel size for premixing of air:DME = 3:1. Three coflow temperatures are presented: T_C = 1275 K, 1325 K and 1400 K.

B.5

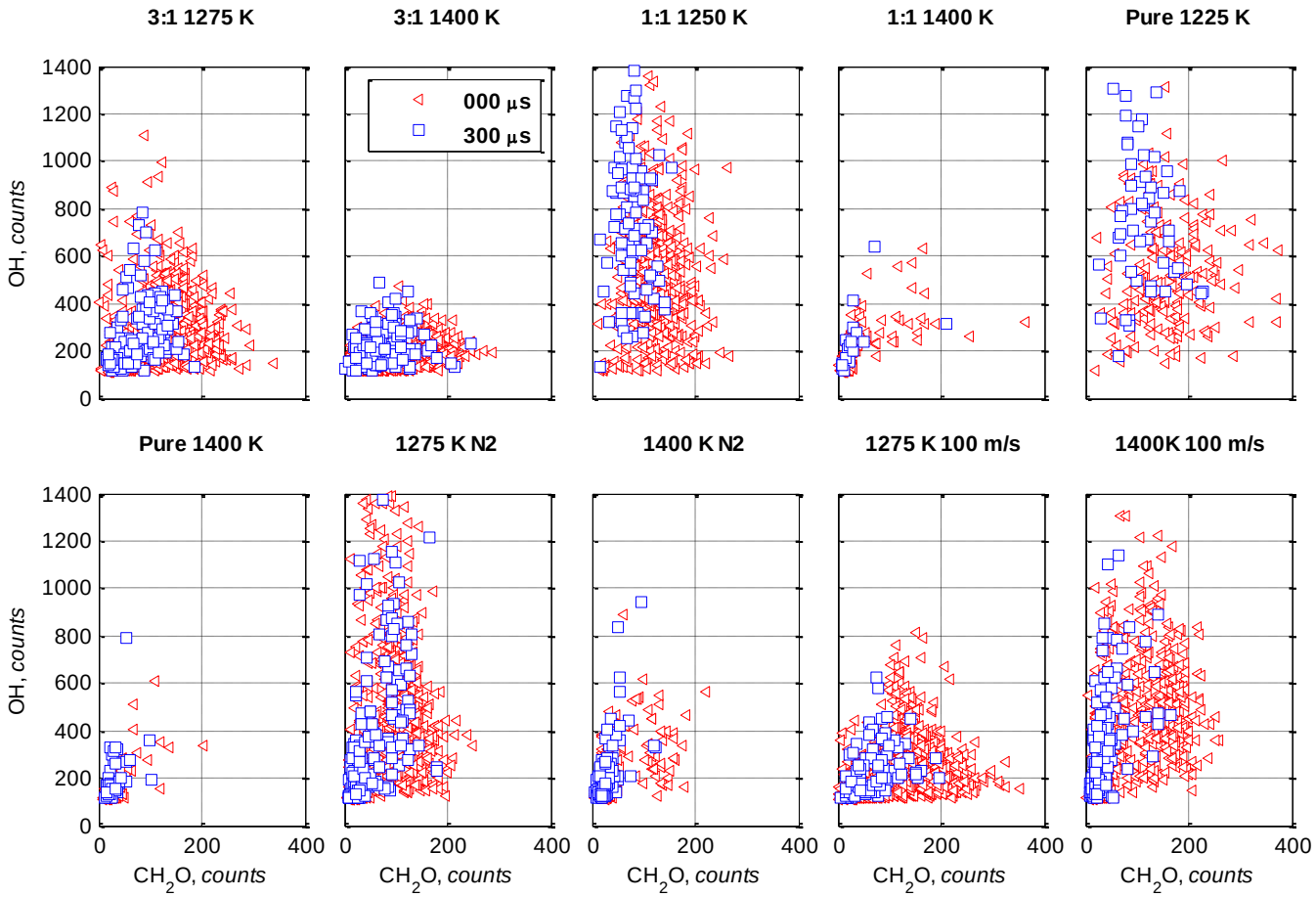

B. 5 Scatter plots of OH vs. CH_2O for all fuels (premixing with air, dilution with nitrogen and two velocity cases) studied in the DME PLIF experiment, including a high and low coflow temperature. Scatter plots for two times are presented, 000 µs (triangles) is defined as kernel initiation and kernel growth after 300 µs (squares) is given (third 10 kHz PLIF image).

B.6

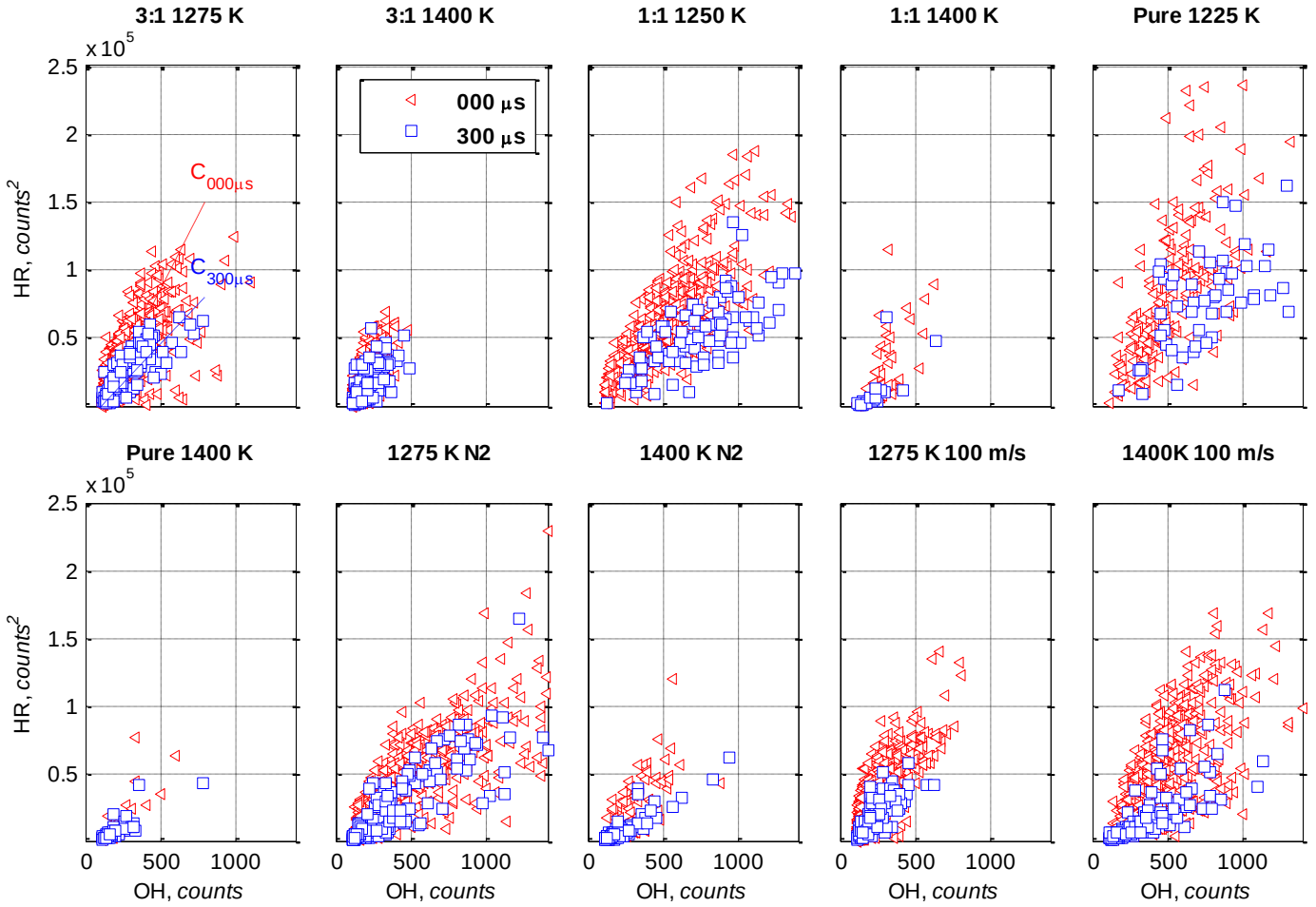

B. 6 Scatter plots of OH vs. *HR* for all fuels (premixing with air, dilution with nitrogen and two velocity cases) studied in the DME PLIF experiment, including a high and low coflow temperature. Scatter plots for two times are presented, 000 µs (triangles) is defined as kernel initiation and kernel growth after 300 µs (squares) is given (third 10 kHz PLIF image).

B.7

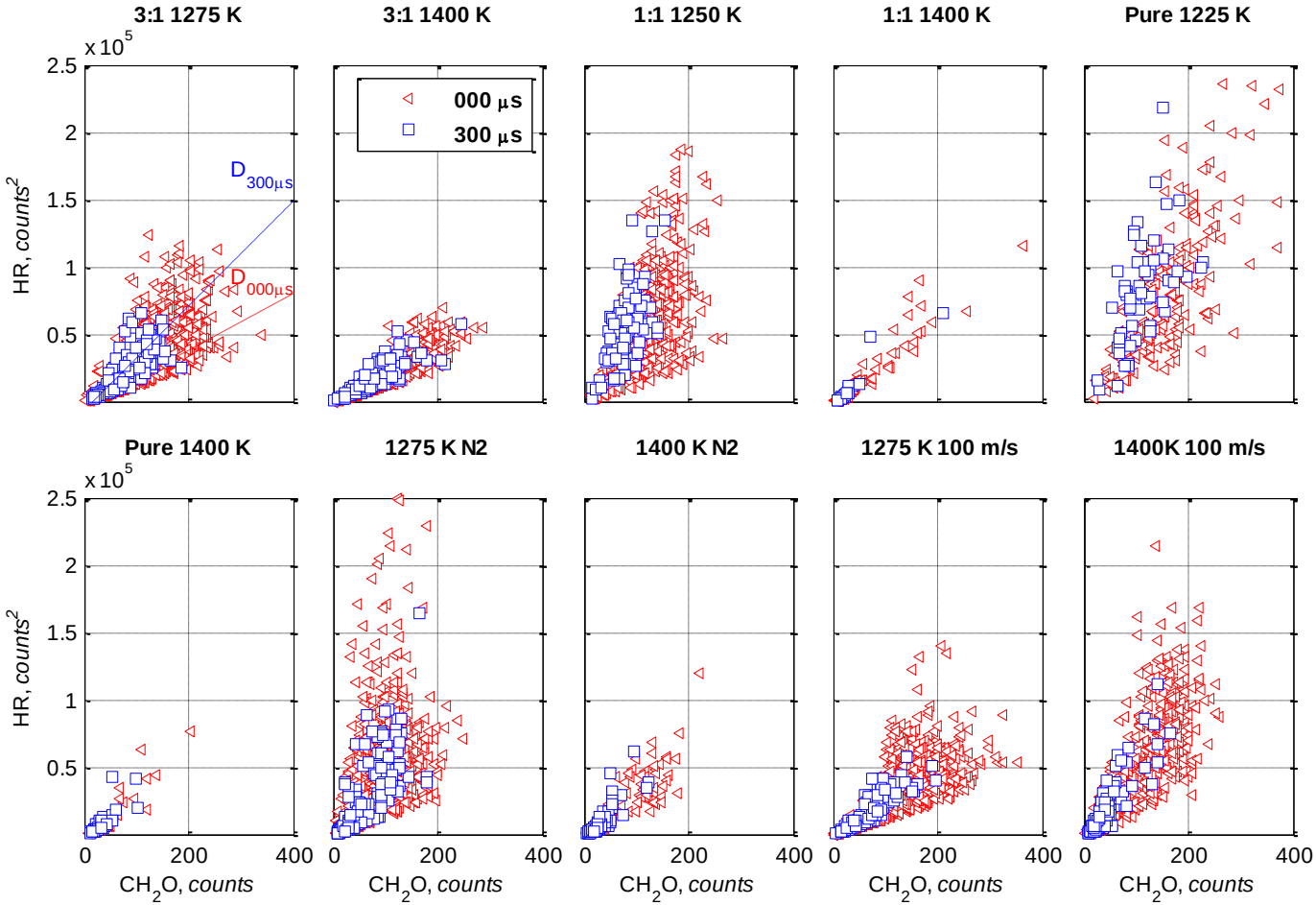

B. 7 Scatter plots of CH_2O vs *HR* for all fuels (premixing with air, dilution with nitrogen and two velocity cases) studied in the DME PLIF experiment, including a high and low coflow temperature. Scatter plots for two times are presented, 000 µs (triangles) is defined as kernel initiation and kernel growth after 300 µs (squares) is given (third 10 kHz PLIF image).

B.8

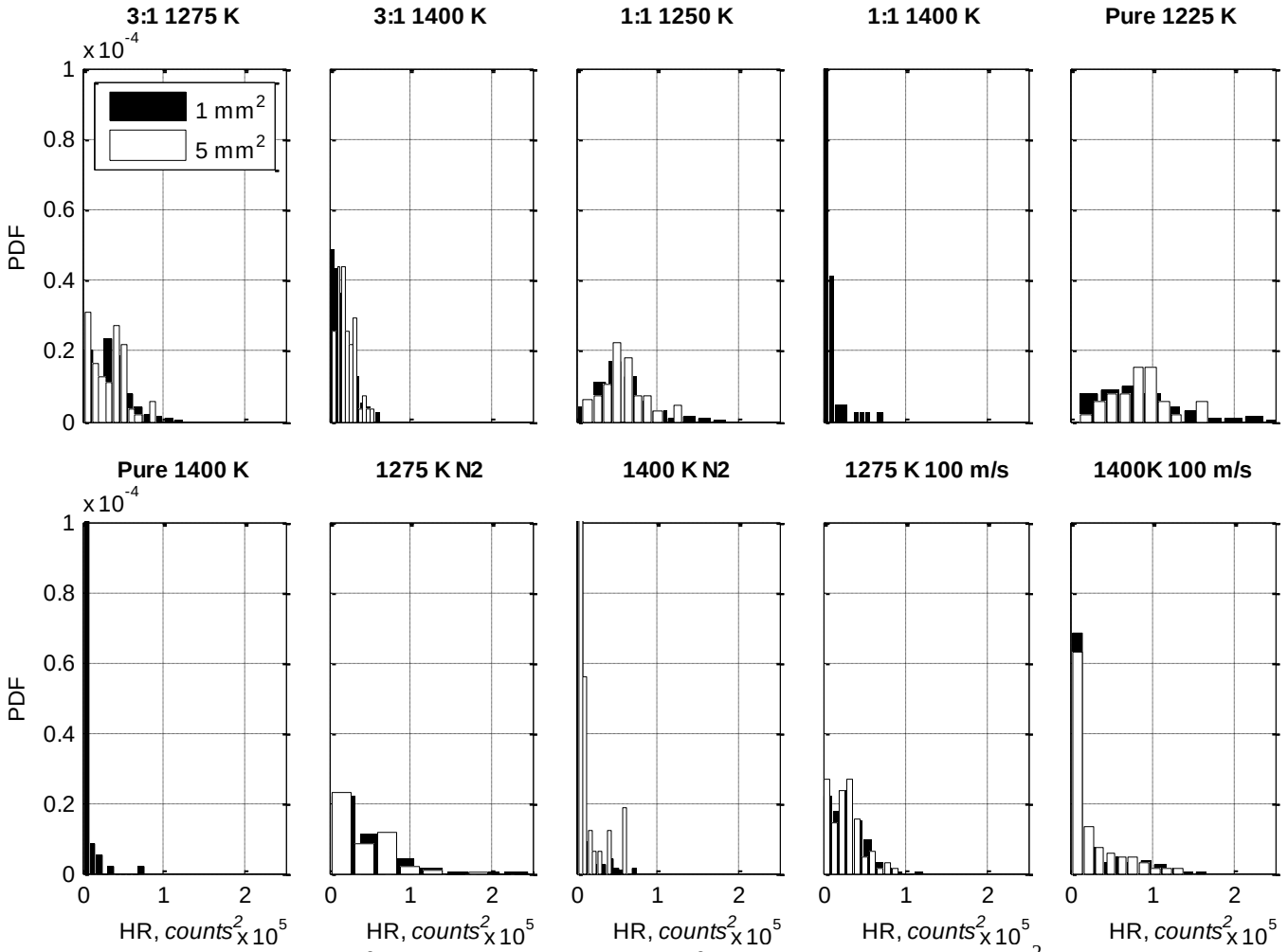

B. 8 Size normalised heat release (CH_2O x OH) PDF for varying diluents and coflow temperatures. A 1 mm^2 kernel represents kernel initiation, 1:1 and pure DME kernels don't grow up to 5 mm^2 so are not presented.

C.1

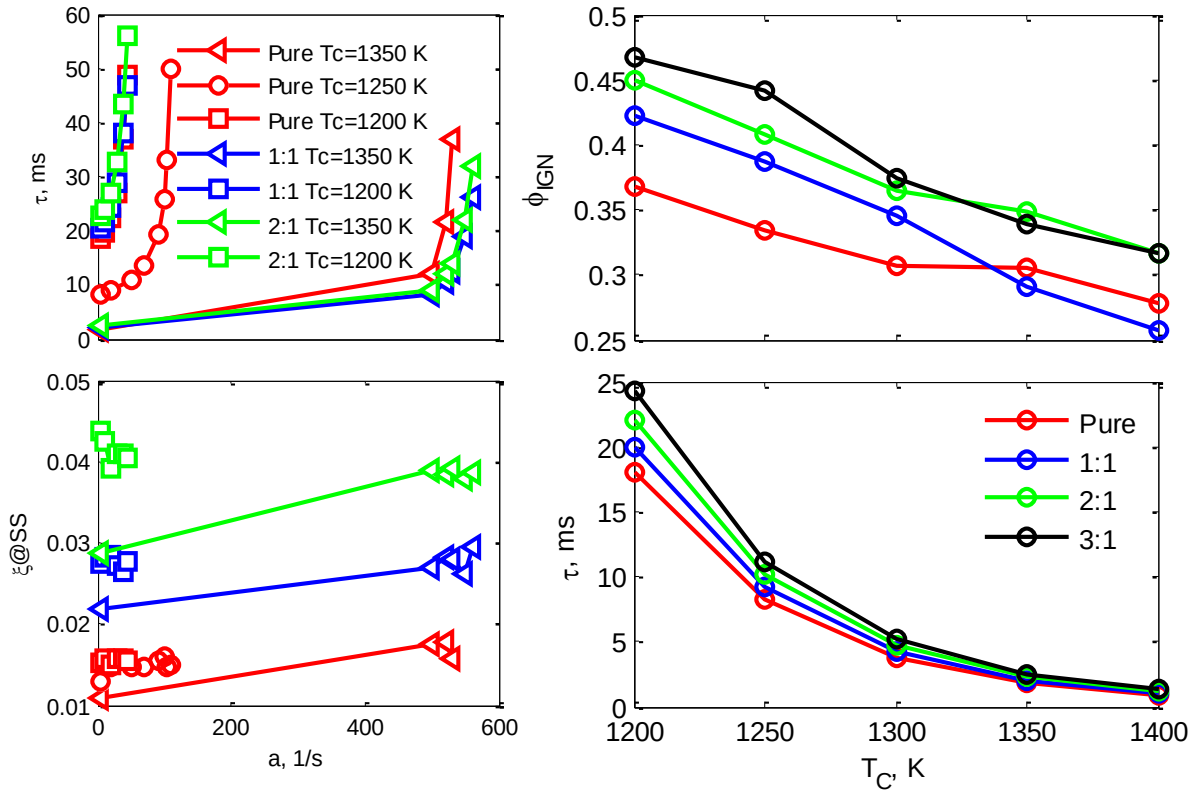

C. 1 Counter-flow simulations using propane. The left figure presents ignition delay times and the most reactive mixture fractions for a range of premixing ratios versus strain rates, for three coflow temperatures. The right figure presents ignition equivalence ratios and delay times for a range of premixing ratios versus coflow temperatures.

C.2

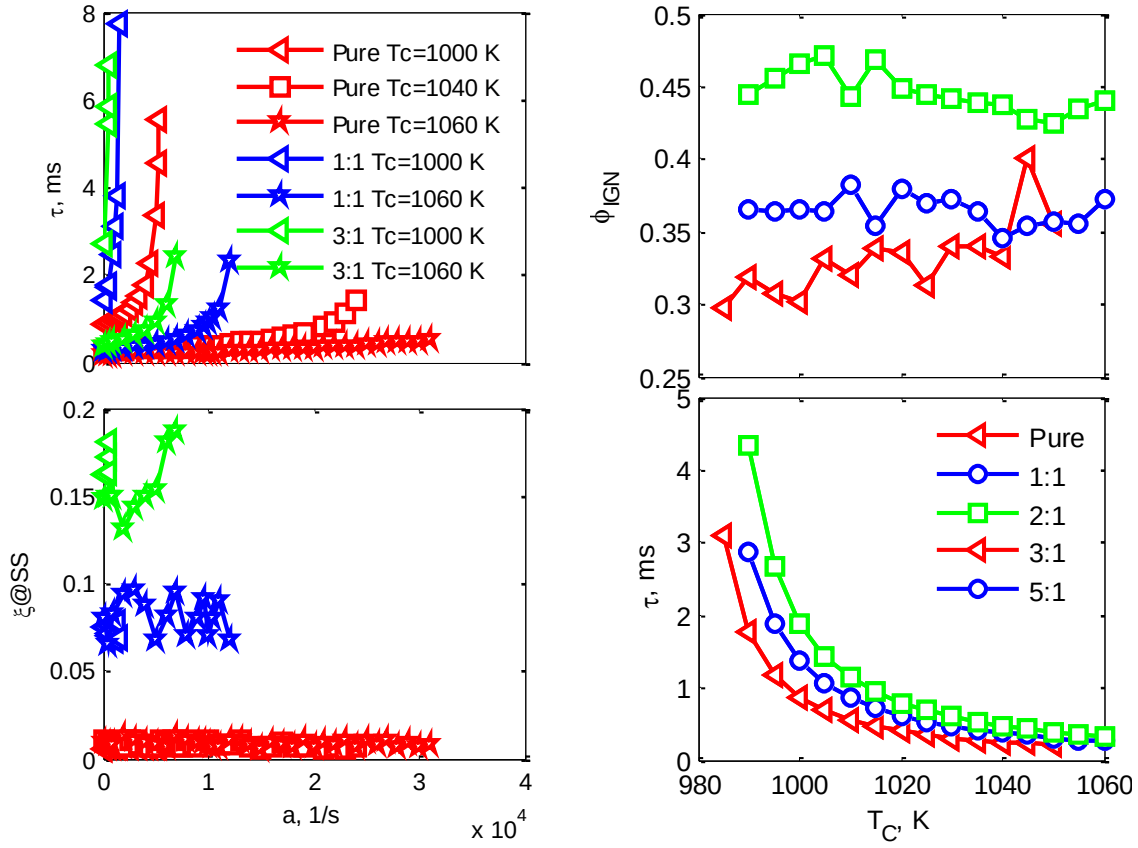

C. 2 Counter-flow simulations using H_2. The left figure presents ignition delay times and the most reactive mixture fractions for a range of premixing ratios versus strain rates, for three coflow temperatures. The right figure presents ignition equivalence ratios and delay times for a range of premixing ratios versus coflow temperatures.

C.3

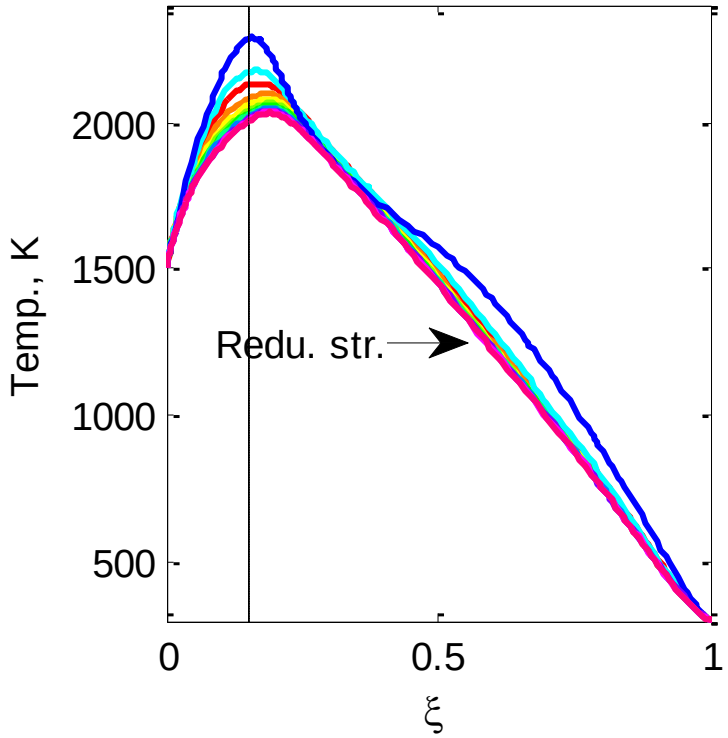

C. 3 Chemkin steady state calculations for reducing strain rates (redu. Str.) for a 2:1 premixed air:methane jet opposed against a *T*c = 1500 K equilibrated H_2/air coflow.

C.4

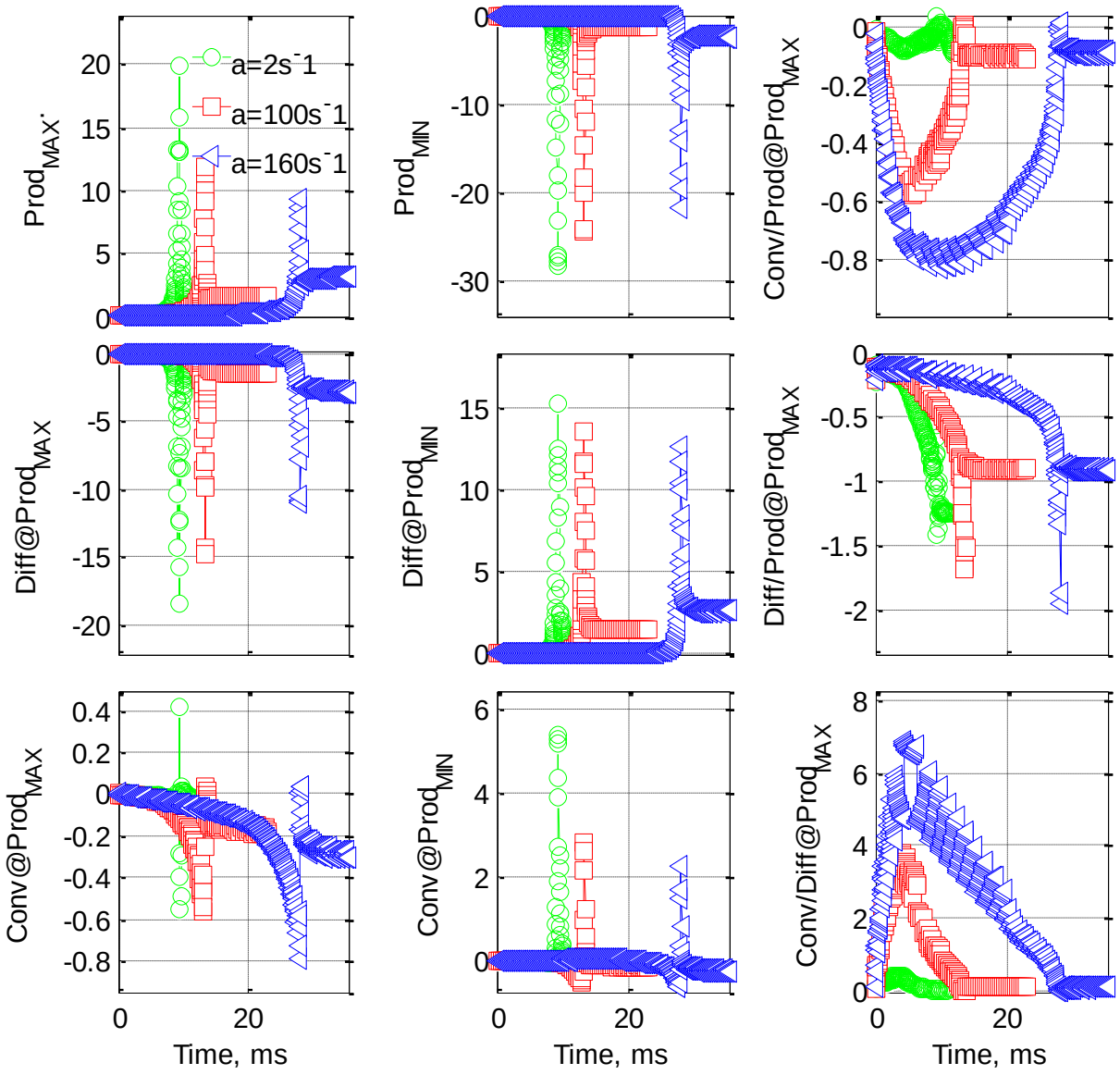

C. 4 Results for the maximum production flux of CH_2O and the equivalent diffusion and convective flux (column 1) at a single strain rate, a = 2, 100 and 160 s^{-1}, for pure CH_4 opposed against a coflow temperature T_C = 1300 K. Ratios between the production, diffusion and convection flux are given for the corresponding maximum production flux within the reactor domain (column 2).

C.5

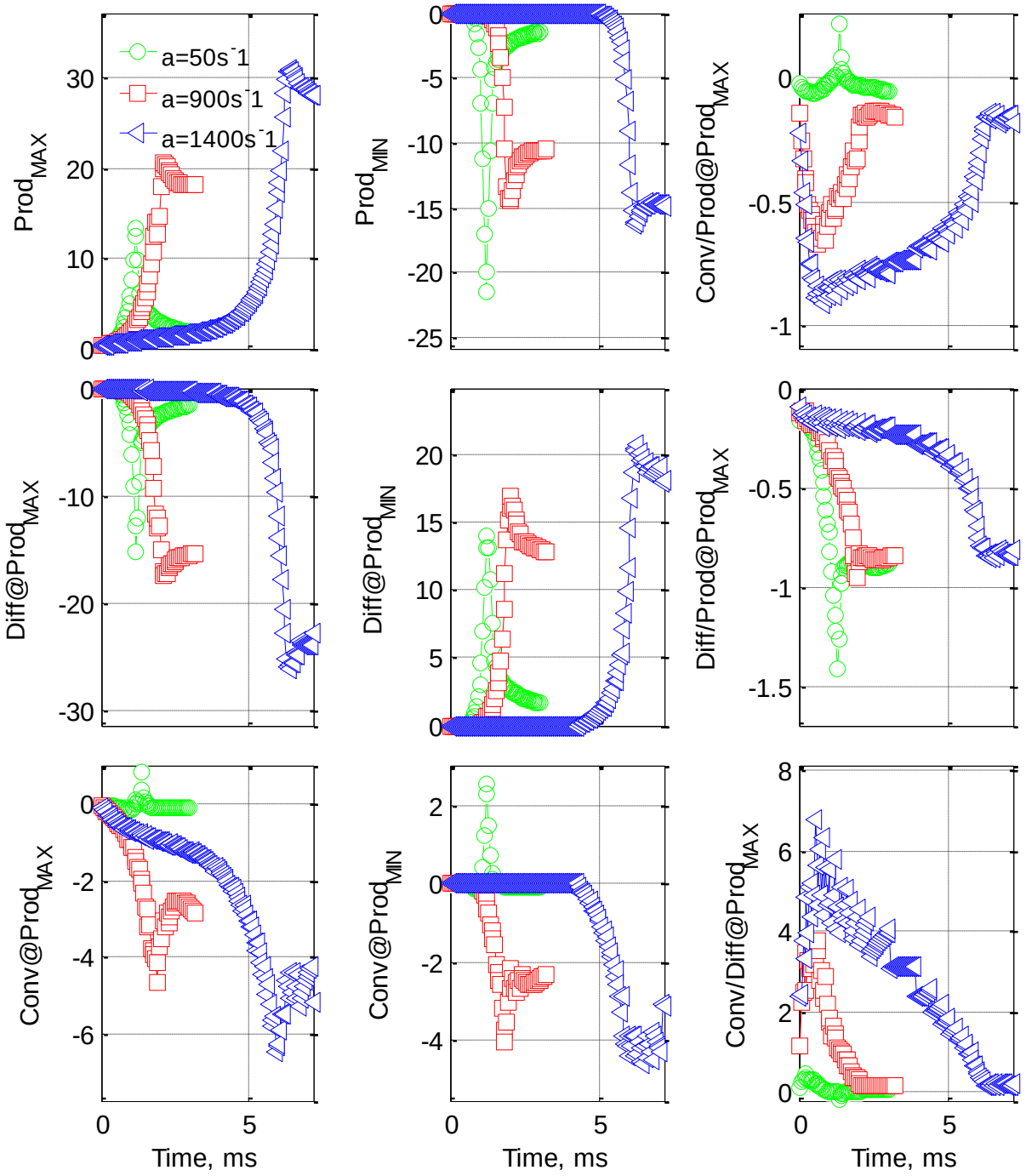

C. 5 Results for the maximum production flux of CH_2O and the equivalent diffusion and convective flux (column 1) at a single strain rate, a = 50, 900 and 1400 s^{-1}, for pure CH_4 opposed against a coflow temperature T_C = 1500 K. Ratios between the production, diffusion and convection flux are given for the corresponding maximum production flux within the reactor domain (column 2).

D.1

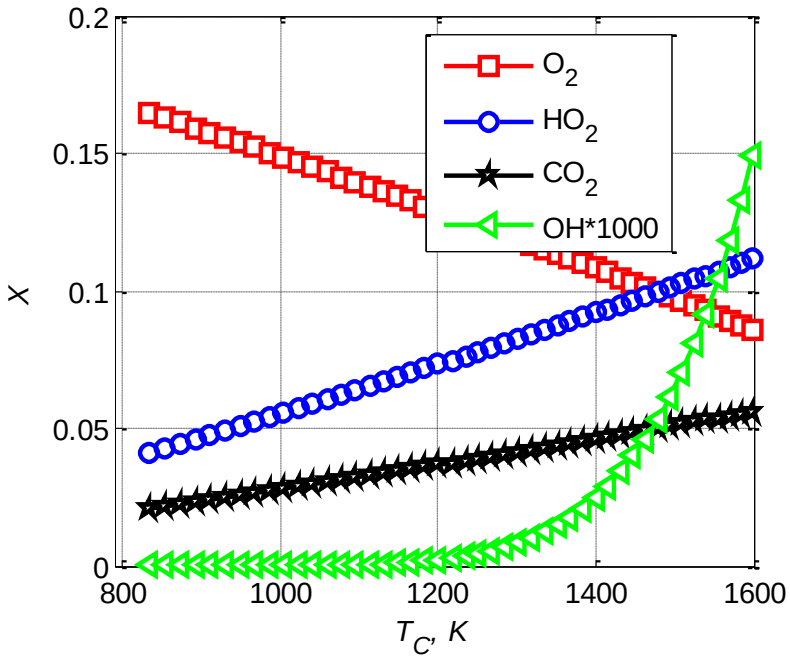

D. 1 Species mole fractions for the equilibrium of CH_4/air for a range of coflow temperatures.

D.2

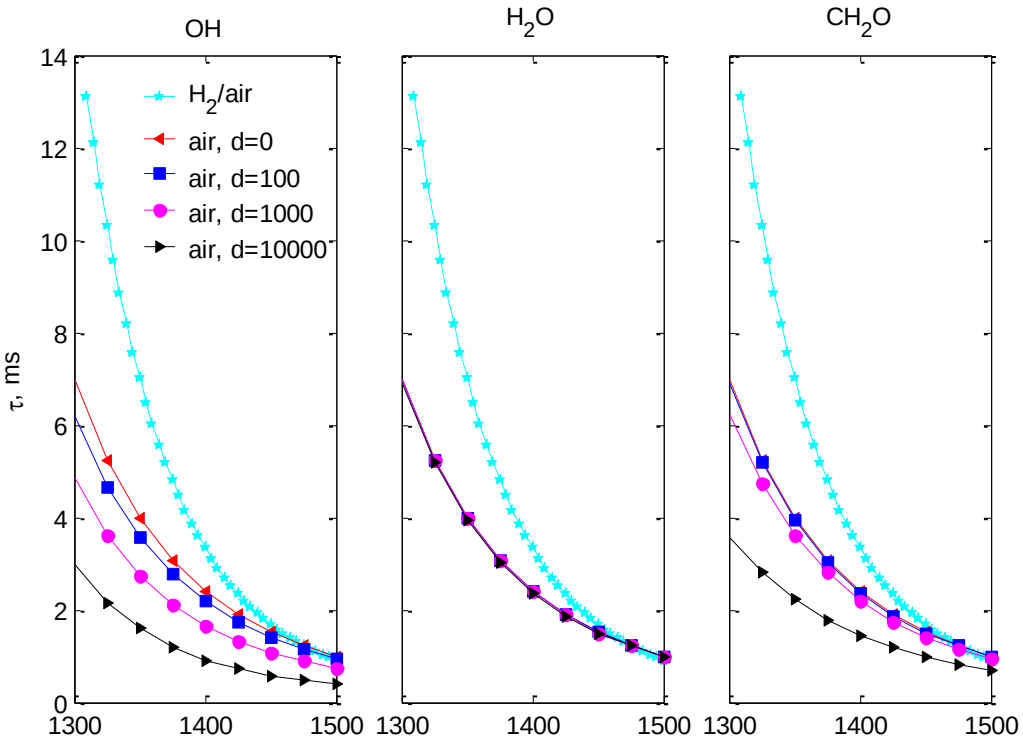

D. 2 The effect of the addition of OH, H_2O and CH_2O in ppm on ignition delay times for an air coflow for a pure CH_4 fuel, with comparative delay times from a H_2/air coflow.

D.3

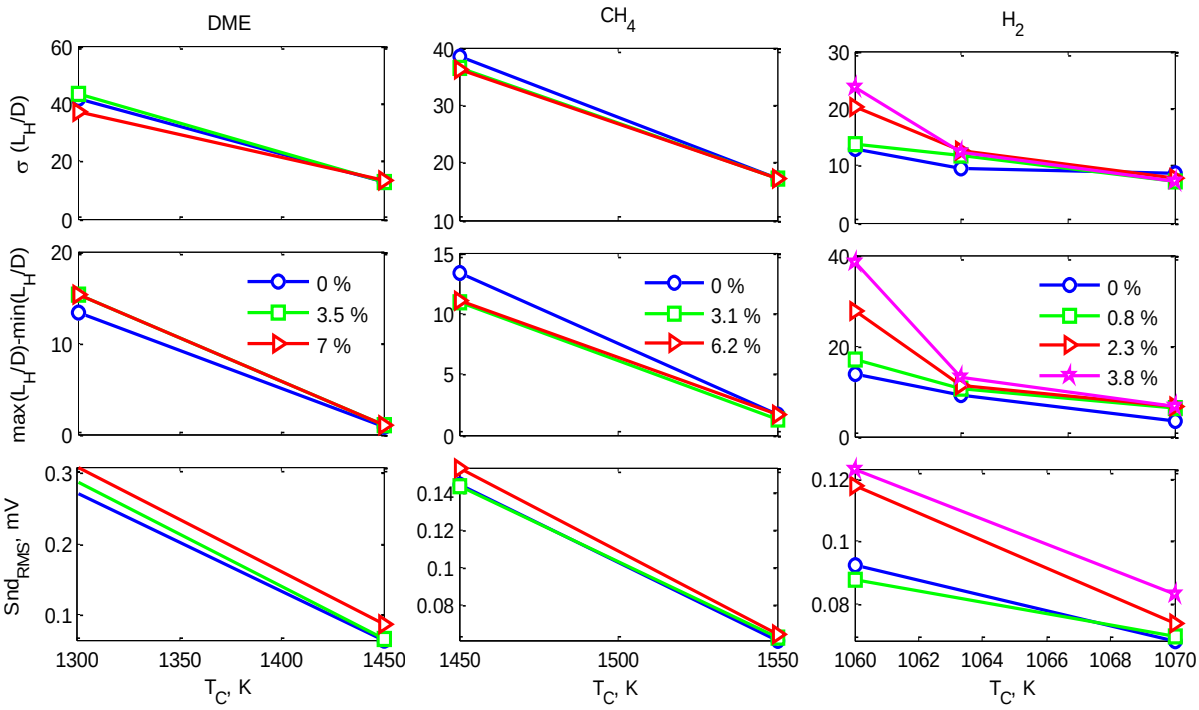

D. 3 Experimentally measured lift-off heights, flame base fluctuation range and sound pressure levels for various N_2O addition for three fuels: DME, CH_4, and H_2 (given in each column). N_2O addition is given as a percentage of the fuel issuing through the jet.

Chapter 14. **References**

[1] A.R.W. Macfarlane, M.J. Dunn, A.R. Masri, The influence of fuel type and partial premixing on the structure and behaviour of turbulent autoigniting flames, Proc. Combust. Inst. 37 (2019) 2277-2285.

[2] A.R.W. Macfarlane, M.J. Dunn, M. Juddoo, A.R. Masri, Stabilisation of turbulent auto-igniting dimethyl ether jet flames issuing into a hot vitiated coflow, Proc. Combust. Inst. 36 (2017) 1661-1668.

[3] A.R.W. Macfarlane, M. Dunn, M. Juddoo, A. Masri, The evolution of autoignition kernels in turbulent flames of dimethyl ether, Combust. Flame 197 (2018) 182-196.

[4] A.R.W. Macfarlane, M.J. Dunn, M. Juddoo, A.R. Masri, Stabilization of Turbulent Auto-Igniting DME Jets Issuing in Hot Vitiated Coflows, The Combustion Institute Australia & New Zealand N/A (2015) 372-375.

[5] A.R.W. Macfarlane, M.J. Dunn, M. Juddoo, A.R. Masri, High-Speed PLIF Measurements of OH and CH2O in Turbulent Auto Igniting Flames of DME, ACLDFMC N/A (2015) 57-60.

[6] A.R.W. Macfarlane, M.J. Dunn, M. Juddoo, A.R. Masri, Stabilization of Turbulent Auto-Igniting Hydrogen Jets Issuing in a Hot Vitiated Coflow, ASPACC 11th (2017).

[7] World Energy Council, World Energy Focus (annual publication), 2017.

[8] World Energy Council, World Energy Resources, accessed 2016. https://www.worldenergy.org/data/.

[9] World Energy Council, World Energy Resources: The Role of Natural Gas (Perspective from the 2016 World Energy Scenarios), Accessed 2017.

[10] W.J. Piel, Transportation fuels of the future?, Fuel Process. Technol. 71 (2001) 167-179.

[11] G. Kalghatgi, H. Levinsky, M. Colket, Future transportation fuels, Prog. Energy Combust. Sci. 69 (2018) 103-105.

[12] UCS, The Hidden Costs of Fossil Fuels. https://www.ucsusa.org/clean-energy/coal-and-other-fossil-fuels/hidden-cost-of-fossils#39, 2018.

[13] EPA, Environmental topics. https://www.epa.gov/environmental-topics/air-topics, 2018.

[14] J.E. Broadwell, W.J.A. Dahm, M.G. Mungal, Blowout of turbulent diffusion flames, Symp. (Int.) Combust 20 (1985) 303-310.

[15] L. Vanquickenborne, A. van Tiggelen, The stabilization mechanism of lifted diffusion flames, Combust. Flame 10 (1966) 59-69.

[16] K.M. Lyons, Toward an understanding of the stabilization mechanisms of lifted turbulent jet flames: Experiments, Prog. Energy Combust. Sci. 33 (2007) 211-231.

[17] W.J.A. Dahm, R.W. Dibble, Coflowing turbulent jet diffusion flame blowout, Symp. (Int.) Combust 22 (1989) 801-808.

[18] E. Mastorakos, Forced ignition of turbulent spray flames, Proc. Combust. Inst. 36 (2017) 2367-2383.

[19] R. Maly, Ignition model for spark discharges and the early phase of flame front growth, Symp. (Int.) Combust 18 (1981) 1747-1754.

[20] C.C. Huang, S.S. Shy, C.C. Liu, Y.Y. Yan, A transition on minimum ignition energy for lean turbulent methane combustion in flamelet and distributed regimes, Proc. Combust. Inst. 31 (2007) 1401-1409.

[21] K. Ishii, O. Aoki, Y. Ujiie, M. Kono, Investigation of ignition by composite sparks under high turbulence intensity conditions, Symp. (Int.) Combust 24 (1992) 1793-1798.

[22] I. Glassman, Combustion, 3rd ed., Academic Press 1987

[23] Y.A. Cengel, M.A. Boles, Thermodynamics: An engineering approach, McGraw-Hill, New York, 2011.

[24] O. Schulz, N. Noiray, Autoignition flame dynamics in sequential combustors, Combust. Flame 192 (2018) 86-100.

[25] O. Schulz, U. Doll, D. Ebi, J. Droujko, C. Bourquard, N. Noiray, Thermoacoustic instability in a sequential combustor: Large eddy simulation and experiments, Proc. Combust. Inst. 37 (2019) 5325-5332.

[26] K. Aditya, A. Gruber, C. Xu, T. Lu, A. Krisman, M.R. Bothien, J.H. Chen, Direct numerical simulation of flame stabilization assisted by autoignition in a reheat gas turbine combustor, Proc. Combust. Inst. 37 (2019) 2635-2642.

[27] J.W. Heffel, NOx emission reduction in a hydrogen fueled internal combustion engine at 3000 rpm using exhaust gas recirculation, Int. J. Hydrogen Energy 28 (2003) 1285-1292.

[28] P. Dagaut, A. Nicolle, Experimental study and detailed kinetic modeling of the effect of exhaust gas on fuel combustion: mutual sensitization of the oxidation of nitric oxide and methane over extended temperature and pressure ranges, Combust. Flame 140 (2005) 161-171.

[29] I. Boxx, M. Stöhr, C. Carter, W. Meier, Temporally resolved planar measurements of transient phenomena in a partially pre-mixed swirl flame in a gas turbine model combustor, Combust. Flame 157 (2010) 1510-1525.

[30] X. Zhen, Y. Wang, S. Xu, Y. Zhu, C. Tao, T. Xu, M. Song, The engine knock analysis – An overview, Applied Energy 92 (2012) 628-636.

[31] N. Kawahara, E. Tomita, Y. Sakata, Auto-ignited kernels during knocking combustion in a spark-ignition engine, Proc. Combust. Inst. 31 (2007) 2999-3006.

[32] R. Bounaceur, P.-A. Glaude, B. Sirjean, R. Fournet, P. Montagne, M. Vierling, M. Molière, Prediction of Auto-Ignition Temperatures and Delays for Gas Turbine Applications, doi:10.1115/GT2015-42011(2015) V04AT04A003.

[33] A. Koch, C. Naumann, W. Meier, M. Aigner, Experimental Study and Modeling of Autoignition of Natural Gas/Air-Mixtures Under Gas Turbine Relevant Conditions, doi:10.1115/GT2005-68405(2005) 311-318.

[34] E. Mastorakos, Ignition of turbulent non-premixed flames, Prog. Energy Combust. Sci. 35 (2009) 57-97.

[35] K.R. McManus, T. Poinsot, S.M. Candel, A review of active control of combustion instabilities, Prog. Energy Combust. Sci. 19 (1993) 1-29.

[36] T. Poinsot, Prediction and control of combustion instabilities in real engines, Proc. Combust. Inst. 36 (2017) 1-28.

[37] J. Shao, D.F. Davidson, R.K. Hanson, A shock tube study of ignition delay times in diluted methane, ethylene, propene and their blends at elevated pressures, Fuel. 225 (2018) 370-380.

[38] S. Deng, P. Zhao, M.E. Mueller, C.K. Law, Autoignition-affected stabilization of laminar nonpremixed DME/air coflow flames, Combust. Flame 162 (2015) 3437-3445.

[39] R. Cabra, T. Myhrvold, J.Y. Chen, R.W. Dibble, A.N. Karpetis, R.S. Barlow, Simultaneous laser raman-rayleigh-lif measurements and numerical modeling results of a lifted turbulent H_2/N_2 jet flame in a vitiated coflow, Proc. Combust. Inst. 29 (2002) 1881-1888.

[40] C.S. Yoo, R. Sankaran, J.H. Chen, Three-dimensional direct numerical simulation of a turbulent lifted hydrogen jet flame in heated coflow: flame stabilization and structure, J. Fluid Mech. 640 (2009) 453-481.

[41] A.R. Masri, R. Cao, S.B. Pope, G.M. Goldin, Pdf calculations of turbulent lifted flames of H2/N2 fuel issuing into a vitiated co-flow, Combust. Theor. Model 8 (2004) 1-22.

[42] E. Oldenhof, M.J. Tummers, E.H. van Veen, D.J.E.M. Roekaerts, Conditional flow field statistics of jet-in-hot-coflow flames, Combust. Flame 160 (2013) 1428-1440.

[43] C.S. Yoo, E.S. Richardson, R. Sankaran, J.H. Chen, A DNS study on the stabilization mechanism of a turbulent lifted ethylene jet flame in highly-heated coflow, Proc. Combust. Inst. 33 (2011) 1619-1627.

[44] C.M. Arndt, J.D. Gounder, W. Meier, M. Aigner, Auto-ignition and flame stabilization of pulsed methane jets in a hot vitiated coflow studied with high-speed laser and imaging techniques, Appl. Phys. B 108 (2012) 407-417.

[45] E. Oldenhof, M.J. Tummers, E.H. van Veen, D.J.E.M. Roekaerts, Transient response of the Delft jet-in-hot coflow flames, Combust. Flame 159 (2012) 697-706.

[46] R.L. Gordon, A.R. Masri, E. Mastorakos, Simultaneous Rayleigh temperature, OH- and CH_2O-LIF imaging of methane jets in a vitiated coflow, Combust. Flame 155 (2008) 181-195.

[47] R. Hilbert, D. Thévenin, Autoignition of turbulent non-premixed flames investigated using direct numerical simulations, Combust. Flame 128 (2002) 22-37.

[48] R.L. Gordon, A.R. Masri, S.B. Pope, G.M. Goldin, A numerical study of auto-ignition in turbulent lifted flames issuing into a vitiated co-flow, Combust. Theor. Model 11 (2007) 351-376.

[49] R. Saksena, J.A. Sutton, Transient and steady-state behavior of auto-igniting propane and dimethyl ether fuel jets in high-temperature vitiated coflows, Proc. Combust. Inst., doi:https://doi.org/10.1016/j.proci.2018.09.022(2018).

[50] E. Oldenhof, M.J. Tummers, E.H. van Veen, D.J.E.M. Roekaerts, Ignition kernel formation and lift-off behaviour of jet-in-hot-coflow flames, Combust. Flame 157 (2010) 1167-1178.

[51] R.E.H. Sims, W. Mabee, J.N. Saddler, M. Taylor, An overview of second generation biofuel technologies, Bioresour. Technol. 101 (2010) 1570-1580.

[52] C. Arcoumanis, C. Bae, R. Crookes, E. Kinoshita, The potential of di-methyl ether (DME) as an alternative fuel for compression-ignition engines: A review, Fuel. 87 (2008) 1014-1030.

[53] S.R.T. Turns, An introduction to combustion concepts and applications, Third ed., Mc Graw Hill 2012.

[54] C. Robinson, D.B. Smith, The auto-ignition temperature of methane, J. Hazard. Mater. 8 (1984) 199-203.

[55] T. Suzuki, Quantitative structure—property relationships for auto-ignition temperatures of organic compounds, Fire and Materials 18 (1994) 81-88.

[56] C.K. Westbrook, H.J. Curran, W.J. Pitz, J.F. Griffiths, C. Mohamed, S.K. Wo, The effects of pressure, temperature, and concentration on the reactivity of alkanes: Experiments and modeling in a rapid compression machine, Symp. (Int.) Combust 27 (1998) 371-378.

[57] C.K. Westbrook, Chemical kinetics of hydrocarbon ignition in practical combustion systems, Proc. Combust. Inst. 28 (2000) 1563-1577.

[58] N. Peters, G. Paczko, R. Seiser, K. Seshadri, Temperature cross-over and non-thermal runaway at two-stage ignition of n-heptane, Combust. Flame 128 (2002) 38-59.

[59] A. Cavaliere, M. de Joannon, Mild Combustion, Prog. Energy Combust. Sci. 30 (2004) 329-366.

[60] J.A. Miller, M.J. Pilling, J. Troe, Unravelling combustion mechanisms through a quantitative understanding of elementary reactions, Proc. Combust. Inst. 30 (2005) 43-88.

[61] D.L. Baulch, C.T. Bowman, C.J. Cobos, R.A. Cox, T. Just, J.A. Kerr, M.J. Pilling, D. Stocker, J. Troe, W. Tsang, R.W. Walker, J. Warnatz, Evaluated Kinetic Data for Combustion Modeling: Supplement II, J. Phys. Chem. Ref. Data 34 (2005) 757-1397.

[62] C.K. Westbrook, What Causes Hydrocarbon Autoignition? An on going debate, National Combustion Meeting, (2017).

[63] A. Burcat, K. Scheller, A. Lifshitz, Shock-tube investigation of comparative ignition delay times for C1-C5 alkanes, Combust. Flame 16 (1971) 29-33.

[64] P.G. Aleiferis, M.F. Rosati, Controlled autoignition of hydrogen in a direct-injection optical engine, Combust. Flame 159 (2012) 2500-2515.

[65] T. Goyal, D. Trivedi, O. Samimi Abianeh, Autoignition and flame spectroscopy of propane mixture in a rapid compression machine, Fuel. 233 (2018) 56-67.

[66] S.K. Ghai, S. De, A Review on Autoignition in Laminar and Turbulent Nonpremixed Flames, in: A.K. Agarwal, S. De, A. Pandey, A.P. Singh (Eds.), Combustion for Power Generation and Transportation: Technology, Challenges and Prospects, Springer Singapore, Singapore, 2017, pp. 11-37.

[67] J. Zhang, E. Hu, Z. Zhang, L. Pan, Z. Huang, Comparative Study on Ignition Delay Times of C1–C4 Alkanes, Energ Fuels 27 (2013) 3480-3487.

[68] E. Ranzi, A. Frassoldati, R. Grana, A. Cuoci, T. Faravelli, A.P. Kelley, C.K. Law, Hierarchical and comparative kinetic modeling of laminar flame speeds of hydrocarbon and oxygenated fuels, Prog. Energy Combust. Sci. 38 (2012) 468-501.

[69] J.M. Simmie, Detailed chemical kinetic models for the combustion of hydrocarbon fuels, Prog. Energy Combust. Sci. 29 (2003) 599-634.

[70] W.K. Metcalfe, S.M. Burke, S.S. Ahmed, H.J. Curran, A Hierarchical and Comparative Kinetic Modeling Study of C1 − C2 Hydrocarbon and Oxygenated Fuels, Int. J. Chem. Kinet. 45 (2013) 638-675.

[71] Y.X. Wang H, D.S. Joshi AV, A. Laskin, F. Egolfopoulos, USC mech version II, (2007).

[72] G. Fast, D. Kuhn, A.G. Class, U. Maas, Auto-ignition during instationary jet evolution of dimethyl ether (DME) in a high-pressure atmosphere, Combust. Flame 156 (2009) 200-213.

[73] U. Burke, K.P. Somers, P. O'Toole, C.M. Zinner, N. Marquet, G. Bourque, E.L. Petersen, W.K. Metcalfe, Z. Serinyel, H.J. Curran, An ignition delay and kinetic modeling study of methane, dimethyl ether, and their mixtures at high pressures, Combust. Flame 162 (2015) 315-330.

[74] L. Pan, S. Kokjohn, Z. Huang, Development and validation of a reduced chemical kinetic model for dimethyl ether combustion, 2015.

[75] L. Pan, S. Kokjohn, Z. Huang, Development and validation of a reduced chemical kinetic model for dimethyl ether combustion, Fuel. 160 (2015) 165-177.

[76] L. Pan, E. Hu, F. Deng, Z. Zhang, Z. Huang, Effect of pressure and equivalence ratio on the ignition characteristics of dimethyl ether-hydrogen mixtures, Int. J. Hydrogen Energy 39 (2014) 19212-19223.

[77] L. Pan, E. Hu, Z. Tian, F. Yang, Z. Huang, Experimental and Kinetic Study on Ignition Delay Times of Dimethyl Ether at High Temperatures, Energ Fuels 29 (2015) 3495-3506.

[78] H. Tsuji, Counterflow diffusion flames, Prog. Energy Combust. Sci. 8 (1982) 93-119.

[79] C.G. Fotache, T.G. Kreutz, C.K. Law, Ignition of counterflowing methane versus heated air under reduced and elevated pressures, Combust. Flame 108 (1997) 442-470.

[80] S. Deng, P. Zhao, D. Zhu, C.K. Law, NTC-affected ignition and low-temperature flames in nonpremixed DME/air counterflow, Combust. Flame 161 (2014) 1993-1997.

[81] X.L. Zheng, T.F. Lu, C.K. Law, C.K. Westbrook, H.J. Curran, Experimental and computational study of nonpremixed ignition of dimethyl ether in counterflow, Proc. Combust. Inst. 30 (2005) 1101-1109.

[82] A. Schönborn, P. Sayad, A.A. Konnov, J. Klingmann, Visualisation of propane autoignition in a turbulent flow reactor using OH^* chemiluminescence imaging, Combust. Flame 160 (2013) 1033-1043.

[83] B.C. Choi, S.H. Chung, An experimental study on turbulent lifted flames of methane in coflow jets at elevated temperatures, Fuel. 103 (2013) 956-962.

[84] J. Buckmaster, Edge-flames, Prog. Energy Combust. Sci. 28 (2002) 435-475.

[85] J.W. Dold, Flame propagation in a nonuniform mixture: Analysis of a slowly varying Triple Flame, Combust. Flame 76 (1989) 71-88.

[86] H. Phillips, Flame in a buoyant methane layer, Symp. (Int.) Combust 10 (1965) 1277-1283.

[87] J. Lee, S.H. Won, S.H. Jin, S.H. Chung, Lifted flames in laminar jets of propane in coflow air, Combust. Flame 135 (2003) 449-462.

[88] C.J. Lawn, Lifted flames on fuel jets in co-flowing air, Prog. Energy Combust. Sci. 35 (2009) 1-30.

[89] B.C. Choi, S.H. Chung, Autoignited laminar lifted flames of methane, ethylene, ethane, and n-butane jets in coflow air with elevated temperature, Combust. Flame 157 (2010) 2348-2356.

[90] S.H. Chung, Stabilization, propagation and instability of tribrachial triple flames, Proc. Combust. Inst. 31 (2007) 877-892.

[91] B.J. Lee, S.H. Chung, Stabilization of lifted tribrachial flames in a laminar nonpremixed jet, Combust. Flame 109 (1997) 163-172.

[92] N. Peters, Turbulent Combustion, Cambridge University Press, Cambridge, 2000.

[93] S. M. Al-Noman, S.K. Choi, S.H. Chung, Numerical study of laminar nonpremixed methane flames in coflow jets: Autoignited lifted flames with tribrachial edges and MILD combustion at elevated temperatures, Combust. Flame 171 (2016) 119-132.

[94] B.C. Choi, S.H. Chung, Autoignited laminar lifted flames of methane/hydrogen mixtures in heated coflow air, Combust. Flame 159 (2012) 1481-1488.

[95] B.C. Choi, K.N. Kim, S.H. Chung, Autoignited laminar lifted flames of propane in coflow jets with tribrachial edge and mild combustion, Combust. Flame 156 (2009) 396-404.

[96] S.M. Al-Noman, B.C. Choi, S.H. Chung, Autoignited lifted flames of dimethyl ether in heated coflow air, Combust. Flame 195 (2018) 75-83.

[97] K.N. Kim, S.H. Won, S.H. Chung, Characteristics of laminar lifted flames in coflow jets with initial temperature variation, Proc. Combust. Inst. 31 (2007) 947-954.

[98] R. Shan, C.S. Yoo, J.H. Chen, T. Lu, Computational diagnostics for n-heptane flames with chemical explosive mode analysis, Combust. Flame 159 (2012) 3119-3127.

[99] A. Krisman, E.R. Hawkes, M. Talei, A. Bhagatwala, J.H. Chen, Polybrachial structures in dimethyl ether edge-flames at negative temperature coefficient conditions, Proc. Combust. Inst. 35 (2015) 999-1006.

[100] P. Domingo, L. Vervisch, Triple flames and partially premixed combustion in autoignition of non-premixed turbulent mixtures, Symp. (Int.) Combust 26 (1996) 233-240.

[101] J.D. Blouch, C.K. Law, Effects of turbulence on nonpremixed ignition of hydrogen in heated counterflow, Combust. Flame 132 (2003) 512-522.

[102] H.G. Im, J.H. Chen, C.K. Law, Ignition of hydrogen-air mixing layer in turbulent flows, Symp. (Int.) Combust 27 (1998) 1047-1056.

[103] S.M. Correa, A.J. Dean, Turbulent broadening of autoignition limits, Symp. (Int.) Combust 25 (1994) 1293-1299.

[104] G.T. Kalghatgi, Blow-Out Stability of Gaseous Jet Diffusion Flames. Part I: In Still Air, Combust. Sci. Technol. 26 (1981) 233-239.

[105] A. Joedicke, N. Peters, M. Mansour, The stabilization mechanism and structure of turbulent hydrocarbon lifted flames, Proc. Combust. Inst. 30 (2005) 901-909.

[106] S. Lamige, J. Min, C. Galizzi, F. André, F. Baillot, D. Escudié, K.M. Lyons, On preheating and dilution effects in non-premixed jet flame stabilization, Combust. Flame 160 (2013) 1102-1111.

[107] K.N. Kim, S.H. Won, S.H. Chung, Characteristics of turbulent lifted flames in coflow jets with initial temperature variation, Proc. Combust. Inst. 31 (2007) 1591-1598.

[108] R. Cabra, J.Y. Chen, R.W. Dibble, A.N. Karpetis, R.S. Barlow, Lifted methane–air jet flames in a vitiated coflow, Combust. Flame 143 (2005) 491-506.

[109] R.L. Gordon, S.H. Stårner, A.R. Masri, R.W. Bilger, Further Characterisation of Lifted Hydrogen and Methane Flames Issuing into a Vitiated Coflow, Proceedings of the 5th Asia-Pacific Conference on Combustion University of Adelaide 333-336 (2005).

[110] B. Johannessen, A. North, R. Dibble, T. Løvås, Experimental studies of autoignition events in unsteady hydrogen–air flames, Combust. Flame 162 (2015) 3210-3219.

[111] Z. Wu, A.R. Masri, R.W. Bilger, An Experimental Investigation of the Turbulence Structure of a Lifted H2/N2 Jet Flame in a Vitiated Co-Flow, Flow. Turb. Combust. 76 (2006) 61-81.

[112] C. Duwig, M.J. Dunn, Large Eddy Simulation of a premixed jet flame stabilized by a vitiated co-flow: Evaluation of auto-ignition tabulated chemistry, Combust. Flame 160 (2013) 2879-2895.

[113] P.R. Medwell, P.A.M. Kalt, B.B. Dally, Imaging of diluted turbulent ethylene flames stabilized on a Jet in Hot Coflow (JHC) burner, Combust. Flame 152 (2008) 100-113.

[114] F. Eitel, J. Pareja, D. Geyer, A. Johchi, F. Michel, W. Elsäßer, A. Dreizler, A novel plasma heater for auto-ignition studies of turbulent non-premixed flows, Exp. Fluids 56 (2015) 186.

[115] J. Ye, P.R. Medwell, M.J. Evans, B.B. Dally, Characteristics of turbulent n-heptane jet flames in a hot and diluted coflow, Combust. Flame 183 (2017) 330-342.

[116] L.D. Arteaga Mendez, M.J. Tummers, E.H. van Veen, D.J.E.M. Roekaerts, Effect of hydrogen addition on the structure of natural-gas jet-in-hot-coflow flames, Proc. Combust. Inst. 35 (2015) 3557-3564.

[117] Y. Tu, H. Liu, W. Yang, Flame Characteristics of CH_4/H_2 on a Jet-in-Hot-Coflow Burner Diluted by N_2, CO_2, and H_2O, Energ Fuels 31 (2017) 3270-3280.

[118] R. Cabra, Turbulent Jet Flames into a Viated Coflow, University of California, Berkeley, 2003, pp. 261.

[119] C.M. Arndt, W. Meier, Influence of Boundary Conditions on the Flame Stabilization Mechanism and on Transient Auto-ignition in the DLR Jet-in-Hot-Coflow Burner, Flow. Turb. Combust., doi:10.1007/s10494-018-9991-6(2018).

[120] C.M. Arndt, M.J. Papageorge, F. Fuest, J.A. Sutton, W. Meier, M. Aigner, The role of temperature, mixture fraction, and scalar dissipation rate on transient methane injection and auto-ignition in a jet in hot coflow burner, Combust. Flame 167 (2016) 60-71.

[121] M.J. Papageorge, C. Arndt, F. Fuest, W. Meier, J.A. Sutton, High-speed mixture fraction and temperature imaging of pulsed, turbulent fuel jets auto-igniting in high-temperature, vitiated co-flows, Exp. Fluids 55 (2014).

[122] C.M. Arndt, R. Schießl, J.D. Gounder, W. Meier, M. Aigner, Flame stabilization and auto-ignition of pulsed methane jets in a hot coflow: Influence of temperature, Proc. Combust. Inst. 34 (2013) 1483-1490.

[123] C.N. Markides, E. Mastorakos, An experimental study of hydrogen autoignition in a turbulent co-flow of heated air, Proc. Combust. Inst. 30 (2005) 883-891.

[124] T. Echekki, S.F. Ahmed, Turbulence effects on the autoignition of DME in a turbulent co-flowing jet, Combust. Flame 178 (2017) 70-81.

[125] T. Echekki, S.F. Ahmed, Autoignition of n-heptane in a turbulent co-flowing jet, Combust. Flame 162 (2015) 3829-3846.

[126] Z. Luo, C.S. Yoo, E.S. Richardson, J.H. Chen, C.K. Law, T. Lu, Chemical explosive mode analysis for a turbulent lifted ethylene jet flame in highly-heated coflow, Combust. Flame 159 (2012) 265-274.

[127] E. Mastorakos, T.A. Baritaud, T.J. Poinsot, Numerical simulations of autoignition in turbulent mixing flows, Combust. Flame 109 (1997) 198-223.

[128] T. Echekki, J.H. Chen, Direct numerical simulation of autoignition in non-homogeneous hydrogen-air mixtures, Combust. Flame 134 (2003) 169-191.

[129] S. Cao, T. Echekki, Autoignition in nonhomogeneous mixtures: Conditional statistics and implications for modeling, Combust. Flame 151 (2007) 120-141.

[130] S. Sreedhara, K.N. Lakshmisha, Direct numerical simulation of autoignition in a non-premixed, turbulent medium, Proc. Combust. Inst. 28 (2000) 25-33.

[131] T. Echekki, J.H. Chen, High-temperature combustion in autoigniting non-homogeneous hydrogen/air mixtures, Proc. Combust. Inst. 29 (2002) 2061-2068.

[132] S. Sreedhara, K.N. Lakshmisha, Autoignition in a non-premixed medium: DNS studies on the effects of three-dimensional turbulence, Proc. Combust. Inst. 29 (2002) 2051-2059.

[133] K. Gkagkas, R.P. Lindstedt, Transported PDF modelling with detailed chemistry of pre- and auto-ignition in CH4/air mixtures, Proc. Combust. Inst. 31 (2007) 1559-1566.

[134] S.M. Mir Najafizadeh, M.T. Sadeghi, R. Sotudeh-Gharebagh, D.J.E.M. Roekaerts, Chemical structure of autoignition in a turbulent lifted H2/N2 jet flame issuing into a vitiated coflow, Combust. Flame 160 (2013) 2928-2940.

[135] R.L. Gordon, A.R. Masri, S.B. Pope, G.M. Goldin, Transport budgets in turbulent lifted flames of methane autoigniting in a vitiated co-flow, Combust. Flame 151 (2007) 495-511.

[136] O. Schulz, T. Jaravel, T. Poinsot, B. Cuenot, N. Noiray, A criterion to distinguish autoignition and propagation applied to a lifted methane–air jet flame, Proc. Combust. Inst. 36 (2017) 1637-1644.

[137] S.S. Patwardhan, S. De, K.N. Lakshmisha, B.N. Raghunandan, CMC simulations of lifted turbulent jet flame in a vitiated coflow, Proc. Combust. Inst. 32 (2009) 1705-1712.

[138] I. Stanković, A. Triantafyllidis, E. Mastorakos, C. Lacor, B. Merci, Simulation of Hydrogen Auto-Ignition in a Turbulent Co-flow of Heated Air with LES and CMC Approach, Flow. Turb. Combust. 86 (2011) 689-710.

[139] S. Navarro-Martinez, A. Kronenburg, LES–CMC simulations of a lifted methane flame, Proc. Combust. Inst. 32 (2009) 1509-1516.

[140] P. Domingo, L. Vervisch, D. Veynante, Large-eddy simulation of a lifted methane jet flame in a vitiated coflow, Combust. Flame 152 (2008) 415-432.

[141] A.M. Steinberg, R. Sadanandan, C. Dem, P. Kutne, W. Meier, Structure and stabilization of hydrogen jet flames in cross-flows, Proc. Combust. Inst. 34 (2013) 1499-1507.

[142] J.A. Wagner, M.W. Renfro, B.M. Cetegen, Premixed jet flame behavior in a hot vitiated crossflow of lean combustion products, Combust. Flame 176 (2017) 521-533.

[143] J. Sidey, E. Mastorakos, R.L. Gordon, Simulations of Autoignition and Laminar Premixed Flames in Methane/Air Mixtures Diluted with Hot Products, Combust. Sci. Technol. 186 (2014) 453-465.

[144] N.L. Le Tan, M. Djehiche, C.D. Jain, P. Dagaut, G. Dayma, Quantification of HO_2 and other products of dimethyl ether oxidation (H_2O_2, H_2O, and CH_2O) in a jet-stirred reactor at elevated temperatures by low-pressure sampling and continuous-wave cavity ring-down spectroscopy, Fuel. 158 (2015) 248-252.

[145] P.R. Medwell, D.L. Blunck, B.B. Dally, The role of precursors on the stabilisation of jet flames issuing into a hot environment, Combust. Flame 161 (2014) 465-474.

[146] D. Thevenin, S. Candel, Diffusion and premixed flame ignition dynamics in a field of variable strain rate, Symp. (Int.) Combust 25 (1994) 1547-1554.

[147] T.G. Kreutz, C.K. Law, Ignition in nonpremixed counterflowing hydrogen versus heated air: Computational study with detailed chemistry, Combust. Flame 104 (1996) 157-175.

[148] V. Gopalakrishnan, J. Abraham, Effects of multicomponent diffusion on predicted ignition characteristics of an n-heptane diffusion flame, Combust. Flame 136 (2004) 557-566.

[149] W. Han, V. Raman, Z. Chen, LES/PDF modeling of autoignition in a lifted turbulent flame: Analysis of flame sensitivity to differential diffusion and scalar mixing time-scale, Combust. Flame 171 (2016) 69-86.

[150] A. Liñán, The asymptotic structure of counterflow diffusion flames for large activation energies, Acta Astronautica 1 (1974) 1007-1039.

[151] ReactionDesign, CHEMKIN 15152, San diego, 2016.

[152] D.G. Goodwin, H.K. Moffat, R.L. Speth, Cantera: An object- oriented software toolkit for chemical kinetics, thermodynamics, and transport processes, URL: http://code. google. com/p/cantera, (2012).

[153] S. Liu, J.C. Hewson, J.H. Chen, Nonpremixed n-heptane autoignition in unsteady counterflow, Combust. Flame 145 (2006) 730-739.

[154] S. Liu, J.C. Hewson, J.H. Chen, H. Pitsch, Effects of strain rate on high-pressure nonpremixed n-heptane autoignition in counterflow, Combust. Flame 137 (2004) 320-339.

[155] H.G. Im, L.L. Raja, R.J. Kee, L.R. Petzold, A Numerical Study of Transient Ignition in a Counterflow Nonpremixed Methane-Air Flame Using Adaptive Time Integration, Combust. Sci. Technol. 158 (2000) 341-363.

[156] S.D. Mason, J.H. Chen, H.G. Im, Effects of unsteady scalar dissipation rate on ignition of non-premixed hydrogen/air mixtures in counterflow, Proc. Combust. Inst. 29 (2002) 1629-1636.

[157] J.B. Martz, G.A. Lavoie, H.G. Im, R.J. Middleton, A. Babajimopoulos, D.N. Assanis, The propagation of a laminar reaction front during end-gas auto-ignition, Combust. Flame 159 (2012) 2077-2086.

[158] A. Krisman, E.R. Hawkes, J.H. Chen, The structure and propagation of laminar flames under autoignitive conditions, Combust. Flame 188 (2018) 399-411.

[159] A.C.Eckbeth, Laser Diagnostics for combustion temperature and species, 1988.

[160] P.H. Egon, L. Sven, Laser diagnostics for studies of turbulent combustion, Meas. Sci. Technol. 11 (2000) R37.

[161] G. Laufer, Introduction to Optics and Laser's in Engineering, Cambridge University Press, Cambridge University Press, 1996.

[162] K. Kohse-Höinghaus, Laser techniques for the quantitative detection of reactive intermediates in combustion systems, Prog. Energy Combust. Sci. 20 (1994) 203-279.

[163] D.R. Crosley, R.K. Lengel, Relative transition probabilities and the electronic transition moment in the A-X system of OH, J. Quant. Spectrosc. Radiat. Transfer 15 (1975) 579-591.

[164] S. Hammack, C. Carter, C. Wuensche, T. Lee, Continuous hydroxyl radical planar laser imaging at 50 kHz repetition rate, Appl. Opt. 53 (2014) 5246-5251.

[165] M. Tamura, P.A. Berg, J.E. Harrington, J. Luque, J.B. Jeffries, G.P. Smith, D.R. Crosley, Collisional Quenching of CH(A), OH(A), and NO(A) in Low Pressure Hydrocarbon Flames, Combust. Flame 114 (1998) 502-514.

[166] J.B. Kelman, A.R. Masri, Quantitative imaging of temperature and OH in turbulent diffusion flames by using a single laser source, Appl. Opt. 33 (1994) 3992-3999.

[167] Z. Yin, C.D. Carter, W.R. Lempert, Effects of signal corrections on measurements of temperature and OH concentrations using laser-induced fluorescence, Appl. Phys. B 117 (2014) 707-721.

[168] P. Desgroux, L. Gasnot, J.F. Pauwels, L.R. Sochet, Correction of LIF temperature measurements for laser absorption and fluorescence trapping in a flame, Appl. Phys. B 61 (1995) 401-407.

[169] D.R.C. J. Luque, LIFBASE database and spectral simulation for diatomic molecules, SRI International Report MP-99-009, 1999.

[170] H.N. Najm, P.H. Paul, C.J. Mueller, P.S. Wyckoff, On the Adequacy of Certain Experimental Observables as Measurements of Flame Burning Rate, Combust. Flame 113 (1998) 312-332.

[171] D.J. Micka, J.F. Driscoll, Stratified jet flames in a heated (1390K) air cross-flow with autoignition, Combust. Flame 159 (2012) 1205-1214.

[172] H. Haessler, H. Bockhorn, C. Pfeifer, D. Kuhn, Formaldehyde-LIF of Dimethyl Ether During Auto-ignition at Elevated Pressures, Flow. Turb. Combust. 89 (2011) 249-259.

[173] J.E. Harrington, K.C. Smyth, Laser-induced fluorescence measurements of formaldehyde in a methane/air diffusion flame, Chem. Phys. Lett. 202 (1993) 196-202.

[174] S. Böckle, J. Kazenwadel, T. kunzelmann, D.-I. Shin, C. Schulz, J. Wolfrum, Simultaneous single-shot laser-based imaging of formaldehyde, OH, and temperature in turbulent flames, Proc. Combust. Inst. 28 (2000) 279-286.

[175] D.I. Shin, T. Dreier, J. Wolfrum, Spatially resolved absolute concentration and fluorescence-lifetime determination of H2CO in atmospheric-pressure CH4/air flames, Appl. Phys. B 72 (2001) 257-261.

[176] C. Brackmann, J. Bood, M. AldÉn, G. Pengloan, Ö. Andersson, Quantitative Measurements of Species and Temperature in a Dme-Air Counterflow Diffusion Flame Using Laser Diagnostic Methods, Combust. Sci. Technol. 178 (2006) 1165-1184.

[177] K.N. Gabet, J.A. Sutton, Narrowband versus broadband excitation for CH2O PLIF imaging in flames using a frequency-tripled Nd:YAG laser, Exp. Fluids 55 (2014).

[178] C. Brackmann, J. Nygren, X. Bai, Z. Li, H. Bladh, B. Axelsson, I. Denbratt, L. Koopmans, P.-E. Bengtsson, M. Aldén, Laser-induced fluorescence of formaldehyde in combustion using third harmonic Nd:YAG laser excitation, Spectrochim. ActA A 59 (2003) 3347-3356.

[179] P.H. Paul, H.N. Najm, Planar laser-induced fluorescence imaging of flame heat release rate, Symp. (Int.) Combust 27 (1998) 43-50.

[180] B. Coriton, M. Zendehdel, S. Ukai, A. Kronenburg, O.T. Stein, S.-K. Im, M. Gamba, J.H. Frank, Imaging measurements and LES-CMC modeling of a partially-premixed turbulent dimethyl ether/air jet flame, Proc. Combust. Inst. 35 (2015) 1251-1258.

[181] S. Popp, F. Hunger, S. Hartl, D. Messig, B. Coriton, J.H. Frank, F. Fuest, C. Hasse, LES flamelet-progress variable modeling and measurements of a turbulent partially-premixed dimethyl ether jet flame, Combust. Flame 162 (2015) 3016-3029.

[182] B.O. Ayoola, R. Balachandran, J.H. Frank, E. Mastorakos, C.F. Kaminski, Spatially resolved heat release rate measurements in turbulent premixed flames, Combust. Flame 144 (2006) 1-16.

[183] F. Ossler, T. Metz, M. Aldén, Picosecond laser-induced fluorescence from gas-phase polycyclic aromatic hydrocarbons at elevated temperatures. I. Cell measurements, Appl. Phys. B 72 (2001) 465-478.

[184] T.B. Settersten, A. Dreizler, R.L. Farrow, Temperature- and species-dependent quenching of CO B probed by two-photon laser-induced fluorescence using a picosecond laser, J. Chem. Phys. 117 (2002) 3173.

[185] T. Metz, X. Bai, F. Ossler, M. Aldén, Fluorescence lifetimes of formaldehyde (H_2CO) in the band system at elevated temperatures and pressures, Spectrochim. ActA A 60 (2004) 1043-1053.

[186] Y. Yamasaki, A. Tezaki, Non-linear pressure dependence of A-state fluorescence lifetime of formaldehyde, Appl. Phys. B 80 (2005) 791-795.

[187] K. Shibuya, E.K.C. Lee, Vibrational and electronic energy transfers from a single vibronic level of H_2CO (A, 1A,2), the 41 level, J. Chem. Phys. 69 (1978) 758.

[188] D.C. Kyritsis, V.S. Santoro, A. Gomez, The effect of temperature correction on the measured thickness of formaldehyde zones in diffusion flames for 355 nm excitation, Exp. Fluids 37 (2004) 769-772.

[189] D J Clouthier, D.A. Ramsay, The Spectroscopy of Formaldehyde and Thioformaldehyde, Annu. Rev. Phys. Chem. 34 (1983) 31-58.

[190] R.L. Gordon, A.R. Masri, E. Mastorakos, Heat release rate as represented by [OH] × [CH_2O] and its role in autoignition, Combust. Theor. Model 13 (2009) 645-670.

[191] F. Eitel, J. Pareja, A. Johchi, B. Böhm, D. Geyer, A. Dreizler, Temporal evolution of auto-ignition of ethylene and methane jets propagating into a turbulent hot air co-flow vitiated with NOx, Combust. Flame 177 (2017) 193-206.

[192] P.R. Medwell, P.A.M. Kalt, B.B. Dally, Simultaneous imaging of OH, formaldehyde, and temperature of turbulent nonpremixed jet flames in a heated and diluted coflow, Combust. Flame 148 (2007) 48-61.

[193] M. Röder, T. Dreier, C. Schulz, Simultaneous measurement of localized heat release with OH/CH_2O-LIF imaging and spatially integrated OH^* chemiluminescence in turbulent swirl flames, Appl. Phys. B 107 (2012) 611-617.

[194] Z.S. Li, B. Li, Z.W. Sun, X.S. Bai, M. Aldén, Turbulence and combustion interaction: High resolution local flame front structure visualization using simultaneous single-shot PLIF imaging of CH, OH, and CH_2O in a piloted premixed jet flame, Combust. Flame 157 (2010) 1087-1096.

[195] M. Dunn, Finite-Rate Chemistry Effects in Turbulent Premixed Combustion, The University of Sydney, The University of Sydney, 2008.

[196] C.R. Wilke, A Viscosity Equation for Gas Mixtures, J. Chem. Phys. 18 (1950) 517-519.

[197] J. Kojima, Y. Ikeda, T. Nakajima, Basic aspects of OH(A), CH(A), and C_2(d) chemiluminescence in the reaction zone of laminar methane–air premixed flames, Combust. Flame 140 (2005) 34-45.

[198] J. Kojima, Y. Ikeda, T. Nakajima, Spatially resolved measurement of OH^*, CH^*, and C_2^* chemiluminescence in the reaction zone of laminar methane/air premixed flames, Proc. Combust. Inst. 28 (2000) 1757-1764.

[199] T. Trindade, A. Ferreira, E. Fernandes, Characterization of Combustion Chemiluminescence: An Image Processing Approach, Proc. Technol. 17 (2014) 194-201.

[200] T. Kathrotia, M. Fikri, M. Bozkurt, M. Hartmann, U. Riedel, C. Schulz, Study of the H+O+M reaction forming OH^*: Kinetics of OH^* chemiluminescence in hydrogen combustion systems, Combust. Flame 157 (2010) 1261-1273.

[201] T. Fiala, T. Sattelmayer, Modeling of the continuous (blue) radiation in hydrogen flames, Int. J. Hydrogen Energy 41 (2016) 1293-1303.

[202] R.W. Schefer, W.D. Kulatilaka, B.D. Patterson, T.B. Settersten, Visible emission of hydrogen flames, Combust. Flame 156 (2009) 1234-1241.

[203] R. Speth, Quasi-one-dimensional, unsteady reacting flow solver, https://github.com/speth/ember, (2015).

[204] R.L. Speth, W.H. Green, S. MacNamara, G. Strang, Balanced Splitting and Rebalanced Splitting, SIAM Journal on Numerical Analysis 51 (2013) 3084-3105.

[205] R. Cabra, J.W. Chen, R.W. Dibble, A.N. Karpetis, R.S. Barlow, Lifted methane–air jet flames in a vitiated coflow, Combust. Flame 143 (2005) 491-506.

[206] M.C. Lee, S.B. Seo, J.H. Chung, Y.J. Joo, D.H. Ahn, Industrial gas turbine combustion performance test of DME to use as an alternative fuel for power generation, Fuel. 88 (2009) 657-662.

[207] H.J. Curran, W.J. Pitz, C.K. Westbrook, P. Dagaut, J.C. Boettner, M. Cathonnet, A wide range modeling study of dimethyl ether oxidation, Int. J. Chem. Kinet. 30 (1998) 229-241.

[208] Z. Wu, Q. Zhang, T. Bao, L. Li, J. Deng, Z. Hu, Experimental and numerical study on ethanol and dimethyl ether lifted flames in a hot vitiated co-flow, Fuel Process. Technol. 184 (2016) 620-628.

[209] E. Oldenhof, M.J. Tummers, E.H. van Veen, D.J.E.M. Roekaerts, Role of entrainment in the stabilisation of jet-in-hot-coflow flames, Combust. Flame 158 (2011) 1553-1563.

[210] S. Meares, V.N. Prasad, M. Juddoo, K.H. Luo, A.R. Masri, Simultaneous planar and volume cross-LIF imaging to identify out-of-plane motion, Proc. Combust. Inst. 35 (2015) 3813-3820.

[211] J. Pareja, A. Johchi, T. Li, A. Dreizler, B. Böhm, A study of the spatial and temporal evolution of auto-ignition kernels using time-resolved tomographic OH-LIF, Proc. Combust. Inst., doi:https://doi.org/10.1016/j.proci.2018.06.028(2018).

[212] G.P. Smith, D.M. Golden, M. Frenklach, N.W. Moriarty, B. Eiteneer, M. Goldenberg, C.T. Bowman, R.K.H. Soonho Song, W.C. Gardiner Jr., V.L. Lissianski, Z. Qin, GRI 3.0, URL: http://www.me.berkeley.edu/gri_mech/, (2018).

[213] Y. Li, C.-W. Zhou, H.J. Curran, An extensive experimental and modeling study of 1-butene oxidation, Combust. Flame 181 (2017) 198-213.

[214] P.R. Medwell, M.J. Evans, Q.N. Chan, V.R. Katta, Laminar Flame Calculations for Analyzing Trends in Autoignitive Jet Flames in a Hot and Vitiated Coflow, Energ Fuels 30 (2016) 8680-8690.

[215] E.M. Fisher, W.J. Pitz, H.J. Curran, C.K. Westbrook, Detailed chemical kinetic mechanisms for combustion of oxygenated fuels, Proc. Combust. Inst. 28 (2000) 1579-1586.

[216] S.L. Fischer, F.L. Dryer, H.J. Curran, The reaction kinetics of dimethyl ether. I: High-temperature pyrolysis and oxidation in flow reactors, Int. J. Chem. Kinet. 32 (2000) 713-740.

[217] Z. Zhao, M. Chaos, A. Kazakov, F.L. Dryer, Thermal decomposition reaction and a comprehensive kinetic model of dimethyl ether, Int. J. Chem. Kinet. 40 (2008) 1-18.

[218] B. Han, C.J. Sung*, M. Nishioka, Effects of Vitiated Air on Hydrogen Ignition in a High-speed Laminar Mixing Layer, Combust. Sci. Technol. 176 (2004) 305-330.

[219] M. Slack, A. Grillo, Investigation of hydrogen-air ignition sensitized by nitric oxide and by nitrogen dioxide, NASA Report CR-2896, (1977).

[220] P. Glarborg, M. Østberg, M.U. Alzueta, K. Dam-Johansen, J.A. Miller, The recombination of hydrogen atoms with nitric oxide at high temperatures, Symp. (Int.) Combust 27 (1998) 219-226.

[221] O. Mathieu, J.M. Pemelton, G. Bourque, E.L. Petersen, Shock-induced ignition of methane sensitized by NO_2 and N_2O, Combust. Flame 162 (2015) 3053-3070.

[222] O. Mathieu, E.L. Petersen, Experimental and modeling study on the high-temperature oxidation of Ammonia and related NOx chemistry, Combust. Flame 162 (2015) 554-570.

[223] A. Frassoldati, T. Faravelli, E. Ranzi, Kinetic modeling of the interactions between NO and hydrocarbons at high temperature, Combust. Flame 135 (2003) 97-112.